530-H-14
NAS1.26;3177
OCT 5 1979
COMPLETED
ORIGINAL

NASA Contractor Report 3177

Effect of Grazing Flow on the Acoustic Impedance of Helmholtz Resonators Consisting of Single and Clustered Orifices

Alan S. Hersh and Bruce Walker

CONTRACT NAS3-19745
AUGUST 1979

NASA

183

NASA Contractor Report 3177

Effect of Grazing Flow on the Acoustic Impedance of Helmholtz Resonators Consisting of Single and Clustered Orifices

Alan S. Hersh and Bruce Walker
Hersh Acoustical Engineering
Chatsworth, California

Prepared for
Lewis Research Center
under Contract NAS3-19745

National Aeronautics
and Space Administration

Scientific and Technical
Information Branch

1979

TABLE OF CONTENTS

SUMMARY 1

DEFINITION OF SYMBOLS 2

1. INTRODUCTION 5

2. SINGLE ORIFICE IMPEDANCE MODEL 7

   2.1 Derivation of Governing Equations 8

   2.2 Boundary Conditions 12

   2.3 Semi-empirical Solution 13

3. SINGLE ORIFICE MEASUREMENT PROGRAM 17

   3.1 Two-Microphone Method 18

   3.2 Determination of C_D 20

   3.3 Comparison Between Predicted and Measured Impedance .. 25

   3.4 Thick Orifices 29

   3.5 Resonator Self-Noise 31

4. IMPEDANCE OF CLUSTERED ORIFICES 32

   4.1 Zero Grazing Flow, Low Sound Amplitude Results 33

   4.2 Effect of Grazing Flow 35

5. CONCLUSIONS 38

APPENDIXES

   A - SINGLE ORIFICE DATA 40

   B - SUMMARY OF FREQUENCY SWEEP DATA FOR SPECIAL MODEL FOR $V_\infty^* = 60$ m/sec and $P_i^* = 120$ dB 66

   C - THICK ORIFICE DATA 67

   D - CLUSTERED ORIFICE DATA 76

REFERENCES 104

TABLES 106

FIGURES 110

SUMMARY

A semi-empirical fluid mechanical model is derived for the acoustic behavior of thin-walled single orifice Helmholtz resonators in a grazing flow environment. The model assumes that the flow field incident to a resonator orifice consists of a spherical sound particle velocity field superimposed upon a mean grazing flow. The incident and cavity sound fields are connected in terms of an orifice discharge coefficient whose values are determined experimentally using the two-microphone method. With regard to its application to aircraft engines, the most important finding of this study is that at high grazing flow speeds, acoustic resistance is almost linearly proportional to the grazing flow speed and almost independent of incident sound pressure. The corresponding values of reactance are much smaller and tend towards zero for increasing grazing flow speed. Because of their insensitivity to the incident sound, the impedance of Helmholtz resonators at high grazing flow speeds is almost "linear".

The effects of grazing flow on the acoustic behavior of thick-walled single orifice Helmholtz resonators were studied experimentally. Test results showed both resistance and reactance to become increasingly less sensitive to the grazing flow as the ratio of plate thickness to orifice diameter increased.

Loud resonant tones were observed to radiate from single orifice Helmholtz resonators due to interaction between the grazing flow shear layer and the resonator cavity. The tones occurred at a grazing flow speed defined as $(V_\infty^*)_{res} = f_{res}^* \, d^*/0.26$ where f_{res}^* is the resonator classical Helmholtz resonant frequency and d^* is the orifice diameter. Measurements show that for grazing flow speeds greater than $(V_\infty^*)_{res}$, the grazing flow dominates the resonator behavior and for grazing flow speeds less than $(V_\infty^*)_{res}$, the sound particle velocity field dominates the resonator behavior.

The two-microphone method was also used to measure the effect of grazing flow on the impedance of Helmholtz resonators consisting of clusters of orifices. The study showed that interaction between nearby orifices occur only for those orifices whose centers are aligned parallel to the grazing flow. Interaction does not occur for orifices whose centers are aligned perpendicular to the grazing flow. In general, both resistance and reactance are virtually independent of orifice relative spacing and number. Orifice end correction, on the other hand, is quite dependent upon orifice spacing. It is fairly insensitive to the number of orifices. These findings are valid with and without grazing flow.

DEFINITION OF SYMBOLS

Symbol	Definition
A; A_f	orifice area; also Fok area defined by Fig. 1.
A_{min}	minimum area enclosed by orifices
c	speed of sound (meters/sec)
c_D	discharge coefficient defined by Eq. (8)
d	diameter of coefficient (meters)
d_e	orifice inertial length (meters)
D	diameter of cylindrical cavity (meters)
E	small parameter defined by Eq. (8)
$\tilde{E}$	small parameter defined by Eq. (26)
b_1	special parameter defined by Eq. (28b)
$f(t)$; f	special function defined by Eq. (14); also frequency
$F(t)$	function of time defined by Eq. (29)
$G(t)$	special function defined by Eq. (24)
L	cavity depth (meters)
L_e	resonator characteristic length (meters)
M_∞	grazing flow Mach number (V_∞/c)
N	number of orifices backed by a common cavity
p	acoustic pressure (Newtons/meters^2)
P_i	amplitude of incident sound wave (Newtons/meters^2)
P_c	amplitude of cavity sound wave (Newtons/meters^2)
q'	sound particle velocity (meters/sec)
r	radial coordinate (meters)
R_o	orifice area-averaged acoustic resistance (Kg/meters^2/sec)
S; S_f	separation distance between adjacent array (m); Fok separation parameter defined in Fig. 1.
S_o	orifice area (meters^2)
S_{vc}	orifice vena contracta area (meters^2)
S_∞	defined in Fig. 8 (meters)
t	time (sec)

Symbol	Definition
u_{vc}	acoustic particle velocity at orifice vena contracta (meters/sec)
u,v,w	radial, polar, azimuthal acoustic particle velocity components (meters/sec)
V_c	resonator cavity volume (meters^3)
V_∞	grazing flow speed (meters/sec)
d_e	resonator orifice inertial length (meters)
X_o	resonator orifice area-averaged reactance (Kg/meters^2/sec)
Z_o	resonator orifice area-averaged impedance (Kg/meters^2/sec)
α	parameter defined by Eq. (20)
ε	small parameter defined by Eq. (8)
ρ	fluid density (Kg/meters^3)
δ	grazing flow boundary-layer thickness (meters)
δ_o	orifice end correction (meters)
ξ	orifice array interaction parameter (d/D)
ω	incident sound field radian frequency (Hz)
η	nondimensional parameter defined by Eq. (46)
σ	resonator orifice percent open area
τ	orifice plate thickness (meters)
$\psi'(\xi)$	Fok interaction function
θ	spherical coordinate polar angle
ϕ	spherical coordinate azimuthal angle
$\phi_{ic}=-\phi_{ci}$	phase angle shift across orifice (deg.)

Subscripts	
i	incident
c	cavity
N	refers to N orifices
BL	boundary layer
o	orifice
o,N	orifice referenced to N
res	refers to resonator resonant frequency
v.c.	refers to orifice vena contracta

Subscripts	Definition
t	refers to total resonator

Superscripts	
( )'	refers to fluctuating quantities
( )*	refers to dimensional quantities

1. INTRODUCTION

The application of arrays of cavity-backed orifices as sound absorbing devices in the inlet and exhaust of jet engines has generated the need to understand their acoustic behavior in a high speed grazing flow environment. This need has prompted a number of research investigations aimed at predicting the effect of grazing flow on the impedance of isolated orifices. Early experimental studies by Mechel, Mertens and Schilz[1], Phillips[2], Ronneberger[3] and Dean[4] showed that relative to their zero grazing flow values, the effects of grazing flow are to increase orifice resistance and decrease orifice reactance. Dean noted that some of the resonators exhibited an increase in reactance with grazing flow while others exhibited a decrease. He offered no explanation for this.

Recent studies by Rogers and Hersh[5], Baumeister and Rice[6], Hersh and Rogers[7] and Rice[8] have added greatly to our understanding of the acoustic behavior of Helmholtz resonators in a grazing flow environment. Rogers and Hersh correlated measurements of the *steady-state* resistance of isolated square-edged orifices in a grazing flow environment in terms of an effective orifice discharge coefficient. By introducing a simple inviscid model based on this airfoil theory to account for the interaction between the grazing flow and the orifice inflow and outflow, Rogers and Hersh showed that the discharge coefficient decreased to very small values relative to its classical zero grazing flow speed value of near 0.6. Rogers and Hersh showed by means of simple flow visualization techniques that the reduction in C_D results from a blockage of the orifice area by interaction between the grazing flow and the orifice inflow and outflow in the form of complicated eddies.

Baumeister and Rice conducted a very detailed visual study of interaction between a steady-state grazing flow and an *oscillating* orifice flow. Flow visualization was achieved by constructing a flow channel and a single orifice side branch Helmholtz resonator out of plexiglass and using water as the fluid medium. An oscillatory flow was applied to the resonator cavity and color dyes were injected in both the orifice and the grazing flow. High speed cameras were used to record the motion of the fluid. An important finding of their study is that interaction between the steady-state grazing flow and the oscillating orifice inflow and outflows reduced the orifice effective open area.

Hersh and Rogers derived a fluid mechanical model of the acoustic behavior of isolated circular orifices for the case of

non-grazing flow. By assuming that the sound particle velocity field approaches the orifice as a spherically symmetric radial flow, they showed to lowest order that the particle velocity field near the orifice is incompressible and unsteady. They further showed that at high incident sound pressure levels, the particle velocity is nonlinear. In this regime, the resistance, proportional to the square root of the amplitude of the incident sound pressure field, is much larger than the orifice inertial reactance or the cavity stiffness reactance.

Rice extended the work of Hersh and Rogers to include the effects of a high speed grazing flow. He derived a physically meaningful solution by assuming that the velocity field consists of a spherically symmetric particle velocity component superimposed upon a uniform grazing flow. Rice showed that when the grazing flow speed is sufficiently large (relative to the amplitude of the sound particle velocity field), the orifice resistance is linearly proportional to the grazing flow speed and independent of the amplitude of the incident sound.

The above review dealt only with isolated orifices. Previous work related to the effects of multiple or clustered orifices is discussed below. In the application of cavity-backed orifices as sound absorbing devices, possible interaction among neighboring orifices has been traditionally ignored in the design process, probably because of the lack of available data to assess its importance. This is especially true for the intense sound pressure levels and high grazing flows within jet engines.

A review of the literature indicates that the previous studies of interacting orifices, conducted by Ingard [9] and Fok[10] considered only the special cases of zero grazing flow ($V^*_\infty = 0$) and low sound pressure levels (i.e., the linear regime). Mellin[11] recently reviewed their models. Briefly, both Ingard and Fok derived theoretical expressions for the interaction. Ingard's solutions indicate that the orifice end correction is strongly dependent upon the spacing between orifices. Mellin applied Fok's model to derive the following expression for the Helmholtz-type specific reactance χ^*_o (ignoring the small viscous contribution),

$$\chi^*_o \simeq \frac{\rho^*\omega^*}{\sigma}\left[\tau^* + \frac{0.85d^*}{\psi'(\xi)}\right] \equiv \frac{\rho^*\omega^* d_e^*}{\sigma} \qquad (1)$$

where ρ^* is the fluid density, ω^* the radian sound frequency, σ is the plate porosity, τ^* is the plate thickness, d^* the (circular) orifice diameter, d_e^* is the orifice effective inertial length, and $\psi'(\xi)$ is the Fok interaction function defined in Fig. 1. Here $\xi = d^*/S^*_f$ is an interaction parameter where d^* is

the orifice diameter and $S_f^* = \sqrt{\frac{4A_f^*}{\pi}}$, A_f^* being the zone area of each orifice as shown in Fig. 1. It is clear from Fig. 1 and Eq. (1) that when $\xi<0.2$, the effect of the interaction function $\psi'(\xi)$ is small. When $\xi=1$, the end correction disappears. Physically, this corresponds to the orifice area equal to the entire plate area - hence the impedance reduces to the characteristic impedance ρ^*c^* of the fluid. In this sense changes of the variable ξ in Fok's model corresponds to changes of the percent open area of the perforated plate.

The purpose of this report is two-fold. The first is to present the results of a semi-empirical prediction model of the effects of grazing flow on the acoustic impedance of Helmholtz resonators consisting of cavity-backed isolated orifices. The second is to present the results of an experimental investigation of the effects of multiple orifices on the impedance of Helmholtz resonators in a grazing flow environment.

The study is organized as follows. In Section 2, the semi-empirical model is derived. The model is refined in Section 3 by comparing it with experimental data measured using the two-microphone method. The results of the investigation of the effects of clustered orifices are presented in Section 4. The main findings of this study are summarized in Section 5.

2. SINGLE ORIFICE IMPEDANCE MODEL

The approach used in the derivation of the model is based in part upon the flow visualization study by Baumeister and Rice. Figure 2, taken from their study, illustrates the complexity of the interaction between the grazing flow and the incident sound field. During the inflow half-cycles, the grazing flow is deflected laterally into the cavity forming the vena contracta shown. During outflow, an equal amount of sound particle volume flow is pumped out of the cavity. In both cases, the effective area through which the sound particle volume flow enters and exits the cavity *appears* to be less than the orifice area ($\pi d^{*2}/4$). The photograph suggests that the sound particle velocity field separates at the orifice upstream lip - it enters and exits the cavity near the orifice downstream lip.

It is clear that a detailed solution of the interaction is not practical. Instead, a semi-empirical solution is sought which assumes that during the inflow half-cycle, the sound particle enters the resonator cavity in the spherical, radically symmetric manner suggested in Figs. (3a,b). The radius $r^*=L_e^*$ shown is defined such that the instantaneous particle volume flow passing through the hemispherical surface area $2\pi L_e^{*2}$ is equal to the actual instantaneous particle volume flow rate

entering the cavity through the vena contracta. The quantity L_e^* must be determined experimentally. The construction of Fig. (3b) is based upon the flow visualization study of Baumeister and Rice.

The spherical inflow model is obviously valid only during the half-cycle when the incident sound particle velocity is approaching the orifice - it is not valid during the other half-cycle when the sound is exiting from the orifice. It is known from the flow visualization studies by Baumeister and Rice that the sound particle flow exits from the orifice in a jet-like manner. The restriction of the model to inflow only is not unduly limiting, however, because the quantity of particle flow pumped into and out of the resonator volume should be equal over a sound period. Thus an approximate solution over a half-cycle should result in an approximate solution over the entire cycle.

The background information described above provides the basis for the following approach. The fluctuating continuity and momentum conservation equations describing the motion of a simply harmonically driven sound particle velocity field in the presence of a steady-state grazing flow are derived. Following this, the equations of motion are normalized by appropriately scaling the dependent and independent variables. The resulting equations are then simplified by retaining only the important terms. The simplified equations of motion are solved so as to satisfy two boundary conditions. One is that the fluctuating pressure must merge smoothly (asymptotically) into the incident driving pressure. The other is that at the hemispherical surface $r^*=L_e^*$ (see Fig. 3b) the inflow instantaneous pressure must be equal to the instantaneous cavity pressure.

2.1 Derivation of Governing Equations

The derivation of the governing equations is based upon the following assumptions: (1) The flow field is decomposed into uniform and fluctuating components. (2) The fluctuating sound particle velocity field approaches the resonator orifice in a spherically symmetric manner. (3) The incident sound is simple harmonic. The sound wave-length is very much larger than the cavity and orifice dimensions. (4) The acoustic pressure and density are adiabatically related. (5) The fluid is inviscid.

Assumptions (1) and (2) are central to the derivation of the semi-empirical model. A spherical coordinate system is used in the analysis. Referring to Fig. (3), V_∞^* represents the steady grazing flow aligned in the x^*-direction. The fluctuating velocity field is written in spherical coordinates with components $(u^{*\prime},v^{*\prime},w^{*\prime})$ aligned in the (r^*,θ,ϕ) directions. The sound field is generated by a source located far away from the resonator orifice (far in terms of the orifice diameter).

From assumption (2) above, the radial component $u^{*\prime}$ of the sound particle velocity field is independent of the polar and azimuthal angles θ and ϕ. Following the approach used by Rice, the steady grazing flow is assumed to be orientated as shown in Fig. (3). Written in spherical coordinates, the grazing flow and sound particle velocity fields are, respectively,

$$\underline{V_\infty^*} = \left(-V_\infty^* \sin\theta\cos\phi,\ -V_\infty^* \cos\theta\cos\phi,\ V_\infty^* \sin\phi \right) \tag{2}$$

$$\underline{q^{*\prime}} = \left(u^{*\prime}, 0, 0 \right) \tag{3}$$

where the asteriks denote dimensional quantities, $(\ )'$ denotes acoustic quantities and $\underline{(\ )}$ denotes a vector quantity.

The flow field is decomposed into steady and fluctuating components. To simplify the analysis, the governing fluctuating continuity and momentum conservation equations (the energy equation is replaced by assumption #4) are nondimensionalized by introducing the reference quantities $(\omega^*)^{-1}, L^*_e, u^{*\prime}_{vc}, V_\infty^*, P_i^{*\prime}$. Here ω^* is the sound radian frequency, L^*_e is a characteristic length to be defined experimentally later, $u^{*\prime}_{vc}$ is the amplitude of the sound particle speed entering the resonator cavity at the orifice vena contracta (i.e., the maximum amplitude), V_∞^* is the steady grazing flow speed, and $P_i^{*\prime}$ is the amplitude of the incident sound field. It is assumed that the quantities $P_i^{*\prime}$, V_∞^* and $u^{*\prime}_{vc}$ are related as follows

$$P_i^{*\prime} = C_D \rho^* V_\infty^* u^{*\prime}_{vc} \tag{4}$$

where C_D is the orifice discharge coefficient which will be defined later (see Eq. 13).

The above dimensional quantities are used to normalize the fluctuating continuity and momentum conservation equations. Introducing the following non-dimensional quantities

$$t^* = (\omega^*)^{-1} t;\ r^* = L_e^* r;\ u^{*\prime} = u^{*\prime}_{vc} u;\ p^{*\prime} = P_i^{*\prime} p;\ \rho^{*\prime} = \frac{P_i^{*\prime}}{c^{*2}} \rho = \frac{P_i^{*\prime}}{c^{*2}} P \tag{5}$$

into the fluctuating continuity and radial momentum equations yields

Continuity Eqn.

$$C_D^2 M_\infty^2 E \frac{\partial p}{\partial t} + \left[1 + C_D M_\infty \frac{u_{vc}^{*\prime}}{c^*} p \right] \frac{1}{r^2} \frac{\partial}{\partial r} \left(r^2 u \right) + C_D M_\infty \frac{u_{vc}^{*\prime}}{c^*} u \frac{\partial p}{\partial r}$$

$$- C_D M_\infty^2 \sin\Theta \cos\phi \frac{\partial p}{\partial r} - \frac{C_D M_\infty^2}{r} \cos\Theta \cos\phi \frac{\partial p}{\partial \Theta} + \frac{C_D M_\infty}{r} \frac{\sin\phi}{\sin\Theta} \frac{\partial p}{\partial \Theta} = 0 \qquad (6)$$

Radial Momentum Eqn.

$$E \frac{\partial u}{\partial t} - \frac{1}{C_D} \sin\Theta \cos\phi \, u + \varepsilon \, u \frac{\partial u}{\partial r} + \frac{\partial p}{\partial r} = 0 \qquad (7)$$

where

$$E \equiv \frac{\omega^* L_e^*}{C_D V_\infty^*} \quad ; \quad \varepsilon \equiv \frac{p_i^{*\prime}}{\rho^* C_D^2 V_\infty^{*2}} \qquad (8)$$

The momentum flux conservation equations in the θ and ϕ directions are not included because they do not contribute directly to the impedance model prediction.

The continuity equation (Eq. 6) can be simplified to

$$\frac{\partial}{\partial r} \left(r^2 u \right) = 0 \longrightarrow u(r,t) = -F(t) / r^2 \qquad (9)$$

providing that

$$C_D^2 M_\infty^2 E \ll 1 \quad ; \quad C_D M_\infty \ll 1 \qquad (10)$$

The constraints described by Eq. (10) will be shown later to be satisfied for *any* subsonic mean flow. Substituting Eq. (9) into Eq. (7) and integrating with respect to r yields the equation

$$\frac{E\dot{F}(t)}{r} - \frac{\sin\Theta\cos\Phi}{C_D r}F(t) + \frac{\varepsilon}{2r^4}\left[F(t)\right]^2 + p(r,\Theta,\Phi,t) = f(t) \qquad (11)$$

where f(t) is an arbitrary function of time to be determined from the boundary conditions described below.

The simplified continuity equation [Eq. (9)] shows that to lowest order, fluid is pumped into and out of the cavity in an unsteady incompressible manner. This is consistent with the interpretation that significant flow field changes occur over distances small relative to the incident sound wavelength (see assumption 3). Under these conditions, flow field changes must occur hydrodynamically rather than acoustically. Referring to Fig. (3b), the incompressibility of the flow pumped into and out of the orifice permits the following interpretation of L_e^*. Recall that the characteristic length L_e^* was defined such that the volume flow rate of fluid pumped through the hemispherical surface area $2\pi L_e^{*2}$ is equal to the actual volume flow rate through the orifice vena contracta (see Fig. 3b). For incompressible flows, conservation of mass leads to the following connection between L_e^* and the orifice diameter d*,

$$\underbrace{S^*_{vc}\left(-u^*\right)_{vc}}_{\substack{\text{volume flow rate}\\ \text{through vena contracta}}} = \underbrace{S^*_o\left(-u^*\right)_o}_{\substack{\text{volume flow rate}\\ \text{through orifice}}} \qquad (12)$$

Here $(-u^*)$ denotes inflow towards the orifice as the spherical coordinate system defined by Fig. (3a) assumes outflow is positive, $S^*_{vc} \equiv 2\pi L_e^{*2}$ is the vena contracta cross-sectional area, $S_o^* \equiv \pi d^{*2}/4$ is the orifice cross-sectional area, $(-u^{*\prime})_{vc}$ is the sound particle speed in the vena contracta and $(-u^{*\prime})_o$ is the orifice area-averaged sound particle speed. The discharge coefficient C_D is defined herein as the ratio of the sound particle orifice-area averaged speed to vena contracta speed. Combining this definition with Eq. (12) leads to

$$C_D \equiv \frac{(-u^{*\prime})_o}{(-u^{*\prime})_{vc}} = \frac{S^*_{vc}}{S^*_o} = 8\left(\frac{L_e^*}{d^*}\right)^2 \qquad (13)$$

Thus the characteristic length L_e^* is related to the orifice discharge coefficient.

2.2 Boundary Conditions

The solution to Eq. (11) requires that the functions f(t) and $p(r,\theta,\phi,t)$ be known. There are two known boundary conditions that suffice to identify f(t) and $p(r,\theta,\phi,t)$. First, the local pressure $p(r,t,\theta,\phi)$ must merge smoothly (asymptotically) into the (normalized) incident sound driving pressure. From Eq. (11), this yields

$$\lim_{r\to\infty} p(r,\theta,\phi,t) = f(t) = \cos(t) \tag{14}$$

The second boundary condition is imposed by the connection between the incident sound particle velocity and the response of the cavity sound pressure. Referring to Fig. (3b), the sound particle field separates at the lip of the orifice. This separation implies that the local acoustic pressure $p(r,\theta,\phi,t)$ must be instantaneously equal to the time-dependent cavity back-pressure. From the sketch shown in Fig.(3b), it is clear that the flow is not spherical within the orifice. To avoid obvious horrendous mathematical problems, the actual instantaneous volume flow entering the cavity will be assumed to do so in a spherical manner. The matching of the spherical to the actual volume flow rate is determined experimentally by measuring indirectly the reference length L_e^*. As far as the cavity pressure is concerned, it responds only to the instantaneous volume flow entering (or exiting) through the orifice (or more precisely through the orifice vena contracta). In this sense it responds only to the instantaneous volume flow rate. This means that within the context of the spherical inflow model, the acoustic pressure is independent of the spherical angles θ and ϕ. Thus the second boundary condition, written in *dimensional terms*, is

$$\frac{\partial p_c^{*\prime}}{\partial t^*}(r^*=L_e^*,t^*) = c^{*2}\frac{\partial \rho_c^{*\prime}}{\partial t^*}(L_e^*,t^*) = \frac{c^{*2}\rho^* S_{vc}^* (-u^*)_{vc}}{V_c^*} \tag{15}$$

Equation (15) uses assumption (#4) of Section 2.1 above to connect adiabatically the time rate of increase of cavity pressure to the particle volume inflow (and by symmetry outflow) into the cavity. Nondimensionalizing Eq. (15) and replacing S_{vc}^* by $C_D S_o^*$ using Eq. (13), the second boundary condition, written in *nondimensional terms*, is

$$\frac{\partial p_c}{\partial t}(r=i,t) = \frac{c^{*2}\rho^* C_D S_o^* u_{vc}^{*\prime} F(t)}{V_c^* \omega^* \underbrace{C_D \rho^* V_\infty^* u_{vc}^{*\prime}}_{p_i^*}} = \frac{c^{*2} S_o^* F(t)}{V_c^* \omega^* V_\infty^*} \tag{16}$$

Equation (16) can be written in a more convenient form by introducing the classical expression for the resonant frequency of a Helmholtz resonator at zero grazing flow exposed to very low incident sound (see Reference 9)

$$\omega_{res}^{*2} = \frac{c^{*2} S_o^*}{V_c^* d_e^*} \tag{17}$$

where d_e^* is the orifice inertial length defined as the orifice thickness plus end correction

$$d_e^* \equiv \tau^* + \delta_o^* \simeq \tau^* + 0.85 d^* \Big/ \left(1 - 1.25 \frac{d^*}{D^*}\right) \tag{18}$$

Using Eqs. (8) and (17) with Eq. (16) yields

$$\frac{\partial p}{\partial t}(i,t) = \left(\frac{\omega_{res}^*}{\omega^*}\right)^2 \left(\frac{\omega^* L_e^*}{C_D V_\infty^*}\right) C_D \left(\frac{d_e^*}{L_e^*}\right) F(t) \equiv E \alpha F(t) \tag{19}$$

where

$$\alpha \equiv \left(\frac{\omega_{res}^*}{\omega^*}\right)^2 C_D \left(\frac{d_e^*}{L_e^*}\right) = \left(\frac{\omega_{res}^*}{\omega^*}\right)^2 \sqrt{8 C_D} \left(\frac{d_e^*}{d^*}\right) \tag{20}$$

The RHS of Eq. (20) follows from the relationship between L_e^* and d^* defined by Eq. (13).

2.3 Semi-empirical Solution

The final equation describing the effect of grazing flow on the sound field follows by combining Eq. (11) with the boundary conditions described by Eqs. (14) and (19). In the process of deriving the final equation, it is important to understand that the instantaneous time rate of change of the cavity pressure described by Eq. (19) is a function of only the instantaneous sound particle volume rate entering (or exiting) the cavity - thus it is independent of the angles θ and ϕ. To relate Eq. (11),

which describes the instantaneous behavior of the acoustic pressure at r=1 to Eq. (19), it must be first *averaged over the hemispherical surface of radius r=1(r*=Le*)* and then differentiated with respect to time. Defining,

$$\left\langle (\ ) \right\rangle \equiv \frac{1}{2\pi} \int_0^{2\pi} d\phi \int_0^{\frac{\pi}{2}} (\ ) \sin\Theta d\Theta \tag{21}$$

and applying it to Eq. (11) yields (at r=1),

$$E\dot{F}(t) + \frac{\varepsilon}{2}\left[F(t)\right]^2 + \left\langle P(1,t) \right\rangle = f(t) \tag{22}$$

What is important here is that upon averaging Eq. (11), the convective term - $\sin\theta\cos\phi F(t)/C_D$ vanishes! Physically, this means that the momentum flux that enters the hemisphere over one-half its surface area leaves it over the other half. Thus the equation describing the behavior of the sound field follows by differentiating Eq. (22) with respect to time and substituting the boundary conditions defined by Eqs. (14) and (19) to yield

$$E\ddot{F}(t) + \varepsilon F(t)\cdot\dot{F}(t) + \alpha E F(t) = -\sin(t) \tag{23}$$

Equation (23) is a highly simplified model of the time behavior of the sound particle velocity that is pumped into and out of the resonator cavity. Although derived only for particle inflow, it is believed to be valid throughout a cycle for the reasons described earlier. The coefficient $\varepsilon F(t)$ of the second term $\varepsilon F\dot{F}$ represents nonlinear damping, the amplitude of which is proportional to the instantaneous particle velocity. To insure that the damping is always positive, Eq. (23) is rewritten as

$$E\ddot{F}(t) + \varepsilon\left|F(t)\right|\dot{F}(t) + \alpha E F(t) = -\sin(t) \tag{23a}$$

Equation (23a) can be written into a more convenient form by introducing the function G(t) defined as

$$G(t) \equiv \sqrt{\varepsilon}\ F(t) \tag{24}$$

Substitution of Eq. (24) into Eq. (23a) and introducing Eq. (20) for α yields

$$|G(t)|\dot{G}(t) + \tilde{E}\left[\ddot{G}(t) + \sqrt{8\,C_D}\left(\frac{d_e^*}{d^*}\right)\left(\frac{\omega_{res}^*}{\omega^*}\right)^2 G(t)\right] = -\sin(t) \quad (25)$$

where

$$\tilde{E} \equiv \frac{E}{\sqrt{\varepsilon}} = \sqrt{\frac{C_D}{8}\,\frac{\rho^*(\omega^* d^*)^2}{P_i^*}} \quad (26)$$

The last term on the RHS of Eq. (26) follows from Eq. (8). With regard to Eq. (25), the only way the effect of grazing flow is present is through the discharge coefficient C_D. This will be clarified in Section 3. Otherwise, Eq. (25) depends upon the amplitude and frequency of the incident sound and the resonator geometry. Equation (25) is nonlinear. This is consistent with the sketches of the particle inflow behavior shown in Figs. (2) and (3) which shows that it separates at the orifice lip. Here the separation is characteristic of a nonlinear Bernouilli type of flow. It is important to note that the model predicts that one of the effects of grazing flow is to generate a nonlinear flow field near the resonator orifice. This is valid providing the steady and acoustic flow fields can be characterized as inviscid and incompressible.

Equation (25) was solved numerically. The computational procedure consisted of numerically integrating it to sufficiently large values of time until a dynamically stable solution was achieved. Standard Fourier analysis followed to match the frequency component of the particle velocity field to the incident sound pressure frequency. Numerical results are presented in terms of the standard Fourier components a_1 and b_1 defined below as

$$a_1 \equiv \frac{1}{\pi}\int_{-\pi}^{\pi} F(t)\cos t\, dt \;;\; b_1 \equiv \frac{1}{\pi}\int_{-\pi}^{\pi} F(t)\sin t\, dt \quad (27)$$

Curve fits of the computations of a_1 and b_1 are

$$a_1 \simeq 1.57 \;;\; b_1 \simeq \frac{E}{\sqrt{\varepsilon}}\left\{2.07 - 0.43\ln\left(\frac{E}{\sqrt{\varepsilon}}\right) - \alpha\left[3.7 - 2.63\left(\frac{E}{\sqrt{\varepsilon}}\right)^{1/3}\right]\right\} \quad (28a,b)$$

The curve fit $a_1 \simeq 1.57$ is quite accurate, to within 5% over the entire range of the parameters α and $E/\sqrt{\varepsilon}$ tested. Figure 4 shows a comparison between the curve fit to b_1 defined by Eq. (28b) and the numerical results. The curve fit is quite accurate for $\alpha<2$ and $E/\sqrt{\varepsilon}<1$.

Written in complex notation where it is understood that only the real part has physical meaning, the numerical solution to Eq. (25) is written

$$F(t) \simeq \frac{e^{it}}{\sqrt{\varepsilon}} \left(1.57 - i\, b_1\right) \tag{29}$$

The sound particle velocity follows directly by combining Eqs. (9) and (29) to yield

$$u(r,t) \simeq \frac{-e^{it}}{r^2\sqrt{\varepsilon}} \left[1.57 - i\,(b_1)\right] \tag{30}$$

With the sound particle velocity specified, the cavity pressure is predicted by Eq. (19). Noting that nondimensionally $P_i = e^{it}$ and $\partial/\partial t = i$, the ratio P_c^*/P_i^* is approximately

$$\frac{P_c^*}{P_i^*} \simeq -\frac{E\alpha}{\sqrt{\varepsilon}} \left[b_1 + i\,(1.57) \right] \tag{31}$$

The absolute value $|P_c^*/P_i^*|$ and relative phase shift across the orifice between P_c^* and P_i^* follows from Eq. (31) to be respectively,

$$\left| \frac{P_c^*}{P_i^*} \right| \simeq \frac{E\alpha}{\sqrt{\varepsilon}} \sqrt{(1.57)^2 + (b_1)^2} \tag{32}$$

$$\tan \phi_{ic} \simeq \frac{-1.57}{b_1} \tag{33}$$

Assuming that $|b_1|^2 \ll (1.57)^2$, Eq. (32) simplifies to

$$\left| \frac{P_c^*}{P_i^*} \right| \simeq \frac{1.57\, E\alpha}{\sqrt{\varepsilon}} = 1.57\, C_D \left(\frac{\omega_{res}^*}{\omega^*}\right)^2 \sqrt{\frac{\rho^* \overline{(\omega^* d e^*)^2}}{P_i^*}} \tag{34}$$

With the velocity field specified by Eq. (30), the predicted values of the resistance and reactance of Helmholtz resonators are derived below. The concept of acoustic impedance refers to the relationship between sound pressure and velocity at a particular frequency. Thus, if the acoustic impedance refers to the driving frequency of the sound pressure, the fundamental harmonic frequency component of the velocity normal to the cavity has to be determined. Accordingly the acoustic impedance of the resonator is defined below as the (complex) ratio of the sound pressure incident to the orifice to the orifice area averaged normal sound particle velocity,

$$Z_o^* \equiv \frac{p^{*\prime}\left(r^* \to \infty, t^*\right)}{C_D\, u^{*\prime}\left(r^* = L_e^*, t^*\right)} = \frac{P_i^*}{C_D\, u_{vc}^{*\prime}} \cdot \frac{p\left(r=\infty, t\right)}{u\left(r=1, t\right)} = \frac{\rho^* V_\infty^* e^{it}}{F(t)} \tag{35}$$

Substituting Eq. (29) for F(t), Eqn. (8) for ε and noting that $P_i'(r\to\infty,t)=e^{it}$, the impedance may be written

$$Z_o^* = \frac{\rho^* V_\infty^* \sqrt{\varepsilon}}{1.57 - i\,(b_1)} = \frac{\sqrt{\rho^* P_i^*}}{C_D} \cdot \frac{1.57 + i\,(b_1)}{(1.57)^2 + (b_1)^2} \tag{36}$$

The normalized orifice area-averaged resistance and reactance becomes approximately

$$\frac{R_o^*}{\rho^* c^*} \simeq \frac{1}{1.57\, C_D} \sqrt{\frac{P_i^*}{\rho^* c^{*\,2}}} \tag{37}$$

and

$$\frac{X_t^*}{\rho^* c^*} \simeq \frac{\omega^* d^* \left\{ 2.07 - 0.43 \ln\left(\frac{E}{\sqrt{\varepsilon}}\right) - \alpha\left[3.7 - 2.63\left(\frac{E}{\sqrt{\varepsilon}}\right)^{1/3}\right]\right\}}{(1.57)^2\, c^* \sqrt{8 C_D}} \tag{38}$$

The only unknown in the above impedance equations is the discharge coefficient C_D. Further interpretation of the impedance as defined by Eqs. (37) and (38) is deferred until experimental measurements of C_D are described below.

3. SINGLE ORIFICE MEASUREMENT PROGRAM

The two microphone method used by Dean, Hersh and Walker, and others is ideally suited to measure both the effect of grazing flow on the impedance of Helmholtz resonators and the discharge

coefficient. The two microphone method is described in Section 3.1 below. Its application to measure discharge coefficient is described in Section 3.2. The single orifice semi-empirical impedance model is described in Section 3.3. Two cases of special interest are described in Section 3.4 and 3.5. They deal with, respectively, the acoustic behavior of very long orifice necks and the self-noise generated by Helmholtz resonators exposed to grazing flows.

3.1 Two-Microphone Method

A schematic of the instrumentation and test set-up required to use the two-microphone method is shown in Figure 5. The resonator consists of a cylindrical cavity of diameter D^*, depth L^*, and an orifice of diameter d^* and thickness τ^*. The resonator system occupies one wall of the 0.127 m by 0.254 m test section. Grazing flow speeds up to 85.7/m sec were generated in the Hersh Acoustical Engineering wind tunnel. For all test velocities considered, the wall boundary-layers were turbulent and closely matched the classical 1/7th power law velocity profile. A typical velocity profile is shown in Figure 6

The resonator orifice area-averaged resistance ($R_o^*/\rho^* c^*$) and reactance ($X_t^*/\rho^* c^*$) is written, following Dean[4], as

$$\frac{R_o^*}{\rho^* c^*} = \sigma \left[10^{\frac{SPL(i)-SPL(c)}{20}} \right] \frac{\sin \phi_{ic}}{\sin\left(\frac{\omega^* L^*}{c^*}\right)} \tag{39}$$

and

$$\frac{X_t^*}{\rho^* c^*} = \sigma \left[10^{\frac{SPL(i)-SPL(c)}{20}} \right] \frac{\cos \phi_{ic}}{\sin\left(\frac{\omega^* L^*}{c^*}\right)} \tag{40}$$

where SPL(i)-SPL(c) represents the sound pressure level difference (in dB) between the incident sound field and the cavity sound field and ϕ_{ic} represents the corresponding phase difference. The radian sound frequency is denoted by ω^*, c^* is the cavity local speed of sound and σ is the ratio of orifice-to-cavity cross-sectional area. The two-microphone method of measuring impedance requires the simultaneous measurement of the incident and cavity sound pressure levels and their relative phase. These measurements are obtained by flush mounting one microphone at the cavity base and the other flush with the wall containing the orifice as shown

in Fig. 5. It is important to locate the incident microphone sufficiently far from the orifice to avoid near field effects (measurements indicate that a separation distance of about 4 or 5 orifice diameters is adequate). The microphone should be located sufficiently close, however, so that the separation distance is small relative to the incident sound wavelength; this is necessary to insure accurate measurement of the incident sound wave amplitude and phase.

A schematic of the instrumentation used to conduct the experiments is shown in Figure (7). To generate incident sound pressure levels up to 160 dB, a JBL type 2480 driver capable of producing in excess of 10 watts of relatively "clean" acoustic power is used as the sound source. The .051m diameter driver throat is coupled to the test section by means of a .051m to .102m diameter exponential expansion, JBL type H-93. Sound pressure levels in excess of 150 dB exceed the input capability of the GR 1560-P42 preamp. A 10 dB microphone Attenuator, GR Type 1962-3200 has been added, which extends the measurement range accordingly.

The signal generated by the Heath 1G-18 audio generator is amplified by the McIntosh MC2100 100 watt/channel power amplifier to power the JBL driver. The audio generator provides a tracking signal for the AD-YU Synchronous Filter and phase meter system. The 1036 system filters the two microphone input signals to the tracking signal frequency $\pm$ 2.5 Hz. The AD-YU Type 524A4 Phase Meter reads phase angle between the signals independent of signal amplitudes. The phase angle output is displayed on the AD-YU Type 2001 digital volt meter. A General Radio-1564 1/10 octave filter together with a Heath Type IM2202 DVM is used to record the output signals from each of the two microphones. Also the two signals are observed on a Tektronix 533 Oscilloscope to visually note approximate phase and distortion effects.

The output of the incident microphone channel of the synchronous filter is used as a control voltage for an automatic level control amplifier. This control amplifier adjusts the drive level to the power amplifier in such a way as to keep the incident level constant, independent of frequency and amplitude response irregularities in the loudspeaker and tunnel.

As a convenience, a triple ganged 5 dB per step ladder attenuator is used to simultaneously increase the power amplifier drive level and decrease the synchronous filter input signals so that the control loop of the automatic level control amplifier always has the same gain. This has the added advantage of keeping the levels at the AD-YU Filter input constant for all testing levels. Since the AD-Yu Filter displays a small amplitude-phase dependency, this improves accuracy as well as speed of data acquisition. A test of both microphones mounted flush in the wind tunnel wall showed phase tracking within $\pm$ .2° over a sound pressure level range of 70-150dB.

3.2 Determination of C_D

As described in Section 3.1 the two-microphone method measures separately the relative amplitudes and phases of the incident and cavity sound pressure fields. Equation (34) shows that for $|b_1|^2 << (1.57)^2$, the discharge coefficient is related to the amplitude $|P_c^*/P_i^*|$ as shown below,

$$C_D \simeq \frac{1}{1.57}\left(\frac{\omega^*}{\omega^*_{res}}\right)^2 \left|\frac{P_c^*}{P_i^*}\right| \sqrt{\frac{P_i^*}{\rho^*(\omega^* d_e^*)^2}} \qquad (41)$$

Although Eq. (41) indicates that C_D varies in a very complicated way with the incident sound pressure amplitude and frequency as well as with resonator geometry (through ω^*_{res} and d^*), it will be shown below that it is independent of frequency. This follows because the sound particle flow is almost incompressible near the orifice - thus it adjusts virtually instantaneously to changes in frequency. The data shows for a fixed incident amplitude P_i^*, that

$$\left| P_c^* / P_i^* \right| \sim (\omega^*)^{-1}$$

Replacing $|P_c^*/P_i^*|$ by this expression, it follows immediately that C_D is independent of frequency.
The two microphone method was used to measure the impedance of a total of sixteen resonator geometries. A list of the resonator geometries tested is summarized in Table I. The orifice diameters tested ranged from 0.914 millimeters (0.036") to 7.137 millimeters (0.28"). *The data is summarized in Appendix A.*

Before applying Eq.(41) to the two-microphone data, it will prove instructive to derive a simple steady state prediction model (since C_D is presumed to be independent of time) of the effect of grazing flow on C_D. Consider the steady-state pumping of grazing flow into an orifice as shown schematically in Fig.(8). Let Δp^* be the driving pressure difference across the orifice of area S_o^*. Application of conservation of momentum flux in the vertical direction yields

$$\underbrace{S_o \Delta p^*}_{\text{vertical force acting on fluid}} = \underbrace{\left(\rho^* S_\infty^* V_\infty^*\right)}_{\text{grazing flow mass flux deflected into orifice}} \cdot \underbrace{u_{vc}^*}_{\text{vertical momentum flux per unit mass}} \qquad (42)$$

Assuming one-dimensional motion in the stream tube shown, application of Bernouilli's equation connects Δp^* and u^*_{vc} as follows

$$\Delta p^* = \frac{1}{2} \rho^* u^{*2}_{vc} \tag{43}$$

Combining Eqs. (42) and (43) yields

$$\sqrt{\frac{\Delta p^*}{\rho^* V^{*2}_\infty}} = \frac{S^*_\infty}{S^*_o} \tag{44}$$

Equations (43) and (44) provide a physical interpretation of how the grazing flow affects the amount of fluid deflected into the orifice. For Δp^* fixed, Eq. (43) shows that the penetration speed u^*_{vc} into the orifice is fixed. Equation (44) shows that as the grazing flow speed V_∞^* is increased, the grazing flow stream tube area S_∞^* and hence the mass flux deflected into the orifice decreases in proportion to $1/V_\infty^*$. This interpretation will have a direct analogue in the acoustic application discussed later. Now assume that the grazing flow stream tube area S_∞^* is proportional to S^*_{vc}, the orifice vena contracta area (see Fig. 8). Then, it follows that

$$C_D \equiv \frac{S^*_{vc}}{S^*_o} \sim \sqrt{\frac{\Delta p^*}{\rho^* V^{*2}_\infty}} \tag{45}$$

The connection between the steady-state and acoustic discharge coefficients can now be made providing the steady-state driving pressure Δp^* is replaced by the amplitude of the incident sound pressure, P_i^*. Thus the acoustic discharge coefficient data should be correlated by plotting C_D vs $\sqrt{P_i^*/\rho^* V^{2}_\infty{}^*}$. In Figures 9 (a-e) which represent typical data, plotting C_D vs $\sqrt{P_i^*/\rho^* V^{*2}_\infty}$ collapses the data remarkably well.

Each resonator was tested at its resonant frequency. This was determined experimentally by setting $V_\infty^*=0$, P_i^* = 70dB and seeking the frequency for which the phase differences between the incident and cavity sound pressure fields were 90 degrees. Thus $\omega^*=\omega^*_{res}$ for all values of P^*_i and V_∞^*.

The correlation of the data in terms of C_D can be roughly divided into three regimes, defined in terms of the correlation parameter $\sqrt{P_i^*/\rho^* V^{*2}_\infty}$. To simplify the expression, the parameter η is introduced defined below as

$$\eta \equiv \sqrt{\frac{P_i^*}{\rho^* V_\infty^{*2}}} \tag{46}$$

The three regimes are loosely defined as Regime (1) $\eta<0.2$ wherein C_D is linearly related to η, Regime (3) $\eta>1$ wherein C_D is constant and Regime (2), $0.2<\eta<1$ wherein C_D is undergoing transition between Regimes (1) and (3).

The correlation of the data summarized in Figs. 9 (a-e) show that in Regime 1, C_D decreases as V_∞^* increases (for a fixed incident sound field). This is equivalent, physically to a reduction of the vena contracta area for increasing V_∞^*. An equivalent interpretation is that less and less sound particle volume flow is pumped into and out of the cavity as the grazing flow increases. This interpretation is consistent with the flow visualization studies of Baumeister and Rice. It also suggests a simple interpretation of the effects of the grazing flow boundary layer. For very high values of V_∞^*, the small values of C_D suggest that only the local grazing flow near the wall is deflected into the orifice. Thus the effect of the boundary layer should be important. The derivation of the model solution assumed that the grazing flow profile was uniform. To account for boundary-layer effects, it appears reasonable to assume that the data correlates in terms of the ratio (δ_{BL}^*/d^*) where δ_{BL}^* is the grazing flow boundary layer thickness and d^* is the orifice diameter. The idea here is that for a given boundary-layer thickness, the smaller orifice diameter should result in a reduced local grazing flow speed being deflected into the orifice. According to the data, a reduction of the grazing flow speed increases both the correlation parameter $\sqrt{P_i^*/\rho^* V_\infty^{*2}}$ and C_D. Pursuing this idea, Figure (10) shows the effect of plotting the slope $dC_D/d\eta$ vs (δ_{BL}^*/d^*) for the sixteen orifice specimens defined in Table I. A least square fit to the Regime 1 data is

$$C_D \simeq \left[1.19+0.11\ \delta_{BL}^*/d^*\right]\sqrt{P_i^*/\rho^* V_\infty^{*2}}\ ;\ \text{valid in Regime 1} \tag{47}$$

It was initially thought that the scatter of the data shown in Fig. (10) was due to the effect of the orifice thickness τ^*. However, plotting the ratio of $dC_D/d\eta$ vs τ^*/d^* showed that this parameter is not important at least for $\tau^*/d^*<1$. Since $\tau^*/d<1$ for all orifices considered in Table I, the effect of large τ^*/d^* may still be important. This is discussed in Section 3.4 below. The scatter in the data may be due to errors in measuring the ratio $|P_C^*/P_i^*|$. Recall from Eq. (41)

that C_D was determined in part, by measuring the ratio $|P_c^*/P_i^*|$. An error in measuring the sound pressure level within the cavity of only 0.4 dB caused by say, a very small leak in the cavity, would result in an error of 5% in predicting C_D. In this regard the lack of correlation of the data with τ^*/d^* and the correlation with (δ^*/d^*) suggests that Eq. (47) is reasonable.

A very simple empirical expression is presented below that correlates the C_D data over the *entire grazing flow velocity range*,

$$C_D \simeq \frac{\left[1.19+0.11\,\delta_{BL}^*/d^*\right]\eta - 1.5\,\eta^2 + 16.5\left[1+\frac{2}{9}\left(\tau^*/d^*\right)\right]\eta^4}{1+30\,\eta^4}\,;\quad \eta \equiv \sqrt{\frac{P_i^*}{\rho^* V_\infty^{*2}}} \qquad (48)$$

The accuracy of using Eq. (48) to predict C_D is shown in Figs. 9 (a-e). There is nothing unique about the magnitudes 1.5, 16.5 and 30 of the coefficients in Eq. (48). They just seem to fit the data "somewhat better" than other values.

With C_D defined, the limitations of the parameters E, ε and $E/\sqrt{\varepsilon}$ introduced in the derivation of the model solution can now be examined. Recall that in the derivation of the resonator impedance, the constraints placed on the parameters E and ε, as defined by Eqs. (10) and the discussion preceeding Eq. (41), are

$$C_D M_\infty \ll 1\,;\ (C_D M_\infty)^2 E \ll 1\,;\ \frac{E}{\sqrt{\varepsilon}} \ll 1\,;\ |b_1| < (1.57) \qquad (49a,b,c)$$

The constraints defined by Eqs. (49 a,b) were imposed in simplifying Eq. (6), the continuity equation. Replacing C_D by Eq. (47) for large V_∞^* (small η),

$$C_D M_\infty \simeq \left[1.19+0.11\left(\delta_{BL}^*/d^*\right)\right]\sqrt{P_i^*/\rho^* c^{*2}} \ll 1 \text{ for } P_c^* \ll \rho^* c^{*2} \qquad (50)$$

Assuming $\rho^* \simeq 1.2 Kg/m^3$ and $c^* \simeq 340$ m/sec, then the constraint that $P^* << \rho^* c^{*2}$ is satisfied for $P_i^* < 160$ dB which is representative of jet engine turbo-machinery noise. The second constraint, $(C_D M_\infty)^2 E << 1$ is easily satisfied. Assuming the following typical aircraft type values of $P^*_i = 160$ dB, $f^* = 1000$ Hz, $d^* = \delta_{BL}{}^* = 5$mm yields

$$\left(C_D M_\infty\right)^2 E \ll 1 \text{ for } V_\infty^* > 1 \text{ meter/sec} \tag{51}$$

Assuming the above typical values and further assuming V_∞^* to be large so that $C_D \simeq 0(.1)$, it is also straight forward to demonstrate that the constraint imposed by Eq. (49c) is satisfied for most aircraft type applications.

With C_D specified, Figures 11(a-e) compare the predicted phase shift across the orifice based on Eq. (33) with measured data. The resonator geometries are the same ones used in Figs. 9(a-e). In general, the comparison is only fair with errors generally less than about 15% at the high grazing flow speeds. The general shape of the predicted ϕ_{ic} vs V_∞^* curves are in good agreement with measurement - particularly the cross-over between the P_i^*=120 dB and P_i^*=130 dB data. At the low to moderate values of V_∞^*, the model solution becomes fairly inaccurate with errors as high as 25%. This will be shown later to be quite serious with regard to predicting reactance because Eq. (40) shows it to be proportional to cos ϕ_{ic}. For the same reasons, resistance, proportional to sin ϕ_{ic} (see Eq. 39), is predicted accurately.

The poor agreement between predicted and measured phase shift across the orifice is believed to be related to the inaccuracy of the curve fit (Eq. 28b) of the numerical solution of Eq. (25). At low values of V_∞^*, Figs. 9(a-e) shows that $C_D \sim 0(0.6)$. Assuming that $d_e^*/d^* \simeq \tau^*/d^* + 0.85$ (providing $d^* << D^*$), and further that $\omega^* = \omega^*_{res}$, then

$$\alpha \simeq 2.2 \left[\tau^*/d^* + 0.85 \right] > 2 \tag{52}$$

From Fig 4, it is clear that Eq. (28b) becomes increasingly inaccurate as α becomes much larger than 2. At high values of V_∞^*, however, $C_D \simeq 0(.1)$ and α becomes

$$\alpha \simeq 0.9 \left[\tau^*/d^* + 0.85 \right] < 2 \text{ for } \tau^*/d^* < 1.4 \tag{53}$$

The inequality described by Eq. (53) is satisfied for the resonator summarized in Table I. This is believed to be the principal reason for the more accurate agreement at high values of V_∞^* between predicted and measured phase shift shown in Figs. 11 (a-e).

Implicit in the derivation of the empirical expression for the discharge coefficient is the assumption that it is independent of frequency. From Eq. (41), this assumption requires that the ratio $|P_c^*/P_i^*|$ vary inversely with frequency for a fixed incident sound field and grazing flow speed. This is verified in Fig. (12a) for P_i^*=120 dB and V_∞^*=60m/sec. A comparison between predicted based on eqs. (28b) and (33) and measured phase shift ϕ_{ic} vs frequency is shown in Fig. 12b. *The raw data is summarized in Appendix B.*

3.3 Comparison Between Predicted and Measured Impedance

With C_D specified by Eq. (48), substitution into Eqs. (37) and (38) yields semi-empirical predictions of the effects of grazing flow on the normalized orifice area-averaged impedance of single orifice Helmholtz resonators. Figures 13(a-e) show typical comparisons between predicted and measured values of impedance. Good agreement to within 10%, is shown between predicted and measured resistance. This accuracy is consistent with the accuracy of predicting C_D as shown in Figs. 9(a-e). The agreement between predicted and measured reactance, however, is not as good. The larger percent errors shown arise from relatively small errors in predicting the phase shift ϕ_{ic} across the orifice. Referring to Eqs. (39) and (40), small errors in measured ϕ_{ic} for values near 90 degrees only negligibly affect measured resistance which is proportional to sin ϕ_{ic}. They significantly affect measured reactance, however, which is proportional to cosϕ_{ic}. The important point here is that both data and model prediction show that reactance remains small as V_∞^* becomes very large. Thus for large value of V_∞^*, resistance is much larger than reactance.

The behavior of the Helmholtz resonator at very large values of V_∞^*, is of special interest for aircraft applications where often V_∞^* is of the order of 150 meters/second (≃ 500 ft/sec). At these speeds C_D is defined by Eq. (47). The corresponding orifice area-averaged resistance and reactance simplify to

$$\frac{R_o^*}{\rho^* c^*} \simeq \frac{M_\infty}{1.87 + 0.17\left(\delta^*_{BL}/d^*\right)} \tag{54}$$

and

$$\frac{X_t^*}{\rho^* c^*} \simeq \frac{0.14\,\frac{\omega^* d^*}{c^*}\left\{2.07 - .43\ln\left(E/\sqrt{\varepsilon}\right) - \alpha\left[3.7 - 2.63\left(E/\sqrt{\varepsilon}\right)^{1/3}\right]\right\}}{\sqrt{1.19 + 0.11\left(\delta^*_{BL}/d^*\right)}} \tag{55}$$

The resistance as predicted by Eq. (54) is in excellent agreement with the theoretical value of $M_\infty/2$ predicted by Rice[8] for the case of uniform flow wherein $\delta_{BL}^* = 0$.

The normalized resistance, defined by Eq. (54), is independent of the incident sound pressure field. The normalized reactance, however, weakly depends upon the incident sound field through the parameters $E/\sqrt{\epsilon}$ and α as shown in Eq. (55). Since $|R_o^*/\rho^*c^*| >> |X_t^*/\rho^*c^*|$ at high grazing flow speeds, it is reasonable to conclude that the impedance of Helmholtz resonators exposed to high grazing flows are *almost* linear.

Figure (14) shows the effect of variations of incident sound frequency on the discharge coefficient and resonator impedance. The tests were conducted with P_i^*=120 dB and V_∞^*=60 meters/sec. Both the discharge coefficient and the resonator resistance are seen to be independent of frequency in accord with Eqs. (48) and (54). The data varies less than 5% from its average value over the frequency range from 350 to 1000 Hz. Good agreement is also shown between predicted via Eq. (55) and measured reactance. *The raw data is summarized in Appendix B.*

With regard to the effect of grazing flow on resonator reactance, Figs 13 (a-e) show that relative to its zero grazing flow values, the reactance is initially reduced (i.e., more negative) then increased. For each resonator, the resonant frequency was determined by setting P_i^*=70 dB and seeking the frequency at which ϕ_{ic}=90 degrees. Since the two-microphone method assumes the cavity reactance to be constant, independent of both the incident sound pressure and grazing flow, the change in reactance is believed to be connected to the orifice inertial reactance (X_o^*). At low levels of incident sound, say P_i^*=70 dB and at V_∞^*=0, orifice inertial reactance is defined as the difference between the total resonator reactance (X_t^*/ρ^*c^*) and the cavity stiffness reactance (X_{cav}^*/ρ^*c^*),

$$\frac{X_o^*}{\rho^*c^*} \equiv \frac{X_t^*}{\rho^*c^*} - \frac{X_{cav}^*}{\rho^*c^*} = \frac{X_t^*}{\rho^*c^*} + \sigma \cot\left(\frac{\omega^* L^*}{c^*}\right) \qquad (56)$$

Using Eq. (56), Figs. 15(a,b,c) summarize the effects of grazing flow on the orifice inertial reactance of the fifteen resonators tested (resonator #16 was omitted for convenience in displaying results). The results of all the resonators are presented because of their different behavior patterns. For modest grazing flow speeds, the orifice inertial reactance of the resonators decreased relative to their V_∞^*=0 values. For very high grazing flow speeds, the orifice inertial reactance data is divided into three groups, one wherein negative values occurred (models #5, 7 and 9 in Fig. 15b and model #11 in Fig. 15c), a second wherein constant or almost constant values occurred

(models #1 and 7 in Fig. (15b) and 8, 12, 13 and 15 in Fig. (15c) and a third wherein significant increases occurred relative to their minimum values (models #2, 3, 4, 6 and 10 in Fig. 15a). There is no obvious explanation for these behavior differences. The most likely explanation is that they arise from errors in measuring phase differences ϕ_{ic} across the orifice. Recall that at high grazing flow speeds, ϕ_{ic} is near 90 degrees and from Eq. (40) total resonator reactance is proportional to cos ϕ_{ic} which is very sensitive to measurement errors of ϕ_{ic}.

Ingard and Ising's[12] hot-wire anemometry investigation of the acoustic behavior of a Helmholtz resonator exposed to intense sound (see Introduction) showed that the resonator orifice inertial reactance decreased to approximately one-half of its very low sound amplitude value. Since the orifice thickness was negligible, they interpreted the decrease in inertia reactance to a decrease in orifice end correction δ_o^* caused by separation of the sound particle velocity at the orifice lip. Upon separating from the lip, the sound particle velocity behaves like a Bernouilli jet-like flow blowing away approximately half of the end correction. Although Ingard and Ising's study did not include grazing flow, their idea is pursued herein because of the close connection between the nonlinearity caused by intense sound pressure amplitudes and the nonlinearity caused by the grazing flow. Following their approach, the experimental behavior of δ_o^* for model #4 is shown in Fig. (16) as a function of incident sound pressure level and grazing flow speed. The values of δ_o^* shown were determined from the data and the connection defined below between δ_o^* and orifice inertial reactance,

$$X_o^* = \rho^* \omega^* \left(\tau^* + \delta_o^* \right) \tag{57}$$

Figure (16a) shows the decrease in end correction as a function of incident sound pressure level for grazing flow speeds V_∞^*=0, 13.6 and 58.4 meters/second. For the V_∞^*=0 case, δ_o^* decreases approximately by 50% as P_i^* increases from 70 dB to 130 dB. This is consistent with the results of Ingard and Ising. Again following Ingard and Ising, if the end correction is divided roughly into equal parts on both sides of the orifice, then the nonlinear jetting blows away one side of the end correction. The effect of grazing flow is summarized in Fig. 16(b). To insure an adequate signal-to-noise (i.e., boundary-layer noise), only values of P_i^*=120 dB and 130 dB are shown. The data shows that grazing flow decreases end correction. Using the phaseology of Ingard and Ising, one might say that the grazing flow "blows

away the end correction. However, this interpretation is not so obvious as the data indicates that δ_o^* decreases by more than 50%. In fact, Fig. 16(b) shows that for P_i^*=130 dB, δ_o^* is reduced by more than 85% between its value at V_∞^*=0 and its value at V_∞^*=60 meters/second. A possible explanation suggested by E. J. Rice in Reference 8 is that Eq. (57) may not be valid. The contribution of the plate thickness $\rho^*\omega^*\tau$ may be excessively high because not all of the orifice area contributes as suggested by Fig. (2).

It is important to remind the reader that the above discussion assumes that the cavity stiffness reactance is defined by Eq. (56) and further that it is independent of both grazing flow and sound pressure level. This pressumes that the cavity responds adiabatically to whatever volume flow rate is pumped into and out of it (see Section 2.3). The important point here is that the connection between reduction of reactance X_o^*/ρ^*c^* and the corresponding reduction of end correction δ_o^* is only an interpretation - it has not been proved. It assumes that the reduction of the resonator total reactance is due solely to the loss of orifice reactance and hence via Eq. (57) to a loss of end correction. In contrast, it was argued in Ref. 8 that the reduction in mass reactance due to grazing flow occurs within the flow in the orifice itself. Thus, it is not an additional end correction loss.

With the resonator impedance predicted at high grazing flow speeds by Eqs. (54) and (55), it is possible to estimate the amplitude of the sound particle velocity at the vena contracta. The connection between the resonator impedance and sound particle velocity is defined by Eq. (35), rewritten as

$$\left|\frac{Z_o^*}{\rho^*c^*}\right| = \sqrt{\left(\frac{R_o^*}{\rho^*c^*}\right)^2 + \left(\frac{X_t^*}{\rho^*c^*}\right)^2} = \frac{P_i^{*\prime}}{\rho^*c^*\ C_D\ u_{vc}^{*\prime}} \tag{58}$$

Assuming for large V_∞^* that $|R_o^*/\rho^*c^*| >> |X_t^*/\rho^*c^*|$ and substituting Eq. (54) for R_o^*/ρ^*c^* yields

$$\frac{P_i^{*\prime}}{\rho^*c^*\ C_D\ u_{vc}^{*\prime}} \simeq \frac{V_\infty^*}{1.57\ c^*\left(1.19+0.11\ \delta_{BL}^*/d^*\right)} \tag{59}$$

Solving for $u^{*\prime}_{vc}$ and substituting Eq. (47) for C_D, yields

$$u_{vc}^{*\prime} = 1.57\sqrt{\frac{P_i^*}{\rho^*}} \tag{60}$$

Thus the maximum velocity in the vena contracta is independent of the grazing flow! This is analogous to the steady-state Bernouilli solution defined by Eq. (43) wherein the amplitude of the incident sound pressure replaces the steady-state driving pressure Δp^* across the orifice. Typical $u^{*'}_{vc}$ are 6.4, 20.3 and 64.1 meters/sec for P_i^*=120, 140 and 160 dB respectively. The orifice *area-averaged* sound particle velocity amplitude $|u_o^{*'}|$ is linearly related to the grazing flow. By definition and substituting Eq. (47) for C_D,

$$\left| u_o^{*'} \right| \equiv C_D \; u^{*'}_{vc} = \left(1.87 + 0.17 \, \frac{\delta^*_{BL}}{d^*} \right) \frac{P_i^*}{\rho^* V_\infty^*}, \qquad (61)$$

$|u_o^{*'}|$ decreases inversely proportional to V_∞^*.

The normalized impedance model and data described herein represents *orifice area-averaged* values. It is customary in industrial applications to define the impedance of Helmholtz resonators relative to the area of the cavity backing. The connection between these two definitions is given below

$$Z_c^* = \frac{Z_o^*}{\sigma} \qquad (62)$$

where Z_c^* is the impedance defined relative to the cavity cross-sectional area and σ is the ratio is the ratio of the orifice area to cavity cross-sectional area. In terms of the resonator geometry used in these tests (see Fig. 3), $\sigma=(d^*/D^*)^2$. Thus, by proper selection of σ, the impedance may be adjusted to achieve, say, a desired optimum value.

3.4 Thick Orifices

The derivation of the semi-empirical expression for C_D, defined by Eq. (48), assumed that the effect of orifice thickness-to-diameter ratios, for values less than unity, is negligible. To explore this further, the results of an experimental investigation of the effects of τ^*/d^* on the impedance of a Helmholtz resonator are presented. Six orifice thicknesses were tested, the geometries of which are summarized in Table II. For each resonator tested, the frequency was adjusted to achieve resonance at P_i^*=70 dB and V_∞^*=0. *For convenience, test results are summarized in Appendix C.*

Figures 17(a-f) summarize the resonator orifice area-averaged impedance data for each configuration as a function of P_i^* and V_∞^*. The data shows the resistance to increase linearly with V_∞^* even for very thick orifices. The corresponding discharge coefficients C_D are shown in Figs. 18(a,b). As suspected from the behavior of the resistance, the data collapses for all values of τ^*/d^* by plotting C_D vs. $\sqrt{P_i^*/\rho^* V_\infty^{*2}}$. The variation with τ^*/d^* of the linear part of the C_D correlation, valid for small values of $\sqrt{P_i^*/\rho^* V_\infty^{*2}}$, is shown in Fig. 19(b). Here, C_D is shown to vary only slightly for $\tau^*/d^*<1$. It increases initially, reaches a maximum for τ^*/d^* slightly less than unity, then decreases for $\tau^*/d^*>1$. The corresponding orifice resistance, shown in Fig. 19(a) shows $R_o^*/\rho^* c^*$ to decrease initially with τ^*/d^*, reach a minimum for τ^*/d^* slightly less than unity, then increase for $\tau^*/d^*>1$. Observe that the slope $d(R_o^*/\rho^* c^*)/d(\tau^*/d^*)$ is quite insensitive of grazing flow speed.

The following physical explanation is offered. The initial decrease of $(R_o^*/\rho^* c^*)$ with (τ^*/d^*) is believed to be related to an increase in the vena contracta area. This increase in vena contracta area is, in turn, related to the increased orifice thickness which permits partial reattachment of the separated orifice jet-like flow. When the orifice thickness becomes sufficiently large, resistance increases due to, perhaps, a reduction of the vena-contracta area related to the sound particle boundary-layer displacement within the orifice thickness.

Figure (20), valid for $V_\infty^*=0$ and $P_i^*=70$ dB, shows the effect of τ^*/d^* on the resonant frequency f_{res}^*, the orifice inertial length d_e^*/d^*, and the orifice and correction δ_o^*/d^*. From classical Helmholtz resonator theory, f_{res}^* and de^*/d^* are related as follows,

$$\frac{de^*}{d^*} = \frac{S_o^*}{V_c^* d^*}\left(\frac{c^*}{\omega_{res}^*}\right)^2 = \frac{\tau^*}{d^*} + \frac{\delta_o^*}{d^*} \tag{63}$$

Equation (63) was used to determine the orifice inertial length de^*/d^* and end correction δ_o^*/d^* from measurements of f_{res}^*. For low values of τ^*/d^*, the orifice end correction contributes most to de^*/d^*. Conversely, for large values of τ^*/d^*, the orifice thickness contributes most to de^*/d^*. The behavior of the end correction is of considerable interest. According to Ingard[9]

$$\frac{\delta_o^*}{d^*} \simeq \frac{0.85}{1-1.25\left(\frac{d^*}{D^*}\right)} = 0.914 \text{ for } \frac{d^*}{D^*} = .056 \tag{64}$$

hence the end correction is independent of orifice thickness. It is clear from Fig. 20(b), that the end correction is very insensitive to the orifice thickness. For larger values of τ^*/d^*, however, the data shows that $1.7<\delta_o^*/d^*<2.0$, instead of the 0.914 value predicted by Ingard.

Figure 21(a,b) shows the effect of τ^*/d^* on reactance and end correction for $P_i^*=120$ dB and $V_\infty^*=0$ and 41.2 meter/sec. Both reactance and orifice end correction increase with increasing τ^*/d^*. The effect of the grazing flow is not especially important. The reactance data shows it to be of some importance for $\tau^*/d^*<2$. Figure 21(c,d) summarizes explicitly the effects of V_∞^* and τ^*/d^* on the normalized orifice end correction. The data shows grazing flow to reduce and orifice thickness to increase end correction. For very thick orifices, grazing flow effects become less important.

3.5 Resonator Self-Noise

To simplify analysis of the grazing flow data, the acoustic signals were maintained at levels at least 20 dB above the hydrodynamic noise generated by the turbulent boundary layer. In the process of measuring the turbulent boundary-layer noise, large resonance tones were observed to be excited. These tones are believed to be generated by an interaction between the grazing flow turbulent boundary layer and the cavity volume. Applying the concepts put forthe by Heller and Bliss[13] and more recently by DeMetz and Farabee[14], the shear layer formed at the orifice upstream separation point, $\theta=\pi/2$, $\phi=0$ is believed to generate a fluctuating mass addition and removal to the resonator cavity. Assuming that the frequency at which this mass addition and removal occurs is proportional to V_∞^*/d^*, then hydrodynamic resonance should occur at the acoustic resonant frequency. The idea here is that in the absence of any external sound, and for small V_∞^*, the acoustic resistance of the resonator is quite small, hence a hydrodynamically induced fluctuating mass flow into and out of the cavity will be strongly amplified at the acoustic resonant frequency. Table III shows the existence of an average Strouhal number equal to 0.26 defined as

$$S_t \equiv \frac{f_{res}^* \, d^*}{(V_\infty^*)_{res}} \simeq 0.26 \qquad (65)$$

for the six resonator cavities tested. According to Rossiter[15], this type of instability is controlled by acoustic feedback.

Figure 22 shows the response of the fluctuating pressure within the cavity of one of the resonators tested with grazing flow. The broadband shape of the response curve with grazing flow

speed is what one would expect from a unstable turbulent shear layer. The noise radiated from the resonator orifice was quite loud - it was heard throughout the test laboratory.

For each resonator tested, the grazing flow speed at which hydrodynamic resonance occurred corresponded to the extrapolation of the asymptotic slope of the resistance data $[d(R^*_o/\rho^*c^*)/dV_\infty^*]$ towards the $R_o^*/\rho^*c^*=0$ axis as shown in Figs. 23(a,b,c). Along this slope, the sound particles are pumped into and out of the resonator cavity in an essentially inviscid manner by the grazing flow.

The dip (or minimum) of the resistance data shown in Figure 23(a) can be explained by the hydrodynamic resonance. For $P_i^*=120$ dB, the dip is observed to occur at a grazing flow speed near the hydrodynamic resonance speed defined by Eq. (65). For incident SPL's sufficiently weak, the cavity pressure will be excessively large due to hydrodynamic resonance and hence the values of $|P_i^*/P_c^*|$ will be corresponding very small resulting in a local (with grazing flow speed) reduction in resistance (see Eq. 39).

Both the resistance and reactance data shown demonstrate that below the hydrodynamic resonance speed, $(V_\infty^*)_{res}$, acoustic effects dominate the behavior of the resonator. Above this speed, the grazing flow dominates the resonator behavior.

4. IMPEDANCE OF CLUSTERED ORIFICES

Since Helmholtz resonators are often designed with two or more cavities backed by a common cavity, an understanding of the manner in which neighboring orifices interact and affect impedance is of considerable theoretical and practical interest. Accordingly, the results of an experimental investigation of the impedance of interacting orifices in the presence of high speed grazing flow and intense sound pressure levels are presented.

The data is correlated in terms of an orifice interaction parameter defined below. The data is presented in two parts, one corresponding to zero grazing flow ($V_\infty^*=0$) and weak incident sound ($P_i^*=70$ dB) in Section 4.1 and the other to high speed grazing flow and intense sound pressure levels in Section 4.2.

The two-microphone method was used to measure the impedance of the clustered orifices. The results of twenty different orifice configurations are presented. The number of orifices tested ranged from one to sixty-four. The diameters of the orifices were sized so that the percent open area of the orifices was held

constant, equal to 1.96%. For the single orifice configuration, this corresponds to a diameter d_1^*=7.1 millimeters (0.28 inches). The diameter of the other configurations follow from the relationship

$$d_N^* = \frac{d_1^*}{\sqrt{N}} \tag{66}$$

The resonator geometry consists of a cylindrical cavity of diameter D*=50.8 millimeters (2 inches) depth L*=38.1 millimeters (1.5 inches) and an orifice thickness τ^*=1.020 millimeters (0.040 inches). By maintaining a constant percent open area, it is impossible to verify directly Fok's interaction model (see Introduction). Despite this drawback, it is essential in terms of application of the test results that the effects of the interaction be measured with the percent open area held constant.

A simple interaction parameter is introduced similar to that proposed by Fok.[10] It is defined as the ratio of the average array spacing S* between neighboring orifice centers and the average orifice diameter (d^*_N), S^*/d_N^*, where N refers to the number of orifices backed by a common cavity. S* is defined as the distance between orifice centers. Orifices are obviously independent whenever $S^*/d_N^* >> 1$. Conversely, interaction should become important whenever S^*/d_N^* is near unity. *For convenience, test results are summarized in Appendix D.*

4.1 Zero Grazing Flow, Low Sound Amplitude Results

Table IV summarizes the results of an experimental investigation of the effects of interacting orifices on the impedance of Helmholtz resonators exposed to weak sound waves for the case V_∞^*=0. During each test, the frequency of the incident sound field was "tuned" to resonance (zero total reactance) at an incident sound pressure level of 70 dB. Data is presented in terms of resonant frequency f_{res}^*, normalized orifice area-averaged resistance $R_o^*/\rho^* c^*$ and reactance $X_t^*/\rho^* c^*$, normalized orifice inertial length d_e^*/d_1^* (normalized with respect to the single orifice (N=1) diameter) and normalized orifice end correction $\delta_{o,M}^*/d_1^*$. The results summarized in Table IV are displayed graphically for convenience in Figs. (24-27).

For a fixed relative spacing between orifices, S^*/d_N^*=constant, the resonant frequency f_{res}^* is seen in Fig. (24a) to be almost independent of the number of orifices. The measurements indicate that f_{res}^* is a strong function of the relative spacing between orifices. This is shown clearly in Fig. 25(a). It suggests the attractive possibility of tuning different parts of an array of cavity-backed perforates to different frequencies by

changing their relative spacing to achieve an increased sound absorption bandwidth (at constant percent open area).

The increase in f^*_{res} with S^*/d^*_N can be explained in terms of a corresponding decreased orifice end correction. Recall from Rayleigh's classical single orifice slug-mass model of the Helmholtz resonator, that the connection between resonator resonant frequency f^*_{res} and single orifice end correction δ^*_o is

$$f^*_{res} = \frac{c^*}{2\pi} \sqrt{\frac{S^*_o}{V^*_c(\tau^* + \delta^*_o)}} \tag{67}$$

Equation (67) was used to determine the orifice end correction $\delta^*_{o,N}/d^*_1$ of Figs. 24(b) and 25(b). At the suggestion of Dr. E. J. Rice, the data shown in Fig. 25(b) is replotted in Fig. 25(c) in terms of S^*, the array spacing and d^*_N, the local orifice diameter. It is clear that the end correction is only a function of the local orifice diameter and array spacing - it is independent of N. A least square fit to the data shows that

$$\frac{\delta^*_{o,N}}{d^*_N} \sim 0.52 + \frac{4.37}{S^*} \tag{68}$$

The above orifice end correction dependance upon S^* is consistent with that proposed by Ingard.[9] Ingard's analysis, however, suggested that the end correction was a function of *both the separation distance and the number of orifices* in contrast to the behavior shown in Fig. 25(c) wherein $\delta^*_{o,N}/d^*_N$ is quite insensitive to N. Since $(\tau^* + \delta^*_{o,N})S^*_o$ is a measure of the volume of mass set into oscillatory motion by the incident sound wave, its increase with decreasing S^* indicates that interacting neighboring orifices increase this volume. Mellin[11] recently proposed an interesting explanation for the increase in $\delta^*_{o,N}$ due to interacting orifices. He suggested that the increase is due to the decreased relative shear of the fluid in the interior of adjacent orifices. Since the spacings between orifices are very small relative to the incident sound wavelength, the pumping of fluid into and out of the orifices are in phase. Thus the particle motion induced by the sound wave by an adjacent orifice reduces the retarding shear stresses on nearby orifices thereby permitting more mass to be excited by the incident sound and hence a larger orifice end correction.

The effect of interaction among the orifices on resistance is shown in Fig. (26). The behavior is in contrast to that of the end correction in that the orifice area-averaged resistance is very insensitive to the relative spacing between orifices (Fig. 26a) but very sensitive to the number of orifices (Fig. 26b). The data shown suggests that the resistance increases with N in a near linear manner. This is in contrast to the $\sqrt{N}$ increase proposed by Ingard.[9] Figure 27 shows the dependence upon fre-

quency of the orifice area-averaged resistance of the N=1, 4, 16, 36 and 64 orifice configurations for a constant orifice spacing of $S^*/d_N^*=2.5$. In all cases, the data showed the resistance to be proportional to $\sqrt{f}$ in agreement with classical theory (e.g., see Ingard [9]). The data shown in Fig. 26(b) has been corrected to the resonant frequency of the N=1 orifice of $f_{res}^*=484$ Hz. Since in all cases, τ^*/d_N^* is of order unity or less, the effect of orifice thickness is not important and hence was neglected in Fig. 26(b).

4.2 Effect of Grazing Flow

Measurements were taken of the effects of grazing flow on the orifice area-averaged impedance of the twenty configurations summarized in Table IV. Representative graphs of the results are summarized in Figs. (28)-(32) for the N=1, 4, 16, 36 and 64 orifice configurations. The data shows that for sufficiently high grazing flow speeds, the resistance becomes a linear function of V_∞^*, virtually independent of incident sound pressure level. The corresponding values of reactance decreases by modest amounts from its value at $V_\infty^*=0$. A detailed discussion of all the data is described below.

Figures 28 and 29(a-d) are of particular importance. Figure (28) represents the base line configuration consisting of a single orifice of diameter $d_1=7.1$ millimeters. Figure 29(a,b) summarize the effects of grazing flow on the impedance of N=4 orifice configurations ($d_4=3.55$ millimeters) orientated so that a line connecting their centers is perpendicular to the incident grazing flow. The values of the interaction parameter is $S^*/d_4^*=3$ in Fig. (29a) and $S^*/d_4^*=2$ in Fig. (29b). The measurements show the resistance and reactance to be reduced somewhat relative to their values shown in Figure 28 for the N=1 configuration. No meaningful impedance changes between these two configurations were measured. On the basis of the limited data shown, orifices, orientated so that a line connecting the centers is perpendicular to an incident grazing flow, operate independently of each other for values of S^*/d_4^* as low as 2.

Figures 29(c,d) summarize the effects of orientating the four orifices in a direction parallel to the incident grazing flow. No meaningful impedance changes between the parallel and perpendicular orientations were observed for the $S^*/d_4^*=3$ configuration (Figures 29(a,c)). The data for the $S^*/d_4^*=2$ configuration of Fig. 29(d), however, showed a considerable reduction in resistance relative to the $S^*/d_4^*=3$ configuration of Fig. 29(b). It also showed a considerable reduction in resistance relative to the $S^*/d_4^*=3$ configuration of Fig. 29(c). The reactance data, particularly the 140 dB incident sound

pressure level data, also was significantly different relative to the $S^*/d_4^*=3$ reactance. It appears from an examination of Figures 29(c,d) that interaction among neighboring orifices occurs when $S^*/d_4^*=2$; the orifices appear to behave independently when $S^*/d_4^*=3$. An important finding from this study is that the effects of grazing flow is important only for orifices orientated in a direction parallel to the grazing flow; it is unimportant for orifices orientated in a direction perpendicular to the grazing flow.

Figures 30(a,b), 31(a,b) and 32(a,b) represent typical data for the N=16, 36 and 64 orifice configurations for array spacings of $S^*/d_N^*=2.5$ and 5.0. Briefly the data shows resonator resistance to increase linearly with grazing flow speed and reactance to decrease to constant or almost constant values. Figures 33(a,b), 34(a,b) and 35(a,b) show that the data can be correlated in terms of an orifice discharge coefficient.

The important effects of grazing flow on the orifice area-averaged impedance for all twenty configurations tested are summarized in Figs. (36-40). Figure(36)shows the effect of array spacing and number of orifices on resistance for various grazing flow speeds and for an incident sound pressure level $P_i^*=120$ dB. While there is some scatter in the data, it is clear that the effects of both array spacing and number of orifices on the resistance of Helmholtz resonators are unimportant. Although not presented, these findings are also valid for other values of incident sound pressure.

Figure(37)summarizes the effect on resonator impedance of increasing number of orifices for a fixed orifice spacing of $S^*/d_N^*=2.5$. Data is presented at $P_i^*=120$ dB for grazing flow speeds of $V_\infty^*=0$ and 70 meters/sec. Figure 37(a) shows a slight increase in resistance with increasing number of orifices for $V_\infty^*=0$ and a slight decrease for $V_\infty^*=70$ meters/second. Figures 37(b) and (c) also show small changes of reactance and orifice end correction with increasing number of orifices. The orifice end correction data was derived by assuming that the cavity stiffness is independent of grazing flow and incident sound amplitude as discussed in Section 2.2.

Figures (38) and (39) summarize the effects of orifice spacing on resonator reactance and orifice end correction. The data is presented as a function of incident sound pressure levels $P_i^*=120$, 130 dB, grazing flow speeds $V_\infty^*=0.70$ meters/sec and number of orifices N=16, 36 and 64. For $V_\infty^*=0$, the reactance data exhibits slight scatter; it is virtually independent of array spacing. However, there is considerable scatter in the $V_\infty^*=70$ meters/sec reactance data. No trend in the data is evident. Thus, to first order, array spacing does not appear to significantly affect reactance.

In contrast to its effect on reactance, the data summarized in Fig. 39 shows orifice end correction to be a strong function of array spacing. It is clear that both number of orifices and incident sound amplitude influence only slightly orifice end correction.

The orifice end correction data of Fig. (39) for the $V_\infty^*=0$ case is shown replotted in Fig. (40). The data shows end correction to be a function of the local orifice diameter, array spacing and incident sound pressure amplitude. A least square fit to the data for $P_i^*=120$, 130 dB is respectively

$$\frac{\delta_{o,N}^*}{d_N^*} \simeq 0.25 + \frac{4.27}{S^*} \tag{69}$$

$$\frac{\delta_{o,N}^*}{d_N^*} \simeq 0.05 + \frac{4.30}{S^*} \tag{70}$$

Comparing Eqs. (68), (69) and (70), the coefficients of the terms inversely proportional to array spacing are only weakly dependent upon incident sound amplitude. The intercept terms, on the other hand, are very sensitive to the incident sound amplitude.

5. CONCLUSIONS

With regard to its application to aircraft engines, the most important finding of this study is that at high grazing flow speeds, the acoustic resistance of Helmholtz resonators is almost linearly proportional to the grazing flow speed and almost independent of of the incident sound pressure. The corresponding values of reactance are much smaller than the resistance and tend towards zero for increasing grazing flow speeds. This is true regardless of the number of orifices or the details of the resonator geometry. Because of their insensitivity to the incident sound, the impedance of Helmholtz resonators at high grazing flow speeds is almost "linear".

The behavior of the reactance requires special comment. Its reduction with grazing flow is "believed to be related to the loss of part of the orifice end correction and to a loss of part of the inertial reactance within the orifice thickness. Due to the vena contracta effect of the grazing flow, a slug-mass type of oscillatory flow no longer exists within the orifice. The above is conjecture at this point - further research is warranted.

Other findings of considerable theoretical and practical interest are:

(1) The amplitudes of the incident and cavity sound fields of Helmholtz resonators in a grazing flow environment have been connected in terms of a discharge coefficient.

(2) For isolated orifices whose thicknesses are smaller than their diameters, a semi-empirical model has been derived, which predicts the effects on impedance of resonator geometry, incident sound amplitude and frequency, grazing flow speed and boundary-layer thickness.

(3) The flow field near the resonator orifice(s) is unsteady and incompressible. This is true regardless of the amplitude of the incident sound pressure providing the grazing flow speed is subsonic.

(4) The response of orifices whose thicknesses are much larger than their diameter are generally less sensitive to grazing flow relative to the response of thin orifices.

(5) Loud resonant tones were observed to radiate from single orifice Helmholtz resonators due to interaction between the grazing flow shear layer and the resonator cavity. The tones occurred at a grazing flow speed defined as $(V^*_\infty)_{res} = f^*_{res}\, d^*/0.26$ where f^*_{res} is the resonator classical Helmholtz resonant frequency

and d* is the orifice diameter. Measurements show that for grazing flow speeds greater than $(V_\infty^*)_{res}$, the grazing flow dominates the resonator behavior and for grazing flow speeds less than $(V_\infty^*)_{res}$, the sound particle velocity field dominates the resonator behavior.

(6) For the case of Helmholtz resonators consisting of multiple orifices in a grazing flow environment, interaction between nearby orifices occurs only for those orifices whose centers were aligned in a direction parallel to the direction of flow. Interaction did not occur for orifices whose centers were aligned perpendicular to the direction of flow. Measurements show resonator resistance and reactance to be only a weak function of the number of orifices and their relative spacing. Orifice end correction, on the other hand, was found to be quite dependent upon orifice spacing. It is fairly insensitive to the number of orifices. These findings are valid with and without grazing flow.

APPENDIX A - SINGLE ORIFICE DATA

The two-microphone impedance test data is summarized herein for the sixteen single orifice resonators described in Table I. The data is presented in terms of C_D, R_o^*/ρ^*c^*, and X_t^*/ρ^*c^* for different values of P_i^* and V_∞^*. They were computed by measuring P_i^*, P_c^* and ϕ_{ic}^* and substituting these values into Eqs. (39), (40) and (41). The orifice reactance X_o^*/ρ^*c^* and end correction can be determined using Eqs. (56) and (57).

Model #1 $d^*=.914$ mm; $\tau^*=.508$ mm; $D^*=19.05$ mm; $L^*=12.7$ mm; $T_\infty^*=70°F$; $P_\infty^*=29.9$"Hg; $f_{res}^*=600$ Hz, $d_e^*/d^*=1.859$

V_∞^* (meters/sec)	P_j^* dB	C_D	R_o^*/ρ^*c^*	X_t^*/ρ^*c^*
15.6	100	.215	.0093	-.0038
	110	.335	.0105	-.0046
	120	.420	.0153	-.0053
	125	.461	.0190	-.0053
	130	.493	.0240	-.0053
	135	.516	.0308	-.0052
	140	.534	.0400	-.0050
	145	.545	.0523	-.0055
24.7	100	.127	.0160	-.0053
	110	.197	.0184	-.0062
	120	.314	.0207	-.0062
	125	.383	.0230	-.0056
	130	.438	.0271	-.0053
	135	.373	.0336	-.0056
	140	.497	.0383	-.0058
	145	.525	.0543	-.0060
33.4	110	.135	.0275	-.0069
	120	.223	.0297	-.0072
	125	.300	.0295	-.0065
	130	.361	.0329	-.0061
	135	.420	.0380	-.0059
	140	.458	.0467	-.0064
	145	.497	.0574	-.0069
40.3	110	.112	.0332	-.0072
	120	.195	.0341	-.0072
	125	.248	.0359	-.0071
	130	.318	.0374	-.0066
	135	.379	.0421	-.0062
	140	.441	.0484	-.0065
	145	.479	.0595	-.0072
54.1	110	.078	.0484	-.0088
	120	.145	.0464	-.0082
	125	.182	.0493	-.0086
	130	.244	.0490	-.0081
	135	.307	.0520	-.0079
	140	.377	.0565	-.0077
	145	.433	.0657	-.0088

V_∞* (meters/sec)	P_i* (dB)	C_D	R_o*/ρ*c*	X_t*/ρ*c*
65.7	110	.066	.0572	-.0082
	120	.115	.0588	-.0076
	125	.149	.0604	-.0083
	130	.198	.0605	-.0083
	135	.255	.0628	-.0080
	140	.322	.0663	-.0080
	145	.393	.0726	-.0086
77.1	110	.053	.0712	-.0093
	120	.094	.0722	-.0087
	125	.122	.0735	-.0092
	130	.166	.0723	-.0093
	135	.218	.0734	-.0095
	140	.275	.0776	-.0103
	145	.352	.0809	-.0106

Model #2 d^*=.914 mm; τ^*=.254 mm; D^*=19.05 mm; L^*=25.4 mm
f_{res}^*=495 Hz; T_∞^*=70° F; P_∞^*=29.9"Hg, d_e^*/d^*=1.191

V_∞* (meters/sec)	P_i* (dB)	C_D	R_o*/ρ*c*	X_t*/ρ*c*
0	70	.185	.0024	0
	80	.323	.0024	-
	90	.490	.0028	-.0002
	100	.605	.0039	-.0011
	110	.632	.0065	-.0023
	120	.620	.0123	-.0023
	130	.620	.0223	-.0014
	135	.634	.0291	-.0009
	140	.630	.0390	-.0001
9.1	90	.290	.0043	-.0021
	100	.449	.0050	-.0022
	110	.561	.0073	-.0027
	120	.610	.0126	-.0022
	130	.640	.0216	-.0011
	135	.639	.0289	-.0006
	140	.614	.0401	+.0001

V_∞* (meters/sec)	P_i* (dB)	C_D	R_o*/ρ*c*	X_t*/ρ*c*
15.2	90	.141	.0093	-.0032
	100	.225	.0103	-.0036
	110	.372	.0113	-.0034
	120	.553	.0144	-.0026
	130	.617	.0224	-.0017
	135	.639	.0287	-.0008
	140	.625	.0394	-.0003
24.4	100	.135	.0180	-.0033
	110	.235	.0183	-.0034
	115	.303	.0190	-.0033
	120	.398	.0193	-.0028
	125	.482	.0214	-.0022
	130	.550	.0251	-.0016
	135	.584	.0318	-.0012
	140	.612	.0402	-.0006
39.3	100	.074	.0331	-.0028
	110	.132	.0330	-.0025
	115	.181	.0322	-.0021
	120	.244	.0318	-.0021
	125	.312	.0332	-.0019
	130	.397	.0348	-.0014
	135	.485	.0380	-.0008
	140	.550	.0448	-.0002
53.3	100	.057	.0430	-.0007
	110	.098	.0446	-.0011
	115	.131	.0444	-.0006
	120	.173	.0450	-.0007
	125	.229	.0454	-.0010
	130	.308	.0449	-.0007
	135	.393	.0470	-.0002
	140	.488	.0504	0
65.2	110	.081	.0542	-.0015
	115	.107	.0545	+.0005
	120	.141	.0550	-.0002
	125	.189	.0548	+.0002
	130	.247	.0561	+.0002
	135	.331	.0558	+.0004
	140	.413	.0597	+.0007
76.2	110	.070	.0624	+.0011
	115	.082	.0636	+.0006
	120	.121	.0644	+.0010

V_∞* (meters/sec)	P_i* (dB)	C_D	R_o*/ρ*c*	X_t*/ρ*c
76.2	125	.160	.0649	.0012
	130	.200	.0690	.0014
	135	.281	.0657	.0013
	140	.367	.0671	.0012

Model #3 d*=1.02 mm; τ*=0.81 mm; D*=19.05 mm; L*=12.70 mm
f_{res}*=590 Hz; T_∞*=64°F; P_∞*=29.91"Hg; d_e*/d*=1.866

V_∞* (meters/sec)	P_i* (dB)	C_D	R_o*/ρ*c*	X_t*/ρ*c*
0	70	.107	.0041	0
	80	.192	.0040	0
	90	.329	.0042	-.0001
	100	.516	.0047	-.0005
	110	.635	.0065	-.0023
	115	.635	.0085	-.0034
	120	.642	.0113	-.0043
	125	.635	.0156	-.0047
	130	.650	.0207	-.0045
	135	.665	.0273	-.0045
	140	.672	.0363	-.0035
	145	.688	.0474	-.0037
7.7	110	.606	.0067	-.0025
	120	.613	.0119	-.0042
	130	.642	.0209	-.0050
	135	.657	.0276	-.0048
	140	.642	.0379	-.0045
	145	.650	.0502	-.0041
13.0	110	.534	.0075	-.0033
	120	.599	.0120	-.0047
	130	.620	.0214	-.0059
	135	.635	.0284	-.0057
	140	.620	.0391	-.0057
	145	.635	.0513	-.0049

V_∞* (meters/sec)	P_i* (dB)	C_D	R_o*/ρ*c*	X_t*/ρ*c*
20.8	110	.326	.0124	-.0052
	120	.424	.0170	-.0068
	130	.528	.0251	-.0072
	135	.559	.0320	-.0077
	140	.579	.0418	-.0069
	145	.606	.0536	-.0062
29.1	110	.189	.0219	-.0072
	120	.304	.0241	-.0083
	130	.449	.0298	-.0073
	135	.504	.0357	-.0074
	140	.534	.0453	-.0074
	145	.566	.0574	-.0065
41.0	110	.124	.0343	-.0078
	120	.215	.0349	-.0088
	130	.349	.0386	-.0084
	135	.434	.0417	-.0073
	140	.493	.0492	-.0074
	145	.534	.0608	-.0069
57.6	110	.087	.0499	-.0069
	120	.154	.0496	-.0082
	130	.256	.0532	-.0089
	135	.326	.0558	-.0084
	140	.401	.0607	-.0078
	145	.465	.0699	-.0072
70.9	110	.073	.0595	-.0064
	120	.121	.0636	-.0080
	130	.210	.0650	-.0086
	135	.274	.0666	-.0084
	140	.341	.0715	-.0074
	145	.429	.0759	-.0069
79.2	110	.063	.0685	-.0055
	120	.113	.0683	-.0068
	130	.189	.0723	-.0082
	135	.247	.0740	-.0082
	140	.304	.0803	-.0082
	145	.396	.0823	-.0068

Model #4 $d^*=0.91$ mm; $\tau^*=0.51$ mm; $D^*=19.05$ mm; $L^*=25.4$ mm
$f_{res}^*=416$ Hz; $T_\infty^*=71°F$; $P_\infty^*=29.92$"Hz; $d_e^*/d^*=1.693$

V_∞^* (meters/sec)	P_j^* (dB)	C_D	R_o^*/ρ^*c^*	X_t^*/ρ^*c^*
0	70	.129	.0034	0
	80	.227	.0034	0
	90	.361	.0036	-.0003
	100	.502	.0046	-.0017
	110	.550	.0071	-.0035
	115	.550	.0096	-.0044
	120	.563	.0129	-.0049
	125	.589	.0162	-.0053
	130	.583	.0229	-.0061
	135	.589	.0305	-.0069
8.5	110	.535	.0075	-.0037
	115	.544	.0098	-.0044
	120	.568	.0129	-.0049
	125	.582	.0170	-.0053
	130	.588	.0229	-.0061
	135	.589	.0304	-.0070
13.4	110	.506	.0077	-.0040
	115	.519	.0101	-.0048
	120	.555	.0131	-.0052
	125	.569	.0172	-.0058
	130	.581	.0230	-.0066
	135	.556	.0321	-.0079
21.0	110	.301	.0131	-.0065
	115	.351	.0150	-.0070
	120	.441	.0164	-.0068
	125	.473	.0206	-.0074
	130	.506	.0262	-.0083
	135	.519	.0342	-.0094
29.3	110	.186	.0221	-.0086
	115	.266	.0203	-.0080
	120	.305	.0240	-.0091
	125	.376	.0261	-.0088
	130	.436	.0306	-.0091
	135	.473	.0376	-.0099

V_∞* (meters/sec)	P_i* (dB)	C_D	R_o*/ρ*c*	X_t*/ρ*c*
41.5	110	.129	.0330	-.0089
	115	.170	.0329	-.0093
	120	.216	.0347	-.0104
	125	.275	.0361	-.0103
	130	.354	.0380	-.0101
	135	.422	.0424	-.0100
58.2	110	.090	.0476	-.0111
	115	.120	.0471	-.0109
	120	.148	.0516	-.0120
	125	.214	.0471	-.0110
	130	.278	.0489	-.0105
	135	.339	.0533	-.0104
70.1	110	.077	.0566	-.0099
	115	.097	.0595	-.0092
	120	.129	.0602	-.0088
	125	.174	.0588	-.0091
	130	.221	.0622	-.0098
	135	.295	.0616	-.0090

Model #5 d*=1.32 mm; τ*=0.81 mm; D*=31.75 mm; L*=12.70 mm
f_{res}*=428 Hz; T_∞*=69°F; P *=30.2"Hg; d_e*/d*=1.665

V_∞* (meters/sec)	P_i* (dB)	C_D	R_o*/ρ*c*	X_t*/ρ*c*
0	70	.114	.0038	0
	80	.198	.0039	0
	90	.328	.0042	-.0001
	100	.502	.0047	-.0010
	110	.570	.0067	-.0035
	115	.577	.0087	-.0048
	120	.564	.0121	-.0063
	125	.577	.0163	-.0070
	130	.557	.0233	-.0076
	135	.577	.0306	-.0077

V_∞* (meters/sec)	P_i* (dB)	C_D	R_o*/ρ*c*	X_t/ρ*c*
7.9	115	.557	.0090	-.0050
	120	.545	.0125	-.0065
	125	.545	.0172	-.0075
	130	.551	.0235	-.0080
	135	.564	.0312	-.0084
13.7	115	.474	.0105	-.0060
	120	.474	.0142	-.0078
	125	.497	.0185	-.0091
	130	.514	.0247	-.0098
	135	.526	.0330	-.0105
21.1	115	.273	.0188	-.0095
	120	.336	.0206	-.0098
	125	.395	.0240	-.0099
	130	.433	.0295	-.0111
	135	.464	.0374	-.0120
29.0	115	.185	.0291	-.0112
	120	.243	.0293	-.0117
	125	.313	.0305	-.0115
	130	.373	.0346	-.0116
	135	.418	.0416	-.0128
41.2	115	.125	.0447	-.0113
	120	.178	.0416	-.0112
	125	.227	.0433	-.0126
	130	.286	.0450	-.0132
	135	.352	.0500	-.0135
57.6	115	.090	.0623	-.0133
	120	.119	.0628	-.0142
	125	.161	.0621	-.0140
	130	.214	.0620	-.0145
	135	.276	.0641	-.0153
70.1	115	.071	.0797	-.0152
	120	.098	.0770	-.0147
	125	.129	.0770	-.0150
	130	.174	.0768	-.0154
	135	.227	.0784	-.0165

V_∞* (meters/sec)	P_i* (dB)	C_D	R_o*/ρ*c*	X_t*/ρ*c*
78.6	115	.066	.0853	-.0167
	120	.086	.0871	-.0180
	125	.116	.0861	-.0178
	130	.148	.0902	-.0185
	135	.207	.0861	-.0177

Model #6 d*=1.32 mm; τ*=0.81 mm; D*=19.05 mm; L*=25.40 mm
f*=493 Hz; T_∞*=64°F; P_∞*=29.9"Hg; d_e*/d*=1.713

V_∞* (meters/sec)	P_i* (dB)	C_D	R_o*/ρ*c*	X_t*/ρ*c*
0	70	.087	.0051	0
	80	.153	.0052	0
	90	.262	.0059	-.0001
	100	.415	.0060	-.0006
	110	.535	.0077	-.0031
	115	.554	.0096	-.0047
	120	.554	.0127	-.0064
	125	.548	.0175	-.0079
	130	.548	.0241	-.0088
	135	.567	.0318	-.0087
	140	.573	.0425	-.0093
7.9	115	.535	.0098	-.0051
	120	.541	.0131	-.0064
	125	.535	.0179	-.0080
	130	.541	.0242	-.0092
	135	.548	.0328	-.0096
	140	.560	.0433	-.0104
14.0	115	.435	.0118	-.0068
	120	.472	.0147	-.0081
	125	.488	.0192	-.0098

V_∞* (meters/sec)	P_i* (dB)	C_D	R_o*/ρ*c*	X_t*/ρ*c*
	130	.494	.0260	-.0114
	135	.511	.0348	-.0115
	140	.529	.0456	-.0120
21.3	115	.284	.0183	-.0098
	120	.326	.0216	-.0109
	125	.388	.0249	-.0108
	130	.425	.0308	-.0119
	135	.456	.0391	-.0125
	140	.499	.0484	-.0123
29.3	115	.192	.0285	-.0117
	120	.250	.0291	-.0121
	125	.308	.0319	-.0122
	130	.366	.0364	-.0119
	135	.415	.0432	-.0126
	140	.461	.0525	-.0131
41.1	115	.136	.0419	-.0118
	120	.173	.0437	-.0128
	125	.245	.0412	-.0123
	130	.294	.0460	-.0127
	135	.362	.0502	-.0123
	140	.420	.0579	-.0130
57.3	115	.090	.0642	-.0148
	120	.125	.0614	-.0137
	125	.163	.0628	-.0143
	130	.213	.0640	-.0154
	135	.271	.0673	-.0149
	140	.350	.0700	-.0141
70.4	115	.074	.0793	-.0112
	120	.101	.0775	-.0107
	125	.138	.0757	-.0110
	130	.173	.0801	-.0124
	135	.234	.0790	-.0132
	140	.298	.0878	-.0133
79.2	115	.064	.0929	-.0045
	120	.083	.0951	-.0048
	125	.116	.0907	-.0054
	130	.154	.0906	-.0072
	135	.203	.0915	-.0092
	140	.204	.0873	-.0098

Model #7 $d^*=1.61$ mm; $\tau^*=0.81$ mm; $D^*=31.75$ mm; $L^*=12.70$ mm
$f_{res}^*=485$ Hz; $T_\infty^*=64°F$; $P_\infty^*=30.14$"Hg; $d_e^*/d^*=1.576$

V_∞^* (meters/sec)	P_i^* (dB)	C_D	R_o^*/ρ^*c^*	X_t^*/ρ^*c^*
0	70	.100	.0043	0
	80	.173	.0045	0
	90	.297	.0046	-.0001
	100	.460	.0053	-.0005
	110	.541	.0079	-.0018
	115	.560	.0098	-.0033
	120	.553	.0131	-.0046
	125	.541	.0181	-.0056
	130	.522	.0254	-.0066
	135	.516	.0352	-.0035
7.9	115	.535	.0102	-.0036
	120	.528	.0138	-.0047
	125	.522	.0188	-.0056
	130	.510	.0261	-.0060
	135	.516	.0351	-.0045
13.9	115	.445	.0120	-.0050
	120	.482	.0148	-.0060
	125	.471	.0206	-.0072
	130	.471	.0278	-.0084
	135	.487	.0368	-.0071
21.5	115	.239	.0218	-.0105
	120	.297	.0235	-.0108
	125	.361	.0264	-.0104
	130	.392	.0331	-.0111
	135	.434	.0401	-.0125
29.3	115	.167	.0317	-.0138
	120	.220	.0320	-.0140
	125	.274	.0348	-.0138
	130	.326	.0397	-.0137
	135	.387	.0449	-.0143
41.4	115	.110	.0494	-.0171
	120	.149	.0488	-.0170
	125	.194	.0501	-.0170
	130	.244	.0533	-.0171
	135	.304	.0576	-.0169

V_∞* (meters/sec)	P_i* (dB)	C_D	R_o /ρ*c*	X_t*/ρ*c*
58.2	115	.081	.0682	-.0211
	120	.109	.0673	-.0230
	125	.139	.0705	-.0220
	130	.179	.0730	-.0217
	135	.231	.0758	-.0229
70.9	115	.065	.0857	-.0234
	120	.086	.0868	-.0231
	125	.114	.0867	-.0236
	130	.147	.0894	-.0255
	135	.185	.0948	-.0268
79.7	115	.058	.0968	-.0236
	120	.076	.0981	-.0232
	125	.098	.1011	-.0251
	130	.131	.1009	-.0265
	135	.167	.1056	-.0281

Model #8 d*=1.78 mm; τ*=0.51 mm; D*=31.75 mm; L*=25.4 mm
f_{res}*=385 Hz; T_∞*=68°F; P_∞*=30.15"Hg; d_e*/d*=1.382

V_∞* (meters/sec)	P_i* (dB)	C_D	R_o*/ρ*c*	X_t*/ρ*c*
0	70	.162	.0027	0
	80	.275	.0028	0
	90	.426	.0032	-.0004
	100	.530	.0042	-.0019
	110	.542	.0069	-.0041
	115	.536	.0094	-.0053
	120	.531	.0133	-.0061
	125	.524	.0184	-.0065
	130	.519	.0257	-.0070
	135	.518	.0345	-.0068

V_∞* (meters/sec)	P_i* (dB)	C_D	R_o*/ρ*c*	X_t*/ρ*c*
7.0	110	.525	.0071	-.0043
	115	.524	.0097	-.0052
	120	.519	.0138	-.0058
	125	.518	.0188	-.0060
	130	.513	.0261	-.0066
	135	.512	.0349	-.0067
13.1	110	.417	.0090	-.0054
	115	.446	.0113	-.0062
	120	.473	.0149	-.0069
	125	.500	.0192	-.0070
	130	.501	.0265	-.0076
	135	.512	.0348	-.0072
21.0	110	.221	.0179	-.0084
	115	.239	.0220	-.0097
	120	.339	.0214	-.0083
	125	.397	.0244	-.0081
	130	.437	.0305	-.0087
	135	.467	.0380	-.0088
29.0	110	.140	.0294	-.0108
	115	.186	.0291	-.0104
	120	.240	.0307	-.0103
	125	.311	.0314	-.0094
	130	.376	.0356	-.0093
	135	.420	.0422	-.0094
41.1	110	.101	.0415	-.0121
	115	.127	.0436	-.0122
	120	.172	.0436	-.0121
	125	.215	.0459	-.0119
	130	.299	.0451	-.0107
	135	.349	.0509	-.0103
57.9	110	.068	.0631	-.0140
	115	.091	.0618	-.0131
	120	.119	.0640	-.0134
	125	.158	.0637	-.0128
	130	.216	.0628	-.0119
	135	.281	.0637	-.0110

V_∞* (meters/sec)	P_i* (dB)	C_D	R_o*/ρ*c*	X_t*/ρ*c*
70.7	110	.059	.0730	-.0135
	115	.072	.0796	-.0126
	120	.098	.0784	-.0132
	125	.121	.0832	-.0136
	130	.172	.0794	-.0129
	135	.225	.0795	-.0123
79.2	110	.051	.0849	-.0147
	115	.062	.0910	-.0159
	120	.086	.0890	-.0152
	125	.117	.0860	-.0147
	130	.153	.0891	-.0142
	135	.203	.0883	-.0135

Model #9 d*=1.78 mm; τ*=0.51 mm; D*=19.05 mm; L*=25.4 mm
f_{res}*=653 Hz; T_∞*=68°F; P_∞*=30.15"Hg; d_e*/d*=1.307

V_∞* (meters/sec)	P_i* (dB)	C_D	R_o*/ρ*c*	X_t*/ρ*c*
0	70	.127	.0035	0
	80	.223	.0035	0
	90	.379	.0037	-.0001
	100	.548	.0045	-.0001
	110	.587	.0067	-.0035
	115	.587	.0088	-.0050
	120	.582	.0121	-.0066
	125	.561	.0170	-.0080
	130	.549	.0243	-.0091
	135	.548	.0329	-.0093
	140	.543	.0457	-.0098

V_∞* (meters/sec)	P_i* (dB)	C_D	R_o*/ρ*c*	X_t*/ρ*c*
7.3	115	.569	.0091	-.0055
	120	.562	.0125	-.0069
	125	.548	.0193	-.0089
	130	.543	.0247	-.0089
	135	.544	.0333	-.0094
	140	.543	.0457	-.0097
13.4	115	.501	.0101	-.0065
	120	.537	.0129	-.0075
	125	.531	.0181	-.0087
	130	.531	.0250	-.0099
	135	.549	.0332	-.0098
	140	.543	.0455	-.0102
21.3	115	.363	.0143	-.0084
	120	.412	.0171	-.0093
	125	.446	.0216	-.0103
	130	.478	.0276	-.0112
	135	.457	.0395	-.0131
	140	.531	.0468	-.0120
28.7	115	.197	.0273	-.0135
	120	.266	.0271	-.0131
	125	.347	.0282	-.0124
	130	.407	.0327	-.0126
	135	.478	.0376	-.0120
	140	.513	.0475	-.0137
41.1	115	.141	.0392	-.0167
	120	.188	.0393	-.0164
	125	.254	.0388	-.0162
	130	.316	.0422	-.0165
	135	.393	.0454	-.0165
	140	.457	.0528	-.0172
58.2	115	.097	.0576	-.0236
	120	.132	.0563	-.0231
	125	.172	.0577	-.0233
	130	.226	.0586	-.0232
	135	.305	.0581	-.0225
	140	.376	.0632	-.0236

V_∞* (meters/sec)	P_j* (dB)	C_D	R_o*/ρ*c*	X_t*/ρ*c*
71.3	115	.077	.0718	-.0314
	120	.112	.0656	-.0285
	125	.135	.0727	-.0315
	130	.172	.0764	-.0324
	135	.248	.0708	-.0292
	140	.320	.0737	-.0292
79.2	115	.067	.0832	-.0343
	120	.091	.0815	-.0331
	125	.126	.0784	-.0326
	130	.172	.0771	-.0308
	135	.214	.0829	-.0323
	140	.288	.0823	-.0311

Model #10 d*=1.85 mm; τ*=0.81 mm; D*=31.75 mm; L*=25.4 mm
f_{res}*=391 Hz; T_∞*=64°F; P_∞*=30"Hg; d_e*/d*=1.389

V_∞* (meters/sec)	P_j* (dB)	C_D	R_o*/ρ*c*	X_t*/ρ*c*
0	70	.142	.0031	0
	80	.250	.0031	0
	90	.415	.0033	-.0002
	100	.580	.0041	-.0012
	110	.607	.0061	-.0038
	115	.607	.0080	-.0054
	120	.580	.0114	-.0078
	125	.560	.0163	-.0089
	130	.545	.0237	-.0099
	135	.541	.0328	-.0098

V_∞* (meters/sec)	P_i* (dB)	C_D	R_o*/ρ*c*	X_t*/ρ*c*
8.0	115	.547	.0088	-.0061
	120	.554	.0120	-.0075
	125	.535	.0170	-.0094
	130	.523	.0244	-.0105
	135	.529	.0334	-.0106
13.9	115	.455	.0109	-.0068
	120	.461	.0144	-.0089
	125	.488	.0185	-.0107
	130	.488	.0259	-.0118
	135	.511	.0343	-.0118
21.0	115	.268	.0188	-.0111
	120	.322	.0214	-.0114
	125	.388	.0245	-.0111
	130	.425	.0302	-.0125
	135	.455	.0385	-.0130
29.2	115	.179	.0294	-.0142
	120	.236	.0299	-.0141
	125	.284	.0338	-.0143
	130	.410	.0363	-.0140
41.2	115	.125	.0437	-.0164
	120	.165	.0441	-.0170
	125	.218	.0448	-.0166
	130	.268	.0491	-.0165
	135	.341	.0522	-.0148
58.1	115	.089	.0635	-.0180
	120	.118	.0633	-.0185
	125	.153	.0656	-.0189
	130	.208	.0644	-.0174
	135	.262	.0690	-.0155
70.1	115	.074	.0778	-.0152
	120	.102	.0751	-.0153
	125	.134	.0757	-.0168
	130	.169	.0803	-.0171
	135	.218	.0837	-.0148
79.4	115	.067	.0857	-.0198
	120	.090	.0849	-.0189
	125	.117	.0869	-.0191
	130	.147	.0923	-.0193
	135	.188	.0974	-.0158

Model #11 $d^*=2.21$ mm; $\tau^*=0.81$ mm; $D^*=31.75$; $L^*=25.4$ mm
$f_{res}{}^*=436$ Hz; $T_\infty{}^*=68°F$; $P_\infty{}^*=29.94$"Hg; $d_e{}^*/d^*=1.335$

$V_\infty{}^*$ (meters/sec)	$P_i{}^*$ (dB)	C_D	$R_o{}^*/\rho^*c^*$	$X_t{}^*/\rho^*c^*$
0	70	.136	.0032	0
	80	.233	.0034	0
	90	.378	.0037	-.0001
	100	.541	.0045	-.0007
	110	.579	.0066	-.0038
	115	.607	.0078	-.0057
	120	.580	.0108	-.0081
	125	.560	.0153	-.0107
	130	.535	.0225	-.0132
	135	.535	.0320	-.0136
7.7	115	.553	.0086	-.0062
	120	.535	.0121	-.0082
	125	.535	.0165	-.0105
	130	.523	.0234	-.0128
	135	.529	.0325	-.0133
13.8	115	.455	.0103	-.0078
	120	.477	.0134	-.0095
	125	.477	.0182	-.0123
	130	.488	.0249	-.0141
	135	.511	.0333	-.0146
21.2	115	.239	.0201	-.0142
	120	.304	.0217	-.0140
	125	.361	.0253	-.0140
	130	.410	.0306	-.0147
	135	.445	.0384	-.0164
29.2	115	.160	.0319	-.0183
	120	.208	.0328	-.0185
	125	.271	.0342	-.0178
	130	.361	.0352	-.0157
	135	.396	.0436	-.0172
41.0	115	.109	.0483	-.0237
	120	.146	.0484	-.0235
	125	.194	.0487	-.0229
	130	.253	.0504	-.0221
	135	.318	.0545	-.0210

V_∞* (meters/sec)	P_i* (dB)	C_D	R_o*/ρ*c*	X_t*/ρ*c*
58.2	115	.076	.0702	-.0336
	120	.104	.0680	-.0321
	125	.133	.0714	-.0331
	130	.179	.0712	-.0315
	135	.233	.0736	-.0305
70.9	115	.063	.0851	-.0388
	120	.083	.0863	-.0389
	125	.116	.0826	-.0366
	130	.144	.0889	-.0384
	135	.199	.0864	-.0360
79.6	115	.056	.0960	-.0425
	120	.071	.1006	-.0443
	125	.097	.0982	-.0435
	130	.130	.0986	-.0426
	135	.175	.0980	-.0408

Model #12

d*=2.67 mm; τ*=0.81 mm; D*=31.75 mm; L*=38.10 mm
f_{res}*=422 Hz; T_∞*=64°F; P_∞=30.0"Hg; d_e*/d*=1.119

V_∞* (meters/sec)	P_i* (dB)	C_D	R_o*/ρ*c*	X_t*/ρ*c*
0	70	.189	.0024	0
	80	.339	.0024	0
	90	.525	.0027	-.0001
	100	.646	.0039	-.0004
	110	.685	.0058	-.0032
	115	.684	.0073	-.0049
	120	.646	.0103	-.0070
	125	.610	.0152	-.0088
	130	.589	.0218	-.0106
	135	.432	.0313	-.0107

V_∞* (meters/sec)	P_i* (dB)	C_D	R_o*/ρ*c*	X_t*/ρ*c*
7.6	115	.610	.0083	-.0053
	120	.582	.0121	-.0065
	125	.576	.0168	-.0080
	130	.569	.0230	-.0099
	135	.563	.0322	-.0102
13.7	115	.479	.0106	-.0068
	120	.507	.0135	-.0082
	125	.513	.0184	-.0098
	130	.543	.0240	-.0105
	135	.543	.0335	-.0102
21.0	115	.266	.0195	-.0115
	120	.335	.0211	-.0113
	125	.394	.0249	-.0110
	130	.437	.0305	-.0117
	135	.479	.0381	-.0112
29.0	115	.197	.0276	-.0130
	120	.251	.0290	-.0133
	125	.306	.0324	-.0132
	130	.363	.0374	-.0121
	135	.422	.0434	-.0122
41.1	115	.135	.0419	-.0152
	120	.172	.0439	-.0157
	125	.229	.0442	-.0150
	130	.282	.0484	-.0146
	135	.351	.0526	-.0124
57.9	115	.092	.0622	-.0193
	120	.120	.0639	-.0190
	125	.160	.0642	-.0182
	130	.197	.0700	-.0181
	135	.260	.0714	-.0156
70.7	115	.074	.0719	-.0179
	120	.102	.0765	-.0171
	125	.129	.0812	-.0171
	130	.166	.0843	-.0167
	135	.216	.0866	-.0150
79.6	115	.062	.0956	-.0192
	120	.084	.0935	-.0185
	125	.116	.0904	-.0173
	130	.148	.0950	-.0165
	135	.195	.0963	-.0152

Model #13 $d^*=3.56$ mm; $\tau^*=0.25$ mm; $D^*=19.05$ mm; $L^*=38.10$ mm
$f_{res}{}^*=937$ Hz; $T_\infty{}^*=80°F$; $P_\infty{}^*=29.8$"Hg; $d_e{}^*/d^*=0.750$

$V_\infty{}^*$ (meters/sec)	$P_i{}^*$ (dB)	C_D	$R_o{}^*/\rho^*c^*$	$X_t{}^*/\rho^*c^*$
0	70	.159	.0034	0
	80	.279	.0035	0
	90	.482	.0026	0
	100	.711	.0043	-.0003
	110	.737	.0071	-.0020
	120	.758	.0119	-.0046
	130	.805	.0199	-.0080
	135	.805	.0267	-.0102
17.1	120	.762	.0098	-.0081
	130	.815	.0195	-.0083
	135	.803	.0270	-.0097
25.3	120	.447	.0153	-.0155
	130	.697	.0216	-.0122
	135	.765	.0278	-.0115
39.0	120	.262	.0322	-.0181
	130	.455	.0343	-.0163
	135	.588	.0363	-.0145
52.9	120	.186	.0488	-.0187
	130	.326	.0499	-.0177
	135	.435	.0503	-.0165
63.4	120	.153	.0605	-.0189
	130	.268	.0616	-.0185
	135	.358	.0620	-.0173
74.9	120	.127	.0740	-.0185
	130	.227	.0741	-.0171
	135	.299	.0752	-.0165

Model #14 $d^*=3.61$ mm; $\tau^*=0.81$ mm; $D^*=31.75$ mm; $L^*=38.10$ mm
$f_{res}{}^*=503$ Hz; $T_\infty{}^*=68°F$; $P_\infty{}^*=29.9$"Hg; $d_e{}^*/d^*=1.062$

$V_\infty{}^*$ (meters/sec)	$P_i{}^*$ (dB)	C_D	$R_o{}^*/\rho^*c^*$	$X_t{}^*/\rho^*c^*$
0	70	.173	.0027	0
	80	.300	.0027	0
	90	.487	.0030	-.0001
	100	.657	.0039	-.0002
	110	.649	.0066	-.0025
	115	.620	.0089	-.0044
	120	.607	.0103	-.0086
	125	.621	.0134	-.0114
	130	.586	.0198	-.0149
	135	.553	.0302	-.0178
7.7	115	.614	.0086	-.0051
	120	.593	.0119	-.0070
	125	.586	.0162	-.0092
	130	.573	.0219	-.0128
	135	.541	.0318	-.0167
13.7	115	.493	.0085	-.0090
	120	.499	.0123	-.0100
	125	.499	.0175	-.0131
	130	.535	.0230	-.0145
	135	.522	.0330	-.0164
21.2	115	.225	.0205	-.0178
	120	.287	.0223	-.0177
	125	.353	.0257	-.0172
	130	.406	.0312	-.0177
	135	.466	.0379	-.0173
29.2	115	.152	.0339	-.0217
	120	.201	.0346	-.0214
	125	.256	.0370	-.0211
	130	.318	.0412	-.0197
	135	.387	.0465	-.0187
41.2	115	.103	.0534	-.0263
	120	.149	.0494	-.0240
	125	.190	.0524	-.0238
	130	.242	.0557	-.0229
	135	.311	.0586	-.0211

V_∞* (meters/sec)	P_j* (dB)	C_D	R_o*/ρ*c*	X_t*/ρ*c*
58.2	115	.080	.0721	-.0261
	120	.101	.0764	-.0275
	125	.134	.0766	-.0271
	130	.169	.0815	-.0276
	135	.223	.0834	-.0249
70.9	115	.059	.1006	-.0288
	120	.079	.0997	-.0275
	125	.109	.0962	-.0270
	130	.142	.0990	-.0256
	135	.177	.1067	-.0250
79.1	115	.054	.1111	-.0238
	120	.068	.1178	-.0233
	125	.090	.1195	-.0221
	130	.127	.1127	-.0215
	135	.161	.1183	-.0209

Model #15 d*=7.11 mm; τ*=1.02 mm; D*=50.80 mm; L*=38.10 mm
f_{res}*=484 Hz; T_∞*=61°F; P_∞*=30"Hg; d_e*/d*=0.873

V_∞* (meters/sec)	P_j* (dB)	C_D	R_o*/ρ*c*	X_t*/ρ*c*
0	70	.214	.0021	0
	80	.368	.0022	0
	90	.569	.0025	0
	100	.733	.0035	+.0001
	110	.700	.0061	-.0008
	115	.692	.0085	-.0018
	120	.633	.0120	-.0046
	125	.611	.0146	-.0101
	130	.604	.0191	-.0144
	135	.584	.0268	-.0193

V_∞* (meters/sec)	P_i* (dB)	C_D	R_o*/ρ*c*	X_t*/ρ*c*
7.6	115	.678	.0087	-.0021
	120	.640	.0122	-.0037
	125	.611	.0169	-.0053
	130	.590	.0227	-.0093
	135	.577	.0307	-.0133
13.7	115	.584	.0069	-.0078
	120	.557	.0111	-.0095
	125	.532	.0161	-.0125
	130	.570	.0224	-.0118
	135	.584	.0299	-.0140
20.7	115	.214	.0148	-.0243
	120	.289	.0169	-.0225
	125	.368	.0207	-.0210
	130	.433	.0266	-.0202
	135	.491	.0337	-.0202
29.3	115	.147	.0302	-.0286
	120	.189	.0322	-.0286
	125	.240	.0358	-.0274
	130	.317	.0375	-.0260
	135	.377	.0447	-.0250
41.5	115	.099	.0527	-.0317
	120	.135	.0517	-.0307
	125	.168	.0562	-.0315
	130	.227	.0574	-.0281
	135	.289	.0613	-.0263
57.9	115	.072	.0793	-.0305
	120	.097	.0767	-.0343
	125	.126	.0781	-.0359
	130	.174	.0754	-.0348
	135	.214	.0829	-.0351
70.7	115	.056	.1014	-.0377
	120	.074	.1033	-.0362
	125	.104	.0983	-.0354
	130	.126	.1080	-.0383
	135	.182	.0996	-.0354
79.2	115	.048	.1218	-.0364
	120	.065	.1188	-.0363
	125	.089	.1162	-.0352
	130	.116	.1189	-.0358
	135	.168	.1094	-.0340

Model #16 $d^*=7.11$ mm; $\tau^*=2.03$ mm; $D^*=31.75$ mm; $L^*=25.4$ mm
$f_{res}^*=892$ Hz; $T_\infty^*=83°F$; $P_\infty^*=29.8$"Hg; $d_e^*/d^*=0.988$

V_∞^* (meters/sec)	P_i^* (dB)	C_D	R_o^*/ρ^*c^*	X_t^*/ρ^*c^*
0	70	.130	.0037	0
	80	.230	.0037	0
	90	.393	.0038	0
	100	.612	.0044	+.0001
	110	.764	.0062	+.0007
	120	.726	.0115	+.0019
	130	.754	.0198	+.0024
	135	.761	.0263	+.0009
	140	.745	.0354	-.0059
25.0	120	.893	.0073	-.0058
	130	.814	.0180	-.0042
	135	.759	.0260	-.0046
	140	.708	.0370	-.0075
53.0	120	.131	.0464	-.0452
	130	.230	.0495	-.0430
	135	.313	.0498	-.0403
	140	.395	.0555	-.0389
75.6	120	.087	.0884	-.0412
	130	.160	.0840	-.0419
	135	.211	.0847	-.0431
	140	.269	.0890	-.0444

APPENDIX B

Summary of frequency sweep data for special model for V_∞^*=60 meters/sec and P_i^*=120 dB

d^*=1.02 mm; τ^*=0.81 mm; D^*=19.05 mm; L^*=25.4 mm
f_{res}^*=590 Hz; T_∞^*=64°F; P_∞^*=30.2"Hg; d_e^*/d^*=2.060

f^* (Hz)	$\lvert P_c^*/P_i^* \rvert$	ϕ_{ic}^* (deg)	C_D	$R_o^*/\rho^* c^*$	$X_t^*/\rho^* c^*$
350	.324	77.5	.135	.0556	-.0123
400	.288	80.2	.138	.0552	-.0095
450	.254	83.8	.137	.0563	-.0061
500	.226	86.4	.135	.0547	-.0036
550	.204	88.4	.134	.0578	-.0016
600	.195	91.1	.140	.0556	.0111
650	.188	92.4	.146	.0532	.0022
700	.168	94.9	.140	.0554	.0048
750	.155	96.8	.139	.0560	.0067
800	.150	98.9	.143	.0543	.0085
850	.140	100.6	.142	.0546	.0102
900	.136	104.4	.147	.0522	.0134
950	.124	104.7	.141	.0543	.0142
1000	.123	107.7	.147	.0516	.0165
1050	.117	108	.147	.0515	.0167

APPENDIX C - THICK ORIFICE DATA

The two-microphone impedance test data is summarized herein for the six thick orifice resonator configurations described in Table II. The data is presented in a manner similar to that of Appendix A.

Model #1 $d^*=1.78$ mm; $\tau^*=0.51$ mm; $D^*=31.75$ mm; $L^*=12.7$ mm; $f_{res}{}^*=552$ Hz; $T_\infty{}^*=66°F$; $P_\infty{}^*=30.1$" Hg

$V_\infty{}^*$ (meters/sec)	$P_i{}^*$ dB	C_D	$R_o{}^*/\rho^*c^*$	$X_t{}^*/\rho^*c^*$
0	70	.116	.0037	0
	115	.575	.0087	-.0051
	120	.549	.0123	-.0068
	125	.536	.0174	-.0081
	130	.542	.0238	-.0085
	135	.536	.0330	-.0087
	140	.549	.0436	-.0089
7.9	120	.524	.0132	-.0065
	125	.524	.0182	-.0073
	130	.530	.0247	-.0078
	135	.542	.0328	-.0081
	140	.542	.0441	-.0089
13.7	120	.489	.0142	-.0068
	125	.506	.0187	-.0080
	130	.524	.0248	-.0084
	135	.542	.0327	-.0082
	140	.549	.0437	-.0086
20.1	120	.375	.0186	-.0088
	125	.431	.0221	-.0091
	130	.467	.0277	-.0099
	135	.506	.0348	-.0097
	140	.530	.0450	-.0099
29.0	120	.275	.0264	-.0096
	125	.350	.0276	-.0100
	130	.407	.0321	-.0105
	135	.456	.0386	-.0109
	140	.500	.0475	-.0111
41.2	120	.197	.0374	-.0101
	125	.254	.0391	-.0108
	130	.316	.0419	-.0117
	135	.389	.0457	-.0116
	140	.462	.0515	-.0121
58.2	120	.132	.0573	-.0124
	125	.190	.0530	-.0108
	130	.237	.0566	-.0126
	135	.312	.0572	-.0127
	140	.380	.0627	-.0140

V_∞* (meters/sec)	P_i* (dB)	C_D*	R_o*/ρ*c*	X_t*/ρ*c*
	120	.117	.0646	-.0126
	125	.151	.0670	-.0124
	130	.204	.0660	-.0132
	135	.257	.0699	-.0141
	140	.338	.0706	-.0150
	120	.098	.0779	-.0137
	125	.138	.0735	-.0131
	130	.174	.0778	-.0143
	135	.221	.0814	-.0152
	140	.305	.0786	-.0151

Model #2 d*=1.78 mm; τ*=1.015 mm; D*=31.75 mm; L*=12.7 mm; f_{res}*=530 Hz; T_∞*=73°F; P_∞=30.07"Hg

V_∞* (meters/sec)	P_i* (dB)	C_D	R_o*/ρ*c*	X_t*/ρ*c*
0	70	.119	.0037	0
	115	.731	.0071	-.0035
	120	.714	.0095	-.0051
	125	.714	.0128	-.0065
	130	.698	.0178	-.0083
	135	.659	.0265	-.0084
	140	.674	.0352	-.0083
7.9	120	.690	.0100	-.0050
	125	.690	.0135	-.0063
	130	.667	.0187	-.0085
	135	.659	.0263	-.0088
	140	.659	.0360	-.0089
13.7	120	.615	.0110	-.0060
	125	.622	.0146	-.0078
	130	.629	.0197	-.0093
	135	.629	.0273	-.0099
	140	.651	.0362	-.0098

V_∞ (meters/sec)	P_i* (dB)	C_D	$R_o^*/\rho^* c^*$	$X_t^*/\rho^* c^*$
20.1	120	.393	.0175	-.0089
	125	.456	.0206	-.0092
	130	.512	.0251	-.0094
	135	.574	.0302	-.0102
	140	.601	.0392	-.0105
28.7	120	.284	.0254	-.0095
	125	.354	.0272	-.0102
	130	.421	.0310	-.0103
	135	.512	.0344	-.0097
	140	.567	.0416	-.0109
41.5	120	.201	.0372	-.0093
	125	.259	.0383	-.0105
	130	.319	.0415	-.0113
	135	.411	.0432	-.0108
	140	.488	.0486	-.0117
58.2	120	.136	.0557	-.0107
	125	.181	.0558	-.0100
	130	.234	.0575	-.0120
	135	.323	.0555	-.0117
	140	.411	.0582	-.0117
71.3	120	.109	.0695	-.0123
	125	.144	.0705	-.0110
	130	.201	.0670	-.0124
	135	.251	.0719	-.0129
	140	.330	.0726	-.0137
79.9	120	.095	.0800	-.0128
	125	.130	.0783	-.0120
	130	.167	.0809	-.0130
	135	.228	.0790	-.0132
	140	.298	.0808	-.0140

Model #3 $d^*=1.78$ mm; $\tau^*=2.032$ mm; $D^*=31.75$ mm; $L^*=12.7$ mm; $f_{res}{}^*=414$ Hz; $T_\infty{}^*=66°F$; $P_\infty{}^*=29.55$"Hg

$V_\infty{}^*$ (meters/sec)	$P_i{}^*$ (dB)	C_D	$R_o{}^*/\rho^*c^*$	$X_t{}^*/\rho^*c^*$
0	70	.058	.0084	0
	115	.465	.0119	-.0038
	120	.481	.0147	-.0062
	125	.487	.0195	-.0086
	130	.504	.0251	-.0110
	135	.504	.0341	-.0131
7.9	115	.460	.0119	-.0044
	120	.470	.0156	-.0064
	125	.481	.0200	-.0078
	130	.504	.0257	-.0095
	135	.510	.0343	-.0114
13.6	115	.410	.0133	-.0049
	120	.449	.0157	-.0067
	125	.476	.0202	-.0081
	130	.510	.0253	-.0096
	135	.516	.0340	-.0110
20.	115	.259	.0213	-.0073
	120	.357	.0205	-.0066
	125	.424	.0230	-.0082
	130	.476	.0273	-.0097
	135	.493	.0356	-.0114
28.3	115	.177	.0316	-.0091
	120	.233	.0314	-.0100
	125	.357	.0278	-.0082
	130	.434	.0301	-.0103
	135	.481	.0365	-.0116
41	115	.136	.0417	-.0101
	120	.173	.0431	-.0108
	125	.239	.0421	-.0104
	130	.337	.0397	-.0103
	135	.424	.0414	-.0132
57.6	115	.101	.0565	-.0125
	120	.129	.0576	-.0137
	125	.177	.0570	-.0133
	130	.225	.0594	-.0150
	135	.293	.0611	-.0143

V_∞* (meters/sec)	P_i* (dB)	C_D	R_o*/ρ*c*	X_t*/ρ*c*
70.1	120	.103	.0727	-.0168
	125	.136	.0746	-.0161
	130	.183	.0736	-.0167
	135	.236	.0764	-.0162
78.3	120	.092	.0820	-.0168
	125	.118	.0858	-.0179
	130	.165	.0818	-.0177
	135	.218	.0829	-.0170

Model #4 d*=1.78 mm; τ*=4.065 mm; D*=31.75 mm; L=12.7 mm
f_{res}*=333 Hz; T_∞*=75°F; P_∞*=30.1" Hg

V_∞* (meters/sec)	P_i* (dB)	C_D	R_o*/ρ*c*	X_t*/ρ*c*
0	70	.049	.0087	0
	115	.467	.0121	-.0025
	120	.489	.0151	-.0042
	125	.524	.0187	-.0058
	130	.578	.0254	-.0070
7.6	115	.457	.0123	-.0029
	120	.484	.0153	-.0041
	125	.524	.0188	-.0054
	130	.518	.0255	-.0067
13.7	115	.417	.0135	-.0031
	120	.457	.0162	-.0045
	125	.484	.0202	-.0062
	130	.513	.0256	-.0073
20.1	115	.278	.0204	-.0033
	120	.371	.0201	-.0047
	125	.441	.0224	-.0062
	130	.473	.0279	-.0075

V_∞* (meters/sec)	P_i* (dB)	C_D	R_o*/ρ*c*	X_t*/ρ*c*
28.7	115	.176	.0324	-.0050
	120	.266	.0281	-.0067
	125	.367	.0271	-.0065
	130	.431	.0308	-.0076
41.5	115	.120	.0475	-.0066
	120	.168	.0454	-.0057
	125	.251	.0406	-.0041
	130	.335	.0400	-.0079
58.2	115	.091	.0628	-.0072
	120	.116	.0657	-.0078
	125	.162	.0628	-.0072
	130	.232	.0588	-.0047
70.4	115	.072	.0802	-.0063
	120	.095	.0800	-.0083
	125	.127	.0802	-.0060
	130	.174	.0782	-.0081
79.6	115	.061	.0943	-.0063
	120	.086	.0889	-.0078
	125	.112	.0911	-.0064
	130	.150	.0909	-.0084

Model #5 d^*=1.78 mm; τ^*=8.127 mm; D^*=31.75 mm; L^*=12.7 mm; f_{res}^*=255 Hz; T_∞^*=74°F; P_∞^*=30.1" Hg

V_∞* (meters/sec)	P_i* (dB)	C_D	R_o*/ρ*c*	X_t*/ρ*c*
0	70	.030		
	115	.338	.0169	-.0019
	120	.330	.0228	-.0045
	125	.362	.0277	-.0054
	130	.379	.0354	-.0062
	135	.393	.0454	-.0074

V_∞* (meters/sec)	P_j* (dB)	C_D	R_o*/ρ*c*	X_t*/ρ*c*
7.6	115	.305	.0184	-.0041
	120	.330	.0227	-.0049
	125	.375	.0267	-.0058
	130	.393	.0340	-.0069
	135	.411	.0435	-.0081
13.7	115	.281	.0202	-.0033
	120	.327	.0231	-.0045
	125	.371	.0269	-.0061
	130	.388	.0343	-.0076
	135	.406	.0438	-.0091
20.7	115	.208	.0274	-.0036
	120	.281	.0270	-.0038
	125	.354	.0285	-.0049
	130	.379	.0354	-.0066
	135	.397	.0450	-.0086
29.0	115	.149	.0381	-.0055
	120	.216	.0353	-.0038
	125	.308	.0329	-.0042
	130	.366	.0367	-.0063
	135	.393	.0456	-.0082
41.1	115	.113	.0505	-.0052
	120	.149	.0510	-.0060
	125	.223	.0456	-.0045
	130	.308	.0439	-.0052
	135	.371	.0485	-.0073
57.9	115	.085	.0673	-.0077
	120	.112	.0683	-.0054
	125	.153	.0667	-.0062
	130	.211	.0644	-.0059
	135	.312	.0580	-.0060
70.4	115	.071	.0800	-.0091
	120	.092	.0831	-.0067
	125	.124	.0820	-.0079
	130	.188	.0810	-.0057
	135	.248	.0732	-.0061
79.2	115	.062	.0918	-.0109
	120	.082	.0930	-.0095
	125	.111	.0920	-.0087
	130	.144	.0941	-.0094
	135	.211	.0859	-.0081

Model #6 d^*=1.78 mm; *=15.875 mm; D^*=31.75 mm; L^*=12.7 mm; $f_{res}{}^*$=197 Hz; $T_\infty{}^*$=66°F; $P_\infty{}^*$=30.1" Hg

$V_\infty{}^*$ (meters/sec)	$P_j{}^*$ (dB)	C_D	$R_o{}^*/\rho^*c^*$	$X_t{}^*/\rho^*c^*$
0	70	.0155	.0275	0
	110	.155	.0278	.0007
	115	.204	.0282	.0007
	120	.260	.0295	.0006
7.6	110	.158	.0272	.0016
	115	.206	.0278	.0009
	120	.257	.0298	.0005
13.7	110	.145	.0297	.0026
	115	.193	.0297	.0031
	120	.251	.0304	.0031
20.1	110	.111	.0388	.0026
	115	.153	.0375	.0026
	120	.206	.0370	.0034
28.0	110	.089	.0483	.0029
	115	.120	.0478	.0026
	120	.157	.0489	.0027
41.1	110	.072	.0594	.0031
	115	.094	.0608	.0029
	120	.126	.0608	.0028
49.4	110	.062	.0699	.0023
	115	.080	.0715	.0022
	120	.108	.0707	.0025
58.2	115	.073	.0784	.0018
	120	.097	.0793	.0025
64.6	115	.067	.0860	.0009
	120	.086	.0890	.0026
70.1	115	.063	.0911	.0011
	120	.079	.0965	.0013
78.6	115	.055	.1046	.0018
	120	.072	.1058	.0018

APPENDIX D - CLUSTERED ORIFICE DATA

The two-microphone impedance test data is summarized herein for the twenty clustered orifice resonator configurations described in Table IV. The data is presented in a manner similar to that of Appendix A.

Model #1 N=1; d^*=7.11 mm; τ^*=1.02 mm; D^*=50.80 mm; L^*=38.10 mm
$f_{res}{}^*$=484 Hz; $T_\infty{}^*$=62°F; $P_\infty{}^*$=30"Hg

$V_\infty{}^*$ (meters/sec)	$P_i{}^*$ (dB)	C_D	$R_o{}^*/\rho^* c^*$	$X_t{}^*/\rho^* c^*$
0	70	.219	.0020	0
	90	.575	.0024	-.000
	100	.770	.0032	+.0001
	110	.768	.0057	-.0006
	120	.672	.0113	-.0032
	130	.650	.0182	-.0116
	135	.630	.0256	-.0155
	140	.605	.0363	-.0204
20.1	120	.293	.0166	-.0217
	130	.457	.0251	-.0182
	135	.522	.0316	-.0178
	140	.577	.0400	-.0174
28.7	120	.202	.0293	-.0264
	130	.336	.0347	-.0238
	135	.434	.0382	-.0208
	140	.491	.0468	-.0209
40.5	120	.142	.0479	-.0293
	130	.250	.0493	-.0278
	135	.314	.0541	-.0261
	140	.404	.0575	-.0239
57.0	120	.101	.0717	-.0323
	130	.168	.0764	-.0359
	135	.241	.0720	-.0311
	140	.298	.0795	-.0286
69.8	120	.077	.0973	-.0367
	130	.139	.0956	-.0355
	135	.185	.0958	-.0348
	140	.241	.0984	-.0349
78.6	120	.069	.1090	-.0386
	130	.117	.1145	-.0376
	135	.163	.1101	-.0368
	140	.210	.1137	-.0375

Model #2 $S^*/d_4^* = 2$; $N = 4$; $d_4^* = 3.56$ mm; $\tau^* = 1.02$ mm; $D^* = 50.80$ mm; $L^* = 38.10$ mm; $f_{res}^* = 555$ Hz; $T_\infty^* = 61°F$; $P_\infty^* = 30"Hg$

V_∞^* (meters/sec)	P_i^* (dB)	C_D	$R_o^*/\rho^* c^*$	$X_t^*/\rho^* c^*$
0	70	.184	.0025	0
	80	.319	.0025	0
	90	.514	.0028	-.0001
	100	.674	.0038	0
	110	.731	.0062	-.0003
	120	.686	.0113	-.0034
	130	.654	.0194	-.0104
	135	.636	.0268	-.0139
	140	.621	.0378	-.0163
20.4	120	.341	.0186	-.0148
	130	.466	.0266	-.0156
	135	.508	.0340	-.0163
	140	.557	.0429	-.0161
28.7	120	.228	.0305	-.0181
	130	.382	.0332	-.0175
	135	.444	.0393	-.0178
	140	.504	.0474	-.0177
40.5	120	.156	.0470	-.0216
	130	.280	.0469	-.0209
	135	.358	.0495	-.0202
	140	.433	.0556	-.0198
57.0	120	.113	.0675	-.0241
	130	.200	.0673	-.0246
	135	.260	.0693	-.0248
	140	.327	.0743	-.0242
69.8	120	.092	.0839	-.0269
	130	.163	.0844	-.0247
	135	.209	.0880	-.0261
	140	.281	.0870	-.0261
78.3	120	.075	.1035	-.0296
	130	.137	.1004	-.0285
	135	.181	.1019	-.0282
	140	.222	.1106	-.0314

Model #3 $S^*/d^*=3$; $N=4$; $d_o^*=3.56$ mm; $\tau^*=1.02$ mm; $D^*=50.80$ mm; $L^*=38.10$ mm; $f_{res}^*=594$ Hz; $T_\infty^*=66°F$; $P_\infty^*=30"Hg$

V_∞^* (meters/sec)	P_i^* (dB)	C_D	$R_o^*/\rho^* c^*$	$X_t^*/\rho^* c^*$
0	70	.185	.0025	0
	80	.323	.0026	0
	90	.518	.0028	0
	100	.676	.0039	0
	110	.736	.0063	-.0001
	115	.723	.0085	-.0011
	120	.696	.0112	-.0038
	130	.682	.0178	-.0120
	135	.653	.0259	-.0150
	140	.619	.0383	-.0173
20.3	120	.370	.0178	-.0136
	130	.494	.0260	-.0148
	135	.541	.0330	-.0152
	140	.577	.0128	-.0152
28.7	120	.248	.0286	-.0175
	130	.404	.0326	-.0168
	135	.470	.0385	-.0164
	140	.516	.0480	-.0165
40.5	120	.166	.0454	-.0212
	130	.298	.0454	-.0198
	135	.378	.0487	-.0186
	140	.450	.0554	-.0180
57.4	120	.122	.0642	-.0217
	130	.213	.0653	-.0233
	135	.275	.0678	-.0225
	140	.363	.0694	-.0205
78.4	120	.084	.0956	-.0259
	130	.159	.0941	-.0255
	135	.202	.0941	-.0244
	140	.265	.0957	-.0247

Model #4 $S^*/d_4=2$; $N=4$; $d_4^*=3.56$ mm; $\tau^*=1.02$ mm; $D^*=50.80$ mm; $L^*=38.10$ mm; $f_{res}^*=553$; $T_\infty^*=61°F$; $P_\infty^*=30"Hg$

V_∞^* (meters/sec)	P_i^* (dB)	C_D	R_o^*/ρ^*c^*	X_t^*/ρ^*c^*
0	70	.187	.0024	0
	80	.324	.0025	0
	90	.521	.0028	0
	100	.679	.0038	0
	110	.733	.0062	-.0004
	120	.693	.0112	-.0034
	130	.657	.0193	-.0106
	135	.639	.0267	-.0140
	140	.622	.0380	-.0163
20.7	120	.418	.0173	-.0089
	130	.549	.0240	-.0093
	135	.577	.0314	-.0111
	140	.589	.0413	-.0139
28.7	120	.305	.0245	-.0103
	130	.477	.0288	-.0094
	135	.528	.0348	-.0108
	140	.564	.0435	-.0132
40.2	120	.208	.0361	-.0149
	130	.359	.0387	-.0107
	135	.442	.0417	-.0095
	140	.494	.0503	-.0127
57.0	120	.147	.0518	-.0188
	130	.261	.0535	-.0144
	135	.331	.0571	-.0110
	140	.418	.0606	-.0100
69.5	120	.114	.0671	-.0232
	130	.211	.0657	-.0195
	135	.285	.0659	-.0147
	140	.349	.0726	-.0115
78.6	120	.097	.0795	-.0253
	130	.184	.0751	-.0221
	135	.251	.0747	-.0168
	140	.327	.0775	-.0127

Model #5 $S^*/d_4^*=3$; $N=4$; $d_4^*=3.56$ mm; $\tau^*=1.02$ mm; $D^*=50.80$ mm; $L^*=38.10$ mm; $f_{res}^*=592$ Hz; $T_\infty^*=62°F$; $P_\infty^*=30"Hg$

V_∞^* (meters/sec)	P_i^* (dB)	C_D	R_o^*/ρ^*c^*	X_t^*/ρ^*c^*
0	70	.185	.0025	0
	80	.320	.0026	0
	90	.510	.0029	0
	100	.670	.0039	0
	110	.728	.0064	0
	115	.716	.0086	-.0010
	120	.694	.0113	-.0036
	125	.682	.0135	-.0088
	130	.674	.0181	-.0121
	135	.643	.0264	-.0151
	140	.615	.0387	-.0174
20.3	120	.348	.0179	-.0156
	125	.417	.0216	-.0151
	130	.496	.0255	-.0150
	135	.523	.0337	-.0164
	140	.569	.0432	-.0150
28.7	120	.244	.0281	-.0188
	125	.315	.0297	-.0185
	130	.404	.0320	-.0170
	135	.472	.0377	-.0171
	140	.517	.0474	-.0172
41.6	120	.170	.0437	-.0210
	125	.228	.0435	-.0210
	130	.285	.0468	-.0214
	135	.366	.0497	-.0195
	140	.453	.0546	-.0181
57.4	120	.123	.0629	-.0226
	125	.162	.0638	-.0228
	130	.215	.0644	-.0222
	135	.279	.0667	-.0216
	140	.349	.0720	-.0199
78.3	120	.091	.0875	-.0236
	125	.116	.0921	-.0233
	130	.153	.0927	-.0239
	135	.205	.0926	-.0225
	140	.262	.0970	-.0221

Model #6 $S/d_4=2.5$; $N=4$; $d_4^*=3.56$ mm; $\tau^*=1.02$ mm; $D^*=50.30$mm; $L^*=38.10$ mm; $f_{res}^*=563$ Hz; $T_\infty^*=66°F$; $P_\infty^*=29.9"Hg$

V_∞^* (meters/sec)	P_j^* (dB)	C_D	R_o^*/ρ^*c^*	X_t^*/ρ^*c^*
0	70	.186	.0025	0
	80	.323	.0025	0
	90	.518	.0028	0
	100	.683	.0038	0
	110	.732	.0063	-.0002
	120	.723	.0109	-.0035
	125	.683	.0147	-.0062
	130	.660	.0198	-.0097
	135	.660	.0265	-.0128
	140	.645	.0372	-.0150
60.6	120	.113	.0688	-.0221
	125	.155	.0671	-.0219
	130	.202	.0688	-.0218
	135	.281	.0661	-.0196
	140	.363	.0696	-.0159

Model #7 $S/d_{16}=1.5$; $N=16$; $d_{16}^*=1.78$ mm; $\tau^*=1.02$ mm; $D^*=5.08$ mm; $L^*=38.10$ mm; $f_{res}^*=564$ Hz; $T_\infty^*=61°F$; $P_\infty^*=30"Hg$

V_∞^* (meters/sec)	P_j^* (dB)	C_D	R_o^*/ρ^*c^*	X_t^*/ρ^*c^*
0	70	.135	.0034	0
	80	.240	.0034	0
	90	.398	.0037	-.0001
	100	.531	.0049	-.0003
	110	.616	.0074	-.0011
	115	.638	.0094	-.0023
	120	.629	.0126	-.0038
	125	.601	.0175	-.0057
	130	.581	.0242	-.0080
	135	.587	.0322	-.0093

V_∞^* (meters/sec)	P_j^* (dB)	C_D	$R_o^*/\rho^* c^*$	$X_t^*/\rho^* c^*$
7.6	115	.644	.0094	-.0025
	120	.637	.0125	-.0039
	125	.622	.0171	-.0051
	130	.608	.0234	-.0066
	135	.608	.0314	-.0082
13.7	115	.615	.0093	-.0044
	120	.587	.0129	-.0058
	125	.601	.0170	-.0072
	130	.594	.0231	-.0091
	135	.601	.0309	-.0110
20.4	115	.461	.0114	-.0072
	120	.494	.0144	-.0087
	125	.530	.0182	-.0103
	130	.523	.0262	-.0106
	135	.561	.0334	-.0108
29.0	115	.251	.0192	-.0158
	120	.312	.0223	-.0145
	125	.318	.0252	-.0134
	130	.446	.0301	-.0140
	135	.500	.0369	-.0138
41.5	115	.160	.0328	-.0210
	120	.206	.0348	-.0205
	125	.272	.0359	-.0193
	130	.430	.0415	-.0193
	135	.411	.0448	-.0172
58.2	115	.102	.0550	-.0266
	120	.143	.0525	-.0253
	125	.186	.0544	-.0244
	130	.239	.0569	-.0241
	135	.312	.0590	-.0227
70.7	115	.090	.0638	-.0270
	120	.116	.0662	-.0275
	125	.154	.0665	-.0268
	130	.194	.0710	-.0271
	135	.248	.0751	-.0262
79.6	115	.077	.0762	-.0288
	120	.092	.0848	-.0311
	125	.133	.0783	-.0284
	130	.167	.0835	-.0286
	135	.234	.0800	-.0265

Model #8 $S^*/d^*=2.5$; $N=16$; $d^*=1.78$ mm; $\tau^*=1.02$ mm; $D^*=50.80$ mm; $L^*=38.10$ mm; $f_{res}{}^*=628$ Hz; $T_\infty{}^*=68°F$; $P_\infty{}^*=29.9$"Hg

$V_\infty{}^*$ (meters/sec)	$P_i{}^*$ (dB)	C_D	$R_o{}^*/\rho^*c^*$	$X_t{}^*/\rho^*c^*$
0	70	.146	.0032	0
	80	.260	.0032	-.0001
	90	.437	.0034	-.0001
	100	.624	.0042	-.0003
	110	.701	.0066	-.0014
	115	.742	.0081	-.0024
	120	.768	.0101	-.0042
	125	.748	.0139	-.0061
	130	.731	.0190	-.0080
	135	.706	.0269	-.0095
	140	.690	.0374	-.0107
7.9	120	.757	.0103	-.0043
	125	.739	.0141	-.0060
	130	.714	.0196	-.0079
	135	.698	.0272	-.0094
	140	.698	.0370	-.0103
13.7	120	.690	.0110	-.0055
	125	.682	.0150	-.0070
	130	.682	.0204	-.0085
	135	.682	.0278	-.0100
	140	.682	.0379	-.0107
21.3	120	.506	.0154	-.0067
	125	.567	.0186	-.0071
	130	.608	.0233	-.0087
	135	.622	.0308	-.0100
	140	.616	.0403	-.0106
29.0	120	.350	.0227	-.0087
	125	.435	.0246	-.0084
	130	.506	.0284	-.0090
	135	.561	.0345	-.0097
	140	.601	.0433	-.0107
41.1	120	.242	.0331	-.0115
	125	.301	.0358	-.0114
	130	.379	.0383	-.0110
	135	.467	.0420	-.0099
	140	.561	.0469	-.0096

V_∞* (meters/sec)	P_i* (dB)	C_D	R_o*/ρ*c*	X_t*/ρ*c*
58.2	120	.175	.0463	-.0142
	125	.218	.0499	-.0143
	130	.284	.0513	-.0137
	135	.366	.0538	-.0113
	140	.456	.0580	-.0101
70.7	120	.136	.0601	-.0168
	125	.182	.0603	-.0160
	130	.234	.0627	-.0153
	135	.312	.0632	-.0132
	140	.397	.0667	-.0110

Model #9 $S^*/d_{16}^*=3.5$; $N=16$; $d_{16}^*=1.78$ mm; *=1.02 mm; $D^*=50.8$ mm; $L^*=38.10$ mm; $f_{res}^*=684$ Hz; $T_\infty^*=67°F$; $P_\infty^*=30$"Hg

V_∞* (meters/sec)	P_i* (dB)	C_D	R_o*/ρ*c*	X_t*/ρ*c*
0	70	.131	.0037	0
	80	.011	.0037	0
	90	.385	.0039	0
	100	.583	.0046	-.0004
	110	.669	.0069	-.0018
	115	.693	.0086	-.0033
	120	.737	.0104	-.0055
	125	.737	.0132	-.0083
	130	.680	.0190	-.0123
	135	.665	.0266	-.0157
7.9	120	.704	.0107	-.0061
	125	.704	.0138	-.0088
	130	.657	.0196	-.0128
	135	.642	.0274	-.0164

V_∞^* (meters/sec)	P_i^* (dB)	C_D	$R_o^*/\rho^* c^*$	$X_t^*/\rho^* c^*$
14.0	120	.635	.0109	-.0081
	125	.657	.0141	-.0104
	130	.627	.0199	-.0143
	135	.635	.0274	-.0171
21.3	120	.444	.0150	-.0124
	125	.493	.0190	-.0137
	130	.546	.0231	-.0161
	135	.559	.0311	-.0195
29.3	120	.293	.0224	-.0179
	125	.365	.0758	-.0182
	130	.439	.0296	-.0187
	135	.493	.0360	-.0209
41.1	120	.205	.0357	-.0224
	125	.262	.0376	-.0230
	130	.333	.0403	-.0225
	135	.400	.0459	-.0227
58.2	120	.151	.0511	-.0263
	125	.198	.0521	-.0257
	130	.244	.0572	-.0265
	135	.307	.0616	-.0257
71.0	120	.121	.0648	-.0302
	125	.159	.0661	-.0293
	130	.201	.0705	-.0300
	135	.265	.0721	-.0284
79.6	120	.105	.0753	-.0327
	125	.128	.0829	-.0350
	130	.181	.0789	-.0316
	135	.241	.0795	-.0300

Model #10 $S^*/d_{16}^*=5.0$; $N=16$; $d_{16}^*=1.78$ mm; $\tau^*=1.02$ mm; $D^*=50.80$ mm; $L^*=38.10$ mm; $f_{res}^*=709$ Hz; $T_\infty^*=66°F$; $P_\infty^*=30$"Hg.

V_∞^* (meters/sec)	P_i^* (dB)	C_D	R_o^*/ρ^*c^*	X_t^*/ρ^*c^*
0	70	.154	.0032	0
	80	.265	.0032	0
	90	.450	.0034	0
	100	.651	.0042	-.0002
	110	.739	.0064	-.0012
	120	.837	.0098	-.0038
	125	.815	.0130	-.0060
	130	.778	.0181	-.0085
	135	.735	.0261	-.0107
	140	.726	.0363	-.0114
7.7	120	.806	.0100	-.0042
	125	.778	.0137	-.0060
	130	.752	.0189	-.0084
	135	.726	.0266	-.0103
	140	.710	.0373	-.0113
13.7	120	.718	.0105	-.0061
	125	.726	.0141	-.0077
	130	.710	.0193	-.0102
	135	.694	.0278	-.0108
	140	.702	.0377	-.0114
21.3	120	.485	.0149	-.0101
	125	.510	.0179	-.0099
	130	.611	.0227	-.0114
	135	.633	.0301	-.0128
	140	.670	.0393	-.0125
29.2	120	.348	.0216	-.0128
	125	.408	.0253	-.0131
	130	.520	.0274	-.0120
	135	.564	.0342	-.0135
	140	.633	.0416	-.0134
41.2	120	.243	.0324	-.0154
	125	.306	.0348	-.0155
	130	.372	.0388	-.0154
	135	.464	.0424	-.0141
	140	.557	.0474	-.0145

V_∞* (meters/sec)	P_i* (dB)	C_D	R_o*/ρ*c*	X_t*/ρ*c*
58.0	120	.164	.0500	-.0178
	125	.219	.0502	-.0174
	130	.273	.0540	-.0181
	135	.364	.0545	-.0165
	140	.464	.0577	-.0150
70.6	120	.132	.0632	-.0195
	125	.180	.0617	-.0190
	130	.232	.0642	-.0188
	135	.292	.0684	-.0186
	140	.386	.0696	-.0168
79.7	120	.122	.0686	-.0206
	125	.161	.0697	-.0200
	130	.212	.0707	-.0193
	135	.276	.0727	-.0184
	140	.348	.0774	-.0181

Model #11 $S^*/d_{16}^*=6.0$; $N=16$; $d_{16}^*=1.78$ mm; $\tau^*=1.02$ mm; $D^*=50.80$ mm; $L^*=38.10$ mm; $f_{res}^*=708$ Hz; $T_\infty^*=67°F$ $P_\infty^*=30$"Hg

V_∞* (meters/sec)	P_i (dB)	C_D	R_o*/ρ*c*	X_t*/ρ*c*
0	70	.123	.0040	0
	80	.223	.0039	0
	90	.375	.0041	0
	100	.548	.0050	-.0002
	110	.622	.0077	-.0016
	115	.659	.0095	-.0029
	120	.679	.0116	-.0050
	125	.679	.0149	-.0079
	130	.637	.0213	-.0118
	135	.615	.0304	-.0142
	140	.594	.0439	-.0150

V_∞* (meters/sec)	P_i* (dB)	C_D	R_o*/ρ*c*	X_t*/ρ*c*
7.9	120	.659	.0120	-.0056
	125	.651	.0159	-.0081
	130	.615	.0225	-.0114
	135	.594	.0320	-.0136
	140	.581	.0453	-.0141
13.4	120	.594	.0126	-.0075
	125	.615	.0164	-.0094
	130	.587	.0232	-.0126
	135	.581	.0327	-.0141
	140	.581	.0455	-.0135
21.3	120	.411	.0178	-.0115
	125	.477	.0213	-.0118
	130	.517	.0269	-.0132
	135	.523	.0365	-.0151
	140	.548	.0485	-.0131
29.3	120	.291	.0268	-.0134
	125	.354	.0300	-.0133
	130	.421	.0349	-.0119
	135	.472	.0420	-.0124
	140	.512	.0527	-.0109
41.1	120	.197	.0419	-.0143
	125	.253	.0436	-.0141
	130	.319	.0470	-.0122
	135	.393	.0518	-.0092
	140	.440	.0620	-.0086
57.6	120	.135	.0632	-.0143
	125	.181	.0626	-.0133
	130	.223	.0682	-.0128
	135	.298	.0688	-.0092
	140	.366	.0750	-.0054
71.0	120	.108	.0775	-.0219
	125	.149	.0751	-.0206
	130	.190	.0788	-.0208
	135	.245	.0821	-.0196
	140	.315	.0857	-.0168

V_∞* (meters/sec)	P_i* (dB)	C_D	R_o*/ρ*c*	X_t*/ρ*c*
79.2	120	.097	.0859	-.0240
	125	.128	.0871	-.0244
	130	.171	.0873	-.0236
	135	.223	.0897	-.0225
	140	.288	.0937	-.0199

Model #12 $S^*/d_{36}^*=1.5$; $N=36$; $d_{36}^*=1.18$ mm; $\tau^*=1.02$ mm; $D^*=50.80$ mm; $L^*=38.10$ mm; $f_{res}^*=563$ Hz; $T_\infty^*=65°F$; $P_\infty^*=30$"Hg

V_∞* (meters/sec)	P_i* (dB)	C_D	R_o*/ρ*c*	X_t*/ρ*c*
0	70	.111	.0042	0
	80	.195	.0042	0
	90	.328	.0044	-.0001
	100	.502	.0052	-.0004
	110	.617	.0073	-.0014
	115	.632	.0095	-.0023
	120	.624	.0126	-.0036
	125	.617	.0170	-.0050
	130	.610	.0231	-.0063
	135	.617	.0306	-.0075
	140	.617	.0410	-.0089
7.9	120	.624	.0127	-.0033
	125	.632	.0168	-.0042
	130	.632	.0225	-.0052
	135	.632	.0301	-.0065
	140	.624	.0408	-.0074
13.6	120	.596	.0133	-.0034
	125	.617	.0172	-.0044
	130	.639	.0222	-.0052
	135	.639	.0298	-.0062
	140	.624	.0409	-.0070

V_∞^* (meters/sec)	P_j^* (dB)	C_D	$R_o^*/\rho^* c^*$	$X_t^*/\rho^* c^*$
21.0	120	.531	.0143	-.0059
	125	.569	.0182	-.0062
	130	.583	.0244	-.0056
	135	.617	.0307	-.0071
	140	.632	.0403	-.0075
28.7	120	.381	.0184	-.0112
	125	.463	.0217	-.0094
	130	.513	.0270	-.0089
	135	.576	.0327	-.0083
	140	.596	.0427	-.0084
40.8	120	.249	.0287	-.0162
	125	.328	.0300	-.0146
	130	.403	.0338	-.0127
	135	.479	.0391	-.0110
	140	.531	.0477	-.0100
57.2	120	.168	.0477	-.0196
	125	.222	.0457	-.0186
	130	.289	.0474	-.0174
	135	.368	.0506	-.0154
	140	.463	.0546	-.0123
69.7	120	.138	.0557	-.0203
	125	.184	.0561	-.0193
	130	.260	.0533	-.0173
	135	.324	.0576	-.0168
	140	.398	.0633	-.0150
78.3	120	.118	.0666	-.0206
	125	.162	.0643	-.0199
	130	.214	.0654	-.0191
	135	.282	.0666	-.0178
	140	.347	.0727	-.0169

Model #13 $S^*/d_{36}^*=2$; N=36; $d_{36}^*=1.18$ mm; $\tau^*=1.02$ mm; $D^*=50.80$ mm; $L^*=38.10$ mm; $f_{res}^*=644$ Hz; $T_\infty^*=69°F$; $P_\infty^*=30"Hg$

V_∞^* (meters/sec)	P_i^* (dB)	C_D	R_o^*/ρ^*c^*	X_t^*/ρ^*c^*
0	70	.103	.0046	0
	80	.178	.0048	-.0001
	90	.309	.0049	-.0001
	100	.484	.0055	-.0005
	110	.616	.0075	-.0020
	115	.653	.0093	-.0030
	120	.668	.0121	-.0040
	125	.668	.0162	-.0049
	130	.645	.0225	-.0067
	135	.638	.0305	-.0082
	140	.623	.0421	-.0092
7.6	120	.676	.0123	-.0027
	125	.676	.0161	-.0047
	130	.653	.0223	-.0061
	135	.645	.0303	-.0075
	140	.631	.0418	-.0085
13.6	120	.616	.0131	-.0044
	125	.645	.0168	-.0052
	130	.623	.0233	-.0066
	135	.638	.0307	-.0075
	140	.623	.0423	-.0085
21.3	120	.501	.0163	-.0047
	125	.562	.0193	-.0058
	130	.515	.0253	-.0070
	135	.595	.0329	-.0079
	140	.602	.0438	-.0089
28.8	120	.384	.0210	-.0068
	125	.452	.0240	-.0072
	130	.513	.0285	-.0076
	135	.556	.0354	-.0082
	140	.588	.0448	-.0090
40.5	120	.272	.0297	-.0098
	125	.343	.0316	-.0097
	130	.407	.0359	-.0096
	135	.484	.0406	-.0093
	140	.543	.0485	-.0100

V_c* (meters/sec)	P_i* (dB)	C_D	R_o*/ρ*c*	X_t*/ρ*c*
57.2	120	.193	.0420	-.0136
	125	.248	.0437	-.0132
	130	.302	.0482	-.0135
	135	.495	.0395	-.0098
	140	.462	.0568	-.0125
70.1	120	.146	.0536	-.0227
	125	.193	.0547	-.0218
	130	.251	.0566	-.0207
	135	.323	.0592	-.0196
	140	.402	.0647	-.0182
78.5	120	.130	.0610	-.0234
	125	.162	.0055	-.0245
	130	.202	.0706	-.0251
	135	.282	.0679	-.0226
	140	.363	.0709	-.0215

Model #14 $S^*/d_{36}^*=2.5$; $N=36$; $d^*=1.18$ mm; $\tau^*=1.02$ mm; $D^*=50.8$ mm; $L^*=38.1$ mm; $f_{res}^*=663$ Hz; $T_\infty^*=66°F$; $P_\infty^*=30"Hg$

V_∞* (meters/sec)	P_i* (dB)	C_D	R_o*/ρ*c*	X_t*/ρ*c*
0	70	.119	.0040	0
	80	.200	.0042	0
	90	.343	.0044	0
	100	.544	.0049	-.0003
	110	.677	.0068	-.0017
	120	.734	.0109	-.0039
	125	.745	.0146	-.0049
	130	.728	.0200	-.0062
	135	.720	.0271	-.0081
	140	.720	.0365	-.0096

V_∞* (meters/sec)	P_j* (dB)	C_D	R_o*/ρ*c*	X_t*/ρ*c*
7.7	120	.737	.0109	-.0040
	125	.737	.0147	-.0050
	130	.737	.0198	-.0062
	135	.720	.0272	-.0078
	140	.712	.0369	-.0096
13.5	120	.696	.0115	-.0046
	125	.712	.0151	-.0055
	130	.696	.0208	-.0071
	135	.696	.0281	-.0083
	140	.704	.0374	-.0096
21.1	120	.534	.0151	-.0056
	125	.613	.0178	-.0057
	130	.613	.0237	-.0077
	135	.649	.0303	-.0083
	140	.672	.0393	-.0094
29.2	120	.374	.0218	-.0074
	125	.460	.0238	-.0074
	130	.540	.0272	-.0078
	135	.579	.0342	-.0085
	140	.627	.0423	-.0096
41.1	120	.264	.0310	-.0098
	125	.322	.0342	-.0099
	130	.424	.0348	-.0093
	135	.510	.0391	-.0085
	140	.579	.0461	-.0090
58.0	120	.185	.0445	-.0133
	125	.233	.0474	-.0131
	130	.300	.0493	-.0128
	135	.396	.0504	-.0107
	140	.492	.0543	-.0099
70.5	120	.144	.0575	-.0165
	125	.194	.0571	-.0155
	130	.247	.0599	-.0155
	135	.337	.0592	-.0125
	140	.429	.0623	-.0115
79.1	120	.128	.0644	-.0196
	125	.173	.0641	-.0172
	130	.238	.0622	-.0155
	135	.287	.0694	-.0155
	140	.396	.0674	-.0130

TABLE OF CONTENTS

SUMMARY 1 1/A5

DEFINITION OF SYMBOLS 2 1/A6

1. INTRODUCTION 5 1/A9

2. SINGLE ORIFICE IMPEDANCE MODEL 7 1/A11

   2.1 Derivation of Governing Equations 8 1/A12

   2.2 Boundary Conditions 12 1/B2

   2.3 Semi-empirical Solution 13 1/B3

3. SINGLE ORIFICE MEASUREMENT PROGRAM 17 1/B7

   3.1 Two-Microphone Method 18 1/B8

   3.2 Determination of C_D 20 1/B10

   3.3 Comparison Between Predicted and Measured Impedance 25 1/C1

   3.4 Thick Orifices 29 1/C5

   3.5 Resonator Self-Noise 31 1/C7

4. IMPEDANCE OF CLUSTERED ORIFICES 32 1/C8

   4.1 Zero Grazing Flow, Low Sound Amplitude Results 33 1/C9

   4.2 Effect of Grazing Flow 35 1/C11

5. CONCLUSIONS 38 1/C14

APPENDIXES

   A - SINGLE ORIFICE DATA 40 1/D2

   B - SUMMARY OF FREQUENCY SWEEP DATA FOR SPECIAL MODEL FOR $V_\infty^* = 60$ m/sec and $P_i^* = 120$ dB 66 1/E14

   C - THICK ORIFICE DATA 67 1/F1

   D - CLUSTERED ORIFICE DATA 76 1/F10

REFERENCES 104 2/A11

TABLES 106 2/A13

FIGURES 110 2/B4

Model #15 $S^*/d_{36}^*=3.5$; $N=36$; $d^*=1.18$ mm; $\tau^*=1.02$ mm; $D^*=50.8$ mm; $L^*=38.1$ mm; $f_{res}^*=716$ Hz; $T_\infty^*=66°F$; $P_\infty^*=30"Hg$

V_∞^* (meters/sec)	P_i^* (dB)	C_D	R_o^*/ρ^*c^*	X_t^*/ρ^*c^*
0	70	.107	.0046	0
	80	.187	.0047	0
	90	.333	.0047	0
	100	.508	.0054	-.0002
	110	.678	.0071	-.0016
	115	.735	.0084	-.0029
	120	.752	.0107	-.0045
	125	.760	.0142	-.0057
	130	.760	.0193	-.0068
	135	.735	.0270	-.0084
	140	.726	.0369	-.0094
7.6	120	.743	.0108	-.0046
	125	.752	.0144	-.0058
	130	.743	.0197	-.0070
	135	.735	.0269	-.0086
	140	.735	.0364	-.0097
13.7	120	.686	.0113	-.0060
	125	.710	.0148	-.0072
	130	.710	.0201	-.0089
	135	.718	.0271	-.0101
	140	.701	.0378	-.0111
21.3	120	.526	.0147	-.0078
	125	.597	.0177	-.0083
	130	.632	.0226	-.0098
	135	.655	.0297	-.0112
	140	.616	.0393	-.0113
29.3	120	.352	.0224	-.0109
	125	.448	.0237	-.0110
	130	.526	.0276	-.0107
	135	.590	.0334	-.0109
	140	.625	.0429	-.0111
40.8	120	.261	.0315	-.0116
	125	.317	.0347	-.0124
	130	.394	.0377	-.0118
	135	.497	.0406	-.0100
	140	.557	.0487	-.0096

V_∞* (meters/sec)	P_i* (dB)	C_D	R_o*/ρ*c*	X_t*/ρ*c*
57.9	120	.176	.0479	-.0132
	125	.232	.0488	-.0121
	130	.296	.0515	-.0110
	135	.394	.0519	-.0085
	140	.474	.0580	-.0062
71.0	120	.148	.0578	-.0121
	125	.202	.0568	-.0102
	130	.249	.0618	-.0097
	135	.332	.0621	-.0075
	140	.423	.0653	-.0048
79.2	120	.132	.0633	-.0195
	125	.166	.0672	-.0201
	130	.224	.0670	-.0178
	135	.292	.0689	-.0170
	140	.372	.0729	-.0146

Model #16 $S^*/d_{36}^*=5.0$; $N=36$; $d_{36}^*=1.18$ mm; $\tau^*=1.02$ mm; $D^*=50.8$ mm; $L^*=38.10$ mm; $f_{res}^*=717$ Hz; $T_\infty^*=64°F$; $P_\infty^*=30.15$"Hg

V_∞* (meters/sec)	P_i* (dB)	C_D	R_o*/ρ*c*	X_t*/ρ*c*
0	70	.098	.0050	0
	80	.172	.0050	0
	90	.295	.0052	-.0001
	100	.473	.0057	-.0004
	110	.609	.0077	-.0018
	115	.653	.0094	-.0032
	120	.684	.0117	-.0047
	125	.6837	.0156	-.0061
	130	.653	.0222	-.0076
	135	.661	.0298	-.0080
	140	.661	.0403	-.0085

V_∞^* (meters/sec)	P_i^* (dB)	C_D	$R_o^*/\rho^* c^*$	$X_t^*/\rho^* c^*$
8.1	120	.661	.0120	-.0050
	125	.668	.0161	-.0060
	130	.653	.0223	-.0072
	135	.653	.0301	-.0083
	140	.653	.0408	-.0087
13.9	120	.609	.0126	-.0063
	125	.631	.0165	-.0076
	130	.631	.0226	-.0089
	135	.645	.0301	-.0096
	140	.645	.0410	-.0096
21.0	120	.462	.0166	-.0085
	125	.537	.0195	-.0089
	130	.575	.0248	-.0097
	135	.589	.0328	-.0112
	140	.624	.0423	-.0108
28.9	120	.331	.0234	-.0114
	125	.412	.0254	-.0114
	130	.484	.0296	-.0111
	135	.549	.0354	-.0112
	140	.589	.0448	-.0115
40.5	120	.229	.0352	-.0133
	125	.292	.0368	-.0139
	130	.367	.0395	-.0133
	135	.452	.0435	-.0122
	140	.519	.0511	-.0118
57.5	120	.172	.0408	-.0143
	125	.216	.0510	-.0146
	130	.269	.0549	-.0147
	135	.343	.0580	-.0137
	140	.412	.0649	-.0124
69.5	120	.136	.0610	-.0162
	125	.180	.0618	-.0161
	130	.226	.0657	-.0160
	135	.288	.0692	-.0151
	140	.371	.0721	-.0131
78.2	120	.122	.0686	-.0176
	125	.158	.0703	-.0175
	130	.204	.0731	-.0169
	135	.260	.0768	-.0163
	140	.339	.0789	-.0199

Model #17 $S^*/d_{64}^*=1.5$; $N=64$; $d_{64}^*=.89$ mm; $\tau^*=1.02$ mm; $D^*=50.8$ mm; $L^*=38.1$ mm; $f_{res}^*=567$ Hz; $T_\infty^*=67°F$; $P_\infty^*=30$"Hg.

V_∞^* (meters/sec)	P_i^* (dB)	C_D	R_o^*/ρ^*c^*	X_t^*/ρ^*c^*
0	70	.077	.0060	0
	80	.134	.0061	0
	90	.237	.0063	-.0001
	100	.357	.0072	-.0005
	110	.470	.0097	-.0016
	115	.510	.0118	-.0023
	120	.530	.0154	-.0033
	125	.561	.0193	-.0042
	130	.555	.0261	-.0054
	135	.561	.0346	-.0063
	140	.568	.0450	-.0070
7.3	120	.561	.0146	-.0028
	125	.574	.0190	-.0036
	130	.568	.0256	-.0046
	135	.574	.0339	-.0056
	140	.568	.0458	-.0068
13.4	120	.536	.0153	-.0026
	125	.568	.0193	-.0033
	130	.568	.0257	-.0044
	135	.581	.0336	-.0051
	140	.568	.0460	-.0058
21.3	120	.512	.0156	-.0047
	125	.536	.0200	-.0052
	130	.542	.0267	-.0055
	135	.524	.0351	-.0058
	140	.555	.0471	-.0056
29.0	120	.411	.0177	-.0097
	125	.472	.0221	-.0081
	130	.506	.0281	-.0080
	135	.542	.0356	-.0075
	140	.555	.0469	-.0072
41.5	120	.263	.0275	-.0157
	125	.342	.0294	-.0138
	130	.416	.0334	-.0122
	135	.472	.0404	-.0107
	140	.524	.0494	-.0090

V_∞* (meters/sec)	P_i* (dB)	C_D	R_o*/ρ*c*	X_t*/ρ*c*
57.9	120	.175	.0432	-.0196
	125	.226	.0453	-.0189
	130	.288	.0481	-.0181
	135	.384	.0492	-.0148
	140	.467	.0550	-.0122
71.0	120	.139	.0561	-.0203
	125	.178	.0590	-.0206
	130	.237	.0592	-.0201
	135	.312	.0606	-.0181
	140	.384	.0667	-.0159
79.2	120	.127	.0621	-.0206
	125	.173	.0608	-.0199
	130	.213	.0663	-.0204
	135	.285	.0667	-.0188
	140	.350	.0730	-.0177

Model #18 $S^*/d_{64}^*=2.5$; N=64; $d^*=.39$ mm; $\tau^*=1.02$; $D^*=50.8$ mm; $L^*=38.10$ mm; $f_{res}^*=654$ Hz; $T_\infty^*=66°F$; $P_\infty^*=29.8$"Hg.

V_∞* (meters/sec)	P_i* (dB)	C_D	R_o*/ρ*c*	X_t*/ρ*c*
0	70	.085	.0056	0
	80	.155	.0055	0
	90	.263	.0057	0
	100	.418	.0064	-.0004
	110	.538	.0087	-.0019
	120	.618	.0133	-.0035
	125	.632	.0174	-.0041
	130	.639	.0230	-.0051
	135	.632	.0312	-.0062
	140	.639	.0413	-.0071

V_∞^* (meters/sec)	P_i^* (dB)	C_D	$R_o^*/\rho^* c^*$	$X_t^*/\rho^* c^*$
7.6	120	.617	.0133	-.0035
	125	.639	.0172	-.0040
	130	.639	.0231	-.0049
	135	.632	.0313	-.0059
	140	.639	.0414	-.0069
13.5	120	.590	.0139	-.0037
	125	.617	.0178	-.0044
	130	.625	.0235	-.0054
	135	.625	.0316	-.0062
	140	.617	.0429	-.0069
20.8	120	.514	.0160	-.0039
	125	.557	.0198	-.0045
	130	.590	.0250	-.0054
	135	.603	.0328	-.0060
	140	.617	.0428	-.0070
28.7	120	.408	.0202	-.0049
	125	.485	.0230	-.0050
	130	.532	.0278	-.0057
	135	.570	.0347	-.0061
	140	.597	.0444	-.0071
40.8	120	.292	.0282	-.0068
	125	.355	.0310	-.0072
	130	.478	.0337	-.0071
	135	.508	.0390	-.0065
	140	.570	.0465	-.0070
57.2	120	.207	.0399	-.0094
	125	.249	.0444	-.0096
	130	.332	.0446	-.0089
	135	.413	.0481	-.0079
	140	.502	.0529	-.0074
69.8	120	.155	.0535	-.0109
	125	.219	.0505	-.0103
	130	.270	.0549	-.0107
	135	.335	.0592	-.0094
	140	.422	.0628	-.0093
78.0	120	.141	.0586	-.0126
	125	.184	.0602	-.0115
	130	.249	.0596	-.0110
	135	.299	.0664	-.0106
	140	.403	.0659	-.0089

Model #19 $S^*/d_{64}^*=3.5$; N=64; $d^*=.89$ mm; $\tau^*=1.02$mm; $D^*=50.8$ mm; $L^*=38.1$ mm; $f_{res}^*=698$ Hz; $T_\infty^*=64°F$; $P_\infty^*29.5$"Hg.

V_∞^* (meters/sec)	P_i^* (dB)	C_D	R_o^*/ρ^*c^*	X_t^*/ρ^*c^*
0	70	.077	.0064	0
	80	.134	.0065	0
	90	.235	.0066	-.0001
	100	.373	.0074	-.0004
	110	.515	.0074	-.0020
	115	.545	.0116	-.0032
	120	.571	.0147	-.0043
	125	.585	.0193	-.0051
	130	.591	.0257	-.0057
	135	.605	.0337	-.0064
	140	.598	.0457	-.0073
7.9	120	.578	.0145	-.0043
	125	.585	.0194	-.0049
	130	.585	.0260	-.0057
	135	.605	.0337	-.0062
	140	.598	.0457	-.0072
13.7	120	.546	.0153	-.0048
	125	.571	.0197	-.0055
	130	.578	.0262	-.0064
	135	.591	.0344	-.0070
	140	.598	.0457	-.0076
21.3	120	.449	.0187	-.0056
	125	.509	.0221	-.0061
	130	.552	.0274	-.0068
	135	.565	.0360	-.0076
	140	.578	.0472	-.0080
29.3	120	.344	.0245	-.0070
	125	.423	.0265	-.0076
	130	.481	.0315	-.0076
	135	.527	.0386	-.0080
	140	.546	.0500	-.0086
40.2	120	.252	.0337	-.0084
	125	.321	.0352	-.0091
	130	.395	.0384	-.0088
	135	.470	.0435	-.0081
	140	.515	.0531	-.0084

V_∞* (meters/sec)	P_i* (dB)	C_D	R_o*/ρ*c*	X_t*/ρ*c*
57.9	120	.185	.0464	-.0095
	125	.244	.0469	-.0100
	130	.307	.0498	-.0100
	135	.386	.0530	-.0089
	140	.489	.0598	-.0079
71.0	120	.152	.0567	-.0103
	125	.203	.0567	-.0099
	130	.255	.0602	-.0101
	135	.325	.0632	-.0093
	140	.386	.0712	-.0082
79.6	120	.134	.0644	-.0111
	125	.175	.0660	-.0109
	130	.230	.0669	-.0104
	135	.303	.0678	-.0094
	140	.360	.0764	-.0082

Model #20 $S^*/d_{64}^*=5.0$; N=64; $d^*=.89$ mm; $\tau^*=1.02$ mm; $D^*=50.8$ mm; $L^*=38.1$ mm; $f_{res}^*=774$ Hz; $T_\infty^*=66°F$; $P_\infty^*=29.6$"Hg.

V_∞* (meters/sec)	P_i* (dB)	C_D	R_o*/ρ*c*	X_t*/ρ*c*
0	70	.090	.0056	0
	80	.160	.0056	0
	90	.281	.0056	0
	100	.456	.0062	-.0004
	110	.623	.0079	-.0017
	120	.672	.0126	-.0041
	130	.695	.0220	-.0056
	135	.707	.0293	-.0058
	140	.703	.0394	-.0064

V_∞* (meters/sec)	P_i* (dB)	C_D	R_o*/ρ*c*	X_t*/ρ*c*
7.6	120	.679	.0125	-.0038
	125	.687	.0166	-.0047
	130	.695	.0220	-.005
	135	.695	.0297	-.0059
	140	.703	.0393	-.0070
13.7	120	.620	.0134	-.0051
	125	.664	.0169	-.0057
	130	.679	.0223	-.0063
	135	.687	.0298	-.0068
	140	.703	.0392	-.0074
21.0	120	.527	.0156	-.0063
	125	.592	.0188	-.0067
	130	.627	.0240	-.0074
	135	.649	.0314	-.0080
	140	.679	.0400	-.0101
28.6	120	.395	.0208	-.0083
	125	.459	.0242	-.0089
	130	.552	.0273	-.0085
	135	.599	.0341	-.0084
	140	.656	.0419	-.0085
40.7	120	.274	.0307	-.0104
	125	.337	.0334	-.0110
	130	.424	.0355	-.0111
	135	.521	.0392	-.0094
	140	.599	.0459	-.0093
57.0	120	.203	.0422	-.0116
	125	.250	.0457	-.0124
	130	.307	.0497	-.0130
	135	.397	.0518	-.0118
	140	.506	.0547	-.0105
69.5	120	.161	.0535	-.0129
	125	.205	.0562	-.0130
	130	.270	.0567	-.0135
	135	.333	.0618	-.0130
	140	.419	.0659	-.0121
78.0	120	.144	.0602	-.0139
	125	.179	.0646	-.0142
	130	.238	.0647	-.0140
	135	.303	.0681	-.0131
	140	.395	.0699	-.0119

REFERENCES

1. F. Mechel; P. Mertens; and W. Schilz: Research on Sound Propagation in Sound Absorbent Ducts with Superimposed Air Streams. AMRL-TDR-62-140, vol. III, Physik, Inst., Univ. Gottingen, West Germany (1962).

2. B. Phillips: Effects of High Wave Amplitude and Mean Flow on a Helmholtz Resonator. NASA TM X-1582 (1968).

3. D. Ronneberger: The Acoustic Impedance of Holes in the Wall of Flow Ducts. Journal of Sound and Vibration, vol. 24, p. 133 (1972).

4. P. D. Dean: An In Situ Method of Wall Acoustic Impedance Measurement in Flow Ducts. Journal of Sound and Vibration, vol. 34, No. 1, p. 97, (1974).

5. T. Rogers and A. S. Hersh: The Effect of Grazing Flow on the Steady-State Resistance of Isolated Square-Edged Orifices. NASA CR-2681, (1976).

6. K. J. Baumeister and E. J. Rice: Visual Study of the Effect of Grazing Flow on the Oscillatory Flow in a Resonator Orifice. NASA TM X-3288 (1975).

7. A. S. Hersh and T. Rogers, "Fluid Mechanical Model of the Acoustic Impedance of Small Orifices" NASA CR-2682, May, 1976.

8. E. J. Rice, "A Theoretical Study of the Acoustic-Impedance of Orifices in the Presence of a Steady Grazing Flow", NASA TM X-71903, April (1976).

9. U. Ingard, "On the Theory and Design of Acoustic Resonators", Jour. Acoust. Soc. Am., V. 25, 1037-1062 (1953).

10. V. A. Fok 1941, Doklady Akademii nank SSSR 31 (In Russian) Alternatively see S. N. Rschevkin 1963, A Course of Lectures on the Theory of Sound, London: pergamon Press.

11. E. H. Mellin, "The Acoustic Impedance of Perforates at Medium and High Sound Pressure Levels", Jour. Sound Vib., V. 29, No.1, 1-65 (1973).

12. U. Ingard and H. Ising, "Acoustic Nonlinearity of an Orifice", J. Acoustic Soc. Am., 42, (1967).

13. Heller, H. H. and Bliss, D. B., "Aerodynamically Induced Pressure Oscillations in Cavities - Physical Mechanisms and Supression Concepts," Tech Rept AFFDL-TR-74-133, Feb 1975, AF Flight Dynamics Laboratory (FY), Wright-Patterson Air Force Base, Ohio 45433.

14. F. C. DeMetz and T. M. Farabee, Laminar and Turbulent Shear Flow Induced Cavity Resonances", AIAA Paper 77-1293 Presented at the AIAA 4th Aeroacoustic Conference held in Atlanta, Georgia, Oct. 1977.

15. Rossiter, J. E., "Wind Tunnel Experiments on the Flow over Rectangular Cavities at Subsonic and Transonic Speeds," Royal Aircraft Establishment, Tech Rept. No. 64037, Oct 1964.

TABLE I

SUMMARY OF SINGLE ORIFICE RESONATOR GEOMETRIES TESTED

Model #	d* (mm)	f_{res} (Hz)	Slope $dC_D/d\eta$	τ^* (mm)	D* (mm)	L* (mm)	τ^*/d^*	d^*/D^*	d^*/L^*
1	.914	500	2.0	.51	19.05	12.7	.556	.048	.071
2	.914	495	2.25	.25	19.05	25.4	.278	.048	.048
3	1.02	590	2.17	.81	19.05	12.7	.800	.055	.053
4	.91	416	1.85	.51	19.05	25.4	.800	.055	.055
5	1.32	428	1.70	.81	31.75	12.7	.615	.047	.042
6	1.32	493	1.70	.81	19.05	25.4	.615	.069	.069
7	1.61	485	1.50	.81	31.75	12.7	.504	.051	.051
8	1.78	385	1.70	.51	31.75	25.4	.286	.056	.072
9	1.78	653	1.80	.51	19.05	25.4	.286	.093	.072
10	1.85	390	1.70	.81	31.75	25.4	.438	.058	.074
11	2.21	436	1.42	.81	31.75	25.4	.368	.070	.070
12	2.67	422	1.70	.81	31.75	38.1	.305	.084	.071
13	3.56	937	1.57	.25	19.05	38.1	.071	.187	.095
14	3.61	503	1.35	.81	31.75	38.1	.225	.114	.095
15	7.11	484	1.35	1.02	50.80	38.10	.143	.140	.184
16	7.11	892	1.13	2.03	31.75	25.4	.286	.224	.280

TABLE II

SUMMARY OF RESONATORS TESTED IN THICK ORIFICE STUDY

D* (mm)	L* (mm)	d* (mm)	τ* (mm)	τ*/d*
31.75	12.7	1.78	.509	.286
"	"	"	1.015	.571
"	"	"	2 032	1.143
"	"	"	4.065	2.286
"	"	"	8.127	4.571
"	"	"	15.875	8.929

TABLE III

MEASUREMENT OF GRAZING FLOW VELOCITY WHERE HYDRODYNAMIC RESONANCE OCCURS

Model No.	f^*_{res} (Hz)	d* (mm)	τ* (mm)	D* (mm)	L* (mm)	V_∞^* (measured m/s)	$f^*_{res} d^*/V^*_\infty$
1	892	7.112	2.032	31.75	25.4	24.4	0.26
2	484	7.112	1.016	50.8	38.1	15.5	0.23
3	1110	3.556	.508	19.05	25.4	16.5	0.24
4	680	.889	.254	19.05	12.7	13.4	0.30
5	600	.889	.500	19.05	12.7	2.1	0.26
6	937	3.556	.251	19.05	38.1	12.2	0.27

Average 0.26

TABLE IV

SUMMARY OF CLUSTERED ORIFICE CONFIGURATION AND RESULTS OF $V_\infty^*=0$, $P_i^*=70$ dB DATA

N	d_N^* (mm)	S^*/d^*_N	f_{res}^* (Hz)	R_o^*/ρ^*c^*	de^*/d_1^*	δ^*/d_1^*
1	7.11	0	484	.0020	.876	.733
4	3.56	2	555	.0025	.656	.513
"	"	3	594	.0025	.574	.431
"	"	2	553	.0024	.661	.518
"	"	3	592	.0025	.574	.431
"	"	2.5	563	.0025	.644	.501
16	1.78	1.5	564	.0034	.634	.491
"	"	2.5	628	.0032	.572	.369
"	"	3.5	684	.0037	.424	.281
"	"	5.0	709	.0052	.392	.249
"	"	6.0	708	.0040	.394	.251
36	1.19	1.5	563	.0042	.642	.499
"	"	2.0	644	.0046	.486	.343
"	"	2.5	663	.0040	.454	.311
"	"	3.5	716	.0046	.384	.241
"	"	5.0	717	.0050	.381	.238
64	.89	1.5	567	.0060	.635	.492
"	"	2.5	654	.0056	.467	.324
"	"	3.5	698	.0064	.404	.261
"	"	5.0	774	.0056	.323	.180

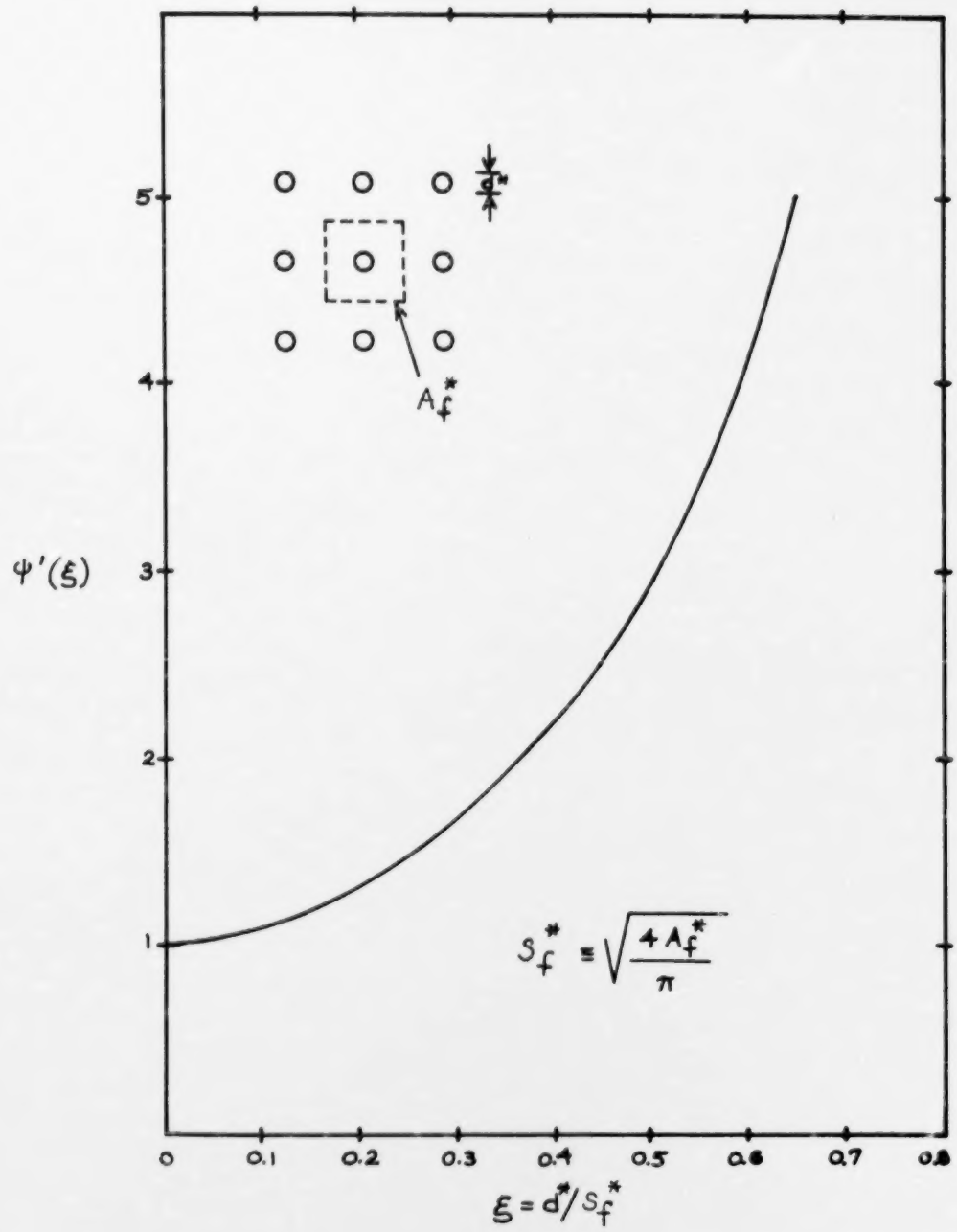

FIGURE 1. DEFINITION OF FOK INTERACTION PARAMETER

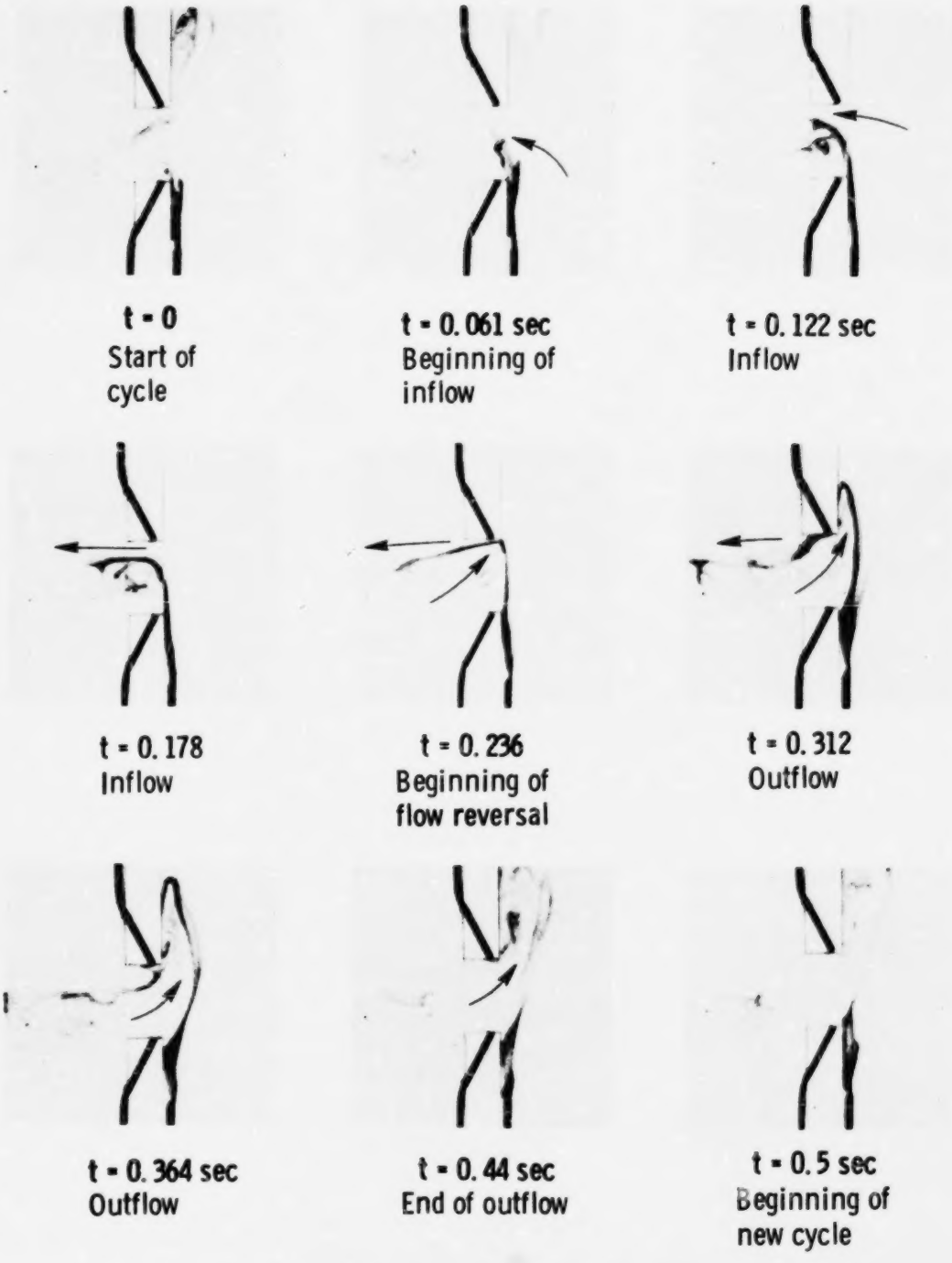

Figure 2 - Non-linear flow regimes with 0.3 meter/sec grazing flow and intermediate oscillating pressure amplitude (0.5 amplitude level). Photographs provided by E.J. Rice (Ref. 6)

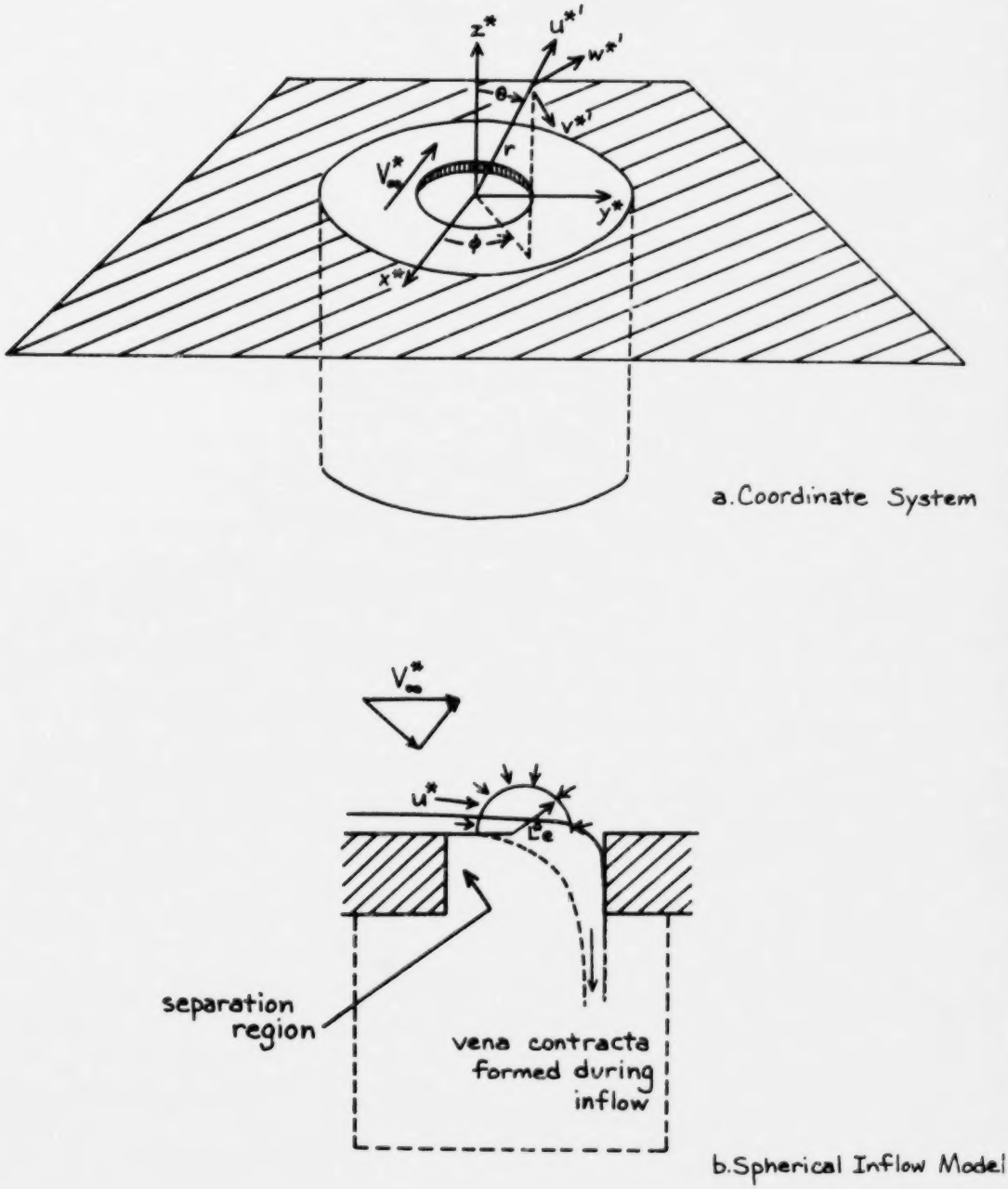

FIGURE 3. SCHEMATIC OF SOUND PARTICLE COORDINATE SYSTEM AND SPHERICAL INFLOW MODEL

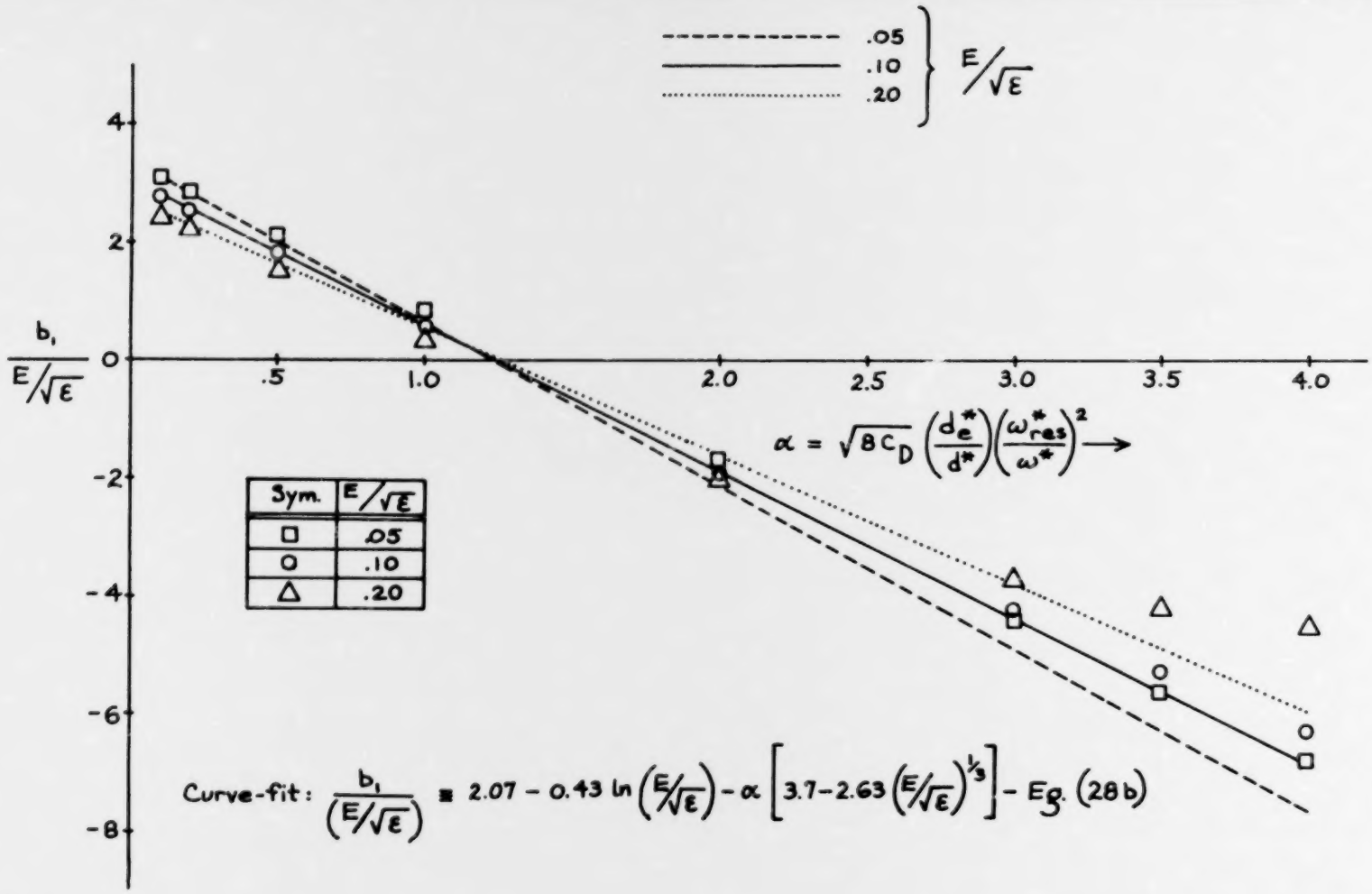

FIGURE 4. COMPARISON BETWEEN NUMERICAL CALCULATIONS OF b_1 AND CURVE-FIT

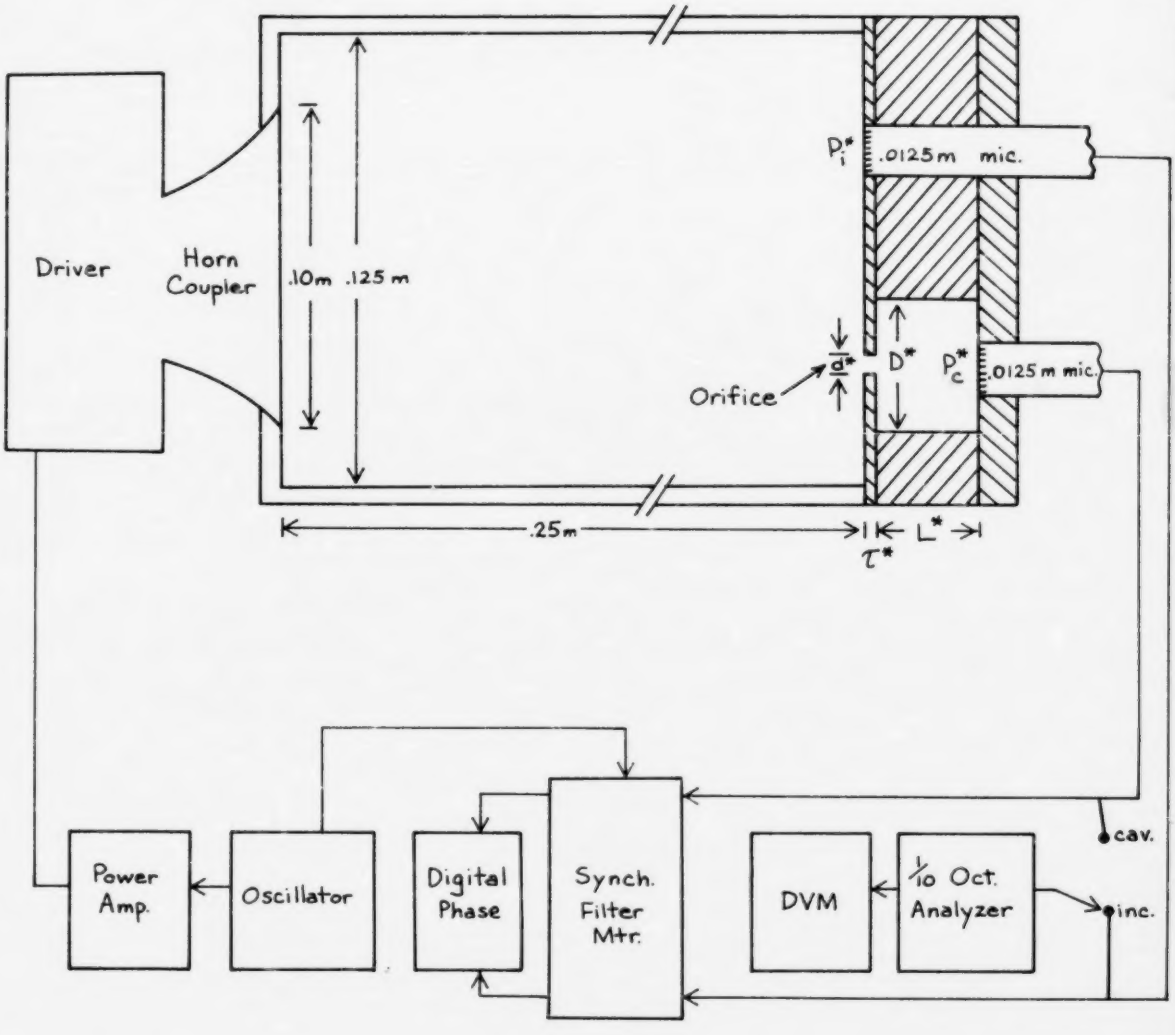

FIGURE 5. SCHEMATIC OF TEST APPARATUS

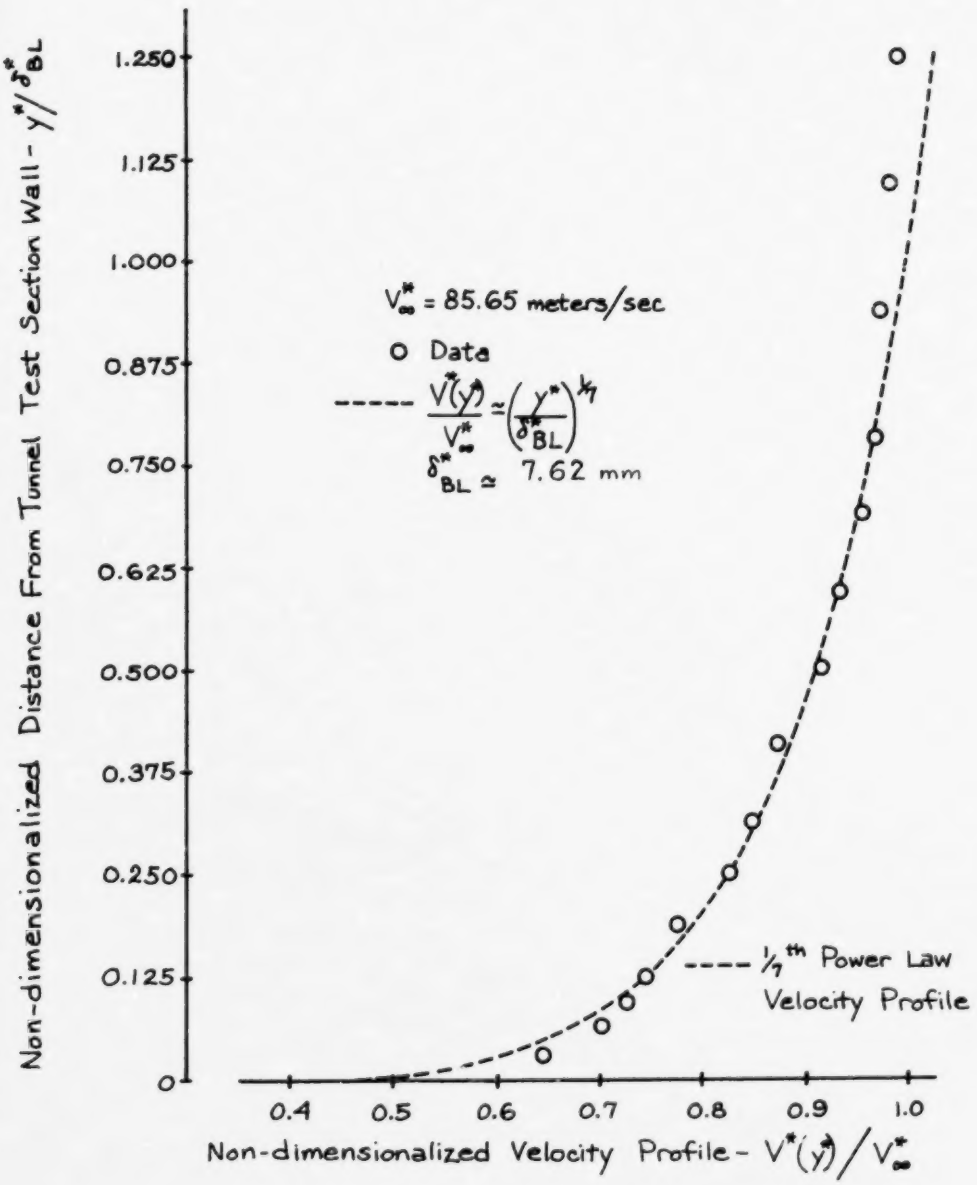

FIGURE 6. TEST SECTION BOUNDARY-LAYER VELOCITY PROFILE

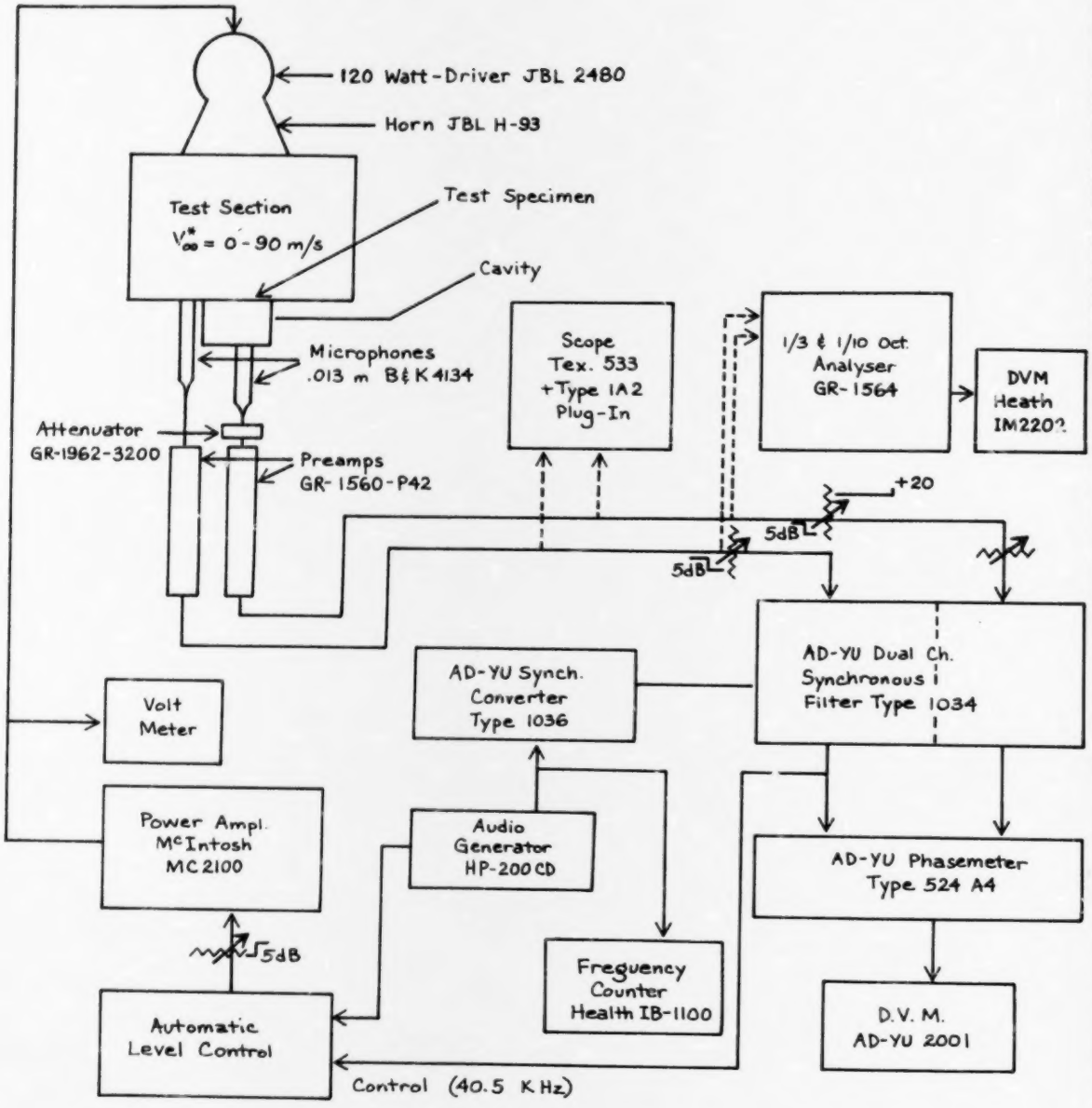

FIGURE 7. SCHEMATIC OF TWO-MICROPHONE MEASUREMENT SYSTEM

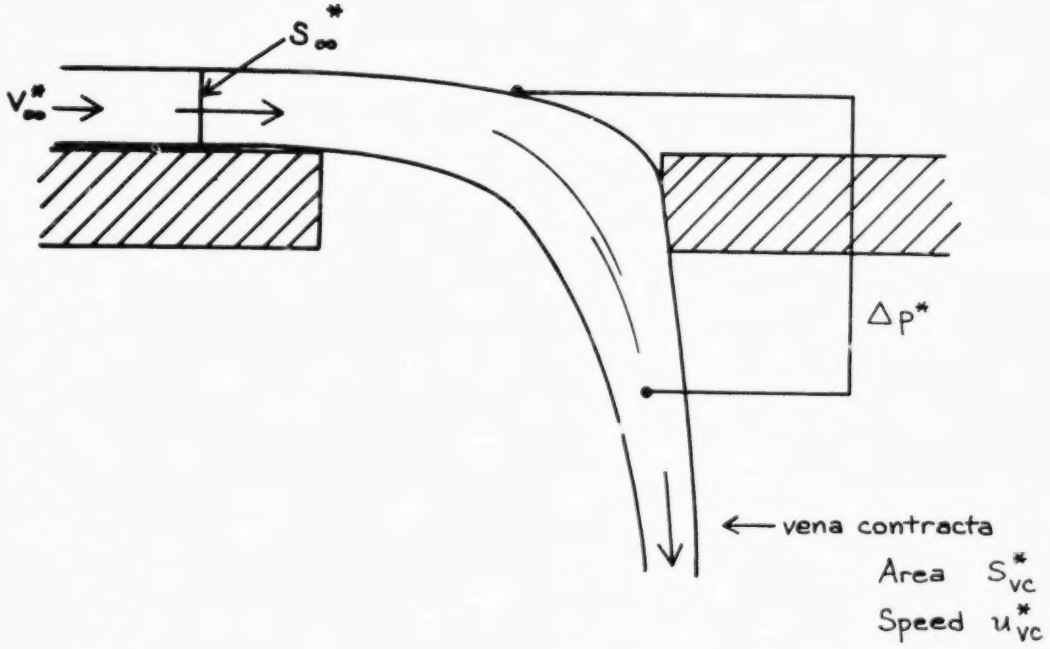

FIGURE 8. SCHEMATIC OF STEADY-STATE DEFLECTION OF GRAZING FLOW THROUGH ORIFICE

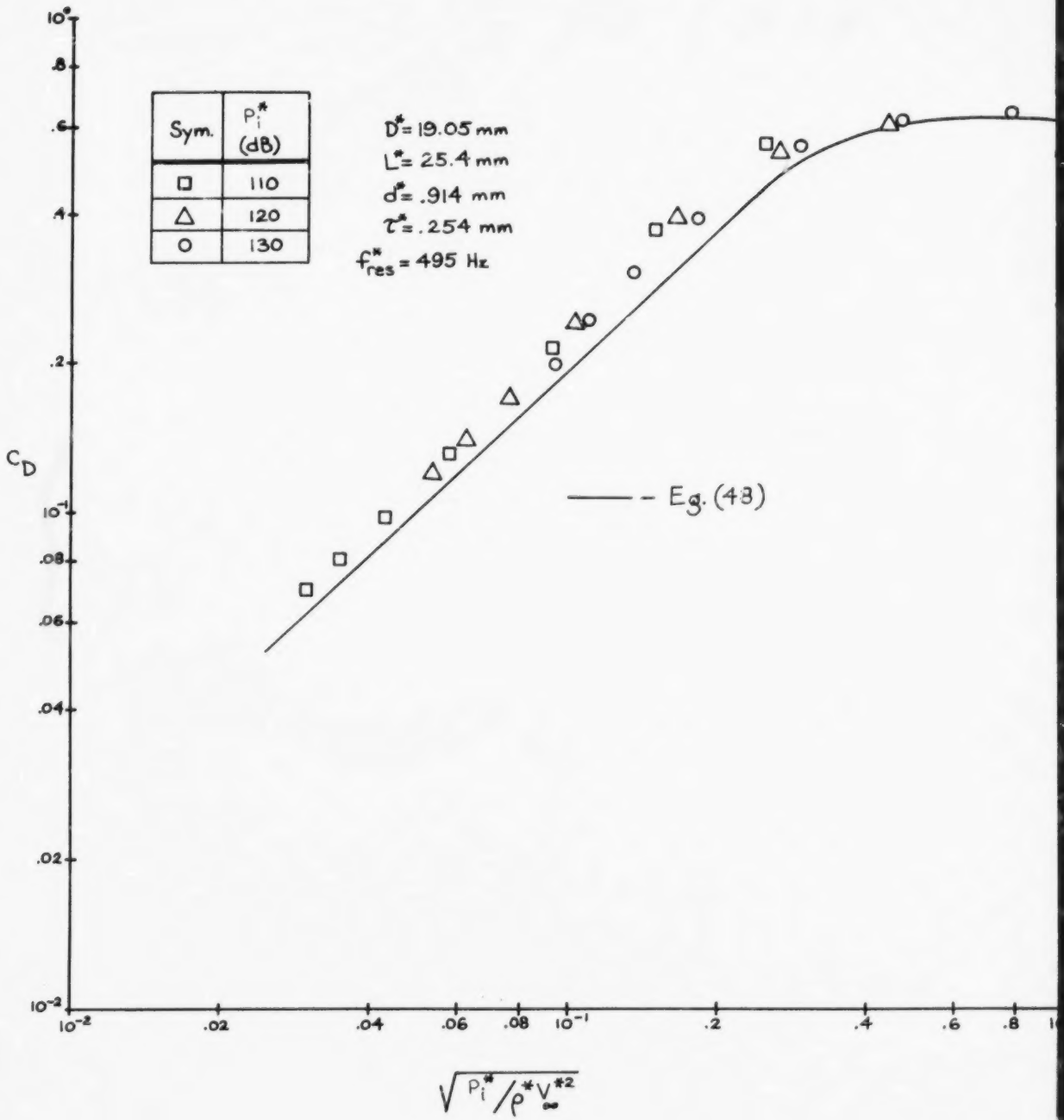

FIGURE 9a. CORRELATION OF MODEL 2 GRAZING FLOW SOUND DATA IN TERMS OF DISCHARGE COEFFICIENT

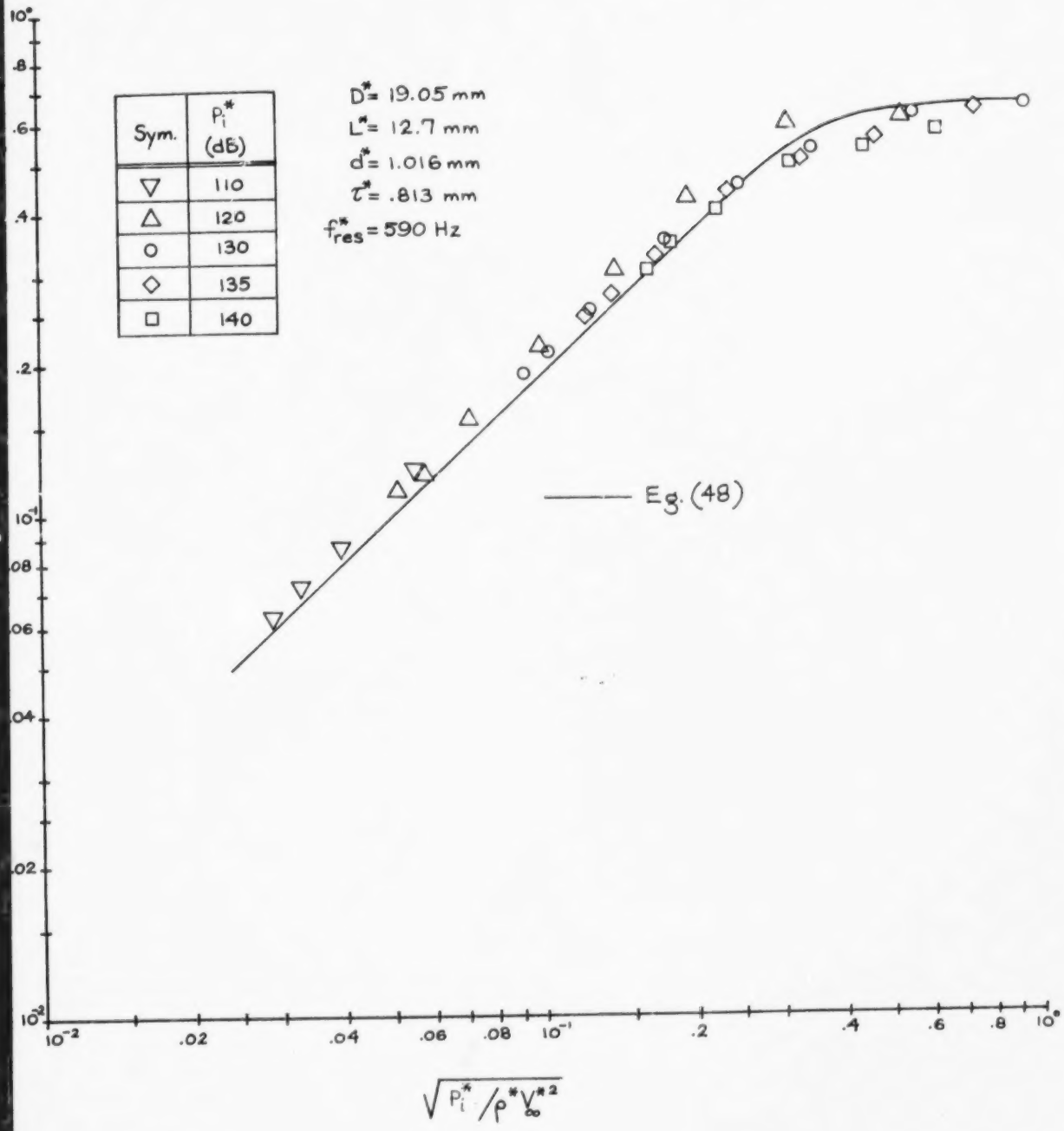

FIGURE 9b. CORRELATION OF MODEL 3 GRAZING FLOW SOUND DATA IN TERMS OF DISCHARGE COEFFICIENT

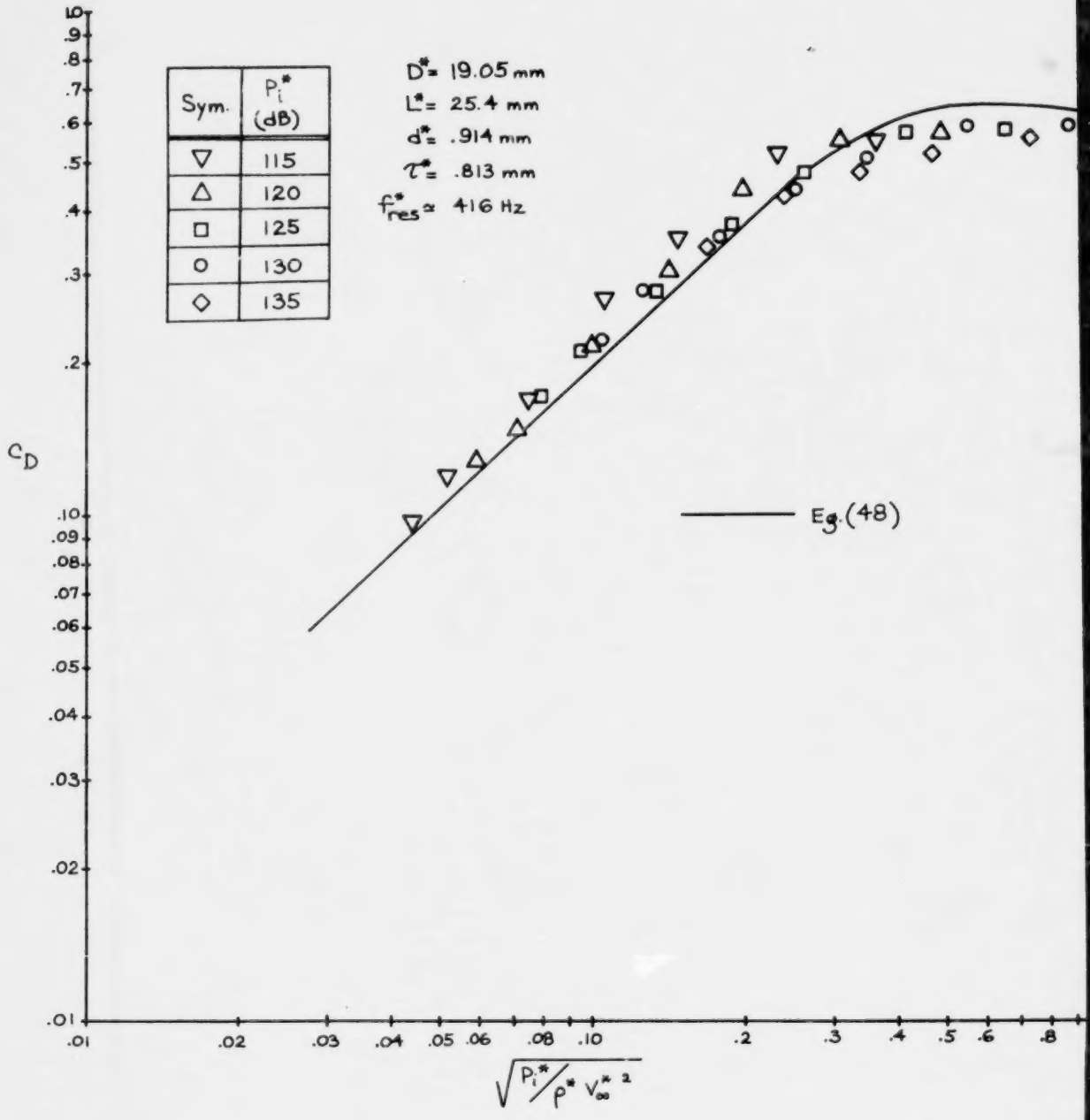

FIGURE 9c. CORRELATION OF MODEL 4 GRAZING FLOW SOUND DATA IN TERMS OF DISCHARGE COEFFICIENT

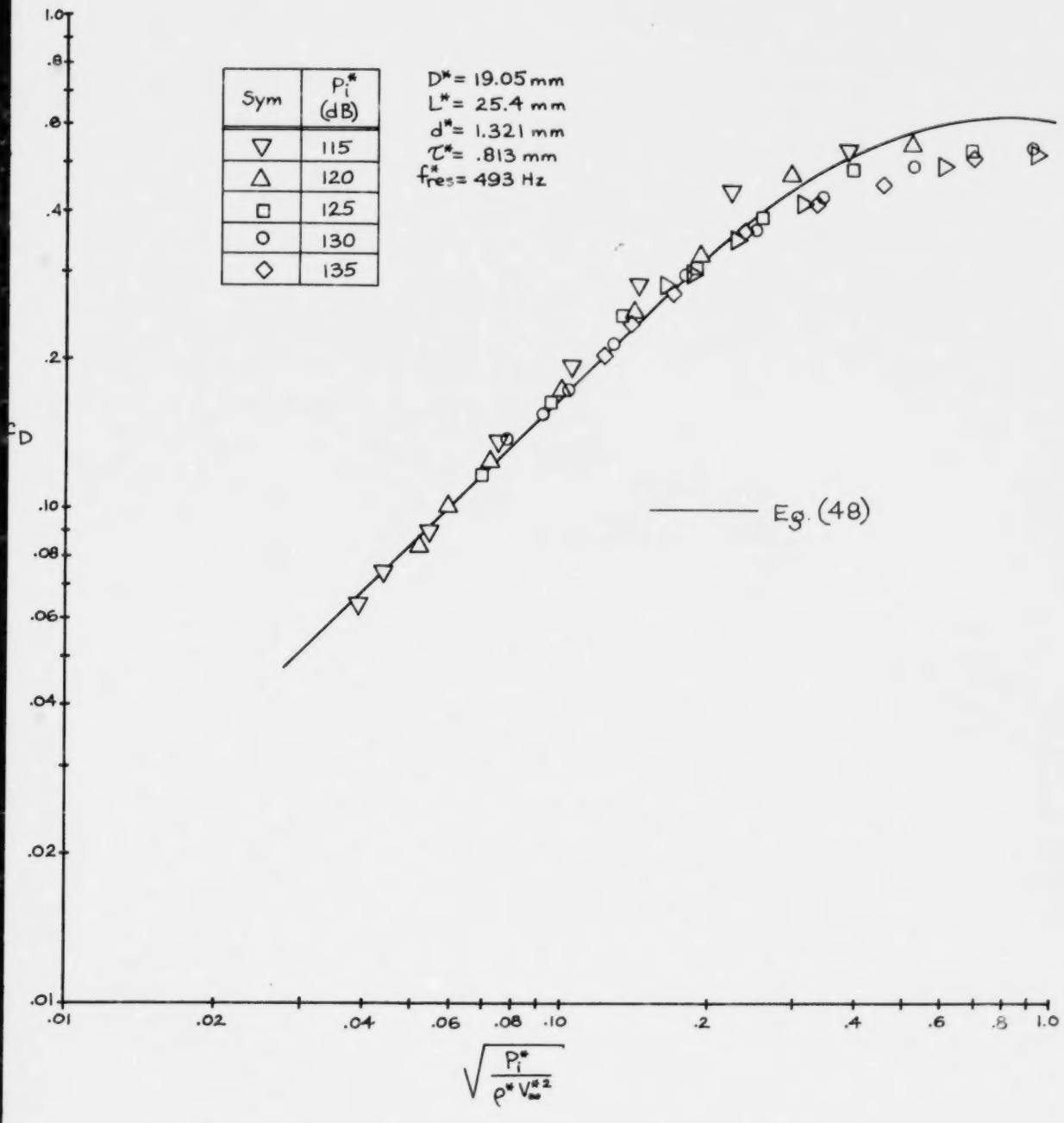

FIGURE 9d. CORRELATION OF MODEL 6 GRAZING FLOW SOUND DATA IN TERMS OF DISCHARGE COEFFICIENT

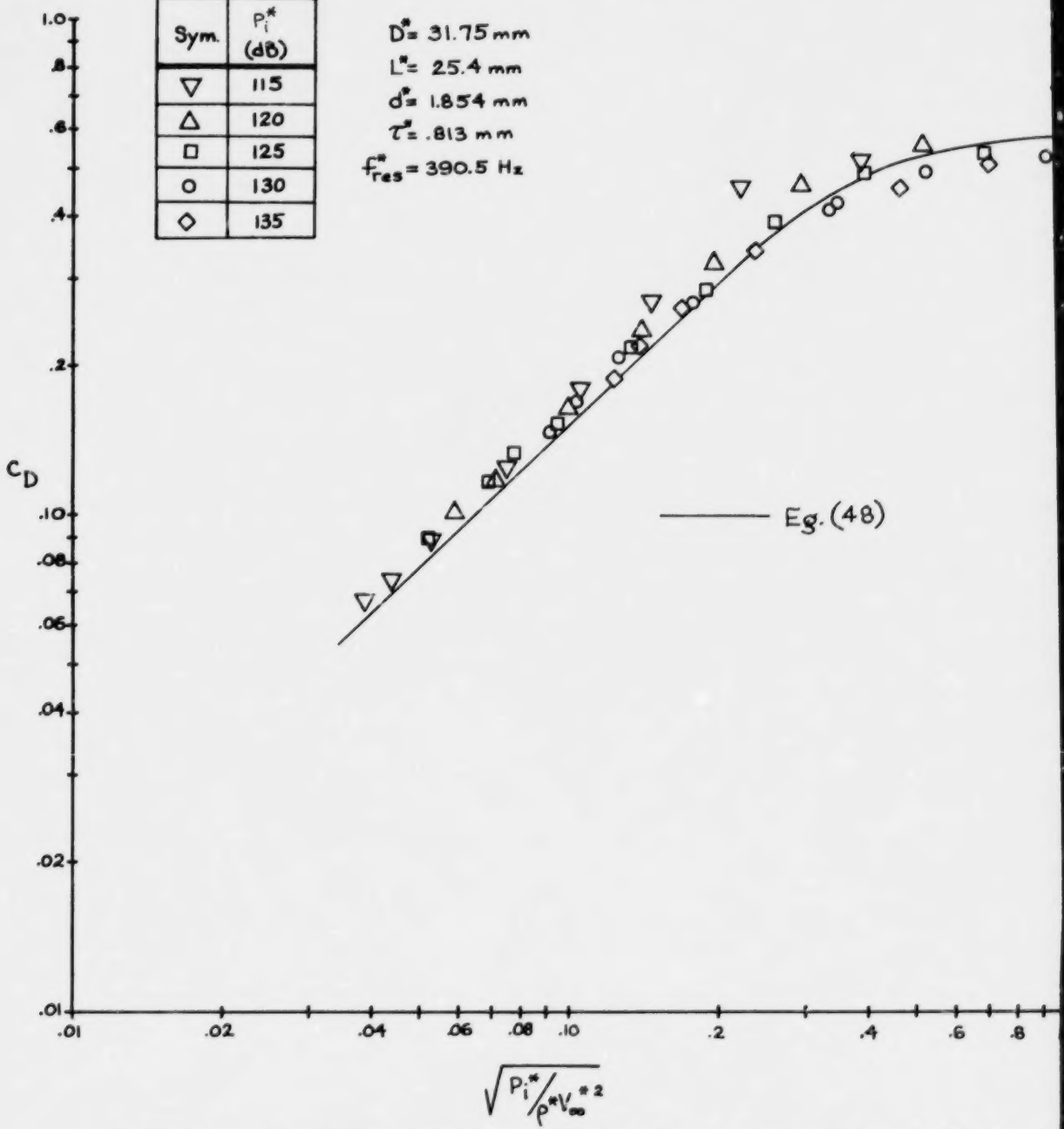

FIGURE 9e. CORRELATION OF MODEL 10 GRAZING FLOW SOUND DATA IN TERMS OF DISCHARGE COEFFICIENT

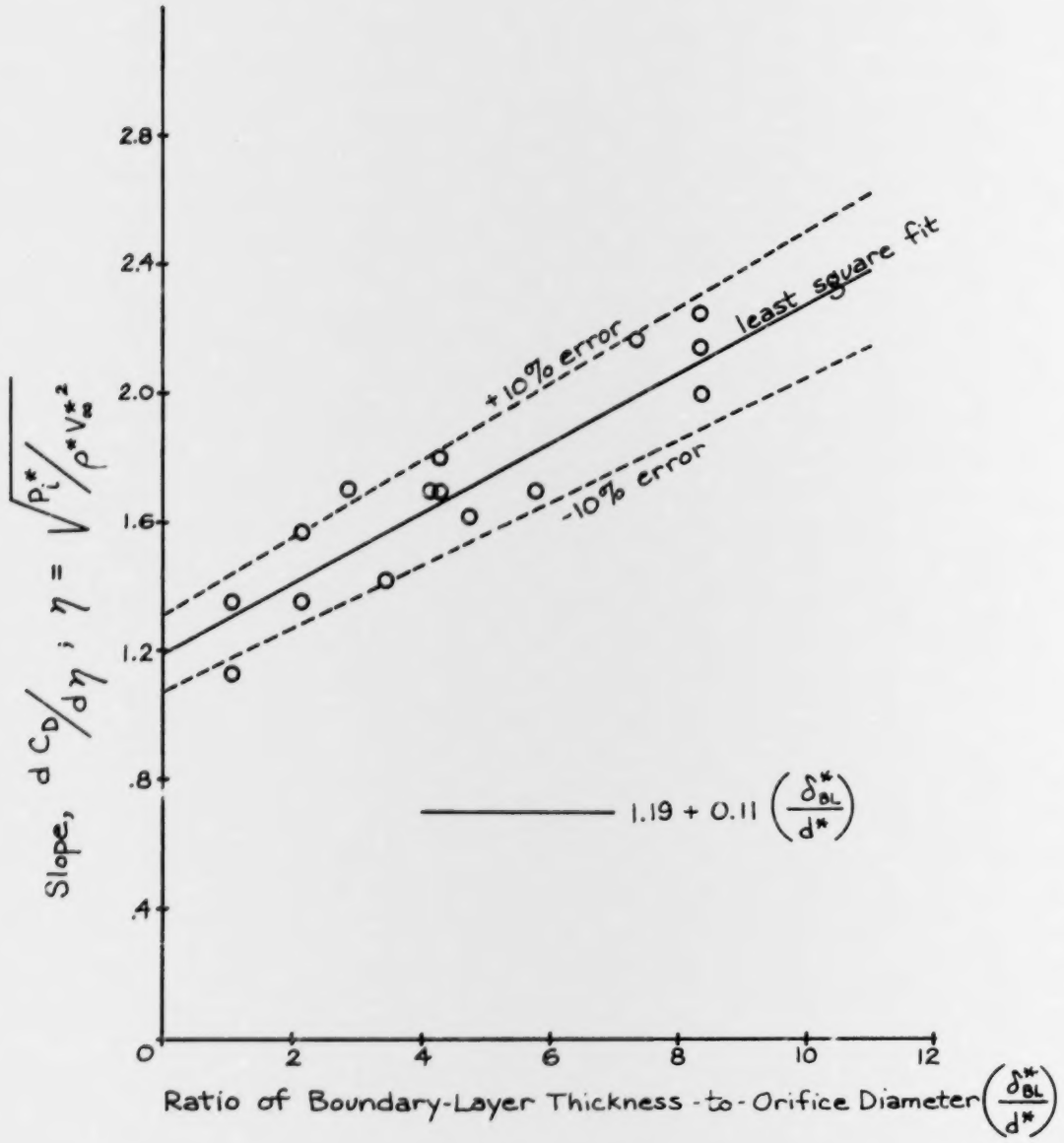

FIGURE 10. EFFECT OF GRAZING FLOW BOUNDARY-LAYER THICKNESS ON LINEAR SLOPE OF DISCHARGE COEFFICIENT

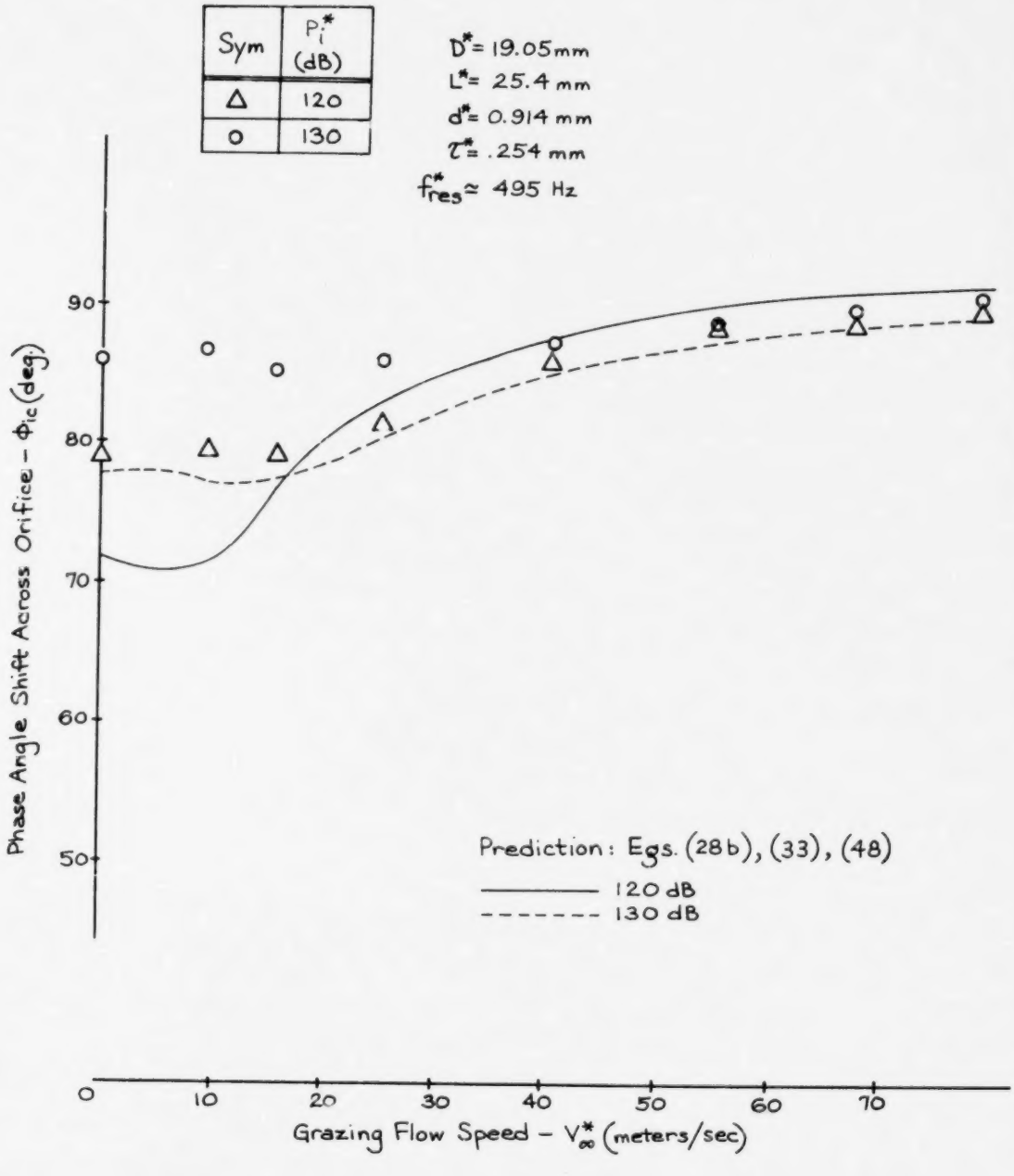

FIGURE 11a. EFFECT OF GRAZING FLOW ON THE PHASE SHIFT ACROSS THE ORIFICE OF MODEL 2

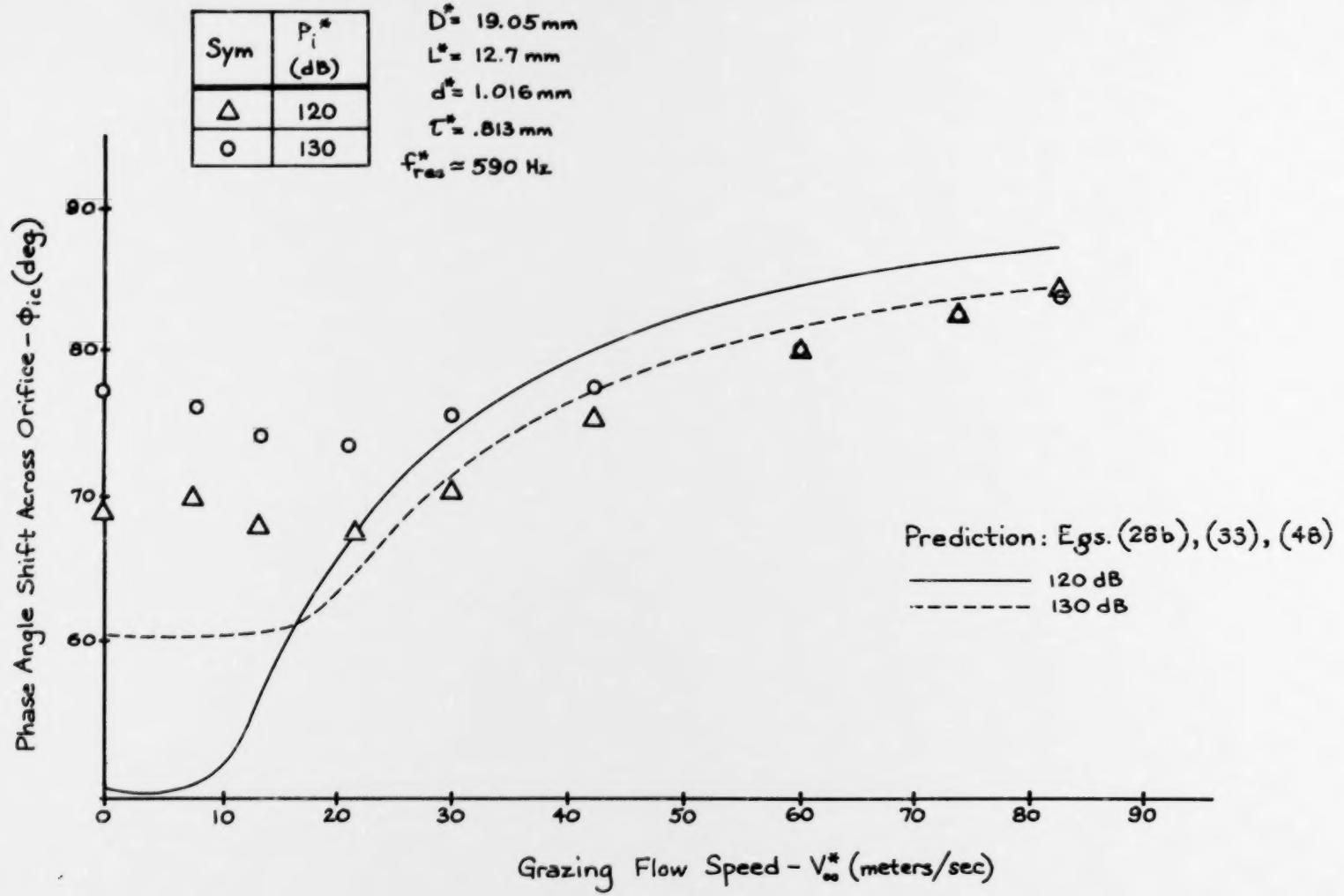

FIGURE 11b. EFFECT OF GRAZING FLOW ON THE PHASE SHIFT ACROSS THE ORIFICE OF MODEL 3

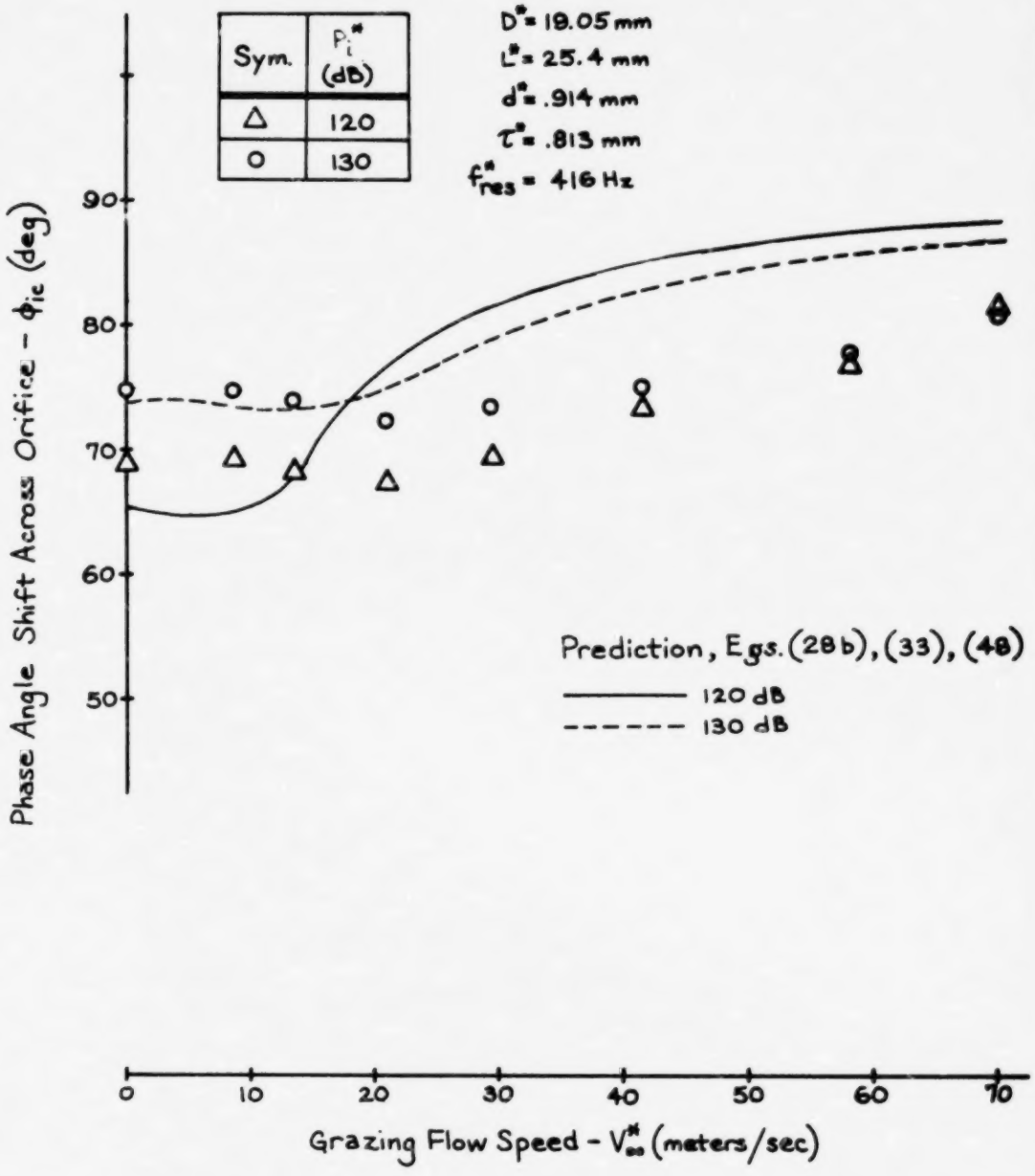

FIGURE 11c. EFFECT OF GRAZING FLOW ON THE PHASE SHIFT ACROSS THE ORIFICE OF MODEL 4

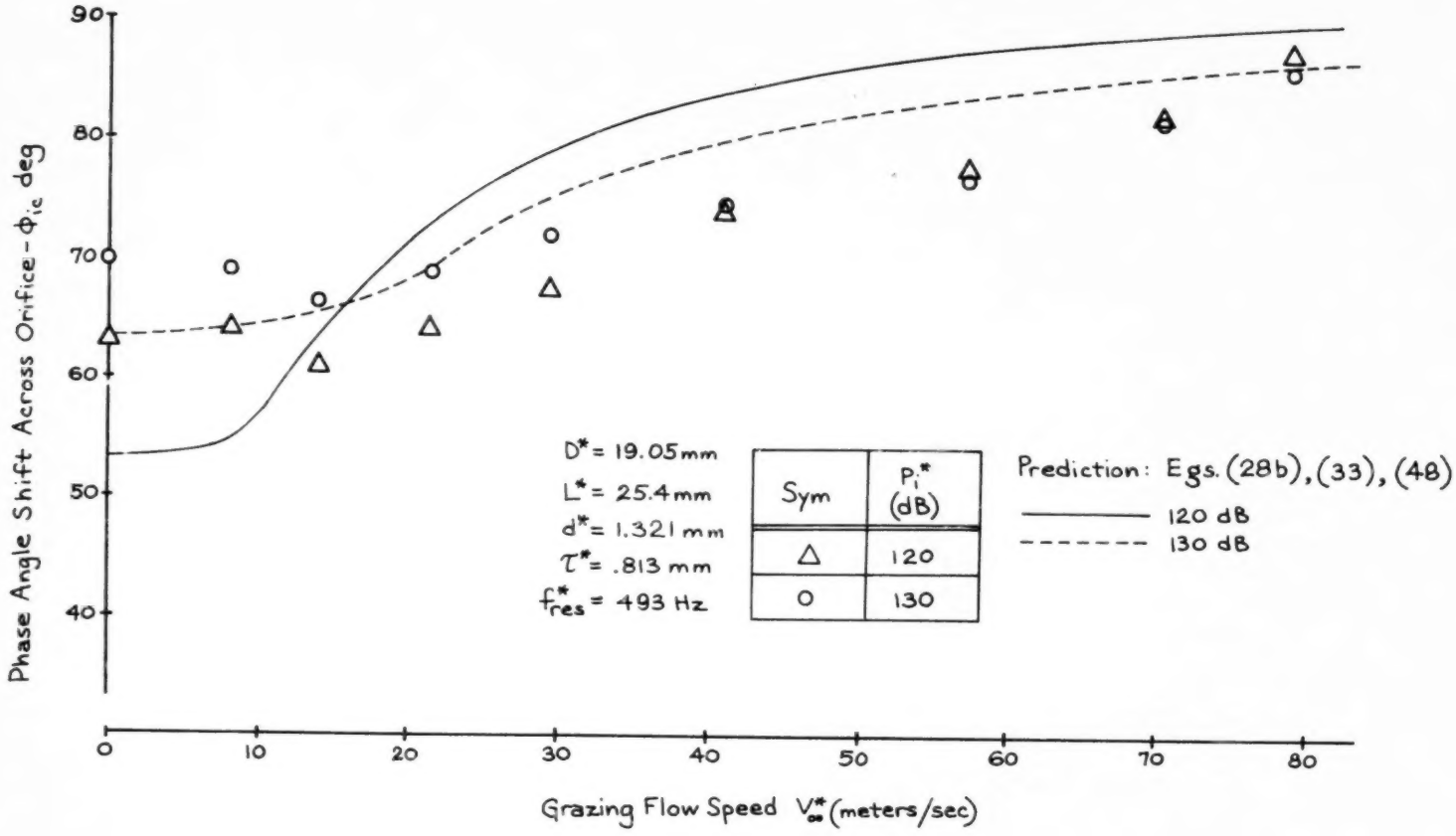

FIGURE 11d. EFFECT OF GRAZING FLOW ON THE PHASE SHIFT ACROSS THE ORIFICE OF MODEL 6

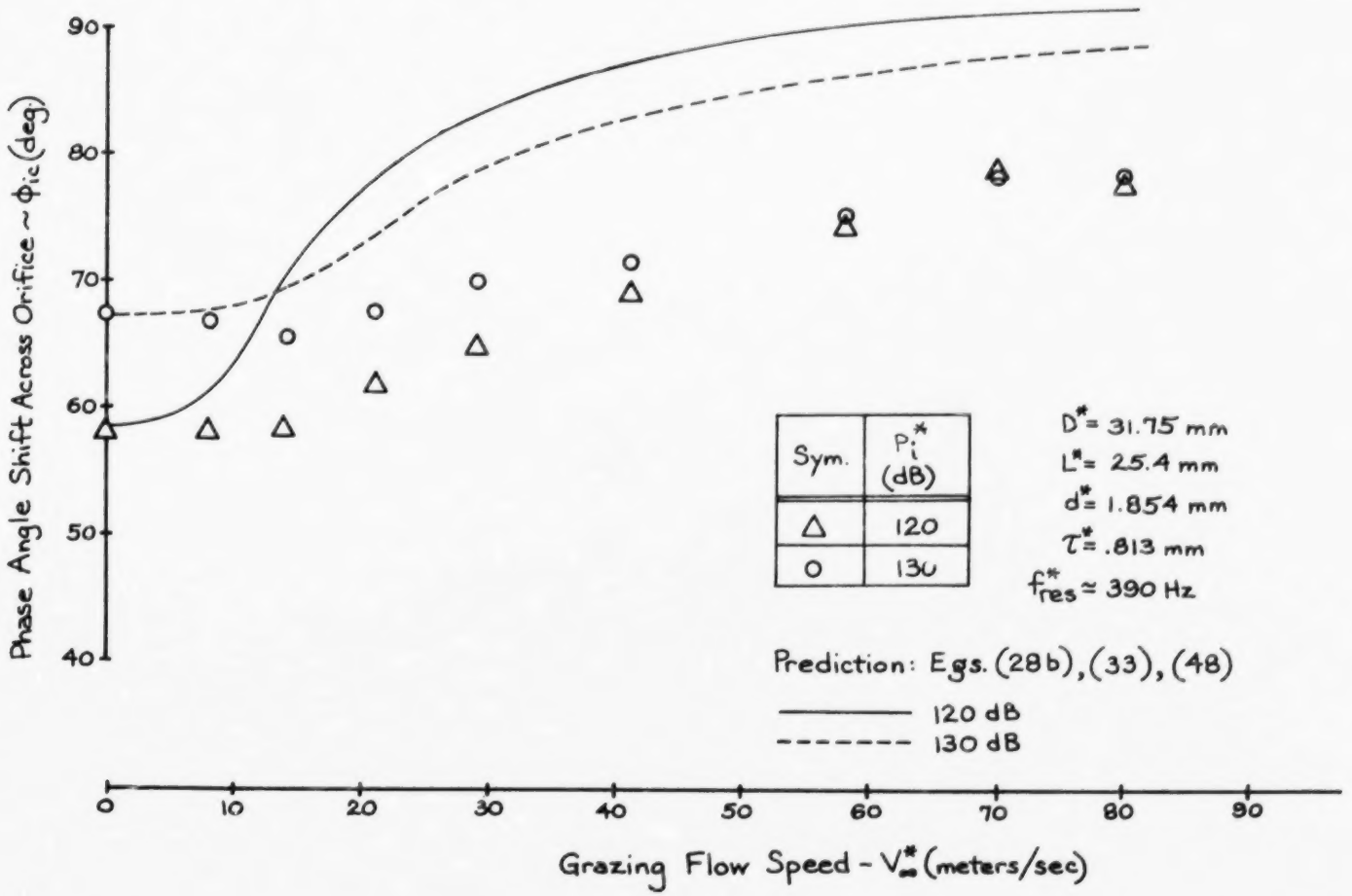

FIGURE 11e. EFFECT OF GRAZING FLOW ON THE PHASE SHIFT ACROSS THE ORIFICE OF MODEL 10

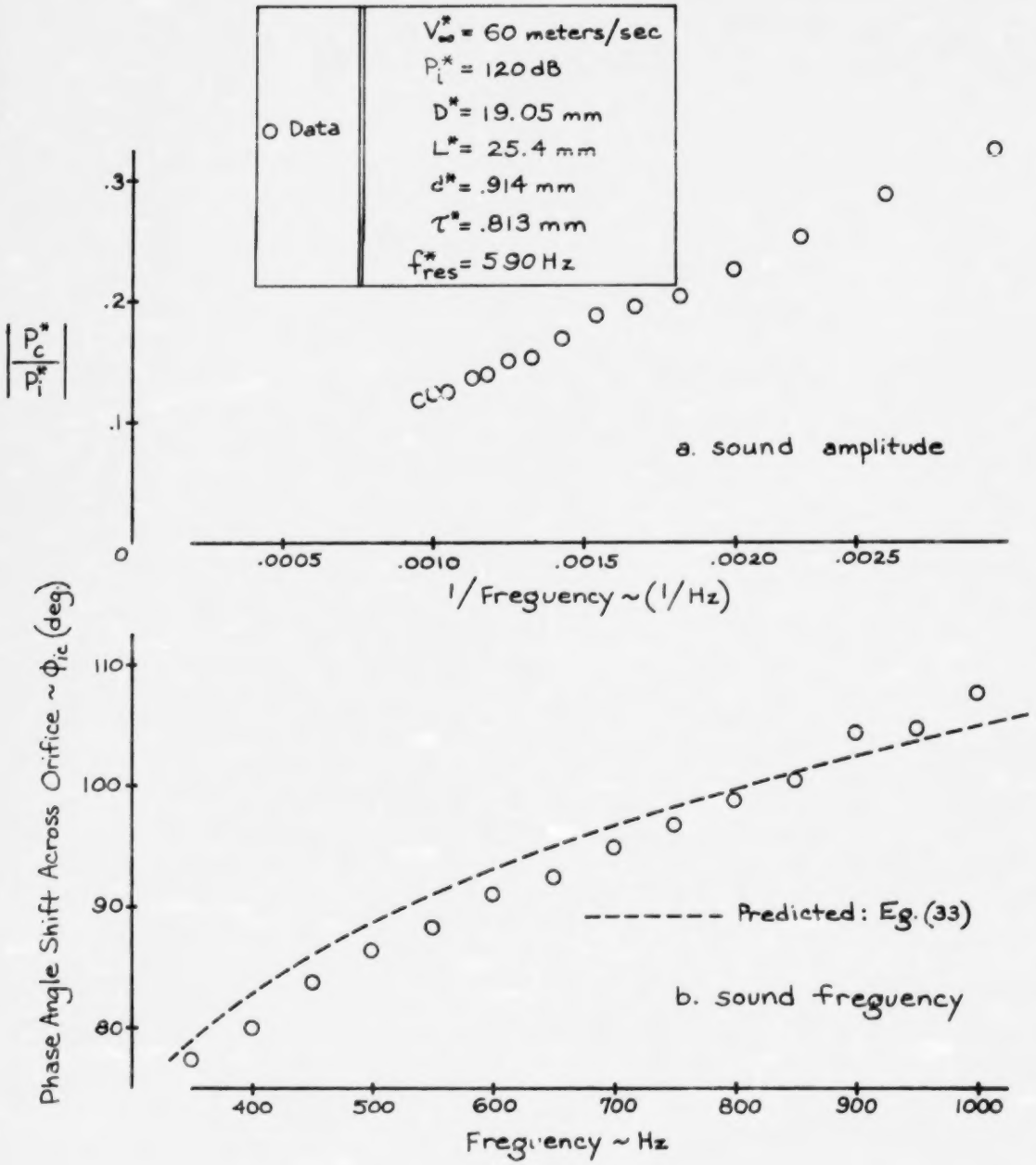

FIGURE 12. EFFECT OF FREQUENCY ON THE INCIDENT AND CAVITY SOUND PRESSURE FIELDS OF THE MODEL DEFINED IN APPENDIX B

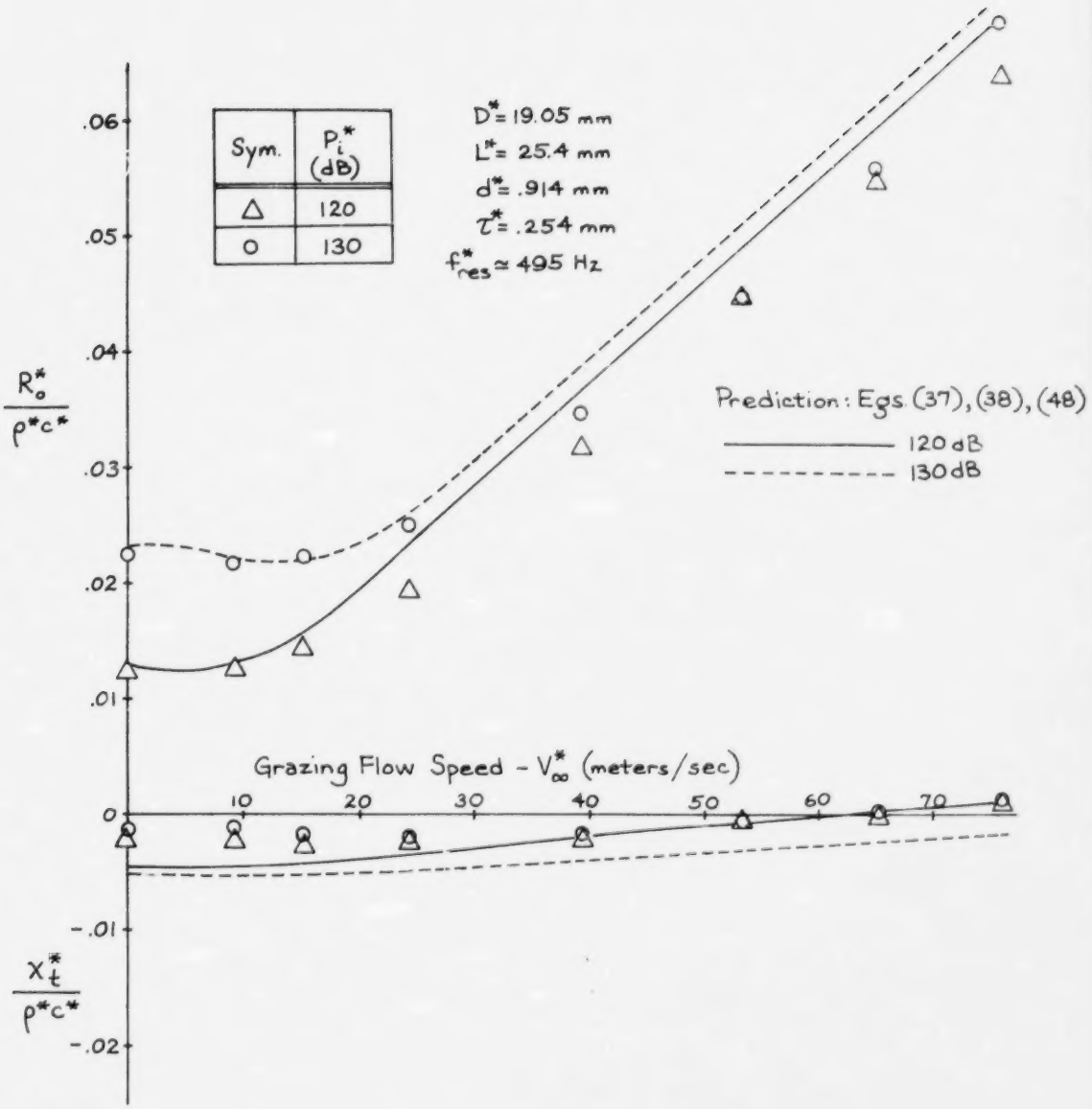

FIGURE 13a. EFFECT OF GRAZING FLOW ON THE ORIFICE AREA-AVERAGED IMPEDANCE OF MODEL 2

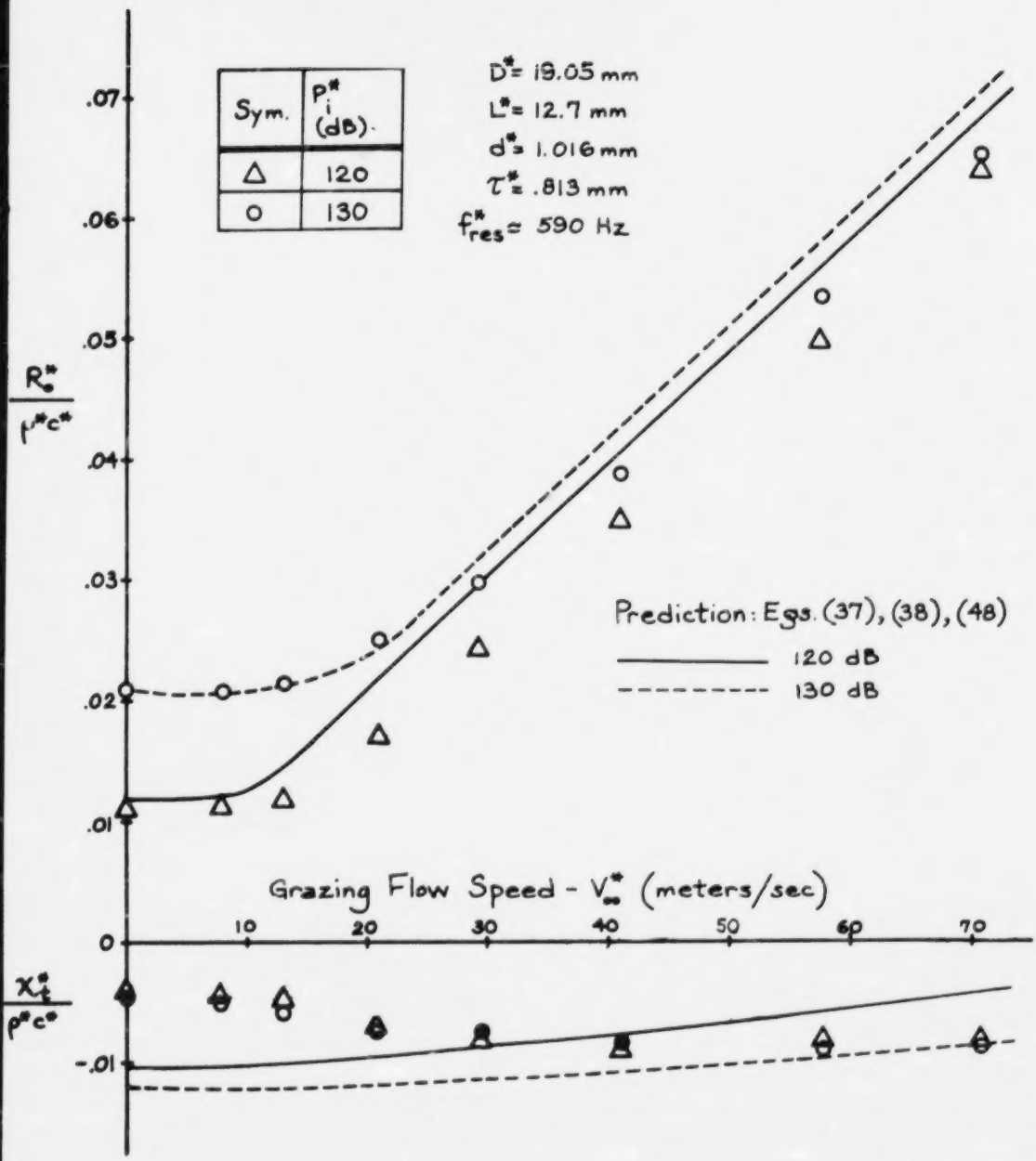

FIGURE 13b. EFFECT OF GRAZING FLOW ON THE ORIFICE AREA-AVERAGED IMPEDANCE OF MODEL 3

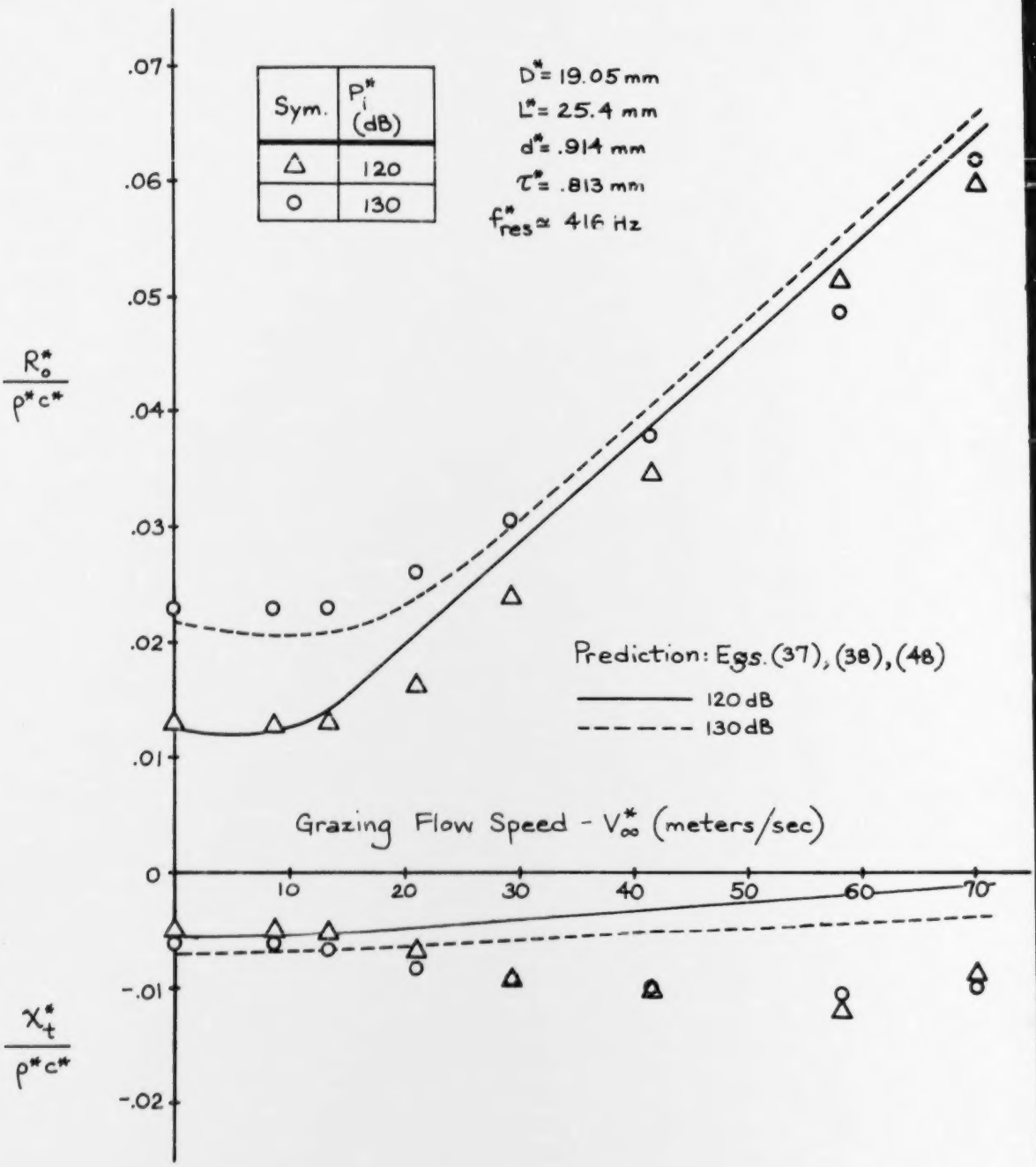

FIGURE 13c. EFFECT OF GRAZING FLOW ON THE ORIFICE AREA-AVERAGED IMPEDANCE OF MODEL 4

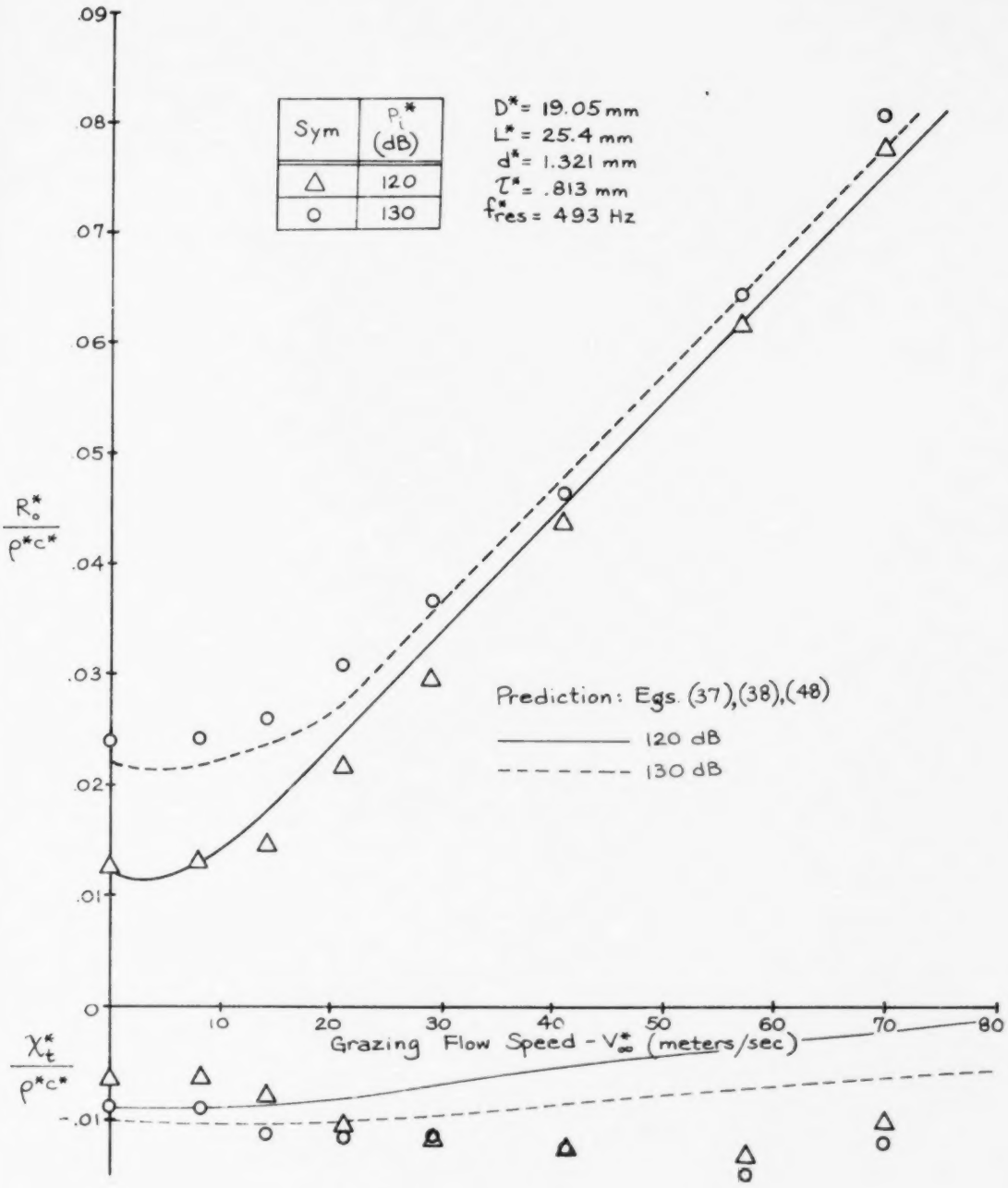

FIGURE 13d. EFFECT OF GRAZING FLOW ON THE ORIFICE AREA-AVERAGED IMPEDANCE OF MODEL 6

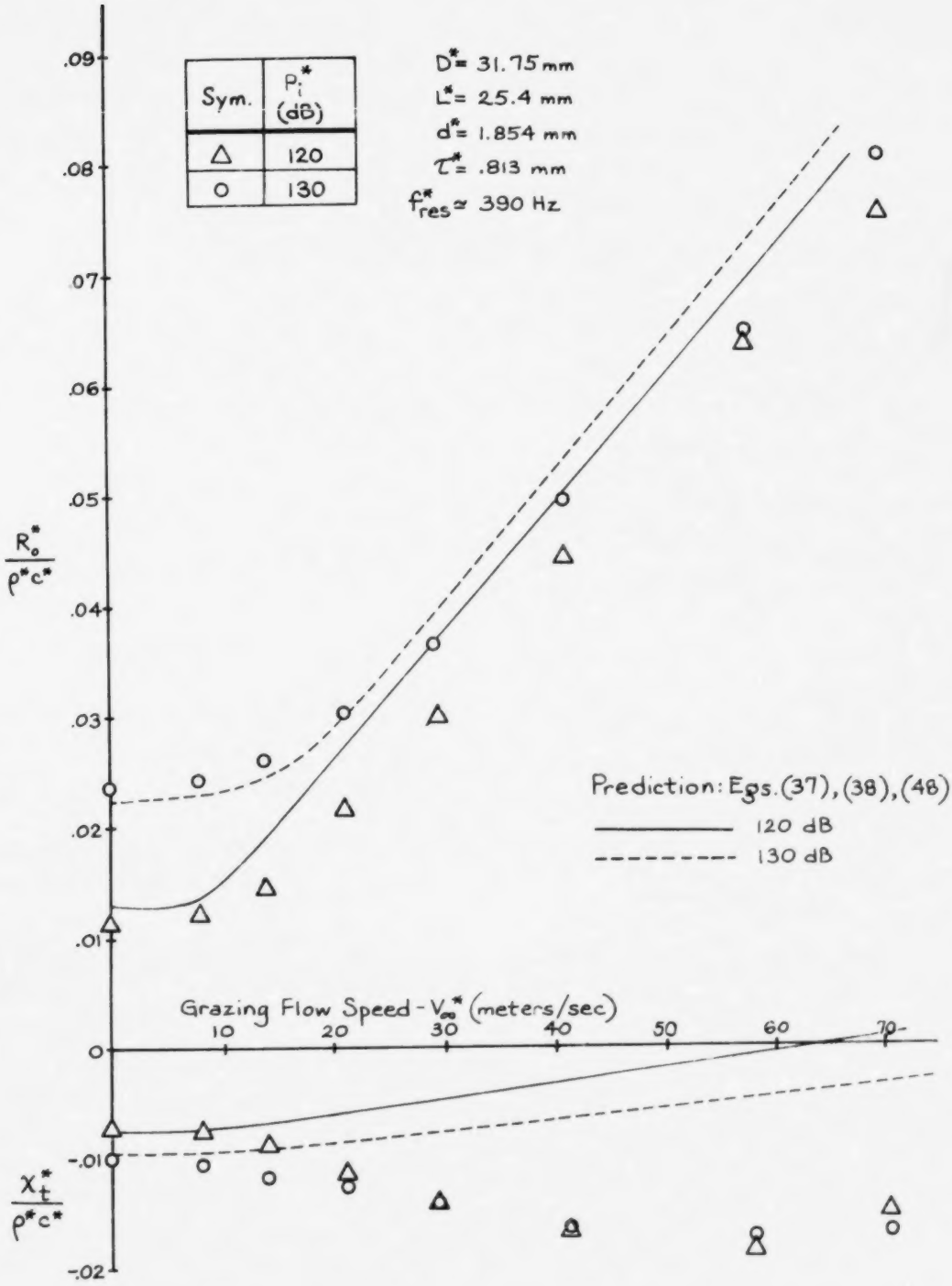

FIGURE 13e. EFFECT OF GRAZING FLOW ON THE ORIFICE AREA-AVERAGED IMPEDANCE OF MODEL 10

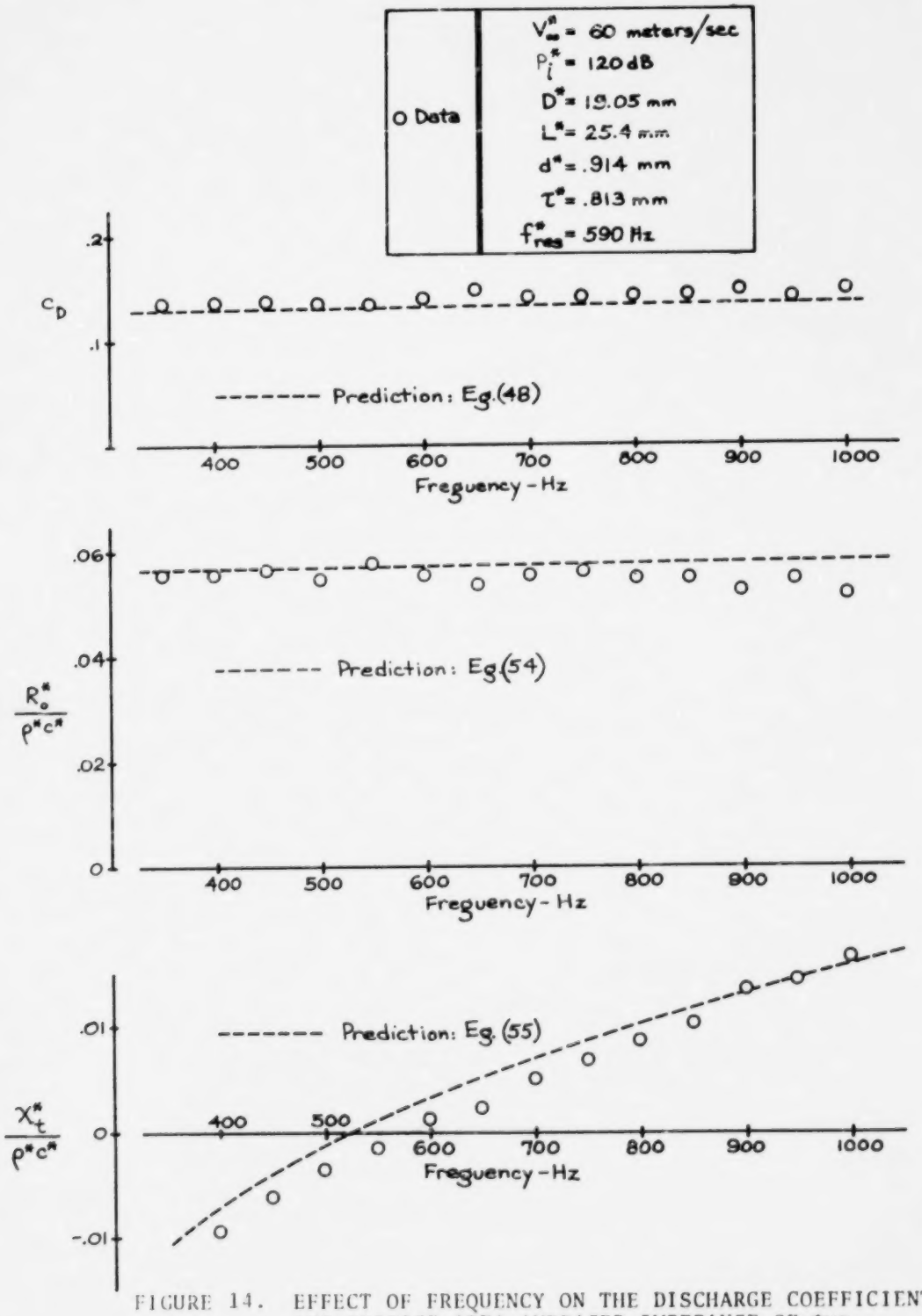

FIGURE 14. EFFECT OF FREQUENCY ON THE DISCHARGE COEFFICIENT AND ORIFICE AREA-AVERAGED IMPEDANCE OF THE MODEL DEFINED IN APPENDIX B

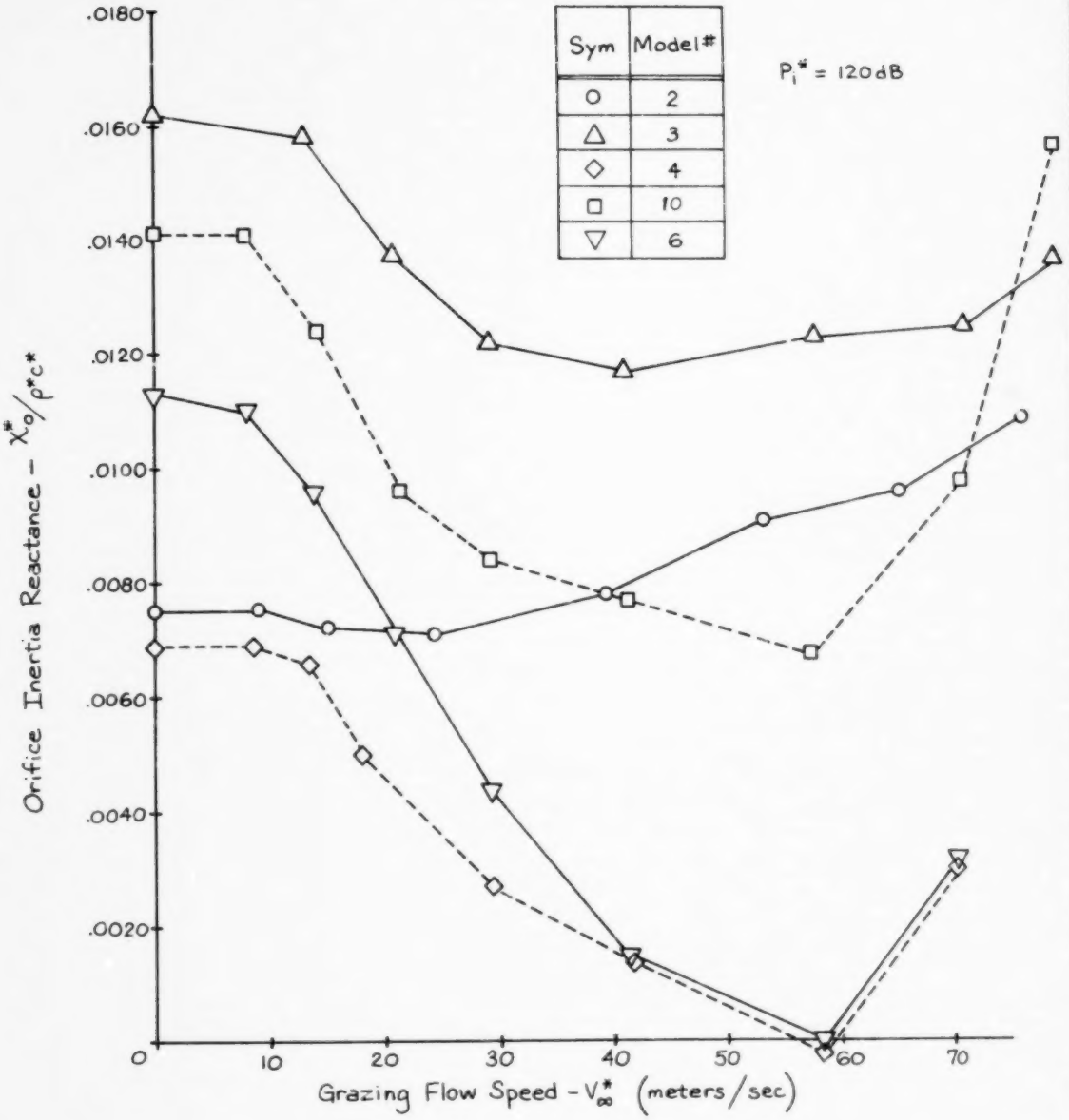

FIGURE 15a. EFFECT OF GRAZING FLOW ON THE ORIFICE INERTIAL REACTANCE OF MODELS #2, 3, 4, 6 and 10

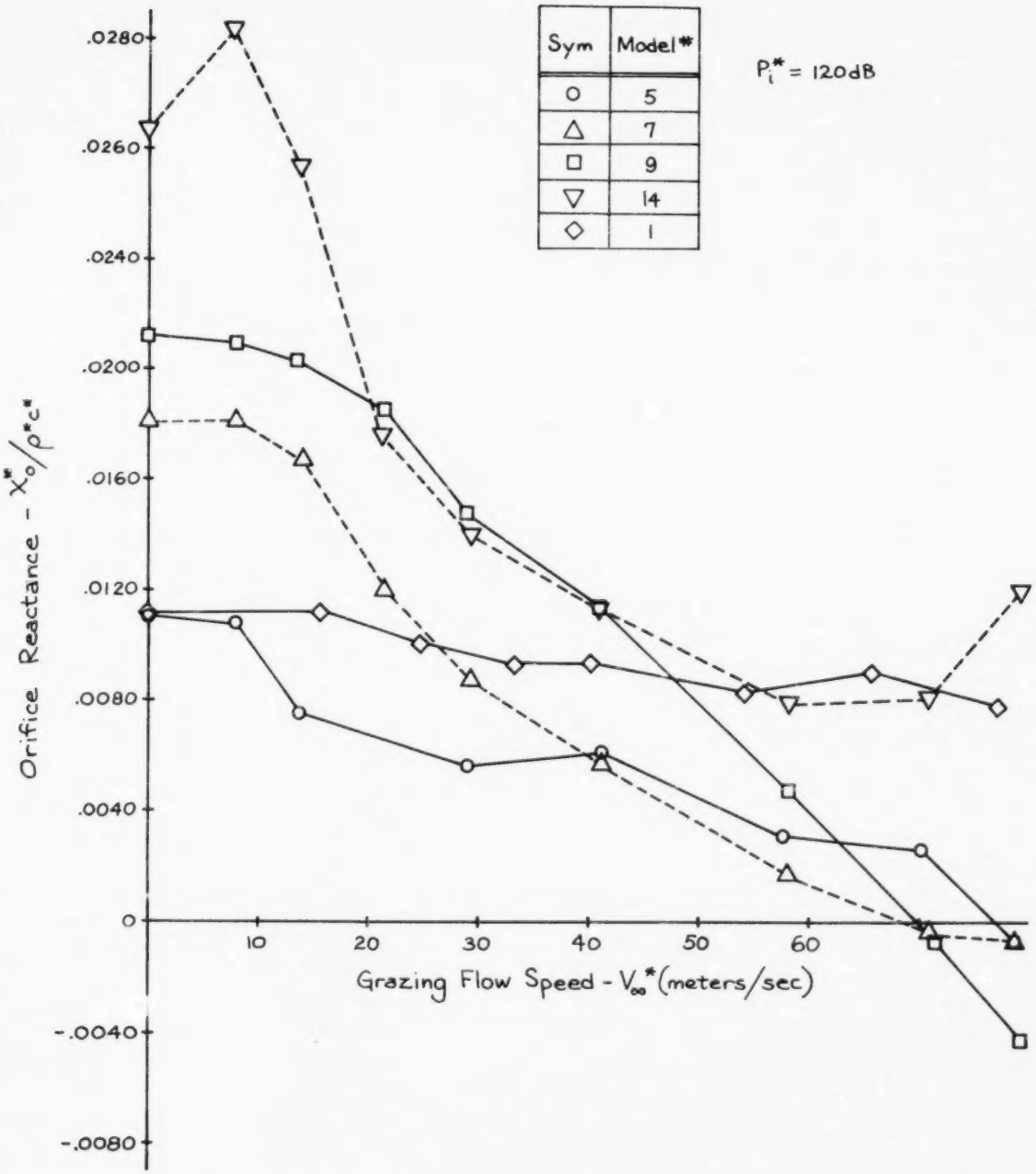

FIGURE 15b. EFFECT OF GRAZING FLOW ON THE ORIFICE INERTIA REACTANCE OF MODELS #1, 5, 7, 9 and 14

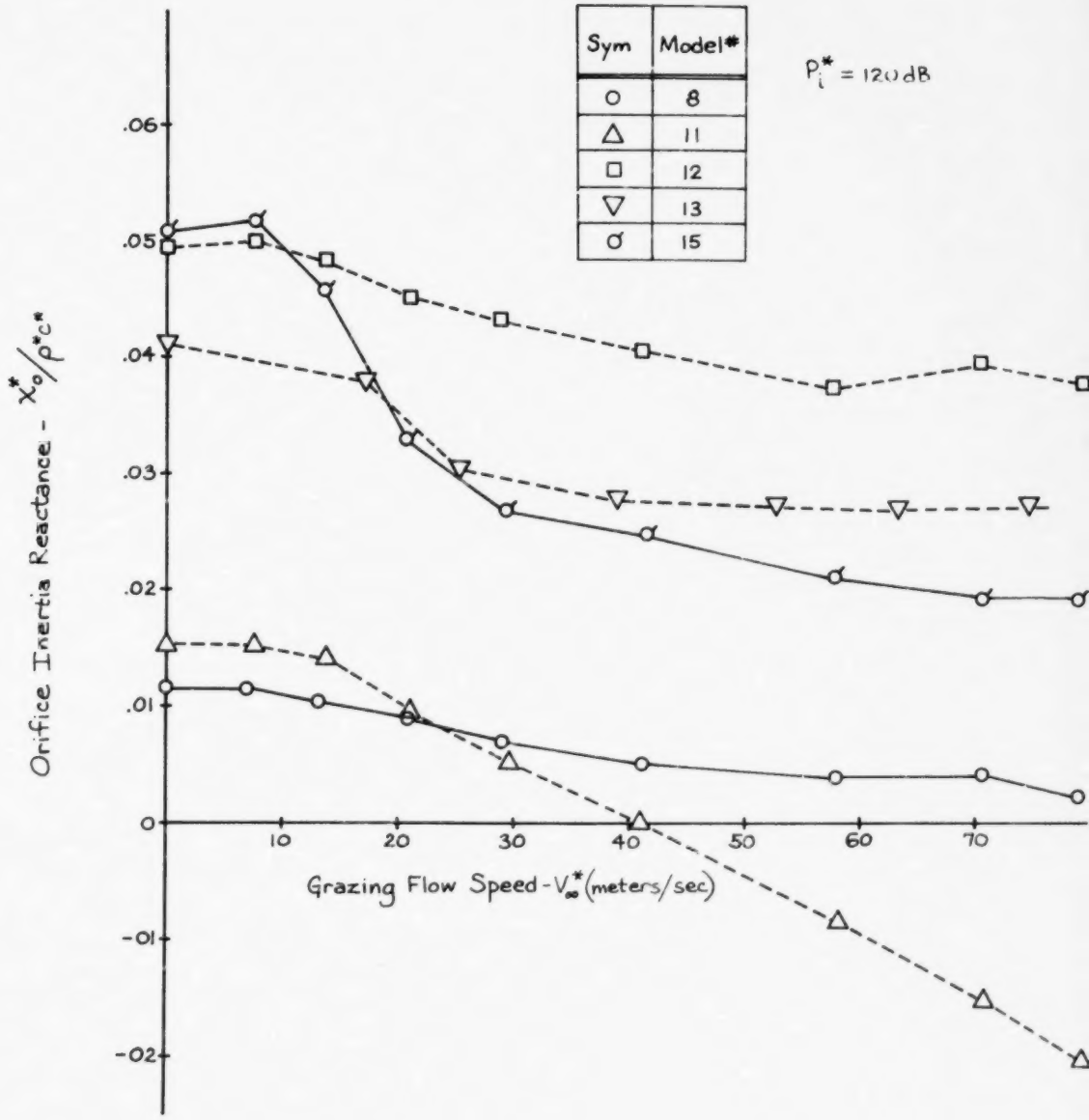

FIGURE 15c. EFFECT OF GRAZING FLOW ON THE ORIFICE INERTIA REACTANCE OF MODELS #8, 11, 12, 13 and 15

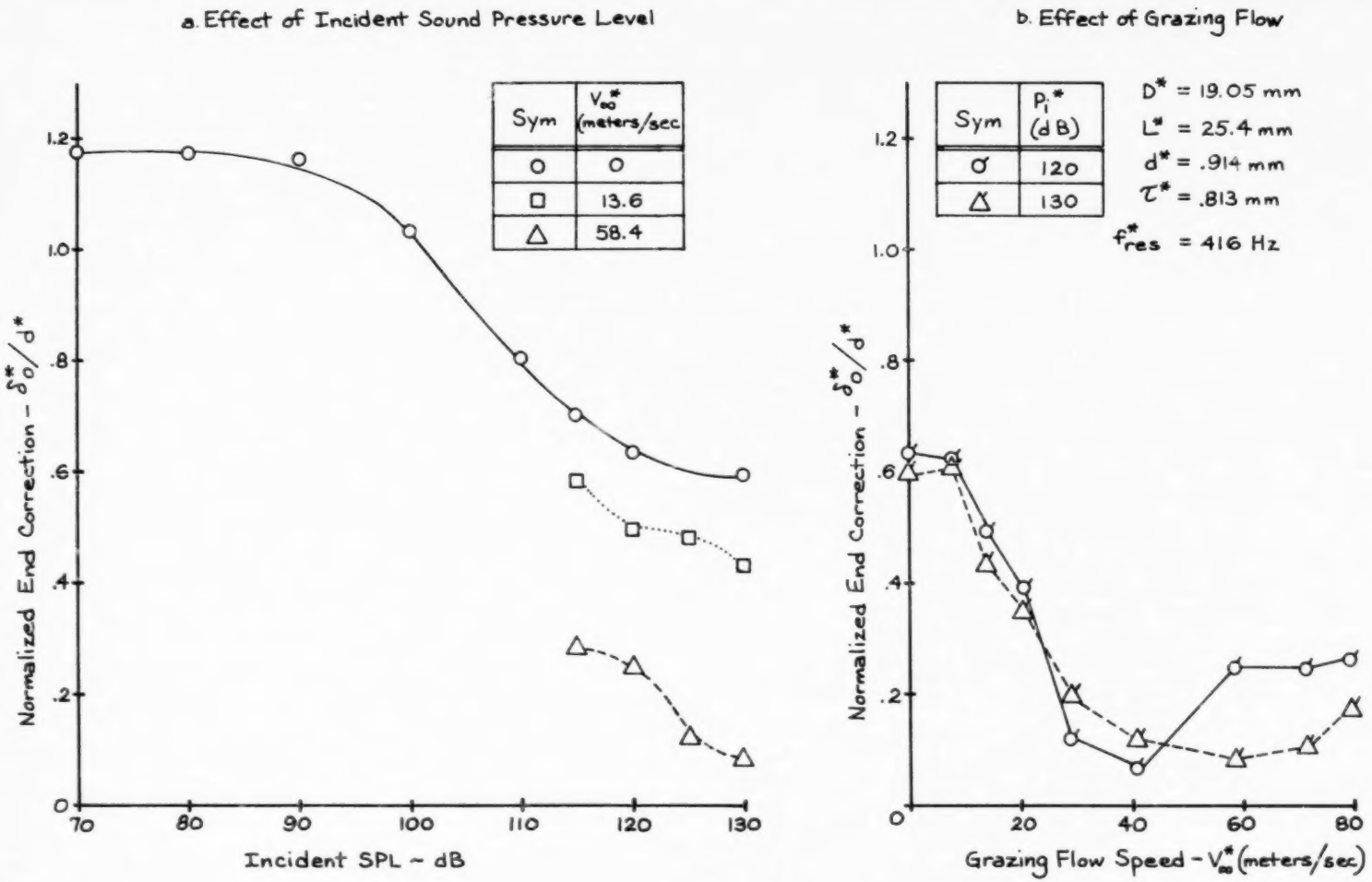

FIGURE 16. EFFECT OF GRAZING FLOW AND INCIDENT SOUND PRESSURE LEVEL ON THE ORIFICE END CORRECTION OF MODEL 4

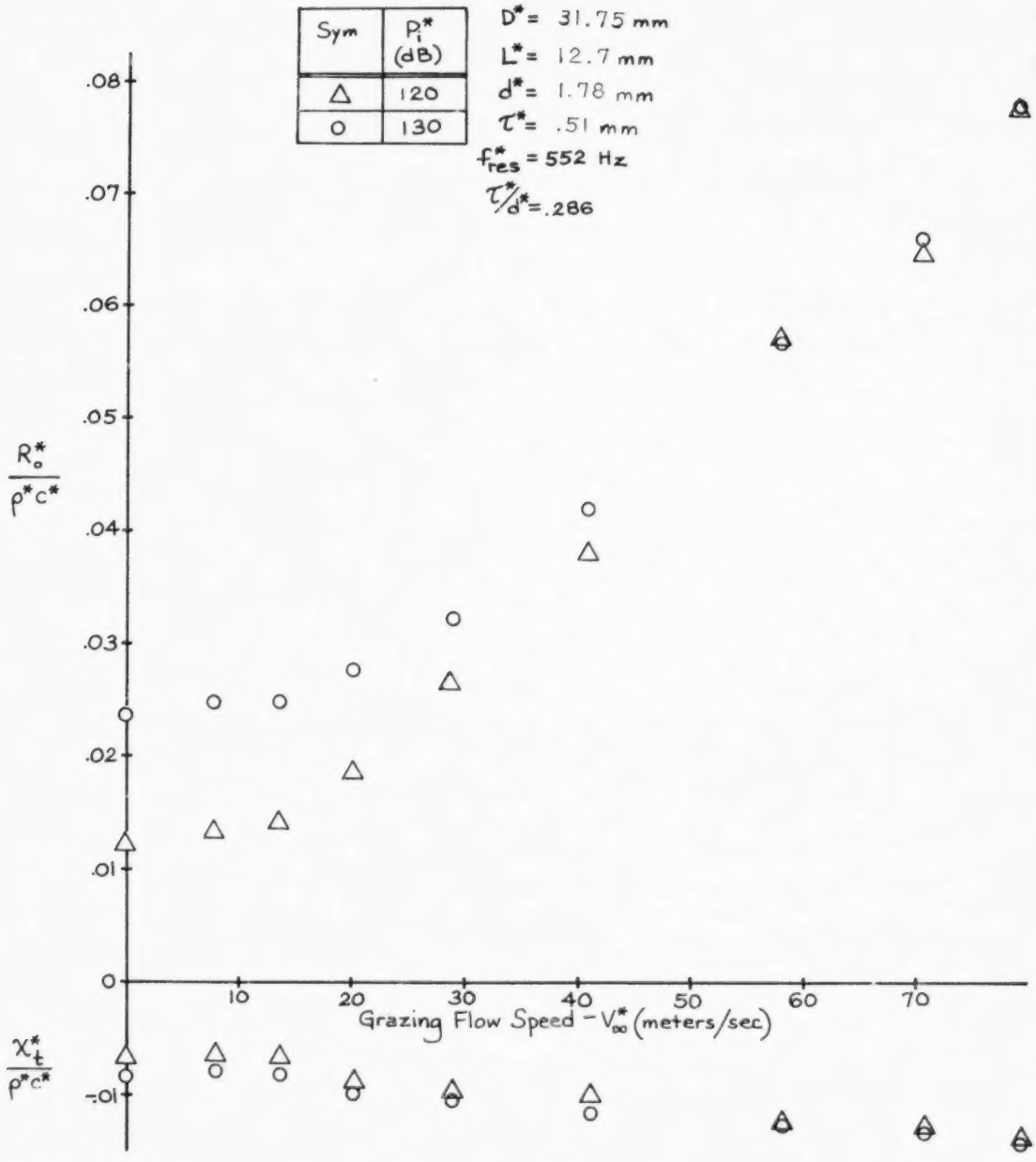

FIGURE 17a. EFFECT OF GRAZING FLOW ON THE ORIFICE AREA-AVERAGED IMPEDANCE ON THE $\tau^*/d^*=0.286$ CONFIGURATION

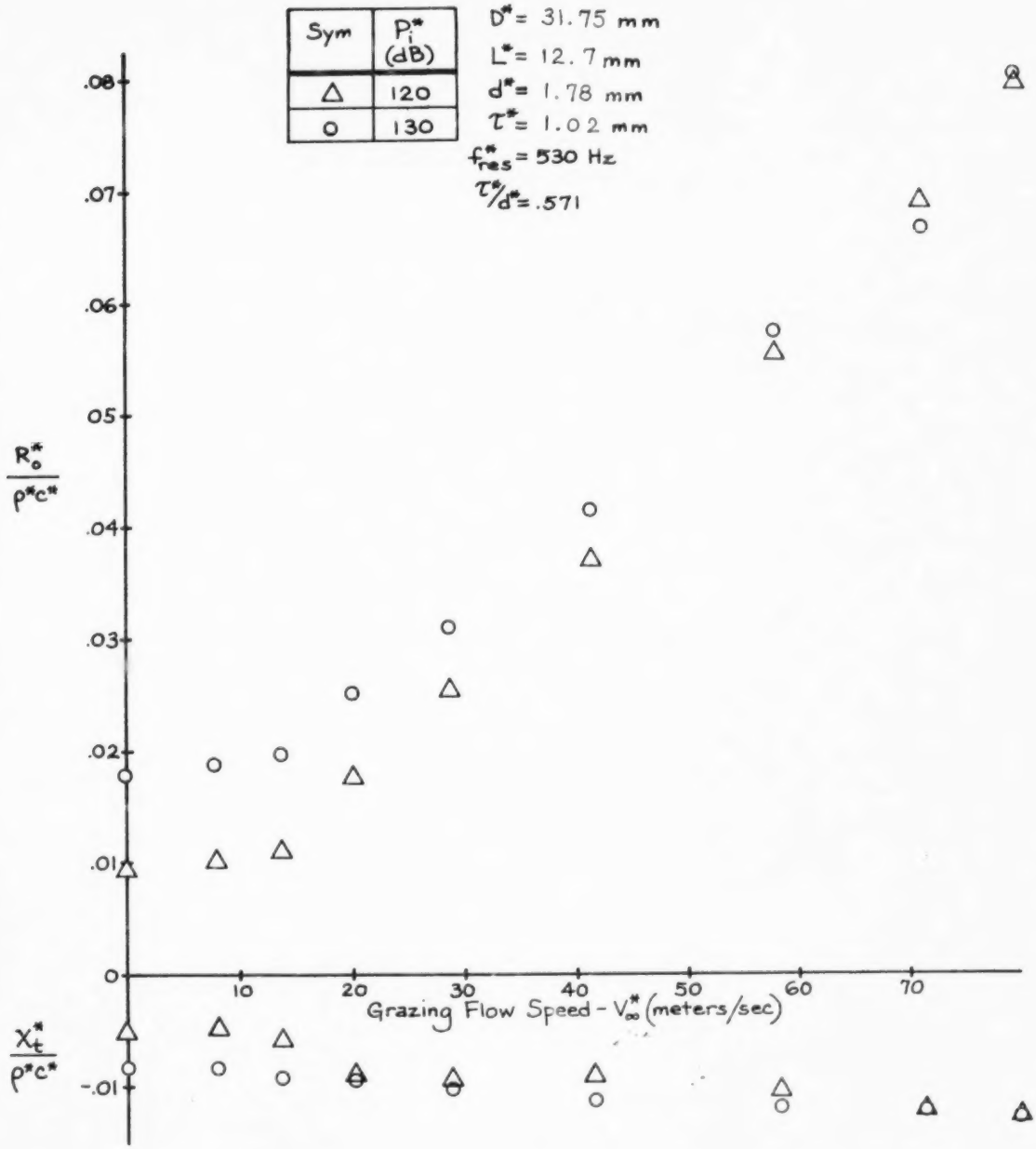

FIGURE 17b. EFFECT OF GRAZING FLOW ON THE ORIFICE AREA-AVERAGED IMPEDANCE ON THE $\tau^*/d^*=0.571$ CONFIGURATION

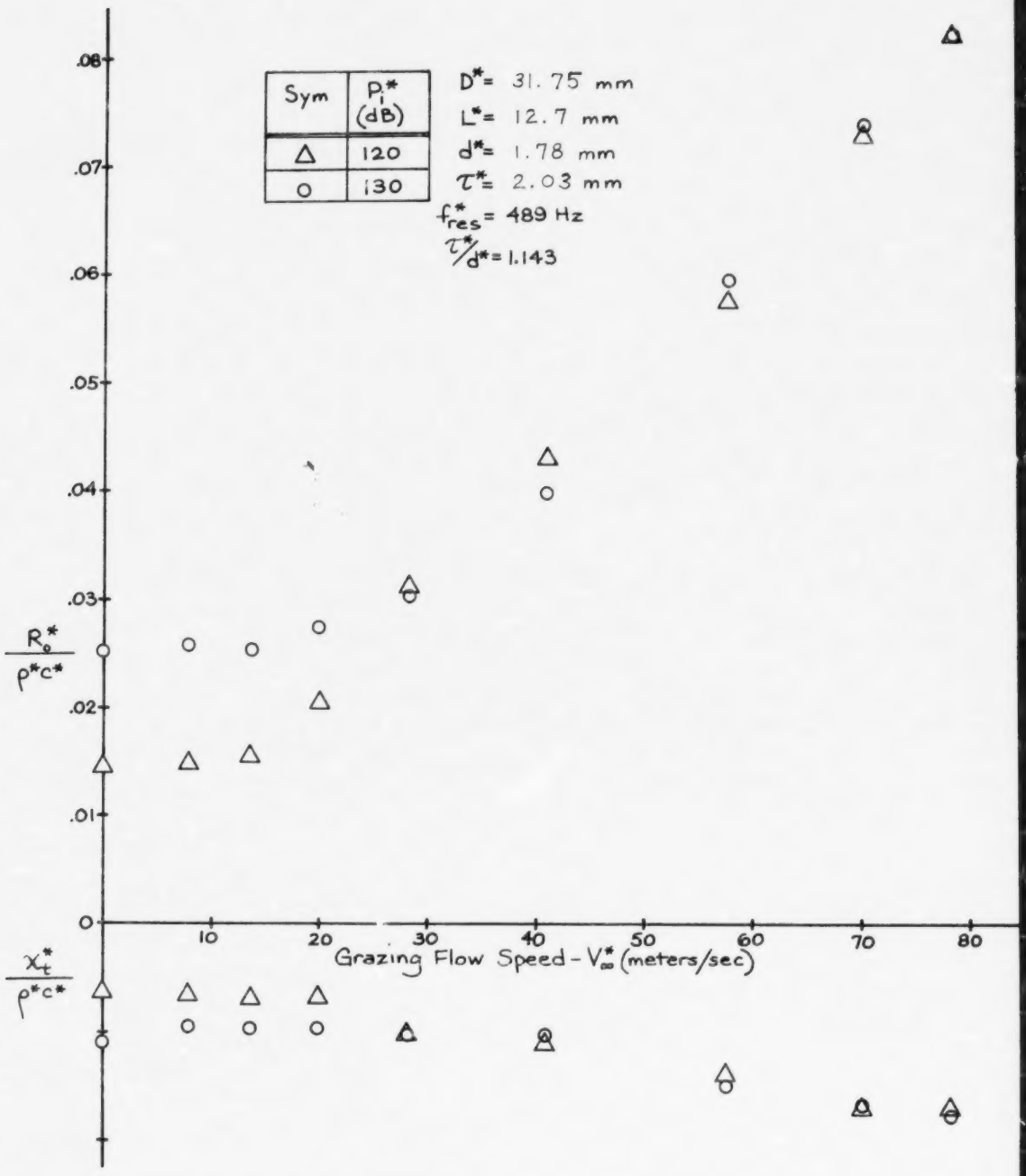

FIGURE 17c. EFFECT OF GRAZING FLOW ON THE ORIFICE AREA-AVERAGED IMPEDANCE ON THE $\tau^*/d^*=1.143$ CONFIGURATION

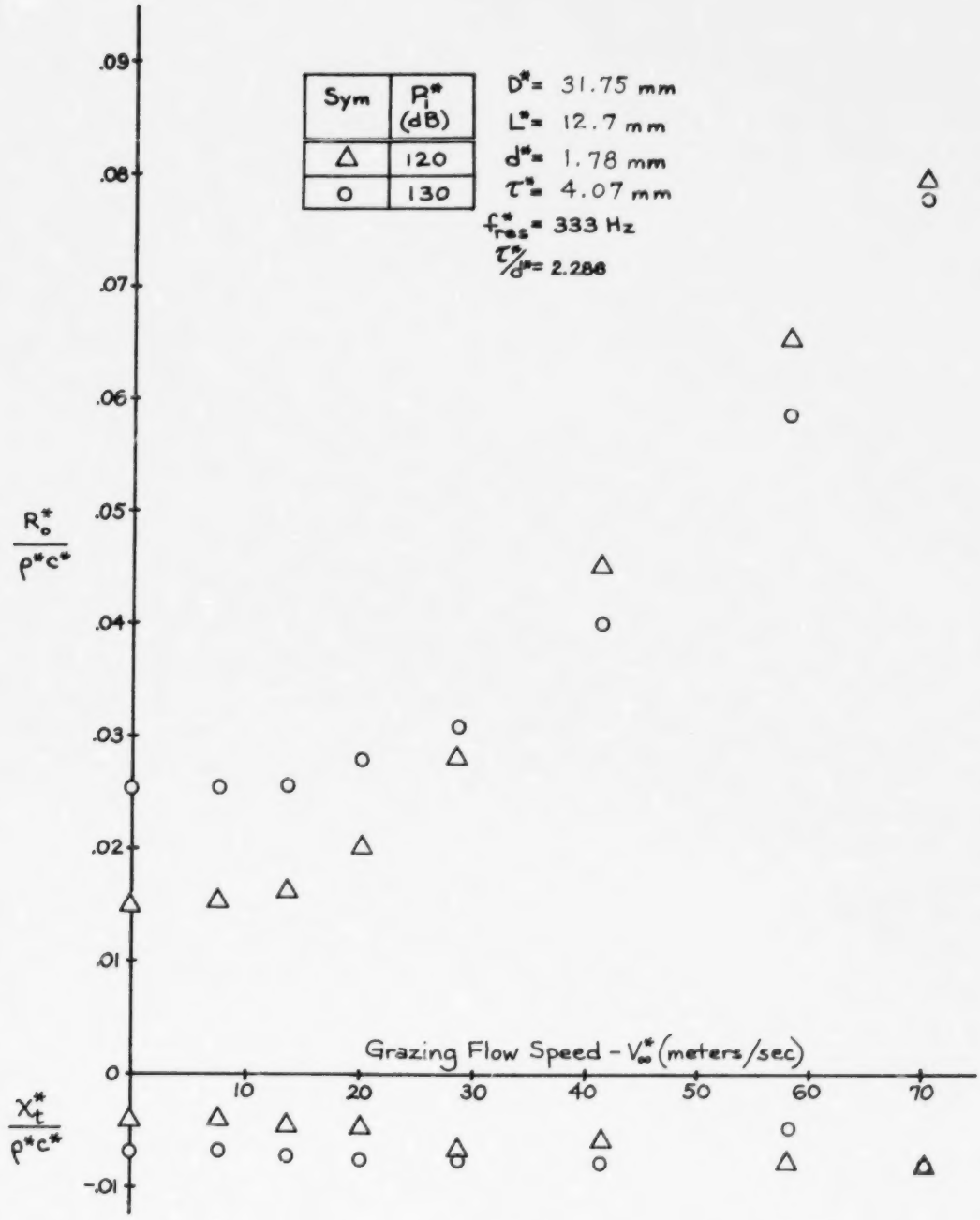

FIGURE 17d. EFFECT OF GRAZING FLOW ON THE ORIFICE AREA-AVERAGED IMPEDANCE ON THE $\tau^*/d^*=2.286$ CONFIGURATION

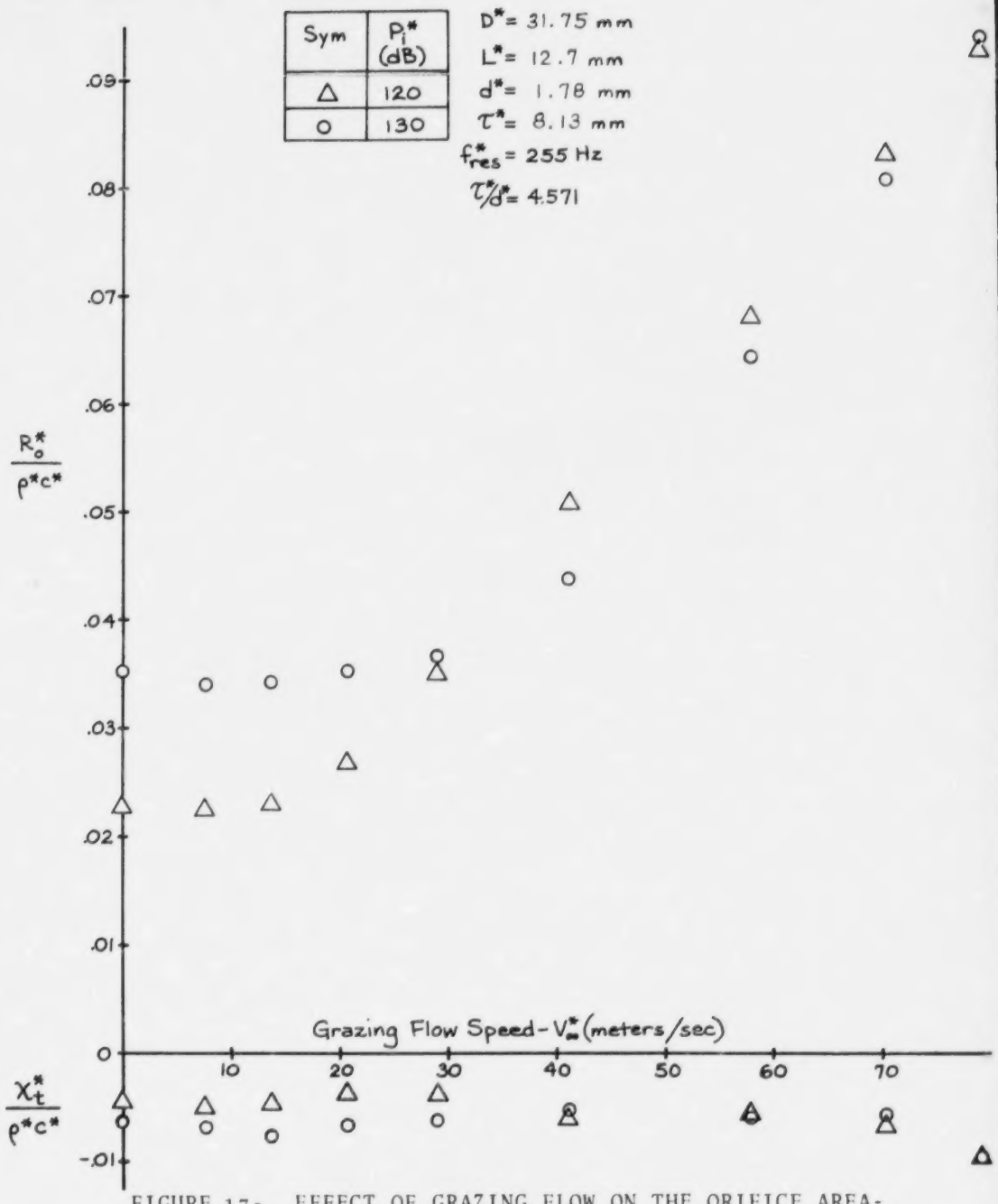

FIGURE 17e. EFFECT OF GRAZING FLOW ON THE ORIFICE AREA-AVERAGED IMPEDANCE ON THE $\tau^*/d^*=4.571$ CONFIGURATION

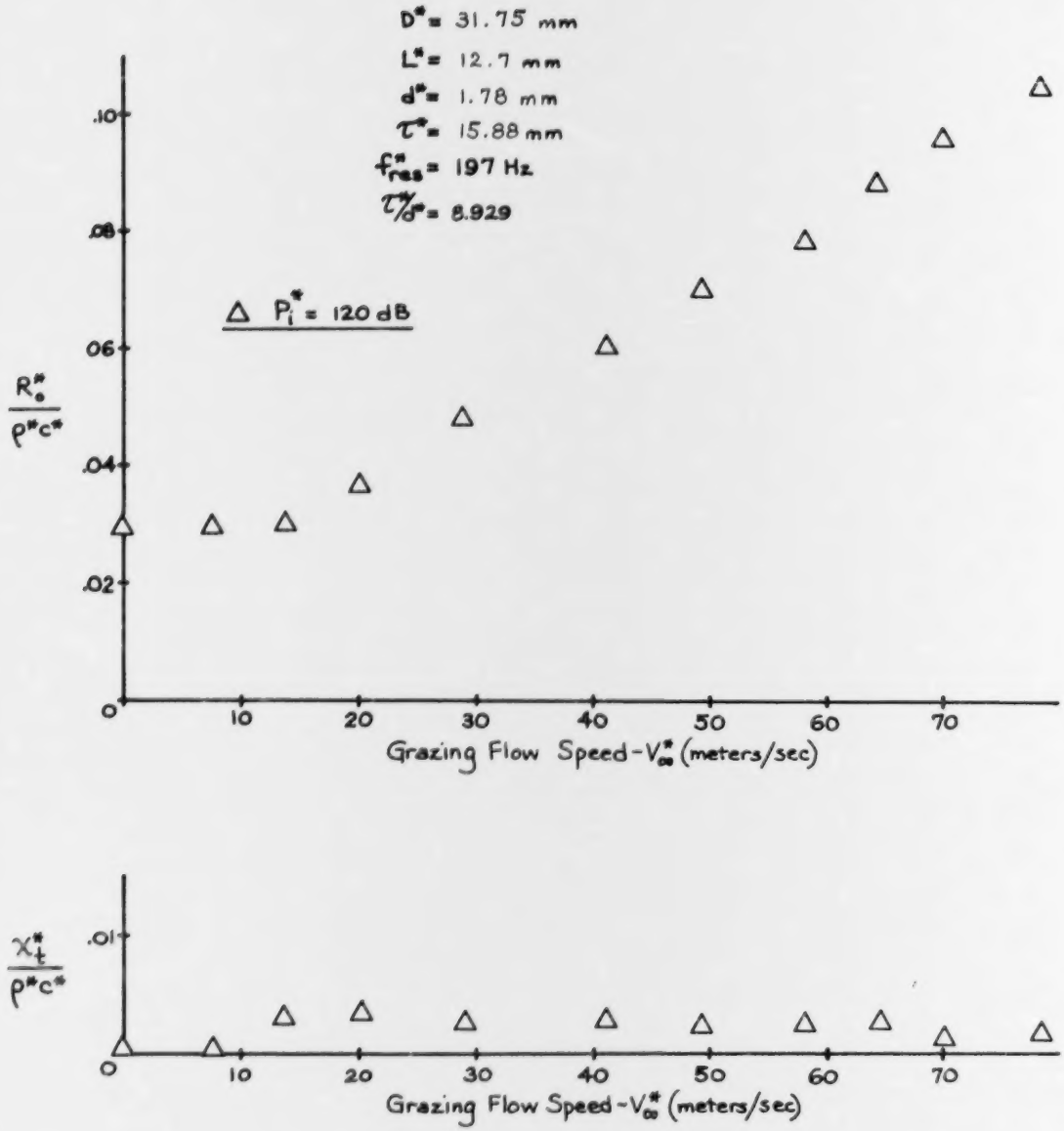

FIGURE 17f. EFFECT OF GRAZING FLOW ON THE ORIFICE AREA-AVERAGED IMPEDANCE ON THE $\tau^*/d^*=8.929$ CONFIGURATION

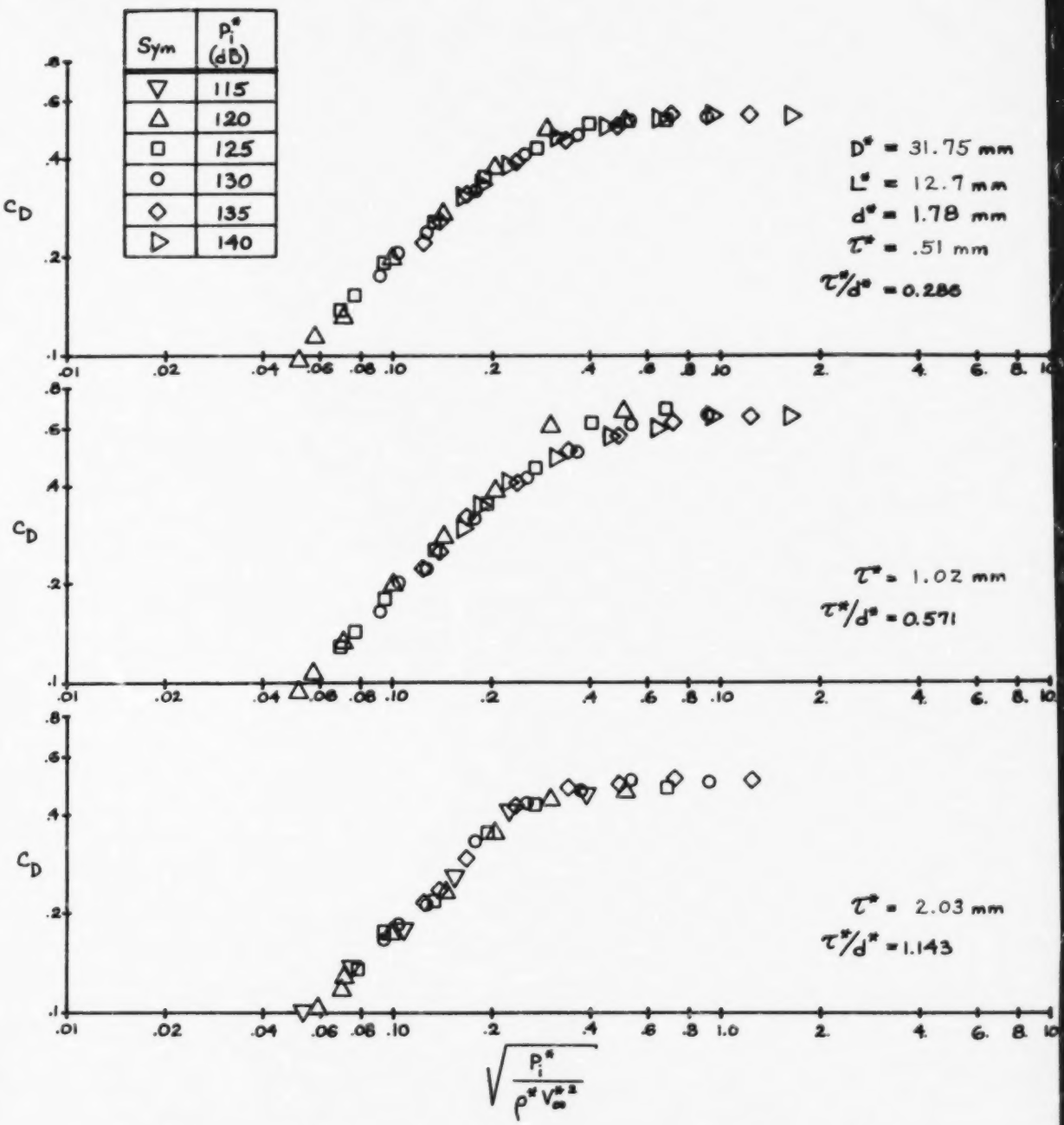

FIGURE 18a. CORRELATION OF THICK ORIFICE GRAZING FLOW SOUND DATA IN TERMS OF DISCHARGE COEFFICIENT FOR τ^*/d^*=0.286, 0.571 AND 1.143

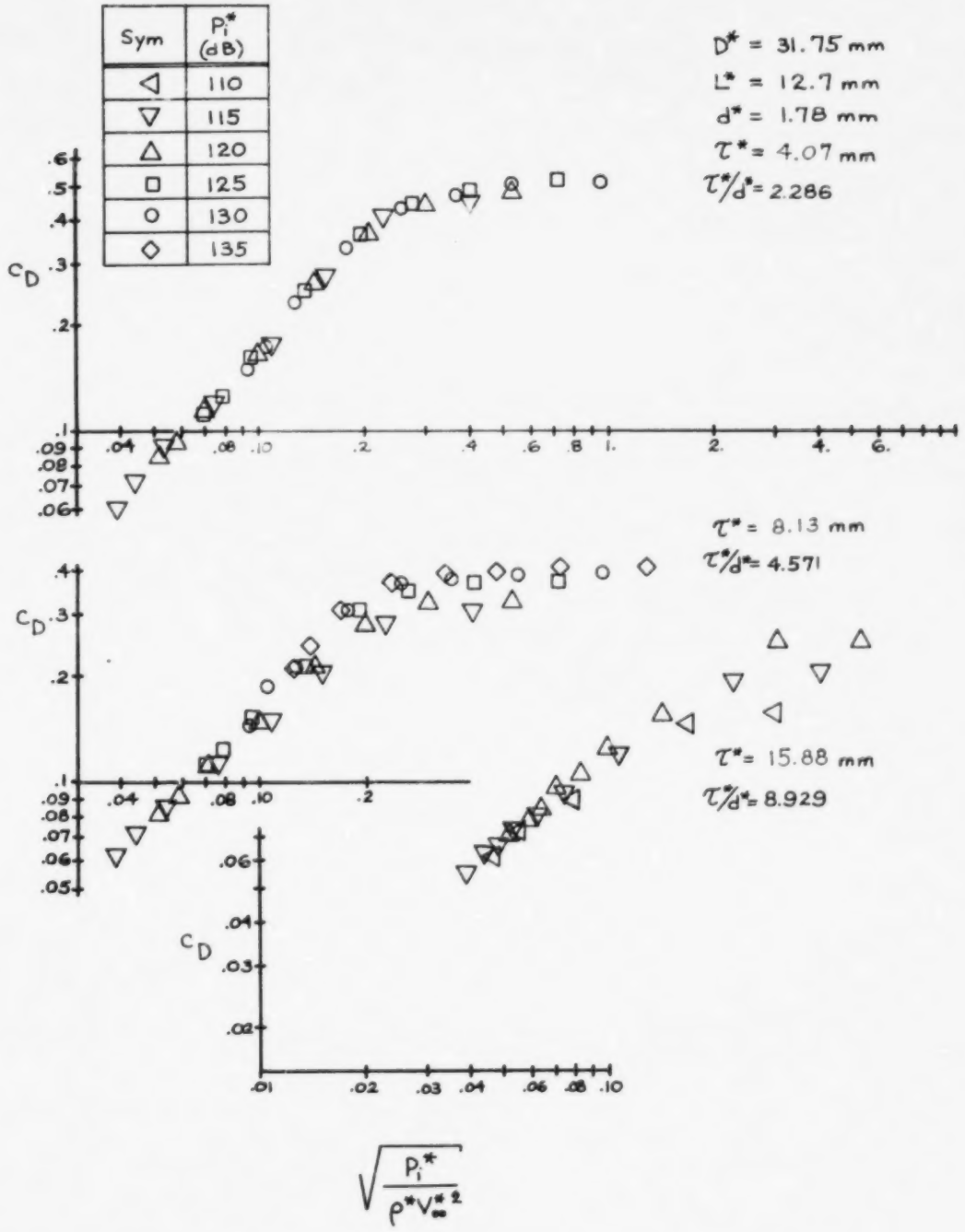

FIGURE 18b. CORRELATION OF THICK ORIFICE GRAZING FLOW SOUND DATA IN TERMS OF DISCHARGE COEFFICIENT FOR τ^*/d^* = 2.286, 4.571 and 8.929

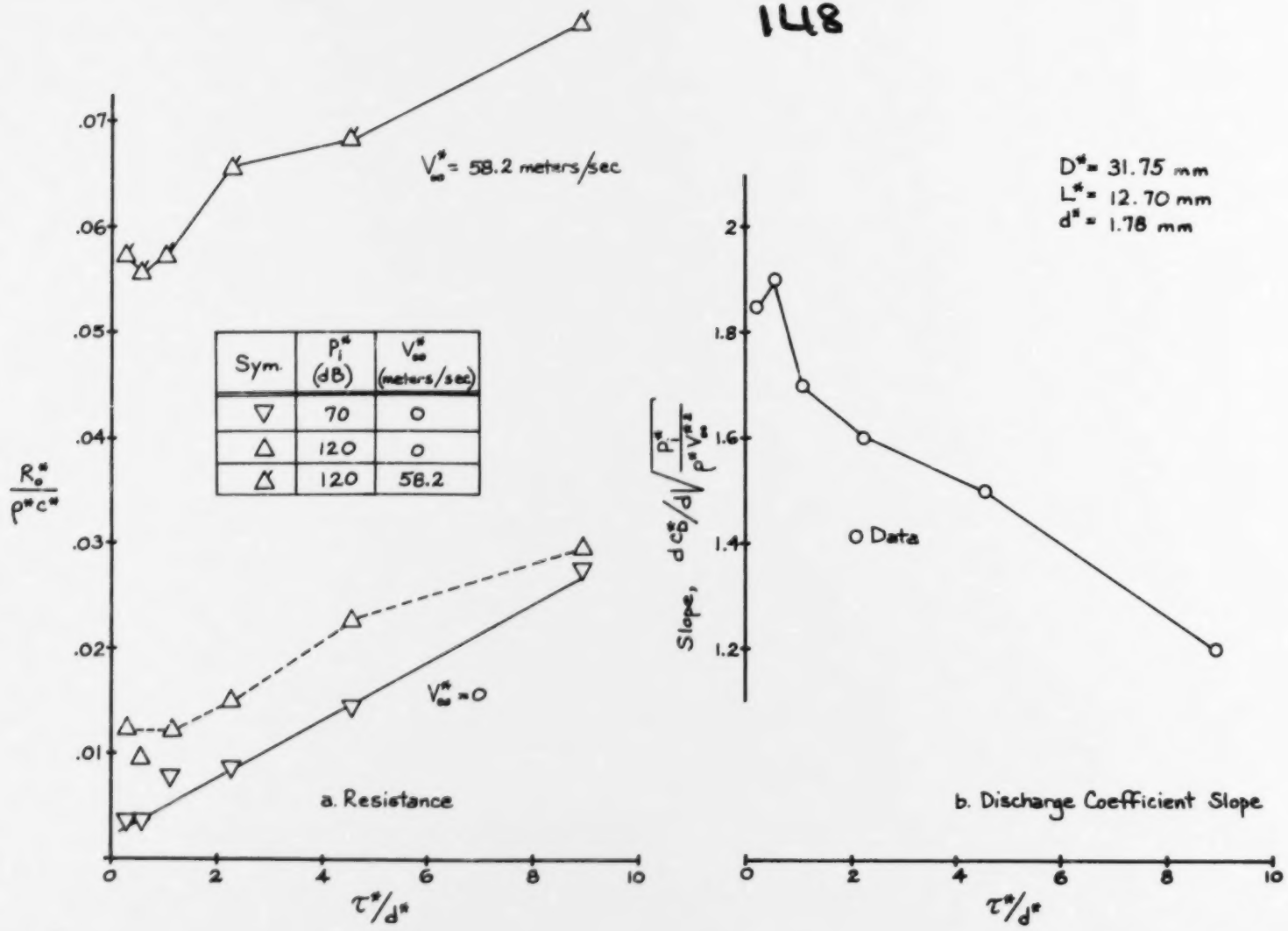

FIGURE 19. EFFECT OF ORIFICE THICKNESS ON THE ORIFICE AREA-AVERAGED RESISTANCE AND DISCHARGE COEFFICIENT

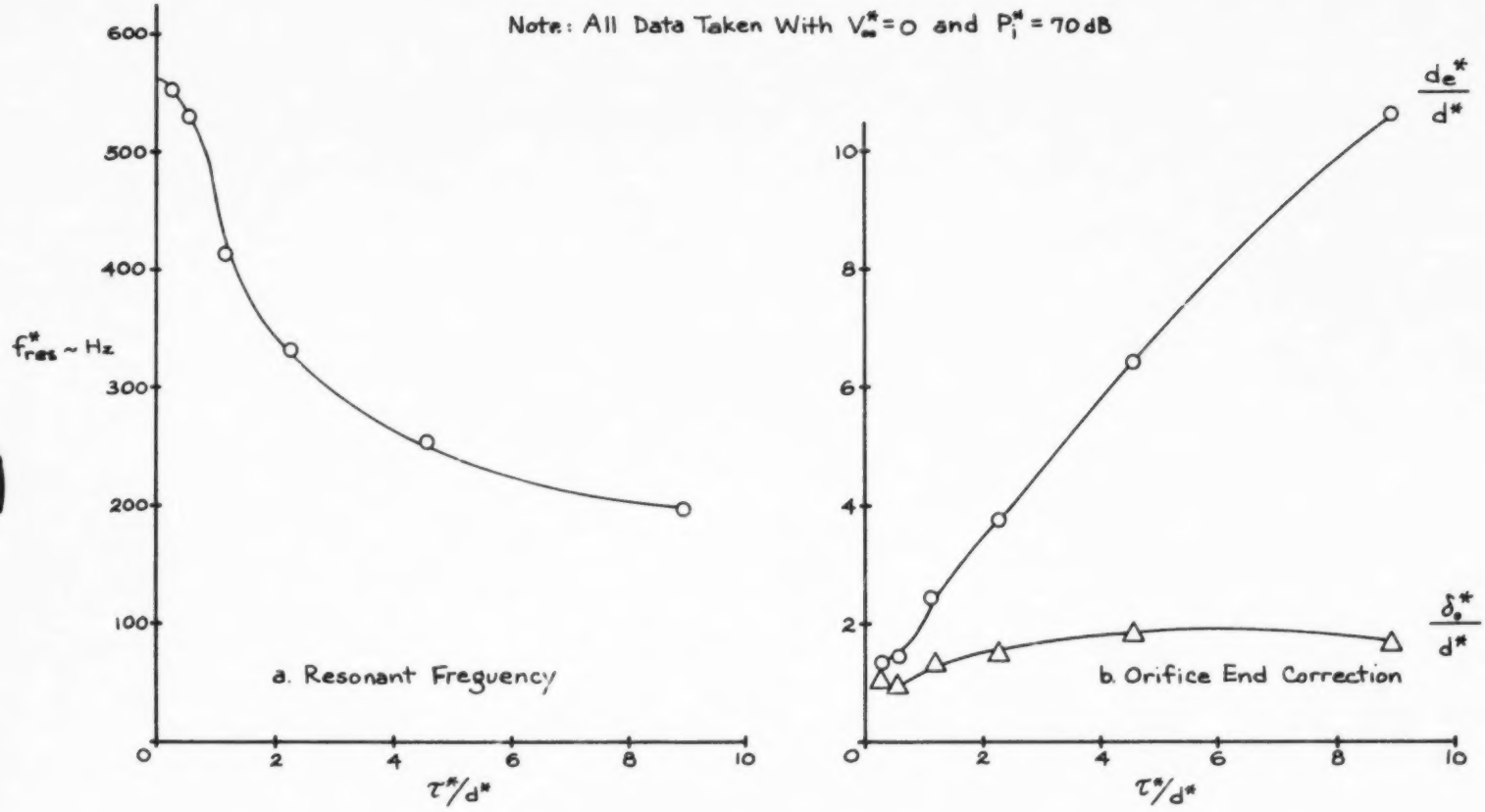

FIGURE 20. EFFECT OF ORIFICE THICKNESS ON RESONANCE FREQUENCY, ORIFICE INERTIAL LENGTH AND ORIFICE END-CORRECTION FOR $V_\infty^*=0$, $P_i^*=70$ dB

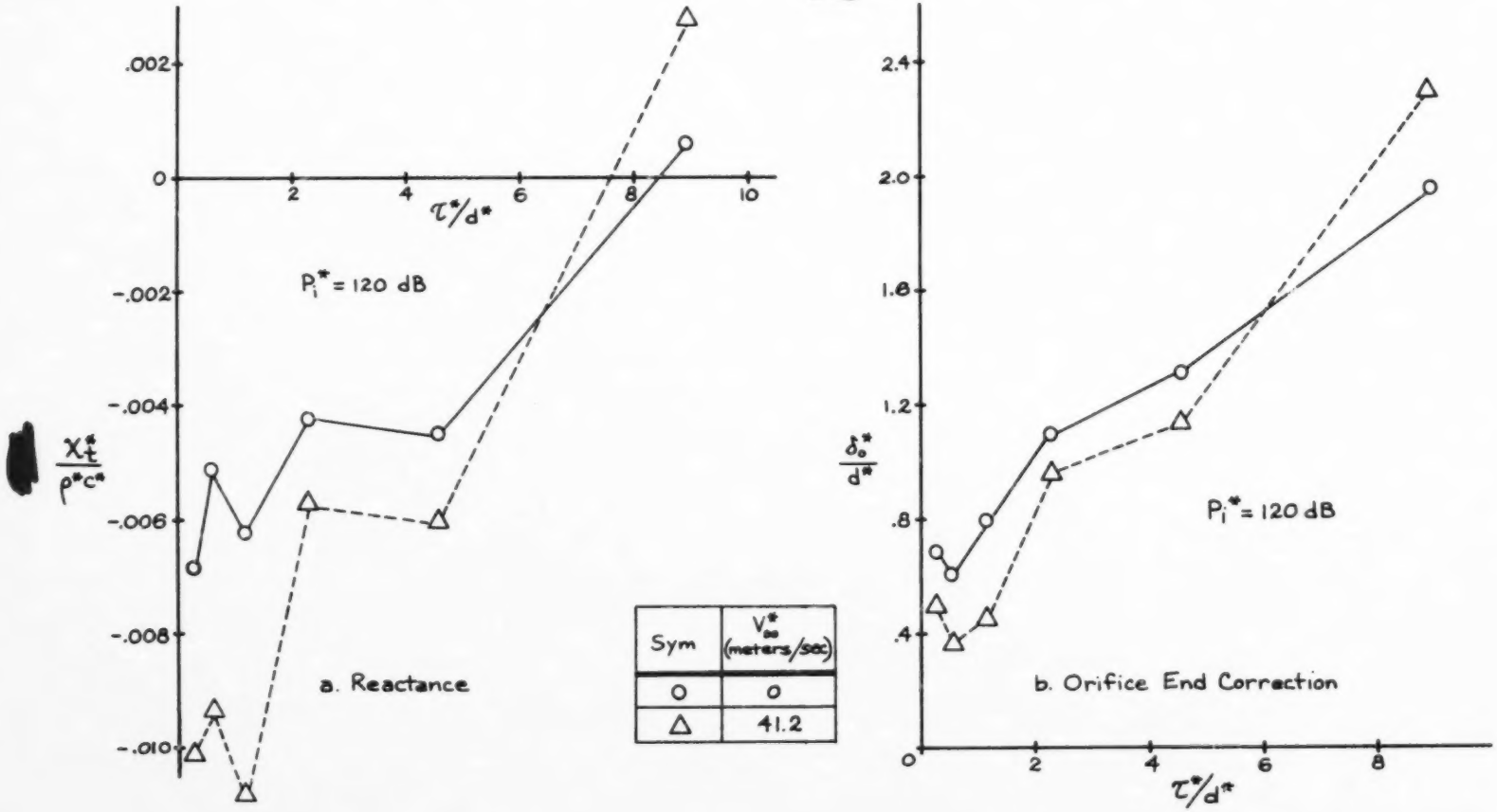

FIGURE 21. (a,b) EFFECT OF ORIFICE THICKNESS ON ORIFICE AREA-AVERAGED REACTANC AND ORIFICE END-CORRECTION FOR V_∞^*=0 and 41.2 METERS/SEC AND P_i^*=120 dB

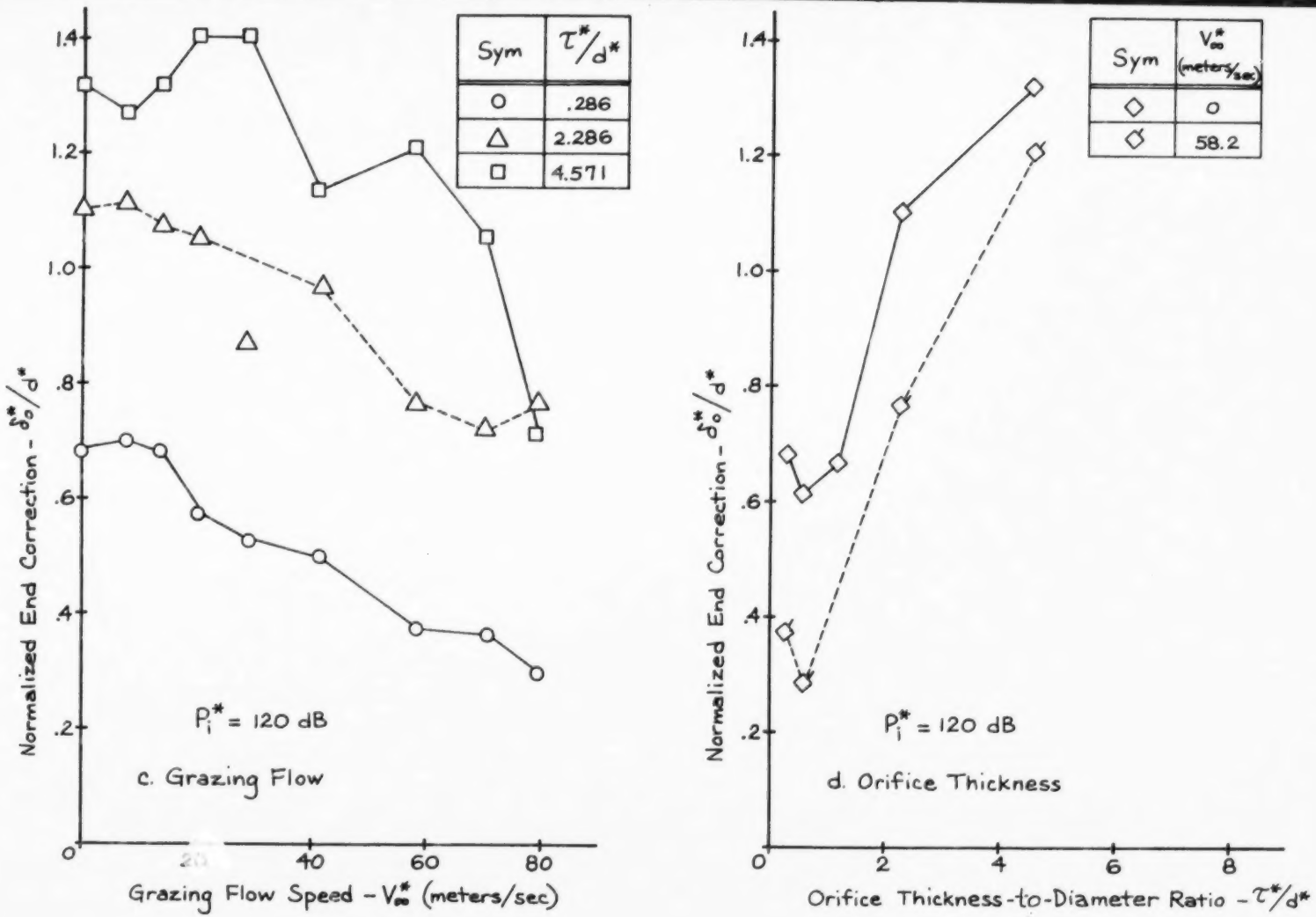

FIGURE 21. (c,d) EFFECT OF GRAZING FLOW AND ORIFICE THICKNESS ON ORIFICE END CORRECTION

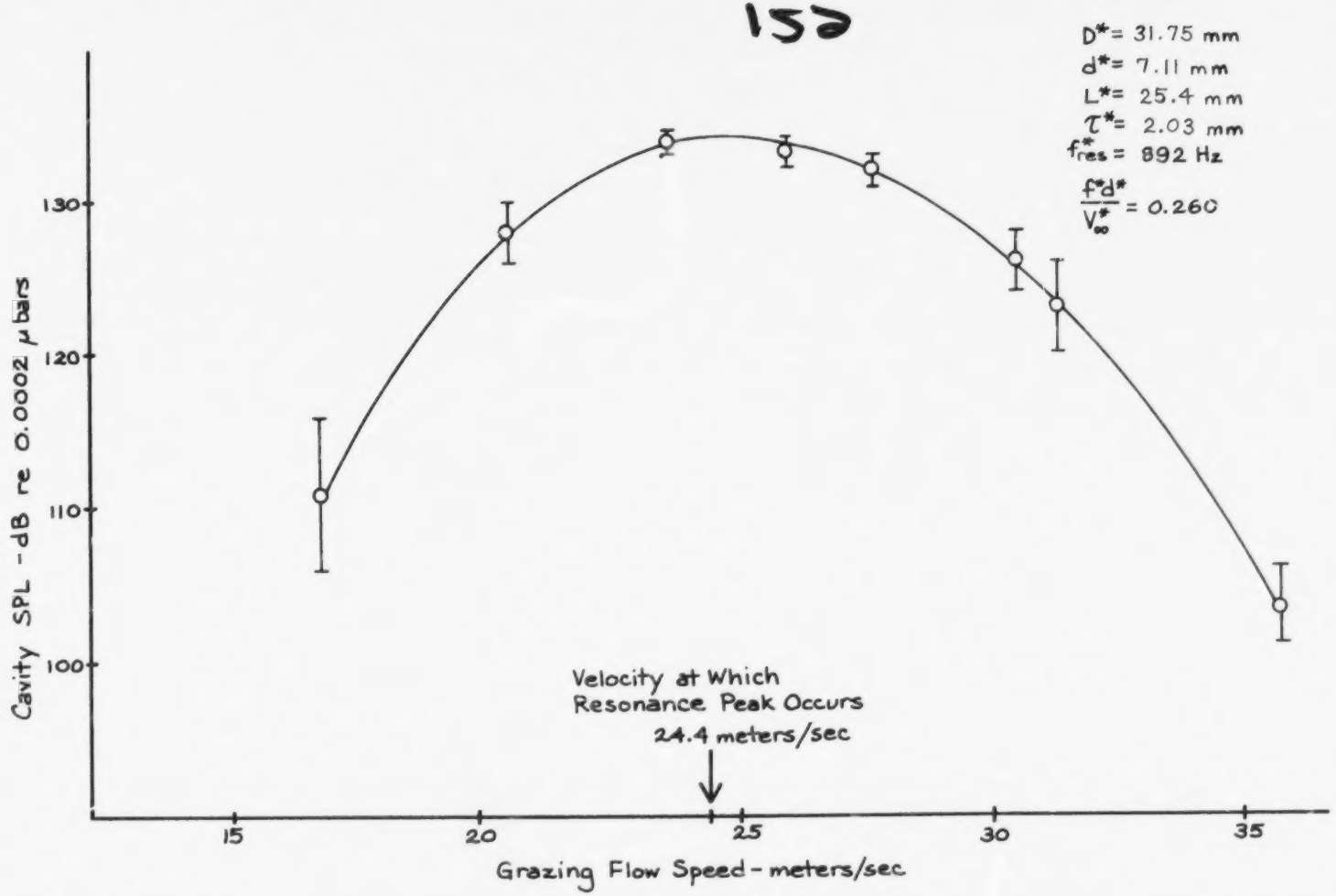

FIGURE 22. MEASUREMENT OF GRAZING FLOW VELOCITY WHERE HYDRODYNAMIC RESONANCE OCCURS

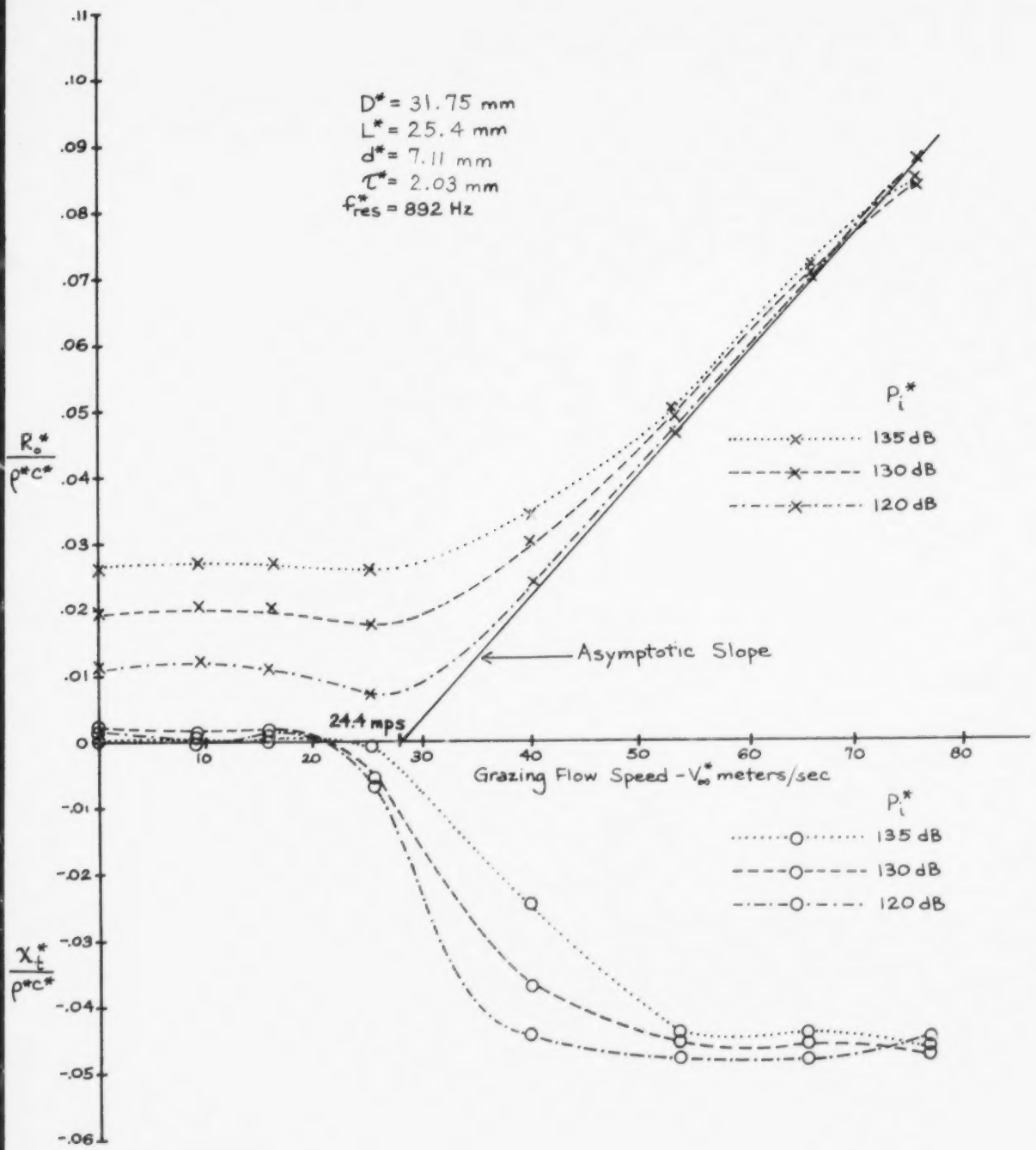

FIGURE 23a. CORRELATION BETWEEN MEASURED AND PREDICTED RESONANT GRAZING FLOW SPEED OF MODEL I

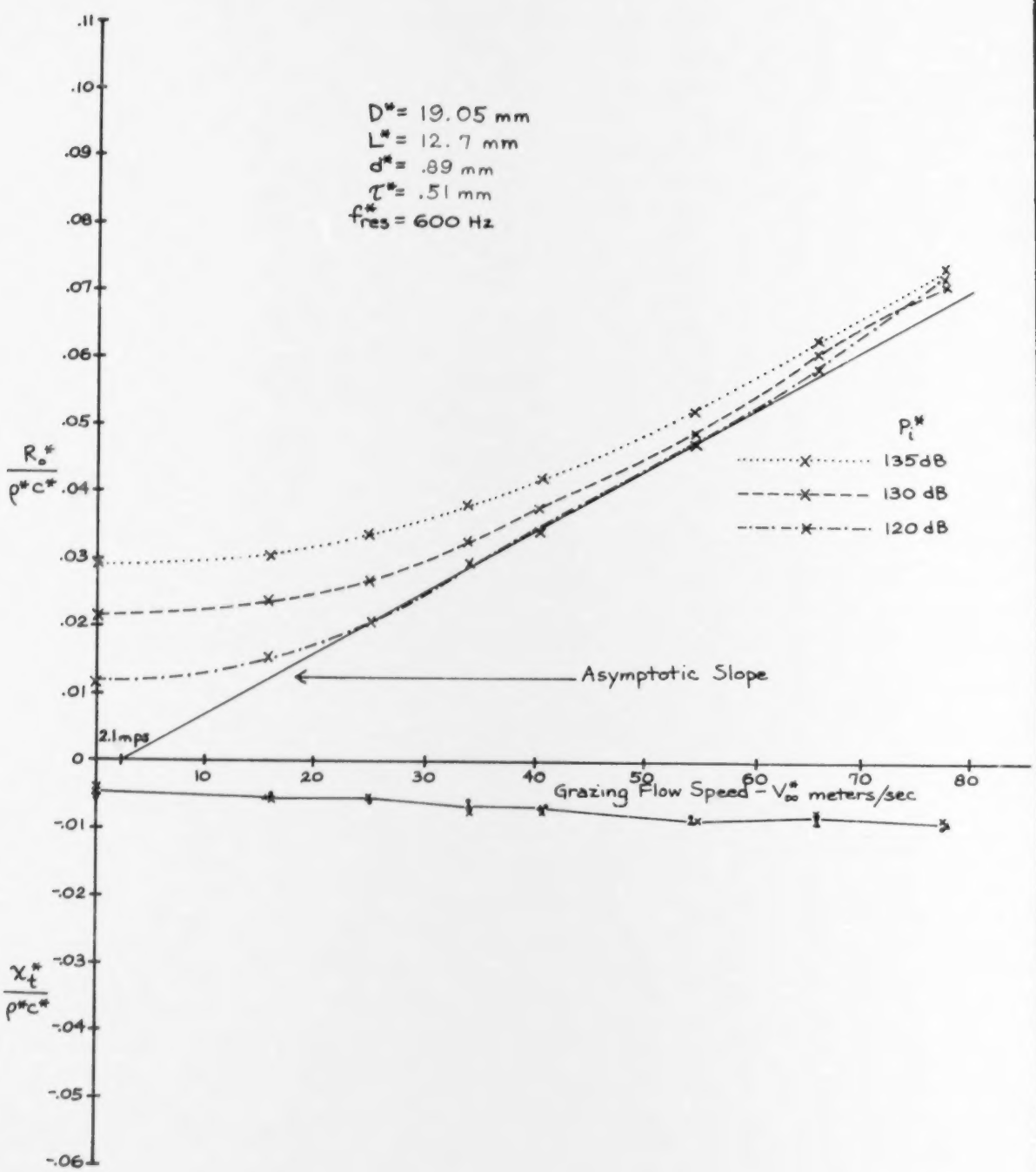

FIGURE 23b. CORRELATION BETWEEN MEASURED AND PREDICTED RESONANT GRAZING FLOW SPEED OF MODEL 5

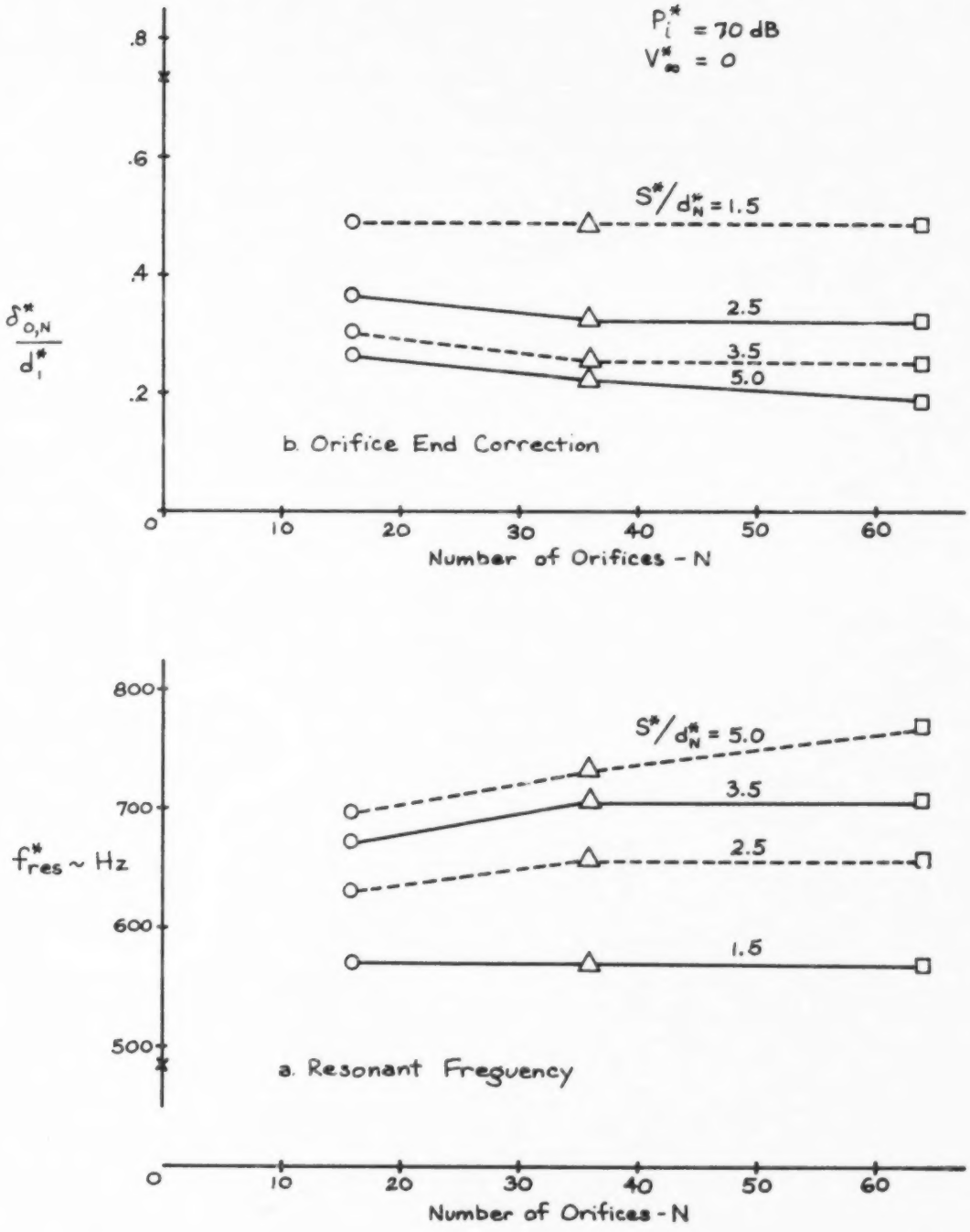

FIGURE 24. EFFECT OF NUMBER OF ORIFICES ON RESONANT FREQUENCY AND ORIFICE END CORRECTION FOR $V_\infty^*=0$ and $P_i^*=70$ dB

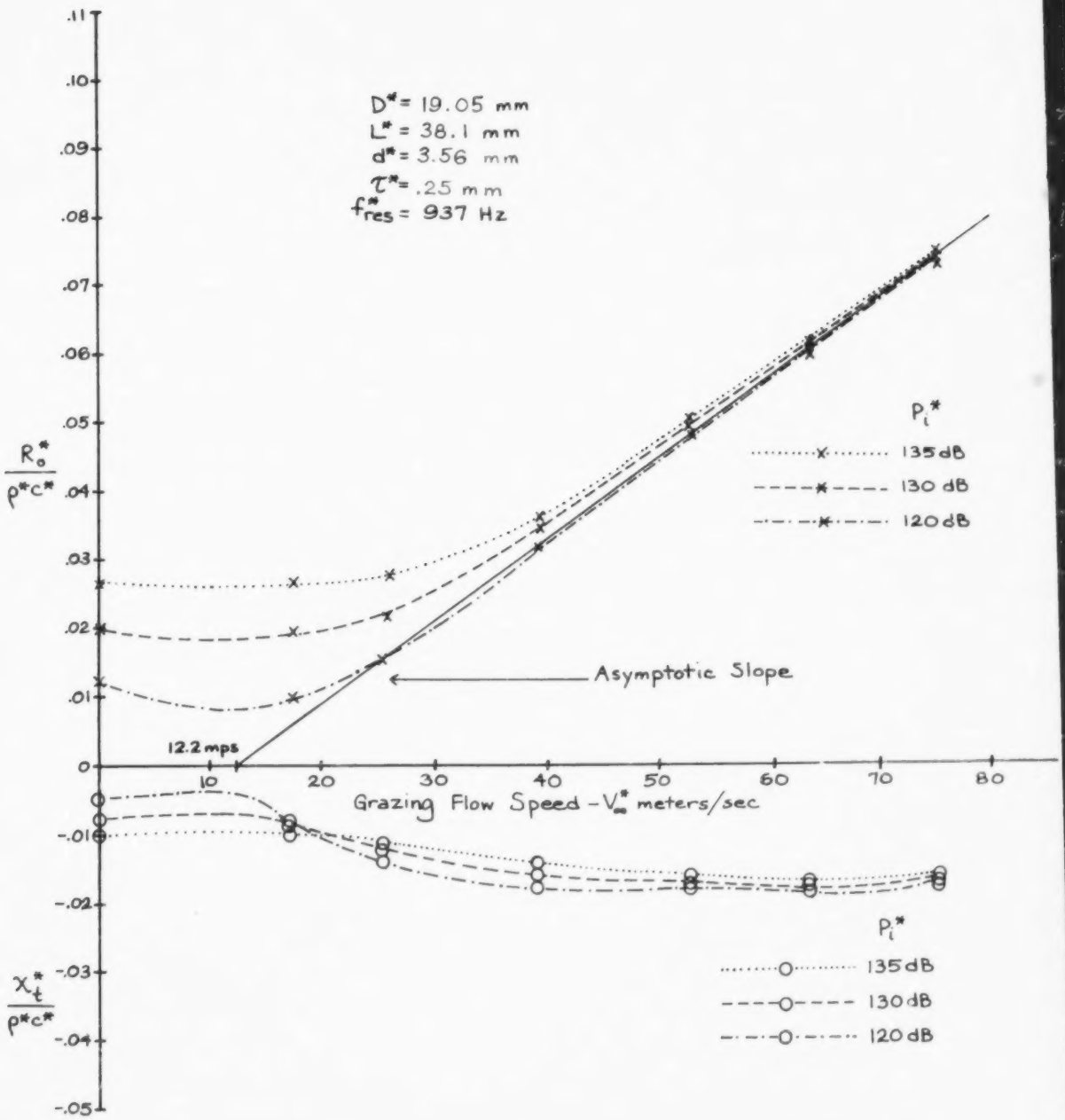

FIGURE 23c. CORRELATION BETWEEN MEASURED AND PREDICTED RESONANT GRAZING FLOW SPEED OF MODEL 6

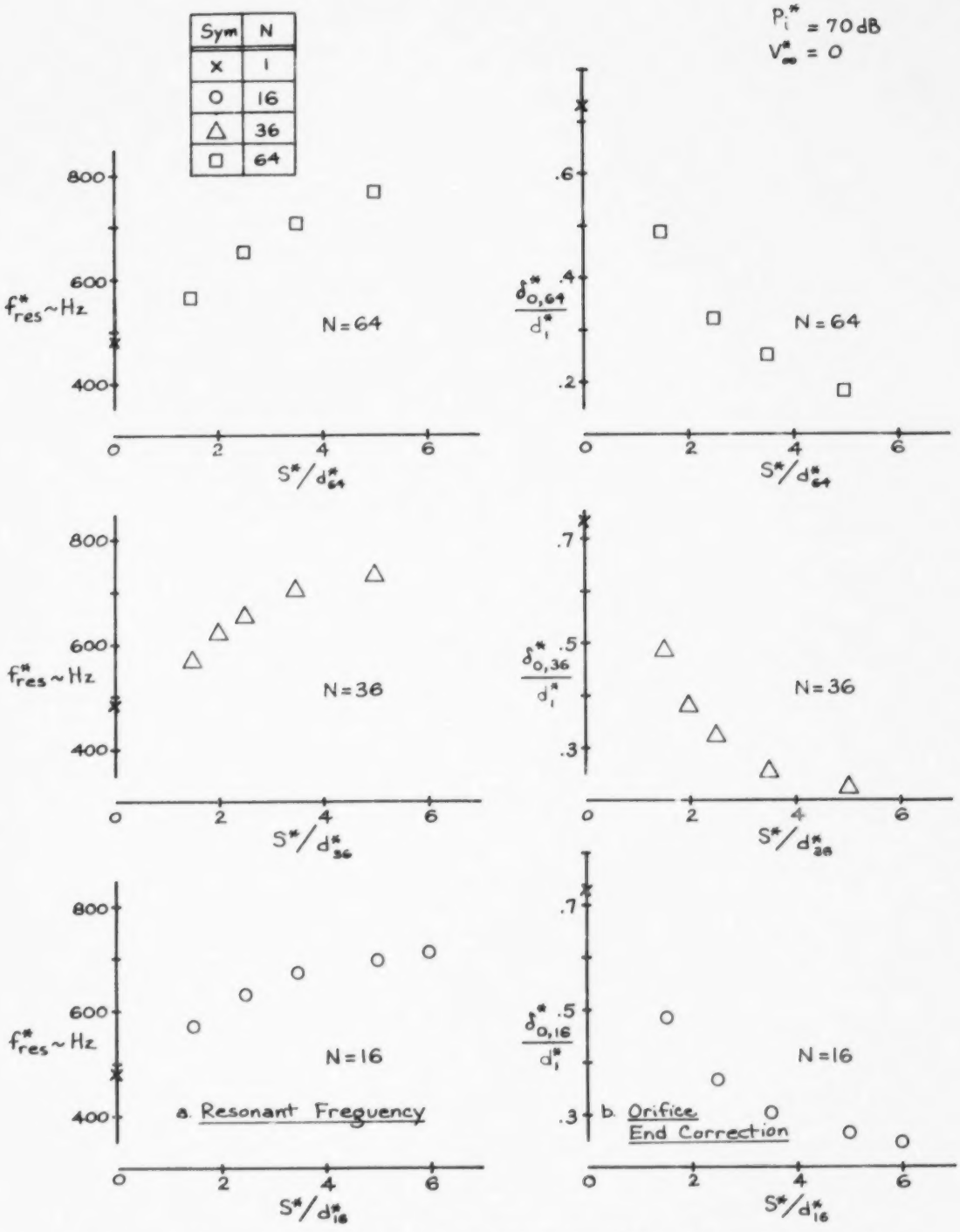

FIGURE 25(a,b) EFFECT OF ARRAY SPACING ON RESONANT FREQUENCY AND ORIFICE END CORRECTION FOR $V_\infty^*=0$ AND $P_i^*=70$ dB

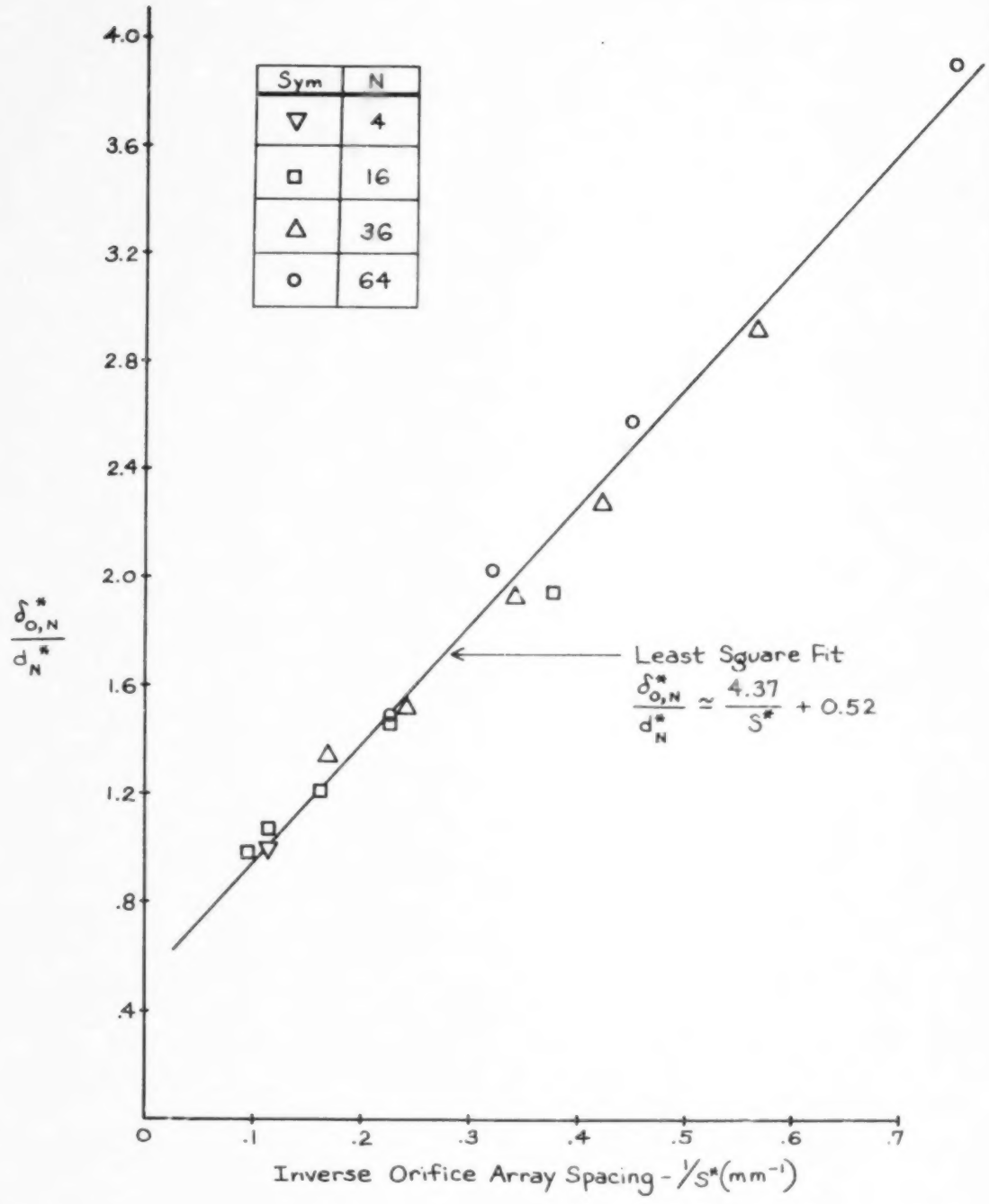

FIGURE 25c. EFFECT OF ARRAY SPACING ON ORIFICE END CORRECTION FOR $V_\infty{}^*=0$ AND $P_i{}^*=70$ dB

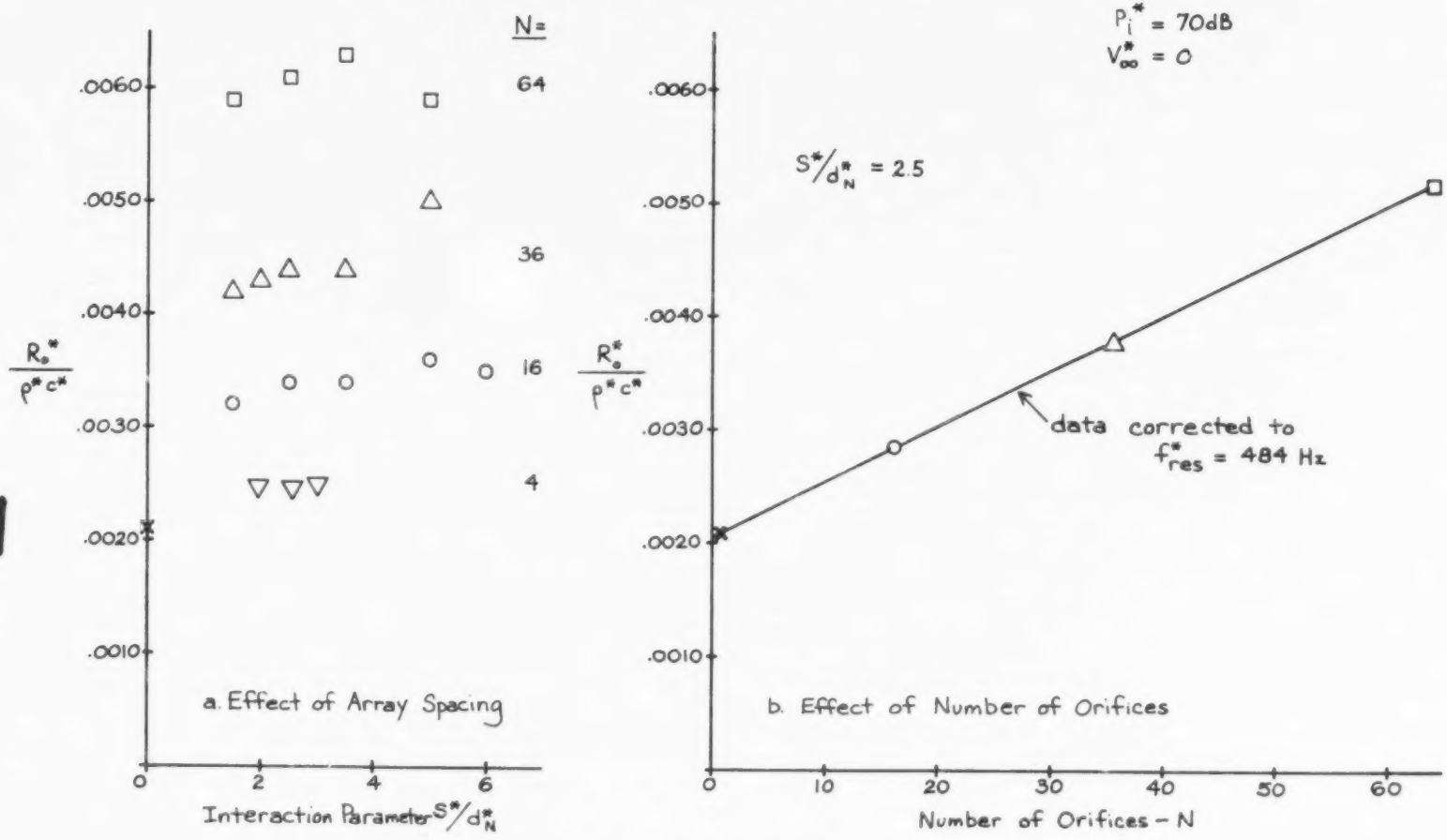

FIGURE 26. EFFECT OF ARRAY SPACING AND NUMBER OF ORIFICES ON THE ORIFICE AREA-AVERAGED RESISTANCE FOR V_∞^*=0 AND P_i^*=70 dB

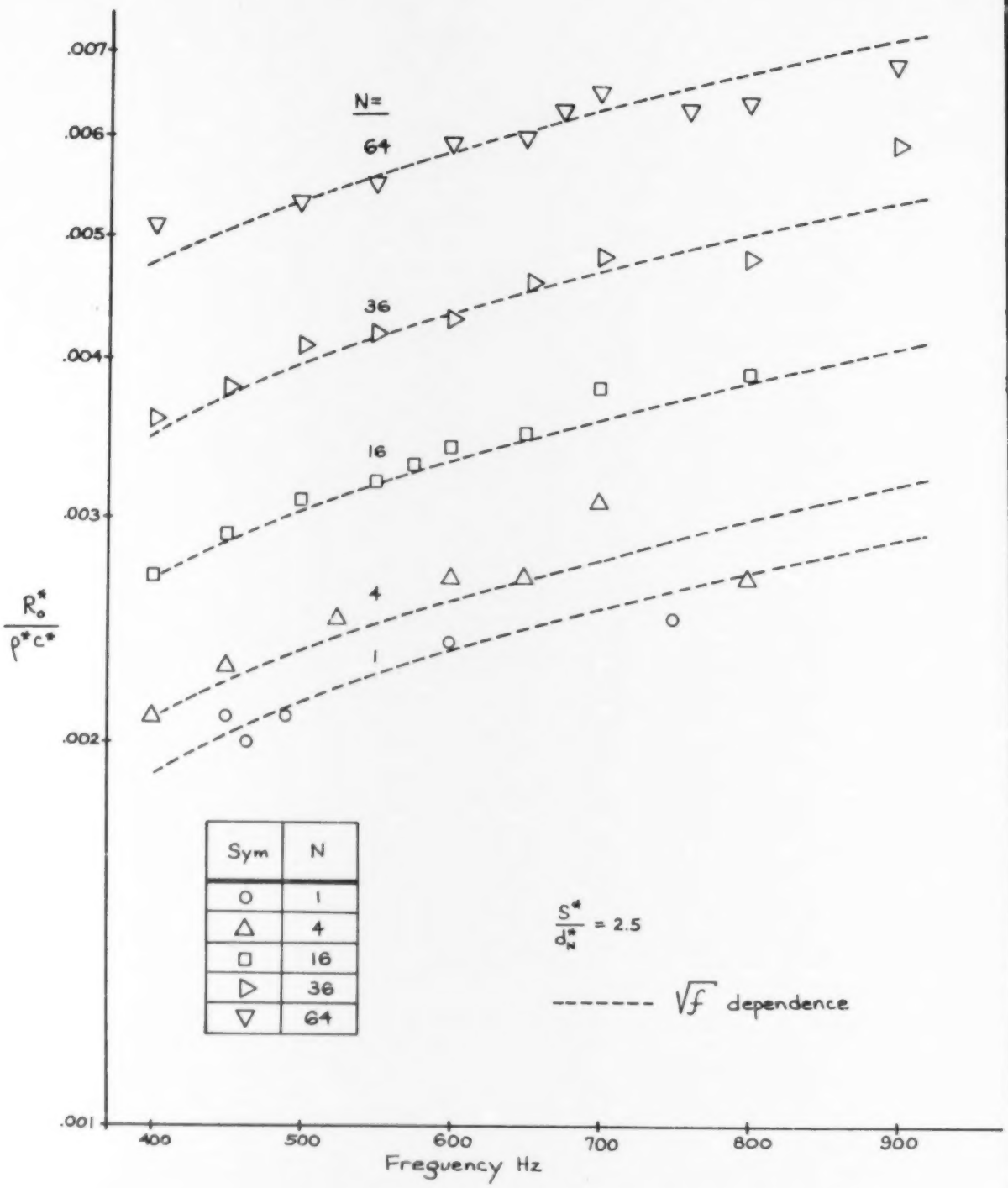

FIGURE 27. EFFECT OF FREQUENCY VARIATION ON THE ORIFICE AREA-AVERAGED RESISTANCE FOR THE N=1, 4, 16, 36 AND 64 CONFIGURATION FOR $V_\infty^*=0$, $P_C^*=70$ dB

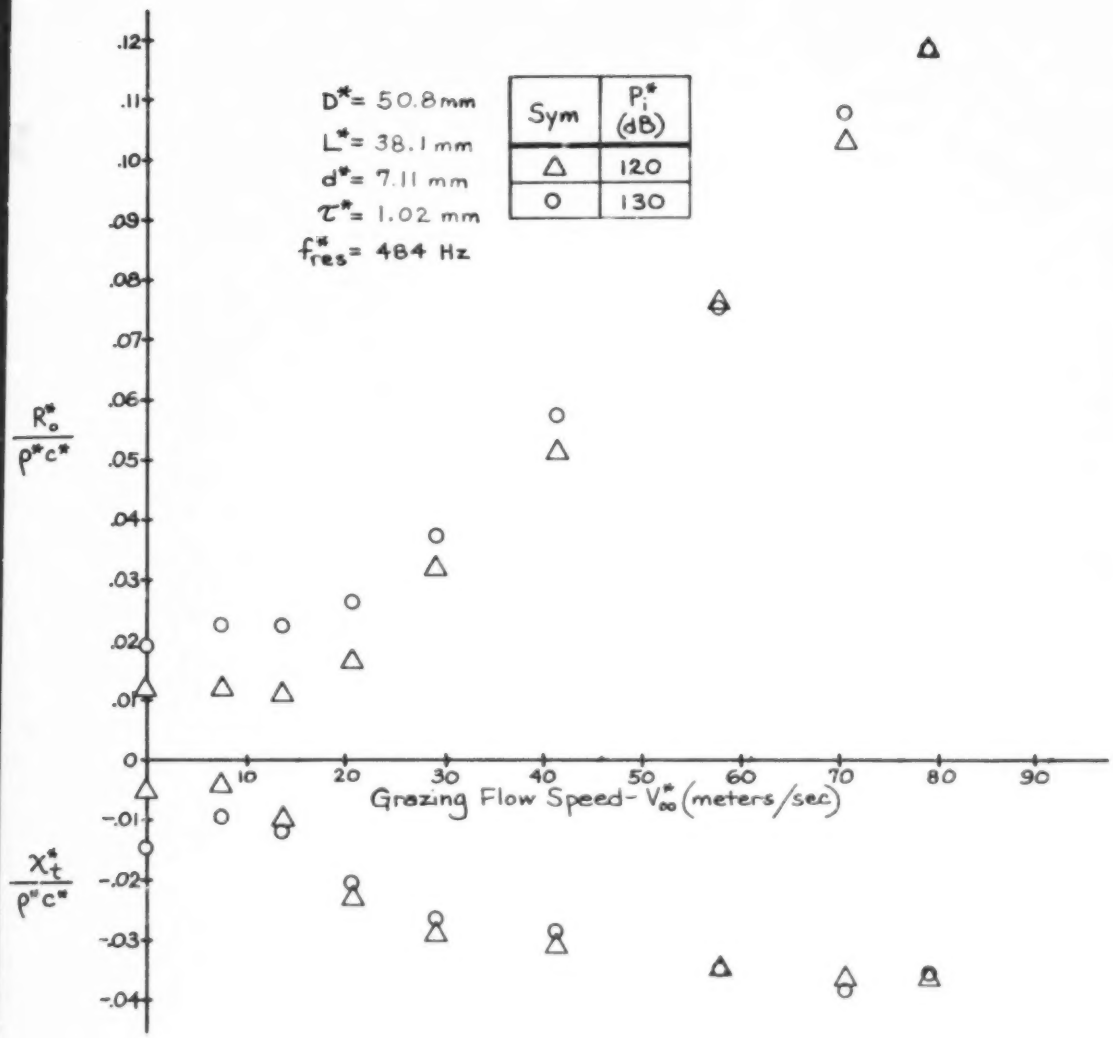

FIGURE 28. EFFECT OF GRAZING FLOW ON THE ORIFICE AREA-AVERAGED IMPEDANCE OF THE N=1 CONFIGURATION

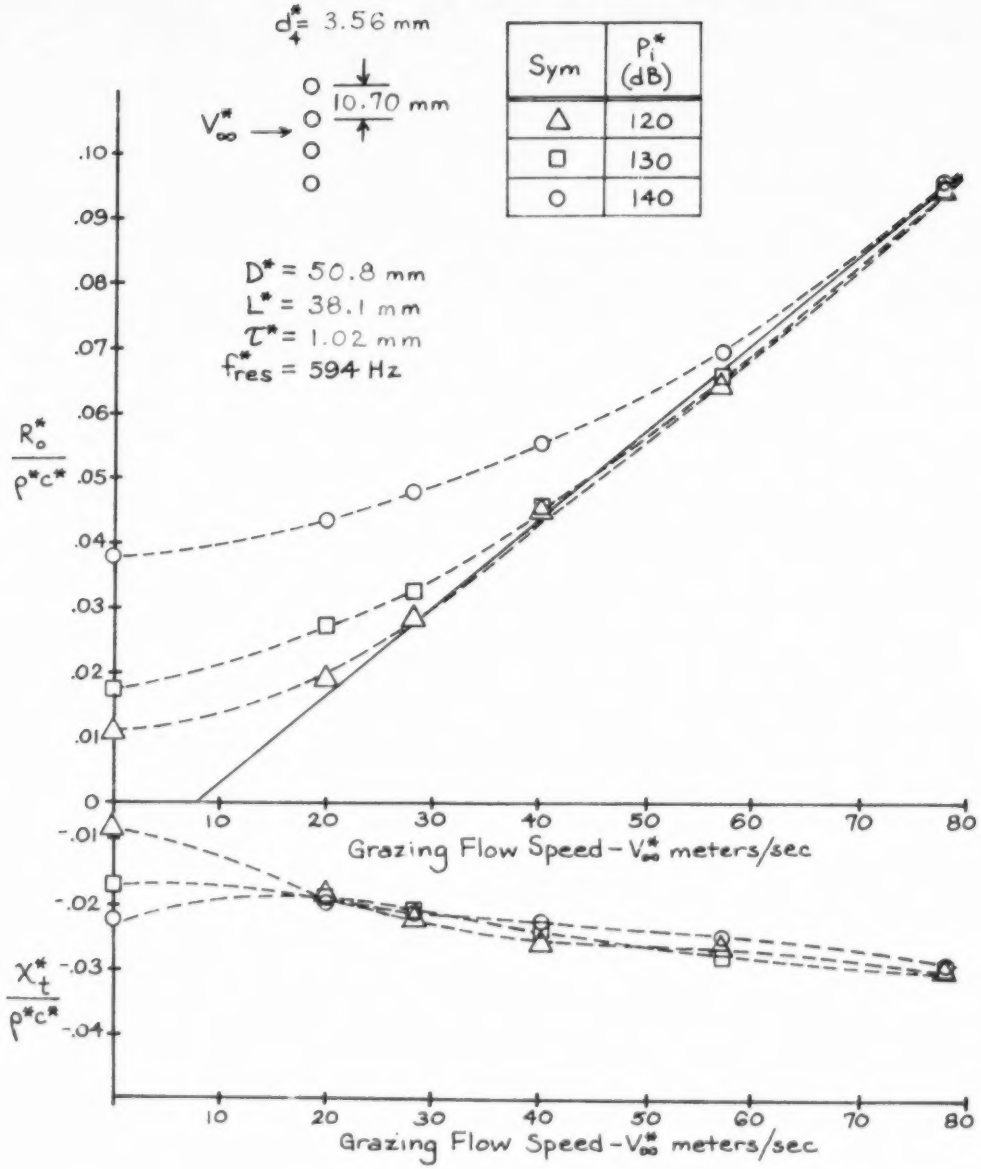

FIGURE 29a. EFFECT OF GRAZING FLOW ON THE IMPEDANCE OF THE PERPENDICULARLY ORIENTATED FOUR-ORIFICE ARRAY CONFIGURATION - $S^*/d_4^* = 3.0$

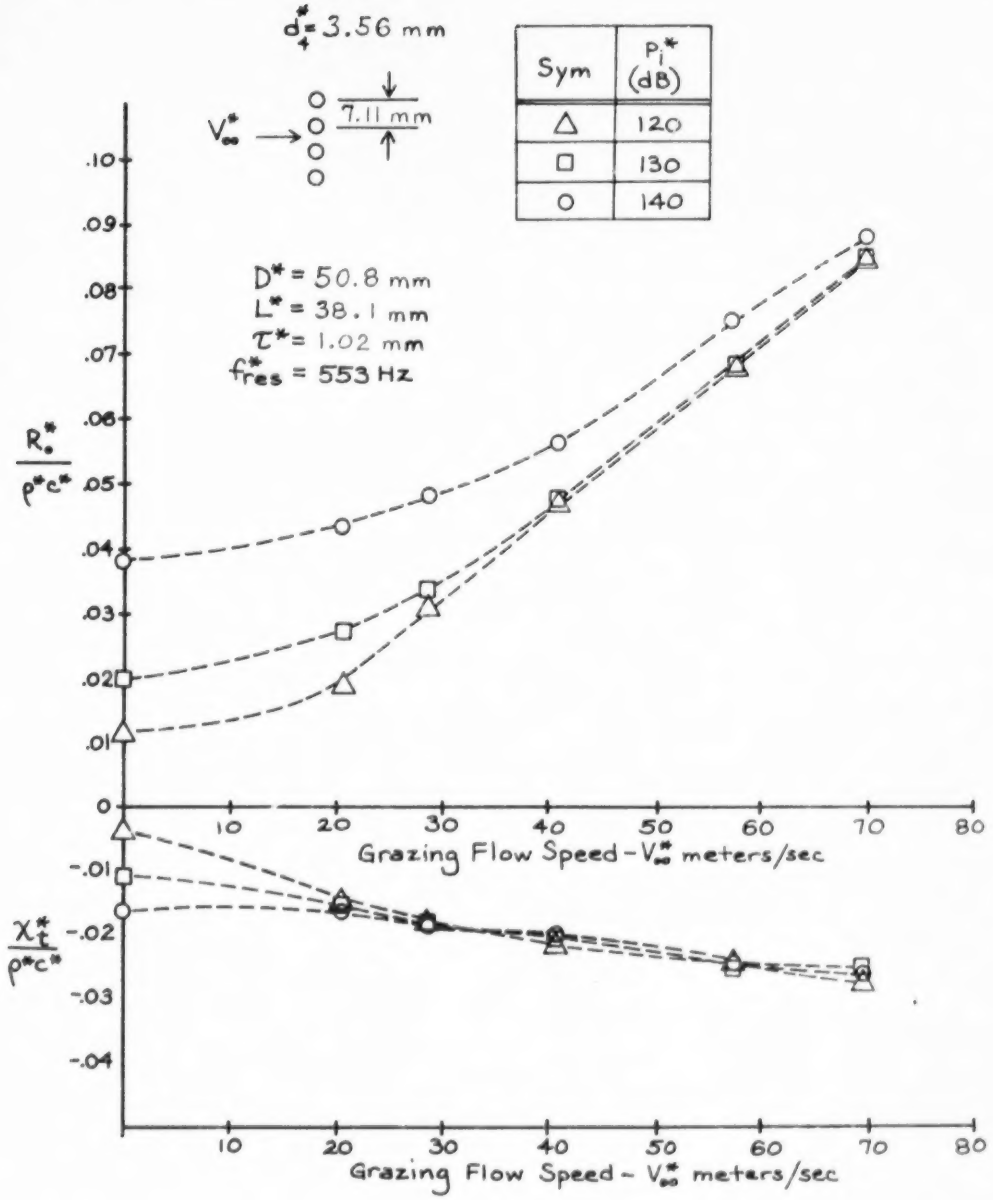

FIGURE 29b. EFFECT OF GRAZING FLOW ON THE IMPEDANCE OF THE PERPENDICULARLY ORIENTATED FOUR-ORIFICE ARRAY CONFIGURATION - $S^*/d_4^* = 2.0$

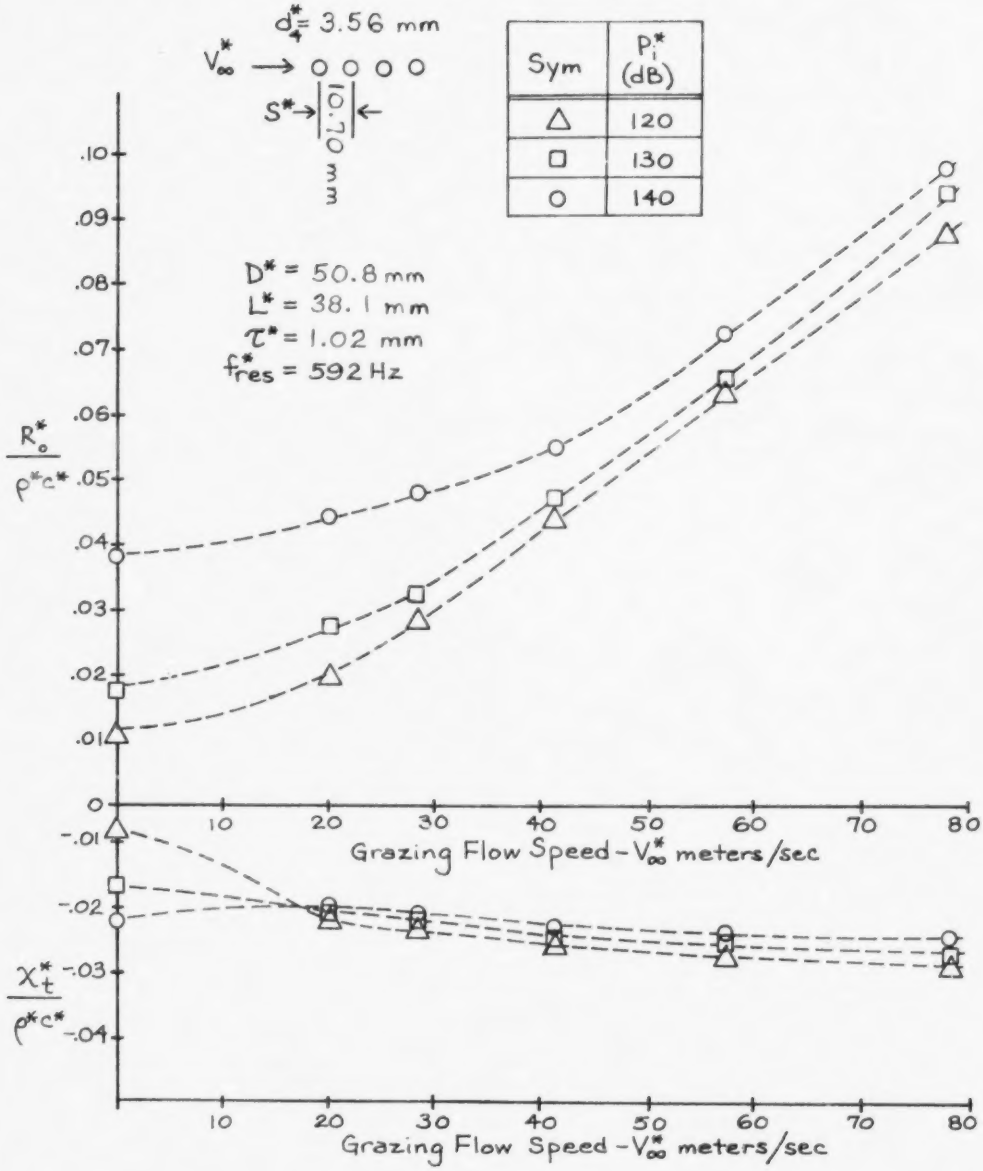

FIGURE 29c. EFFECT OF GRAZING FLOW ON THE IMPEDANCE OF THE COLINEARLY ORIENTATED FOUR-ORIFICE ARRAY CONFIGURATION - $S^*/d_4^* = 3.0$

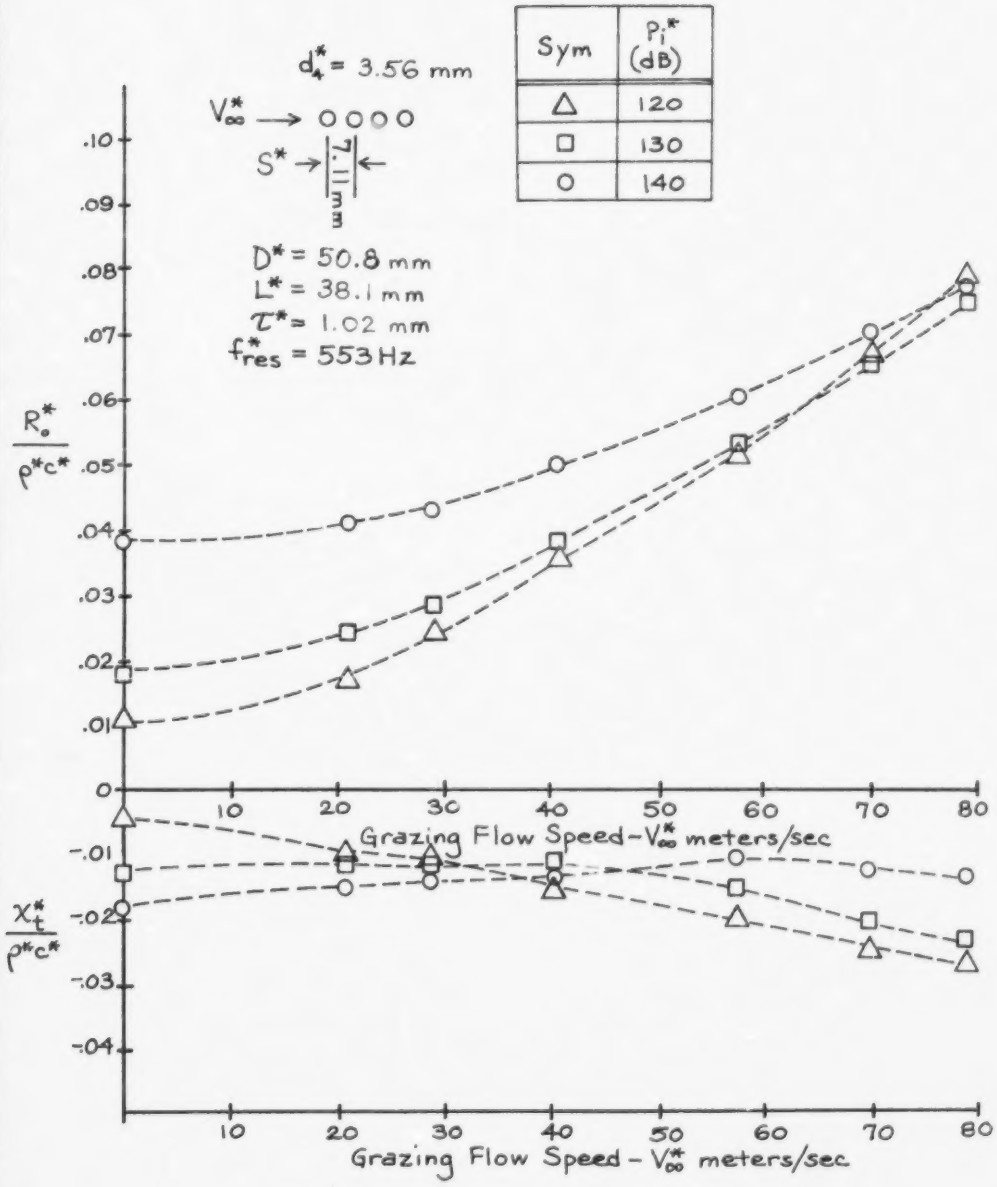

FIGURE 29d. EFFECT OF GRAZING FLOW ON THE IMPEDANCE OF THE COLINEARLY ORIENTATED FOUR-ORIFICE ARRAY CONFIGURATION - $S^*/d_4^* = 2.0$

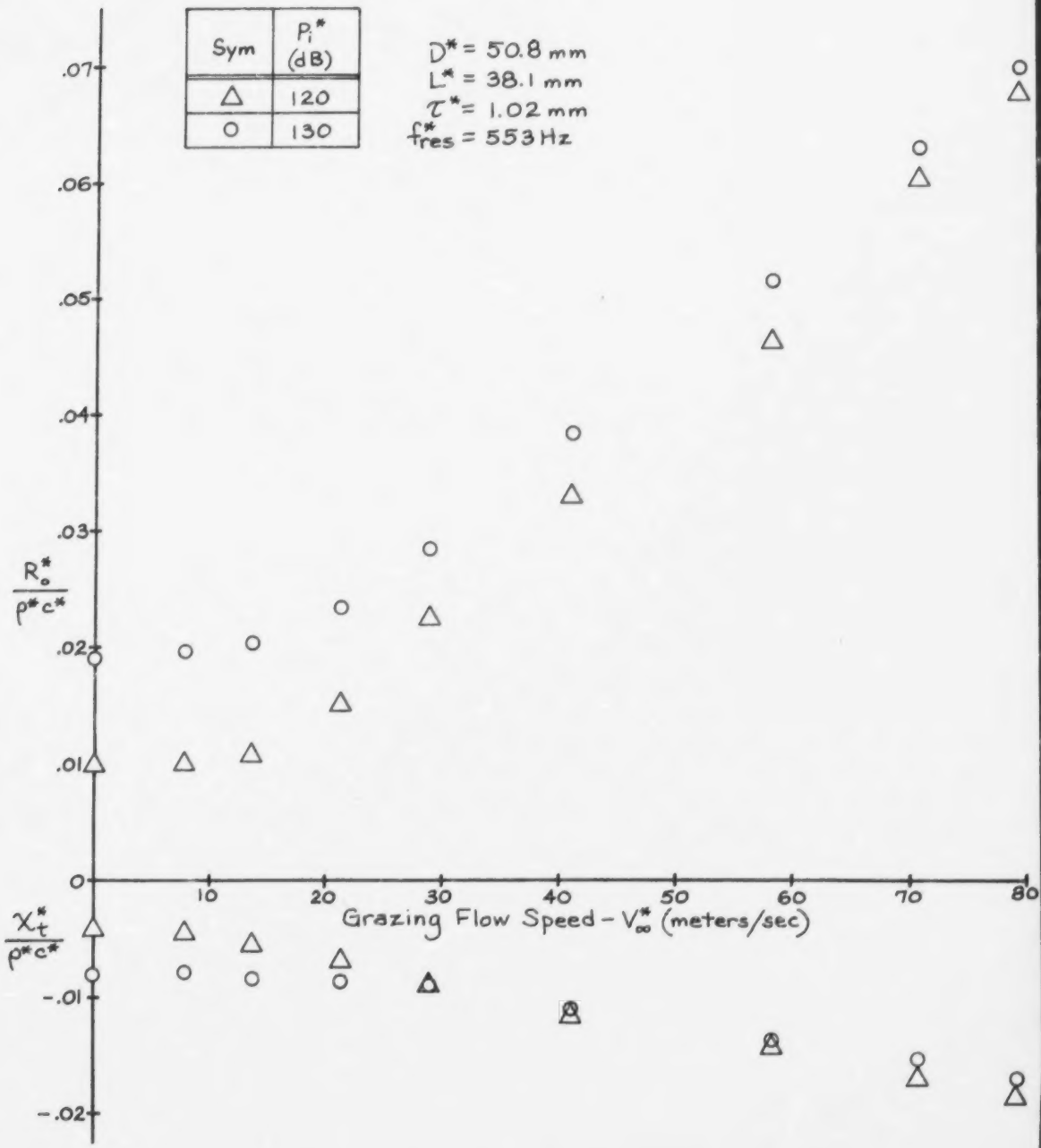

FIGURE 30a. EFFECT OF GRAZING FLOW ON THE ORIFICE AREA-AVERAGED IMPEDANCE OF THE N=16, $S^*/d_{16}^*=2.5$ CONFIGURATION

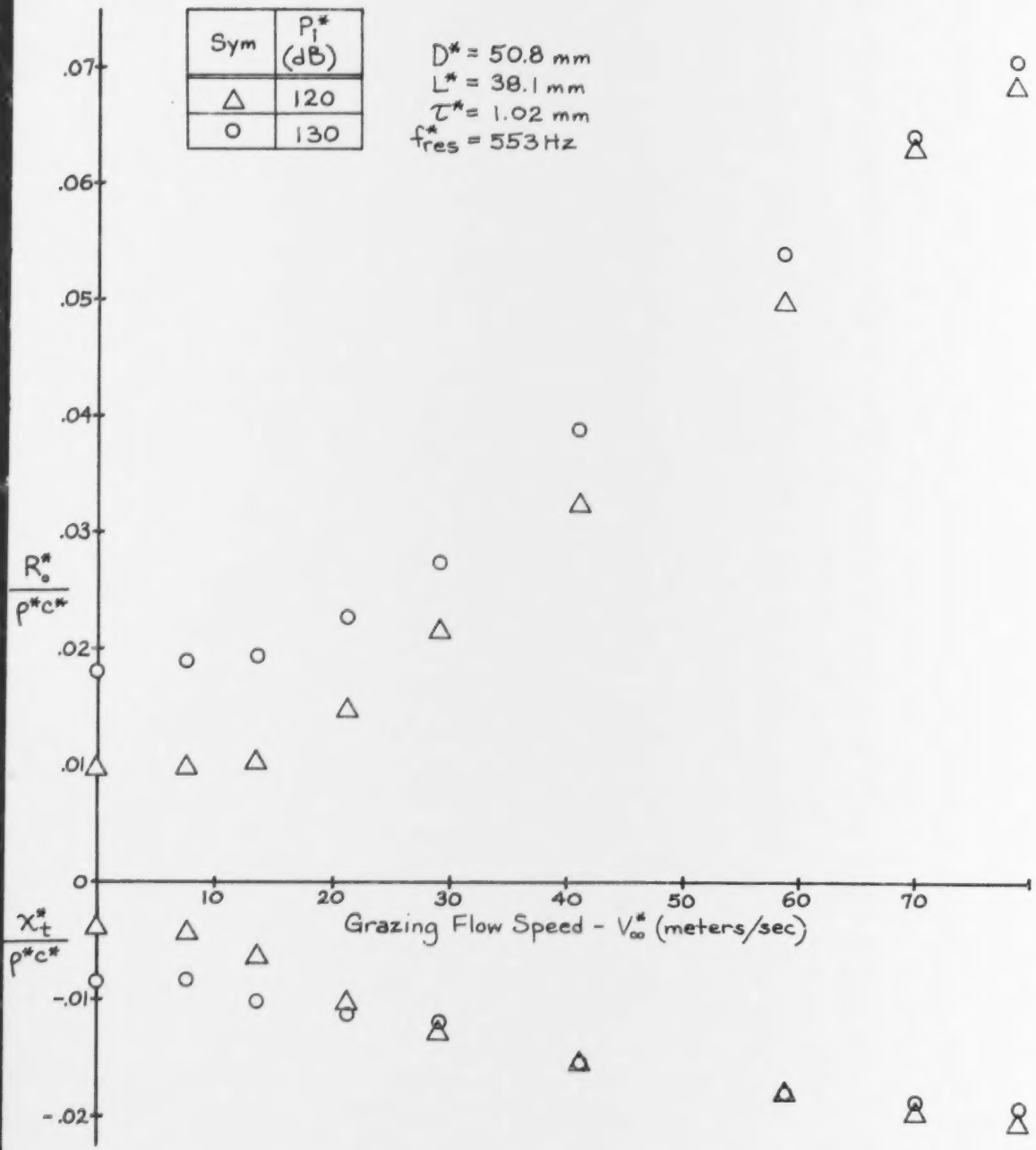

FIGURE 30b. EFFECT OF GRAZING FLOW ON THE ORIFICE AREA-AVERAGED IMPEDANCE OF THE N=16, $S^*/d_{16}^*=5$ CONFIGURATION

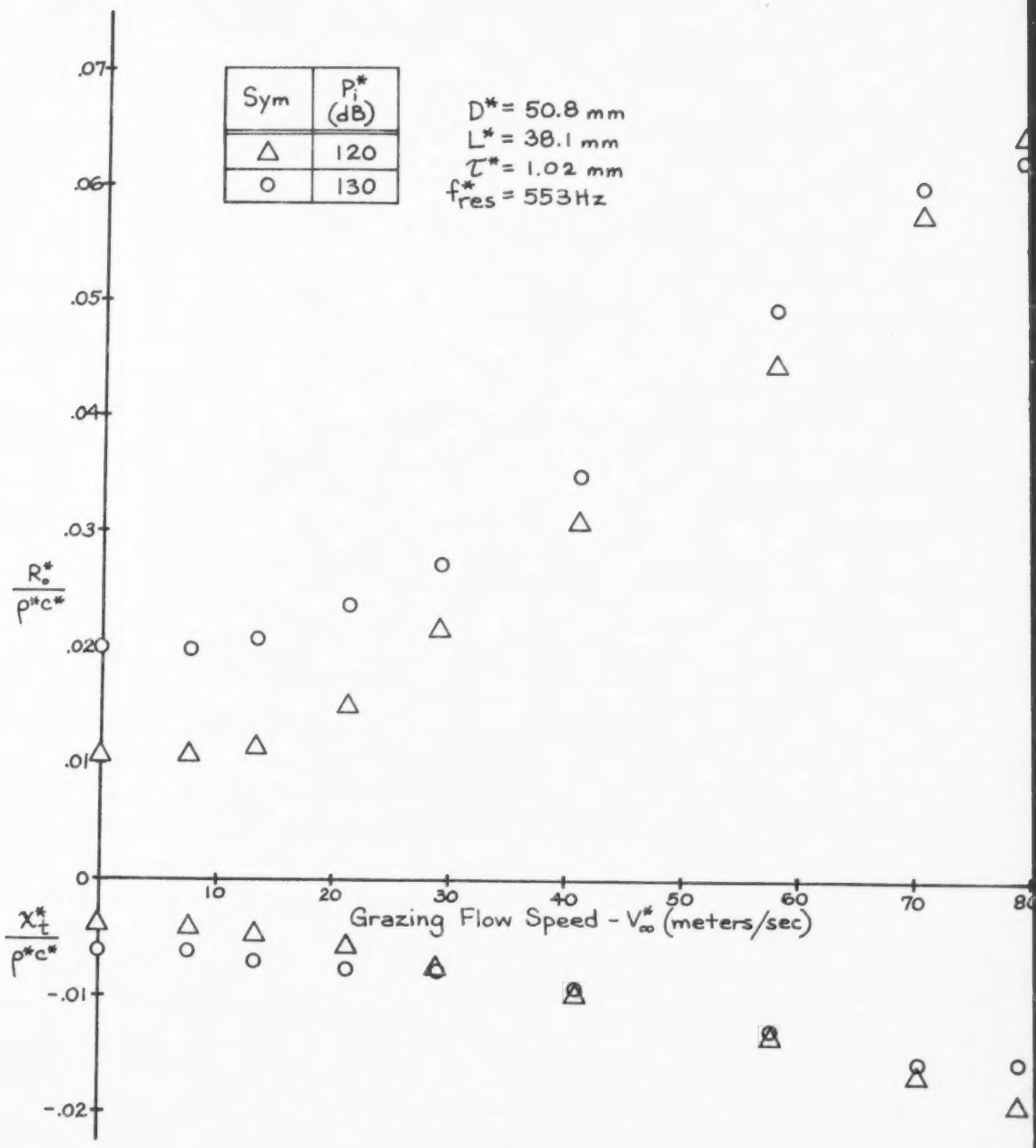

FIGURE 31a. EFFECT OF GRAZING FLOW ON THE ORIFICE AREA-AVERAGED IMPEDANCE OF THE N=36, $S^*/d_{36}^* = 2.5$ CONFIGURATION

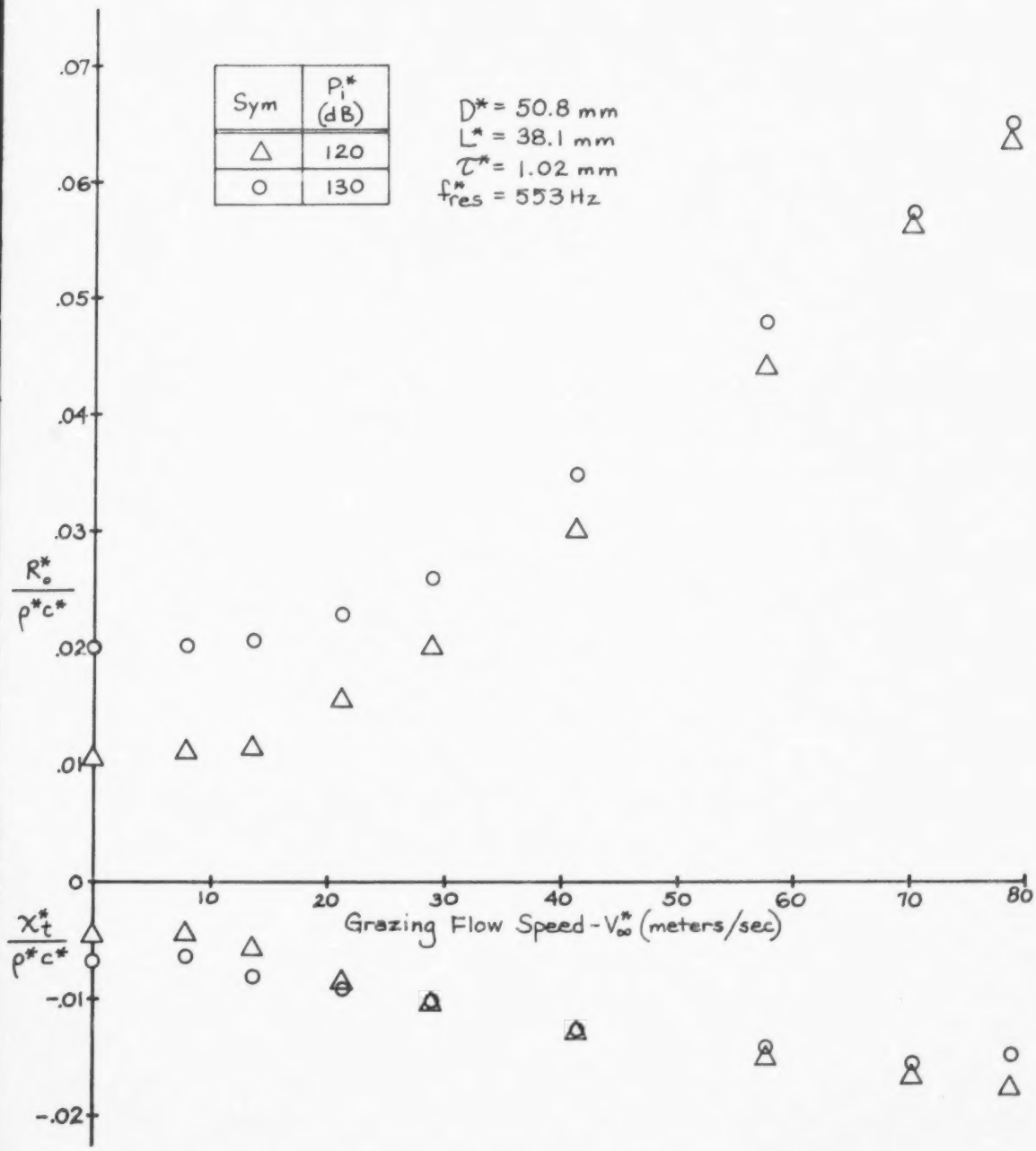

FIGURE 31b. EFFECT OF GRAZING FLOW ON THE ORIFICE AREA-AVERAGED IMPEDANCE OF THE N=36, $S^*/d_{36}^* = 5$ CONFIGURATION

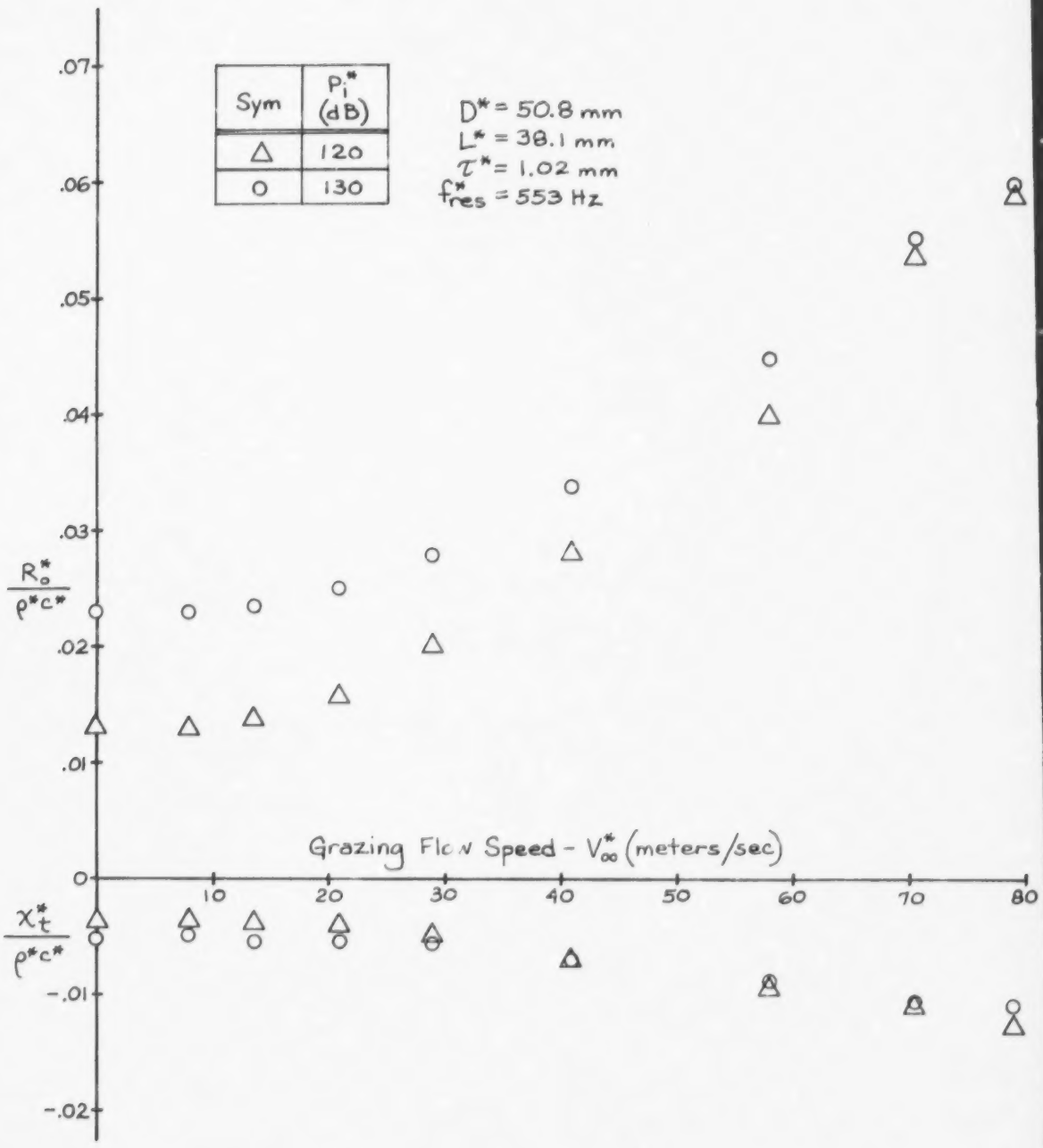

FIGURE 32a. EFFECT OF GRAZING FLOW ON THE ORIFICE AREA-AVERAGED IMPEDANCE OF THE N=64, $S^*/d_{64}^* = 2.5$ CONFIGURATION

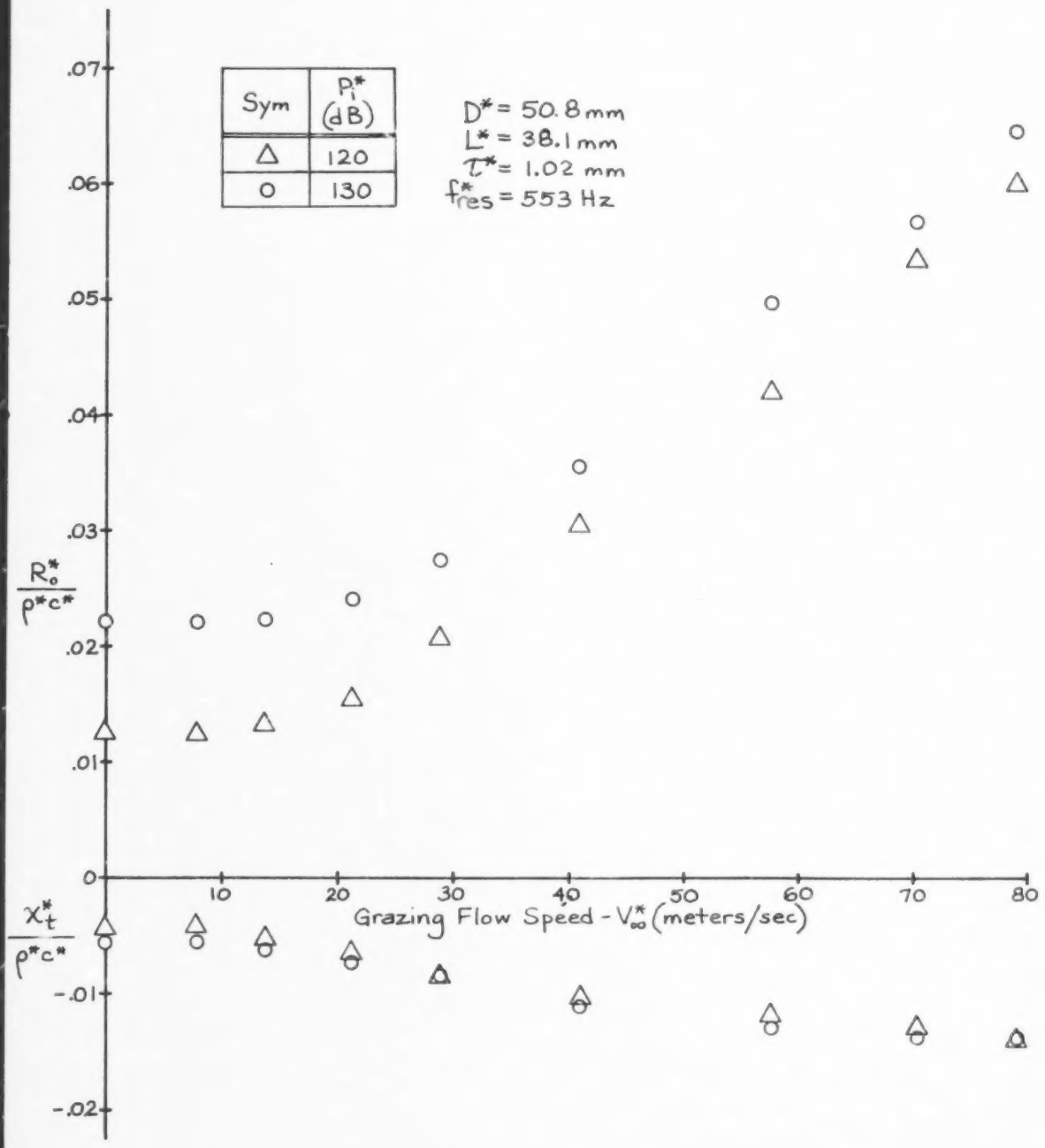

FIGURE 32b. EFFECT OF GRAZING FLOW ON THE ORIFICE AREA-AVERAGED IMPEDANCE OF THE N=64, $S^*/d_{64}^* = 5$ CONFIGURATION

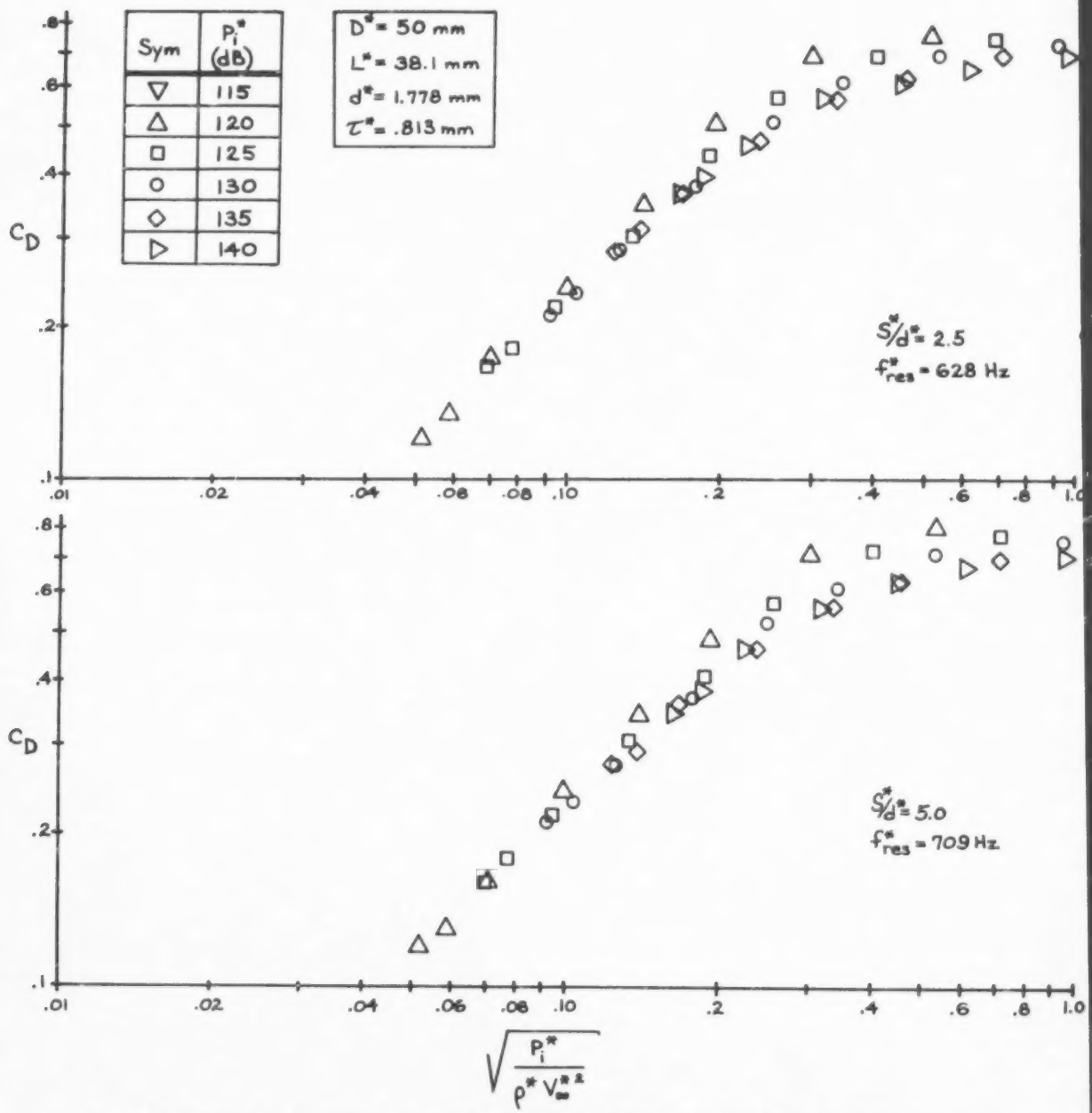

FIGURE 33(a,b) CORRELATION OF ORIFICE ARRAY SPACING DATA FOR N=16 IN TERMS OF DISCHARGE COEFFICIENT

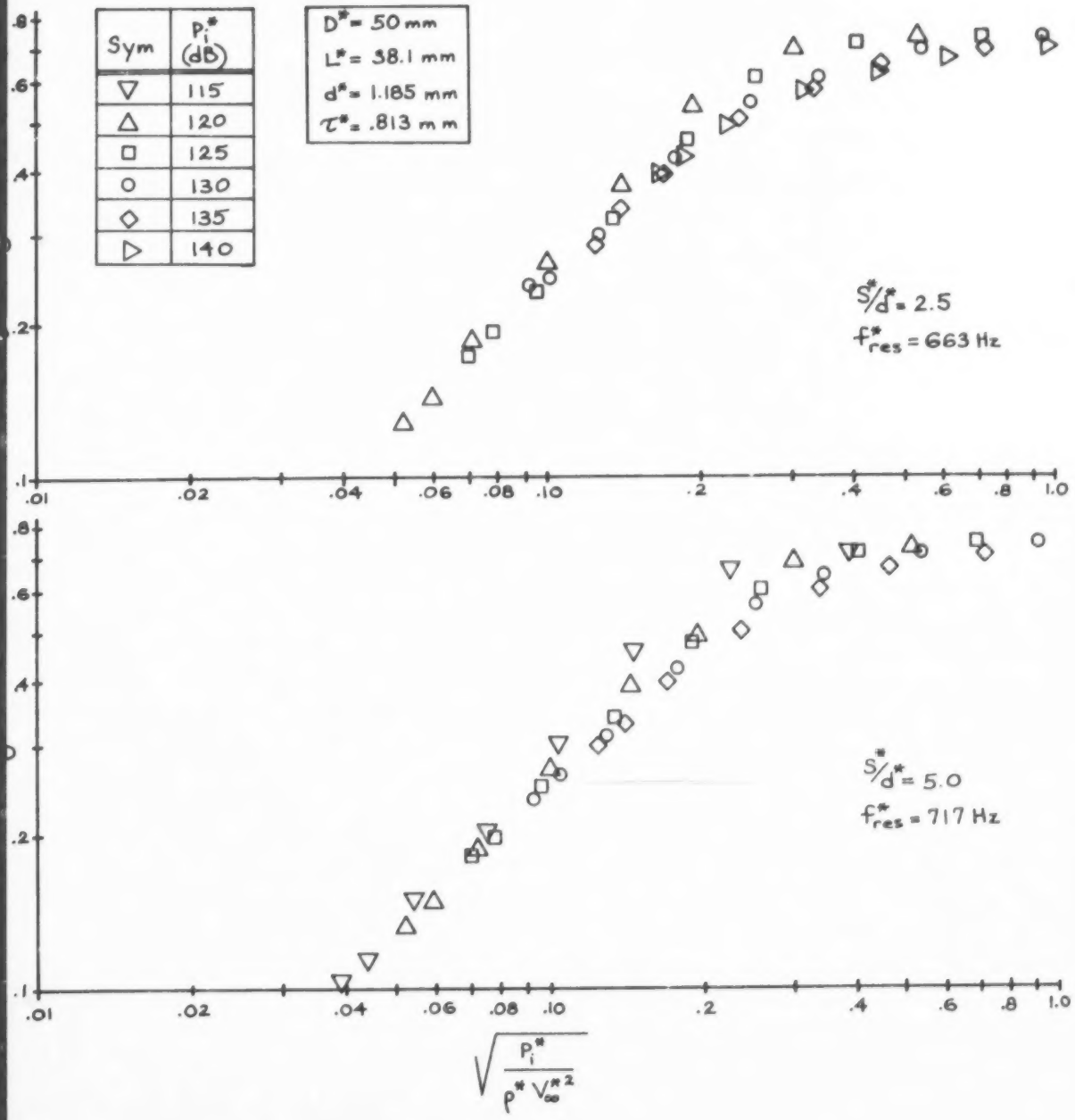

FIGURE 34(a,b) CORRELATION OF ORIFICE ARRAY SPACING DATA FOR N=36 IN TERMS OF DISCHARGE COEFFICIENT

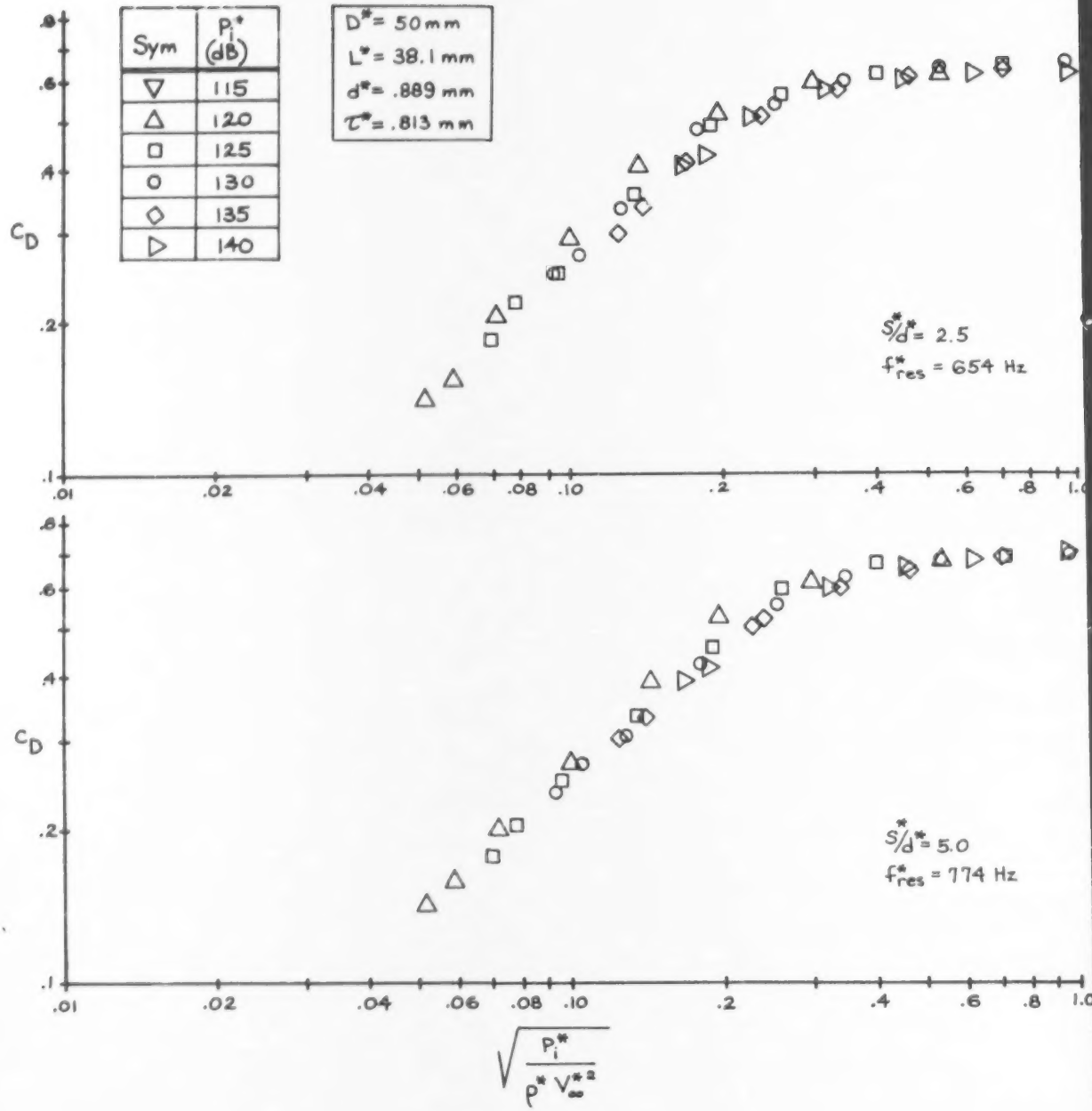

FIGURE 35(a,b). CORRELATION OF ORIFICE ARRAY SPACING DATA FOR N=64 IN TERMS OF DISCHARGE COEFFICIENT

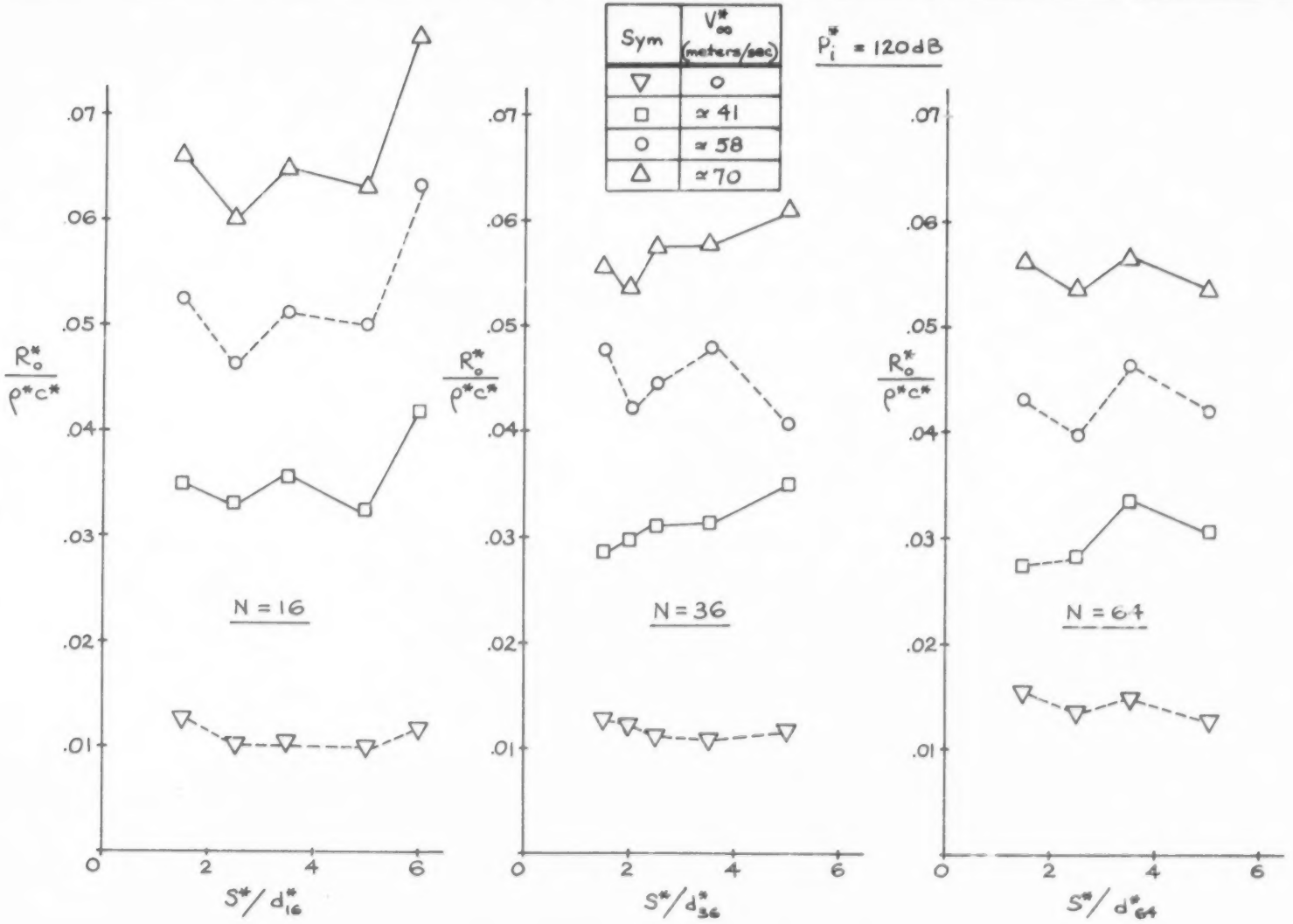

FIGURE 36. EFFECT OF ARRAY SPACING ON ORIFICE AREA-AVERAGED RESISTANCE FOR N=16, 36 AND 64 CONFIGURATIONS

TABLE OF CONTENTS

	SUMMARY	1	1/A5
	DEFINITION OF SYMBOLS	2	1/A6
1.	INTRODUCTION	5	1/A9
2.	SINCLE ORIFICE IMPEDANCE MODEL	7	1/A11
	2.1 Derivation of Governing Equations	8	1/A12
	2.2 Boundary Conditions	12	1/B2
	2.3 Semi-empirical Solution	13	1/B3
3.	SINGLE ORIFICE MEASUREMENT PROGRAM	17	1/B7
	3.1 Two-Microphone Method	18	1/B8
	3.2 Determination of C_D	20	1/B10
	3.3 Comparison Between Predicted and Measured Impedance	25	1/C1
	3.4 Thick Orifices	29	1/C5
	3.5 Resonator Self-Noise	31	1/C7
4.	IMPEDANCE OF CLUSTERED ORIFICES	32	1/C8
	4.1 Zero Grazing Flow, Low Sound Amplitude Results	33	1/C9
	4.2 Effect of Grazing Flow	35	1/C11
5.	CONCLUSIONS	38	1/C14
	APPENDIXES		
	A - SINGLE ORIFICE DATA	40	1/D2
	B - SUMMARY OF FREQUENCY SWEEP DATA FOR SPECIAL MODEL FOR $V_\alpha^* = 60$ m/sec and $P_i^* = 120$ dB	66	1/E14
	C - THICK ORIFICE DATA	67	1/F1
	D - CLUSTERED ORIFICE DATA	76	1/F10
	REFERENCES	104	2/A11
	TABLES	106	2/A13
	FIGURES	110	2/B4

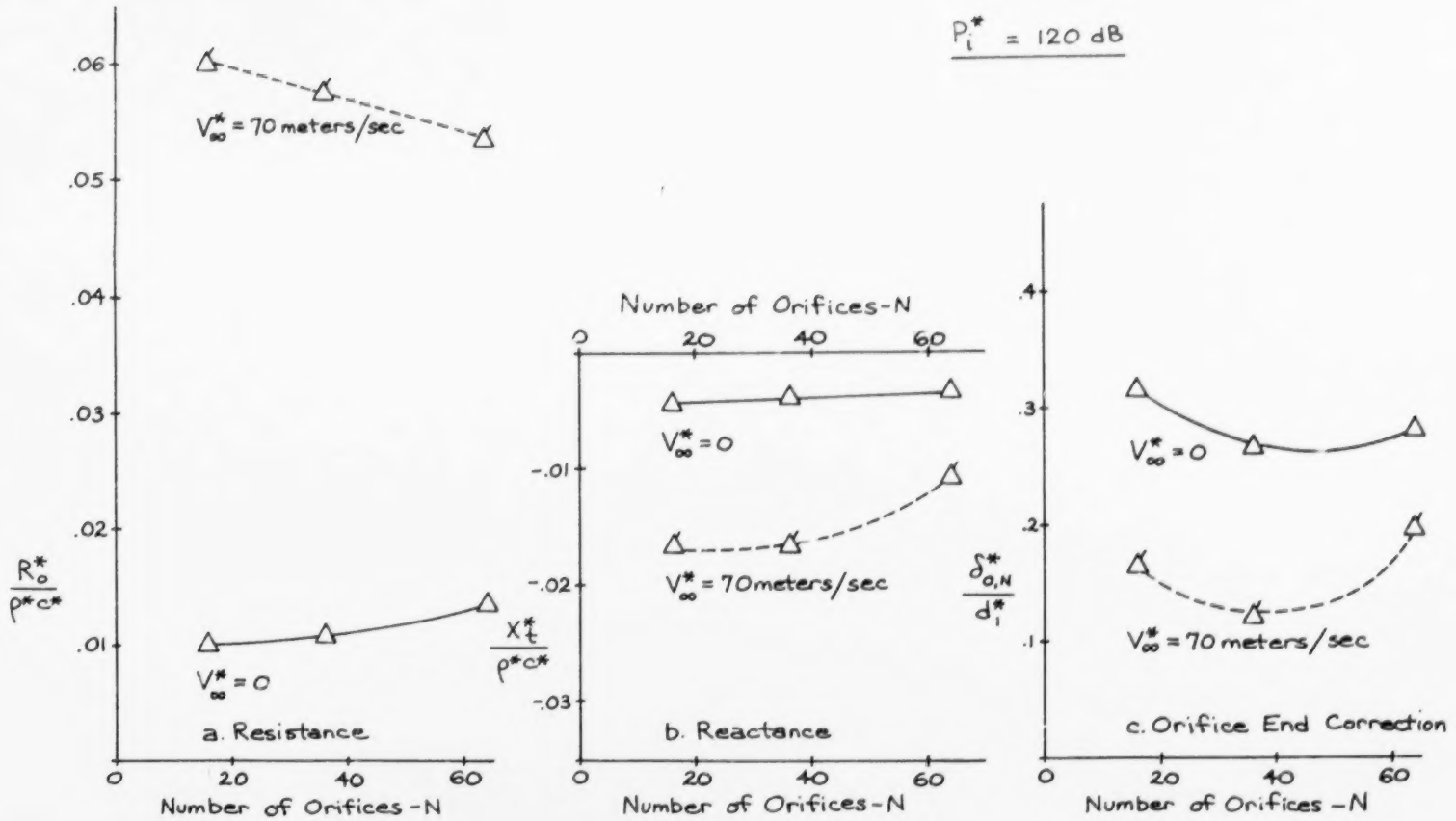

FIGURE 37. EFFECT OF NUMBER OF ORIFICES ON THE ORIFICE AREA-AVERAGED IMPEDANCE FOR $S^*/d_N^* = 2.5$

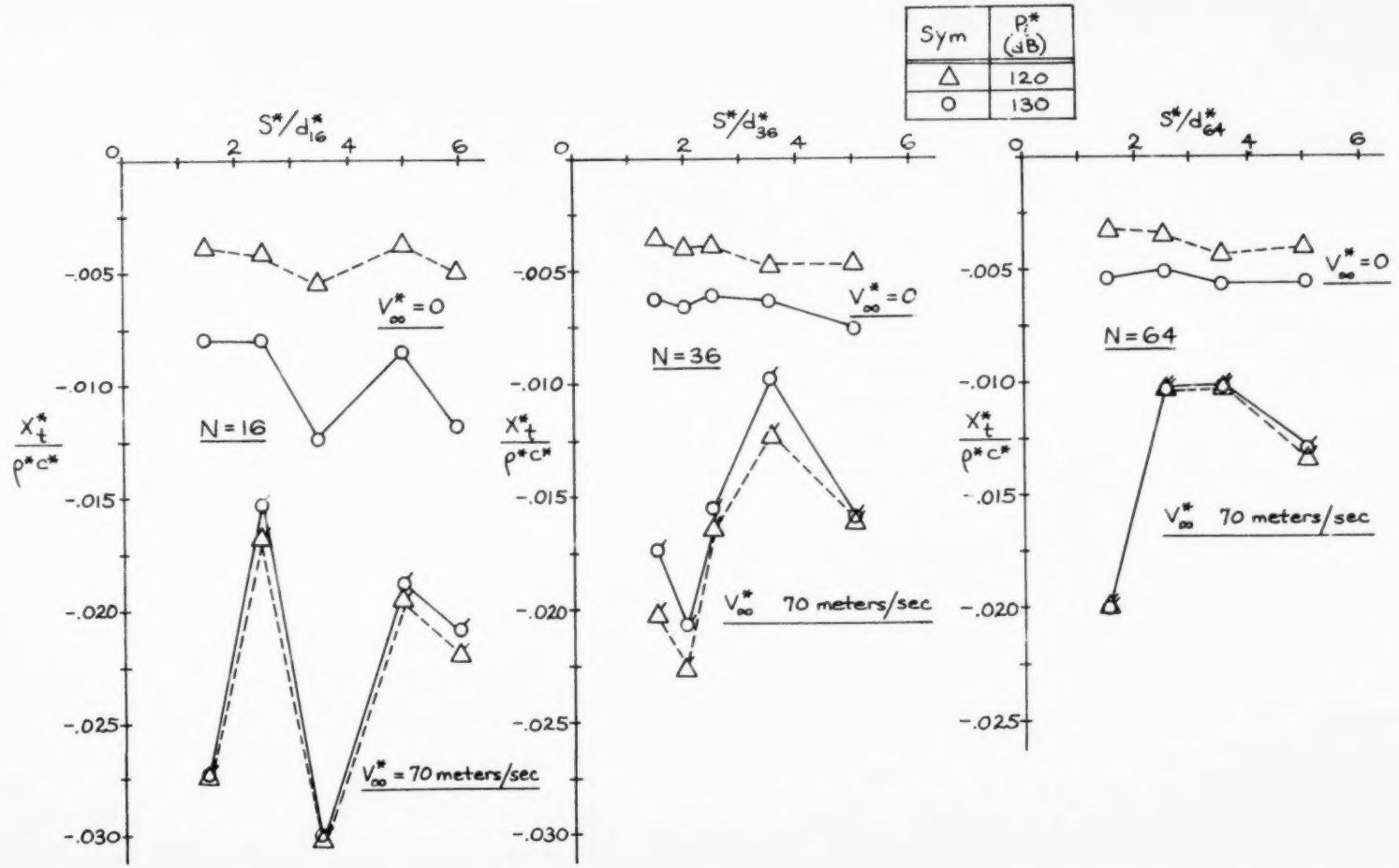

FIGURE 38. EFFECT OF ARRAY SPACING ON THE ORIFICE AREA-AVERAGED REACTANCE FOR THE N=16, 36 AND 64 CONFIGURATIONS

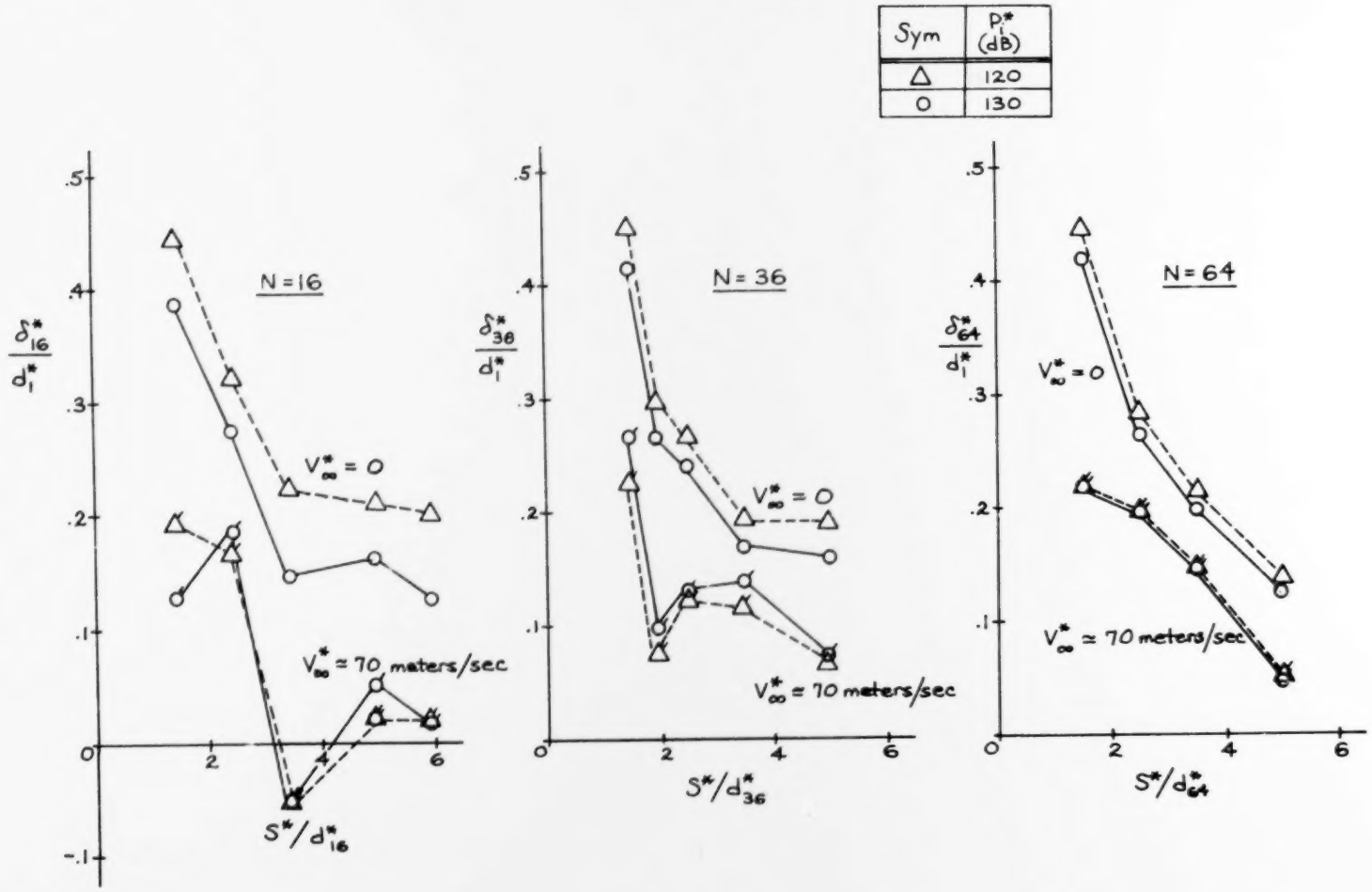

FIGURE 39. EFFECT OF ARRAY SPACING ON THE ORIFICE END CORRECTION FOR THE N=16, 36 AND 64 CONFIGURATIONS

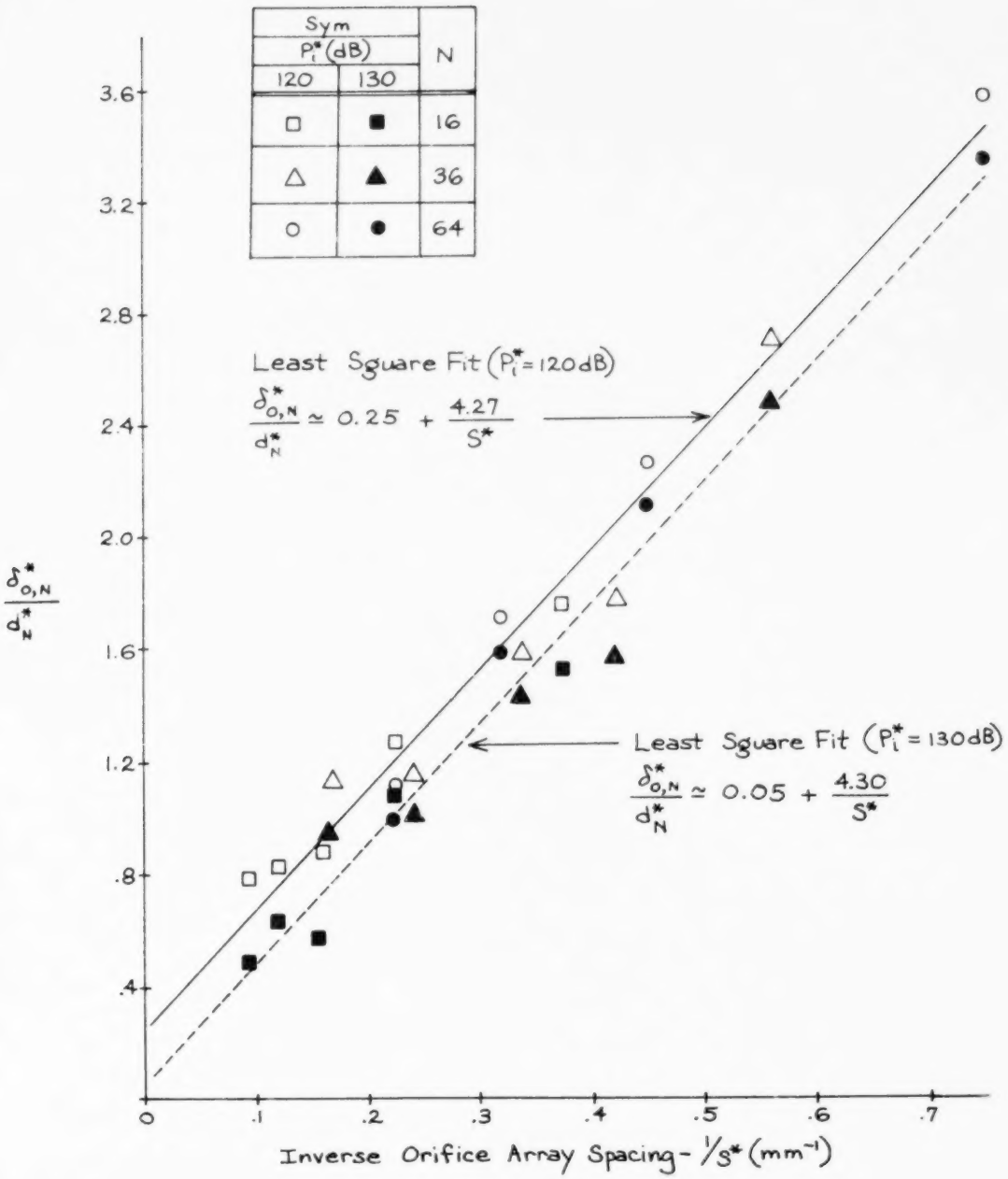

FIGURE 40. EFFECT OF ARRAY SPACING ON ORIFICE END CORRECTION FOR V_∞^*=0 and P_i^*=120, 130 dB

1. Report No. NASA CR-3177	2. Government Accession No.	3. Recipient's Catalog No.
4. Title and Subtitle **EFFECT OF GRAZING FLOW ON THE ACOUSTIC IMPEDANCE OF HELMHOLTZ RESONATORS CONSISTING OF SINGLE AND CLUSTERED ORIFICES**		5. Report Date August 1979 6. Performing Organization Code
7. Author(s) **Alan S. Hersh and Bruce Walker**		8. Performing Organization Report No. None 10. Work Unit No.
9. Performing Organization Name and Address **Hersh Acoustical Engineering 9545 Cozycroft Avenue Chatsworth, California 91311**		11. Contract or Grant No. NAS3-19745 13. Type of Report and Period Covered Contractor Report
12. Sponsoring Agency Name and Address **National Aeronautics and Space Administration Washington, D.C. 20546**		14. Sponsoring Agency Code

15. Supplementary Notes
Final report. Project Manager, Edward J. Rice, V/STOL and Noise Division, NASA Lewis Research Center, Cleveland, Ohio 44135.

16. Abstract

A semiempirical fluid mechanical model is derived for the acoustic behavior of thin-walled single orifice Helmholtz resonators in a grazing flow environment. The incident and cavity sound fields are connected in terms of an orifice discharge coefficient whose values are determined experimentally using the two-microphone method. Measurements show that at high grazing flow speeds, acoustical resistance is almost linearly proportional to the grazing flow speed and almost independent of incident sound pressure. The corresponding values of reactance are much smaller and tend towards zero. For thicker-walled orifice plates, resistance and reactance were observed to be less sensitive to grazing flow as the ratio of plate thickness to orifice diameter increased. Loud tones were observed to radiate from a single orifice Helmholtz resonator due to interaction between the grazing flow shear layer and the resonator cavity. Measurements showed that the tones radiated at a Strouhal number equal to 0.26. The effects of grazing flow on the impedance of Helmholtz resonators consisting of clusters of orifices was also studied. In general, both resistance and reaction were found to be virtually independent of orifice relative spacing and number. These findings are valid with and without grazing flow.

17. Key Words (Suggested by Author(s))	18. Distribution Statement
Sound absorbers; Acoustics; Nonlinear acoustic impedance; Acoustic impedance; Helmholtz resonators; Grazing flow effects; Helmholtz resonator; Orifice interaction	**Unclassified - unlimited STAR Category 71**

19. Security Classif. (of this report)	20. Security Classif. (of this page)	21. No. of Pages	22. Price*
Unclassified	**Unclassified**	**181**	**A09**

* For sale by the National Technical Information Service, Springfield, Virginia 22161

NASA-Langley, 1979